University of Alberta

SFRC Slabs Longitudinally Reinforced with High Strength Steel

by

Laura Nicole Talboys

A thesis submitted to the Faculty of Graduate Studies and Research
in partial fulfillment of the requirements for the degree of

Master of Science
in
Structural Engineering

Department of Civil and Environmental Engineering

Spring 2012
Edmonton, Alberta

Abstract

Combining steel fiber reinforced concrete (SFRC) and high strength longitudinal reinforcement in a structural member creates the potential for increased strength and durability compared to conventional reinforced concrete members. There is however limited research into the structural behaviour of this member configuration.

The objectives of the current study were twofold. First, the size effects in both compression and flexural tension at the material scale in SFRC were examined through testing of geometrically scaled cylinders and prisms. Second, the size and strain effects on the shear behaviour of structural slabs were examined through the testing of six large scale specimens in three point bending. The overall member height and longitudinal reinforcement ratio were the primary variables of interest while the shear span to effective depth ratio was held constant at 3. No transverse reinforcement was included. Comparisons of the specimen performance to existing design provisions for reinforced concrete members were completed.

Acknowledgments

This research project was completed at the University of Alberta and would not have been possible without the support and encouragement from Dr. Adam Lubell. Dr. Vivek Bindiganavile was also instrumental in the materials development phase of this study. I am forever grateful for all you both have taught me.

The financial support provided by the Natural Sciences and Engineering Research Council (NSERC) of Canada, AECOM Canada and City of Edmonton Drainage Services is gratefully acknowledged. Material donations were kindly provided by Lehigh Hanson Materials Limited, Bekaert and MMFX Technologies.

Many people assisted in the development and testing of the experimental program described in this thesis. Rizaldy Mariano aided in the concrete mix development stages completed at the University of Alberta while John Dutton assisted with the larger scale mix development at Inland Concrete Ltd. The patience and guidance from Greg Miller with the test and instrumentation setups was greatly appreciated, as was the help from Michael Leitch and Sean Hudson with the specimen testing. Fellow graduate students, in particular Admasu Desalegne and Matthias Andermatt, also assisted with the experimental program.

The never-ending support and patience from my family, in particular my parents and my husband Greg, made this work feasible. Thank you!

Table of Contents

1 Introduction 1

- 1.1 Steel Fiber Reinforced Concrete Members with ASTM A1035 Longitudinal Reinforcement 1
- 1.2 Research Significance 2
- 1.3 Project Objective and Scope 3
- 1.4 Thesis Organization 3

2 Background 5

- 2.1 Overview 5
- 2.2 Concrete Reinforcement Types 6
  - 2.2.1 Steel Fibers 6
  - 2.2.2 ASTM A1035 Steel Reinforcement 8
- 2.3 Previous Experimental Research 10
  - 2.3.1 Shear Strength of Steel Fiber Reinforced Concrete 10
  - 2.3.2 Shear Strength of ASTM A1035 Longitudinally Reinforced Specimens 17
  - 2.3.3 Shear Behaviour of Steel Fiber Reinforced Concrete Specimens Containing ASTM A1035 Longitudinal Steel Reinforcement 19
- 2.4 Strength Models 19
  - 2.4.1 Shear Strength 19
  - 2.4.2 Flexural Strength 25
- 2.5 Serviceability Models 30
  - 2.5.1 Crack Control 30
  - 2.5.2 Deflection Control 31
  - 2.5.3 Curvature and Deflection Models 32
- 2.6 Summary 33

3 Materials Characterization – Experimental Program 35

- 3.1 Introduction 35
- 3.2 Specimen Configurations 35
  - 3.2.1 Trial Mixes 36
  - 3.2.2 Production Mixes 36
- 3.3 Mix Development 37
  - 3.3.1 Trial Mixes 37

3.3.2 Production Mix 40
3.4 Production Mix Test Setups and Procedures 41
3.4.1 Compression 41
3.4.2 Flexure 41
4 Material Characterization – Test Results and Discussion 44
4.1 Compression Response 45
4.1.1 Strength Development Results 45
4.1.2 Large Scale Structural Companion Results 46
4.2 Flexural Response 47
4.2.1 Strength Development Results 49
4.2.2 Large Scale Structural Companion Results 54
4.2.3 Equivalent Uniform Tensile Stress Across Cracks 58
4.2.4 ACI 318-08 Fiber Reinforced Concrete Performance Requirements 65
4.3 Summary 66
4.3.1 Compression Response Summary 66
4.3.2 Flexural Response Summary 66
5 Large Scale Structural Specimens – Experimental Program 68
5.1 Introduction 68
5.2 Specimen Configurations 68
5.3 Specimen Fabrication 71
5.4 Material Properties 73
5.4.1 Steel Fiber Reinforced Concrete 73
5.4.2 ASTM A1035 Reinforcing Steel 73
5.5 Test Setup 76
5.6 Instrumentation 77
5.6.1 Physical Instruments 77
5.6.2 Photogrammetry 79
5.6.3 DIC System 79
5.7 Test Procedure 82
6 Large Scale Structural Specimens – Test Results and Discussion 83
6.1 General 83
6.2 Failure Mechanisms 84
6.2.1 Specimen S300-B1 84

6.2.2 Specimen S300-A2 86
6.2.3 Specimen S1000-B1 88
6.2.4 Specimen S1000-B2 92
6.2.5 Specimen S1000-A3 94
6.2.6 Specimen S1000-A4 98
6.2.7 Summary 100
6.3 Load Deflection Behaviour 100
6.4 Crack Patterns and Crack Widths 103
6.5 Longitudinal Reinforcement Strains 114
6.6 Shear Capacity Trends 117
6.7 Summary 122
7 Analytical Predictions 123
7.1.1 Shear Capacity Predictions 123
7.1.2 Flexural Capacity Predictions 127
7.1.3 Deflection Predictions 132
7.1.4 Recommendations 137
7.2 Summary 138
8 Summary and Conclusions 139
8.1 Summary 139
8.2 Conclusions 140
8.2.1 Materials Characterization 140
8.2.2 Large Scale Structural Specimens 141
8.3 Recommendations for Future Work 142
References 144
Appendix A: Steel Fiber Reinforced Concrete Properties 149
Appendix B: ASTM A1035 Reinforcement Details 170
Appendix C: Large Scale Structural Specimen Details 172

List of Tables

Table 2-1: Summary of Large Scale Specimens Tested by Adebar et al. (1997) 11
Table 2-2: Summary of Large Scale Specimens Tested by Dinh (2009) 13
Table 2-3: Summary of Large Scale SFRC Specimens Tested by Minelli and Plizzari (2010) 15
Table 2-4: Summary of Large Scale SFRC Specimens Tested by Shoaib et al. (2010) 17
Table 3-1: Coarse and Fine Aggregate Properties (Adapted from EBA Report E12201546 June 18, 2010) 38
Table 3-2: Trial Mix Development Details and Results 39
Table 3-3: Production Mix Proportions For Castings A and B 40
Table 4-1: Cylinder and Prism Labels for Strength Development and Structural Companion Specimens 45
Table 4-2: Summary of Strength Development Compression Test Results 46
Table 4-3: Summary of Structural Companion Compression Test Results 47
Table 4-4: Structural Companion Prism Details 48
Table 4-5: Average Flexural Toughness Values for Strength Development Prisms 53
Table 4-6: Average Flexural Toughness Values for Structural Companion Prisms 57
Table 4-7: Comparison of Average Peak Equivalent Uniform Tensile Stresses and CMOD from Strength Development Prisms with Various Researchers 63
Table 4-8: Summary of Average Peak Equivalent Uniform Tensile Stresses and CMODs from Structural Companion Prisms 65
Table 5-1: Large Scale Structural Specimen Configuration Details 70
Table 5-2: Properties of ASTM A1035 Reinforcing Steel Coupons 75
Table 6-1: Large Scale Structural Specimen Properties and Results Summary 83
Table 6-2: Mid-Span Service Deflections for Large Scale Structural Specimens 102
Table 6-3: Failure Crack Details for h = 300 mm Specimens 106
Table 6-4: Failure Crack Details for h = 1000 mm Specimens 106
Table 6-5: Large Scale Structural Specimen Failure Crack Widths at Service and Peak Loads 107
Table 6-6: Large Scale Structural Specimen Loads Corresponding to Non-Linear and Rapid Failure Crack Growth 112
Table 6-7: Percentage of Peak Load at a Crack Width of 0.25 mm for h = 300 mm Specimens 112
Table 6-8: Percentage of Peak Load at a Crack Width of 0.25 mm for h = 1000 mm Specimens 113
Table 6-9: Large Scale Structural Specimen Mid-Span Reinforcement Strains Recorded at Peak and Service Loads 115
Table 7-1: Shear Capacity Prediction Summary 124

Table 7-2: Flexural Capacity Predictions.. 129
Table 7-3: Nominal Flexural Capacity Increases Compared to CSA A23.3-04 Predictions 129
Table 7-4: Large Scale Structural Specimens Maximum Applied Moment 130

List of Figures

Figure 2-1: Shear Transfer Mechanisms in a Concrete Member without Transverse Reinforcement (Dinh, 2009) 5
Figure 2-2: Stress-Strain Curves for ASTM A1035 and Conventional ASTM A615 Steel Reinforcement (NCHRP Report 679, 2011) 9
Figure 2-3: Large Scale Specimens Tested by Adebar et al. (1997) 12
Figure 2-4: Large Scale Specimens Tested by Dinh (2009) 14
Figure 2-5: Large Scale SFRC Specimens Tested by Minelli and Plizzari (2010) 15
Figure 2-6: Large Scale SFRC Specimens Tested by Shoaib et al. (2010) 17
Figure 2-7: Model of ASTM C1609 Un-Notched Flexural Prism Behaviour from Dinh (2009) 24
Figure 2-8: Stress Blocks at the Cracked Section (Adapted from Dinh (2009)) 24
Figure 2-9: Reinforced Plain Concrete Member a) Cross-Section b) Strains c) Equivalent Stress Blocks and d) Forces 26
Figure 2-10: ACI ITG-6R-10 Stress-Strain Curves for ASTM A1035 Grade 690 Reinforcement 29
Figure 3-1: Production Mix Specimen Size Variation in a) Cylinders and b) Notched Prisms 37
Figure 3-2: a) Hooked End Steel Fibers and b) Fiber Balling During Casting 37
Figure 3-3: Coarse and Fine Aggregate Grading Chart (Adapted from EBA Report E12201546 June 18, 2010) 39
Figure 3-4: Compression Test Setup on a 100 mm Diameter Cylinder 41
Figure 3-5: a) Prism Speckling for DIC System and b) ASTM C1609-10 Flexural Test Setup with LVDT 43
Figure 4-1: Materials Characterization Specimen Labelling System 44
Figure 4-2: Average Compressive Stress-Strain Curves from Casting A and B Strength Development Cylinders 46
Figure 4-3: Specimen S1000-B2 Structural Companion Cylinder Stress-Strain Curves 47
Figure 4-4: a) Horizontal Strain Field for P150-A1 and b) DIC Data Extraction Points 49
Figure 4-5: a) P100A Average Prism Vertical Displacement and b) Comparison of P100-B2 DIC and LVDT Measurements 50
Figure 4-6: Relationship between CMOD and Mid-Span Deflection for Strength Development Prisms from a) Casting A and b) Castings A and B 51
Figure 4-7: a) Average Load-Deflection Curves for Casting A Strength Development Prisms and b) Relationship between MOR and Member Depth for Strength Development Prisms 52
Figure 4-8: Relationship between MOR and CMOD at Peak Load for Strength Development Prisms 53

Figure 4-9: Relationship between a) Average Flexural Toughness and Member Depth and b) Average Equivalent Flexural Strength Ratio and Member Depth for Strength Development Prisms 54
Figure 4-10: Relationship between CMOD and Mid-Span Deflection for Structural Companion Prisms from a) Casting A and b) Castings A and B... 55
Figure 4-11: a) Average Load-Deflection Curves for Casting A Structural Companion Prisms and b) Relationship between MOR and Member Depth for Structural Companion Prisms... 56
Figure 4-12: Relationship between MOR and CMOD at Peak Load for Structural Companion Prisms 56
Figure 4-13: Relationship between a) Average Flexural Toughness Values and Member Depth and b) Average Equivalent Flexural Strength Ratio and Member Depth for Structural Companion Prisms 57
Figure 4-14: ASTM C1609-10 Flexural Prism Layout and Deformation Model (Adapted from Armelin and Banthia, 1997).. 58
Figure 4-15: Flexural Prism a) Cross Section at Notch Location, b) Stress Diagram, and c) Force Diagram 59
Figure 4-16: Average Equivalent Uniform Tensile Stress-CMOD Curves for Strength Development Prisms from a) Casting A and b) Casting B 61
Figure 4-17: Peak Uniform Tensile Stresses for Strength Development Prisms from a) Casting A and a) Casting B.. 62
Figure 4-18: Comparison of Average Normalized Peak Equivalent Uniform Tensile Stresses from Various Researchers... 63
Figure 4-19: Average Uniform Tensile Stress-CMOD Relationships from Casting A and B Structural Companion Prisms 64
Figure 4-20: Peak Uniform Tensile Stresses for Structural Companion Prisms............... 64
Figure 5-1: Large Scale Structural Specimen Cross-Sections 70
Figure 5-2: Typical Layout for a) h = 300 mm and b) h = 1000 mm Specimens 71
Figure 5-3: Formwork and Reinforcement Layout for a) h = 300 mm and b) h = 1000 mm Specimens 72
Figure 5-4: a) h = 1000 mm Specimen Cast in Layers and b) After Screeding................ 73
Figure 5-5: ASTM A1035 Reinforcement #6 Coupon Test a) With Extensometer and b) After Rupture.. 74
Figure 5-6: Average Stress-Strain Curves for a) #6 and b) #9 ASTM A1035 Reinforcing Steel Coupons.. 75
Figure 5-7: Large Scale Structural Specimen Support Details 76
Figure 5-8: a) MTS Frame Around S1000-A4 and b) Specimen S300-B1 Setup............. 76
Figure 5-9: Typical Instrumentation Layouts for a) h = 300 mm and b) h = 1000 mm Specimens 78
Figure 5-10: a) PI Gauges and Mid-Span Cable Potentiometer on a h = 1000 mm Specimen and b) LVDT Setup at Support.................................... 79
Figure 5-11: Typical DIC System Locations on a) h = 300 mm and b) h = 1000 mm Specimens 81

Figure 5-12: a) Photogrammetry Setup on S300-B1 and b) DIC Speckling with Grid on a h = 1000 mm Specimen 82
Figure 6-1: Vertical Surface Strains from DIC System 2 on S300-B1 at a) 400 kN and b) Peak Load 85
Figure 6-2: Vertical Surface Strains from DIC System 2 on S300-B1 a) Immediately After Failure and b) at Approximately 205 kN Post-Peak 86
Figure 6-3: Overall Failure Crack on South Face of S300-B1 86
Figure 6-4: Horizontal Surface Strains from DIC System 2 on S300-A2 at a) 360 kN and b) Peak Load 87
Figure 6-5: Vertical Surface Strains from DIC System 2 on S300-A2 Immediately After Failure 87
Figure 6-6: Overall Failure Crack on South Face of S300-A2 88
Figure 6-7: Voids and Compression Strut in East End of S1000-B1 89
Figure 6-8: Vertical Surface Strains from DIC System 0 on S1000-B1 at a) Peak Load and b) Immediately before Failure 90
Figure 6-9: Specimen S1000-B1 DIC System 0 Image Immediately After Failure 91
Figure 6-10: Overall Failure Crack on South Face of S1000-B1 91
Figure 6-11: Specimen S1000-B2 Primary Cracks on West End 92
Figure 6-12: Vertical Surface Strains from DIC System 0 on S1000-B2 at a) Peak Load and b) Immediately Before Failure 93
Figure 6-13: S1000-B2 DIC System 0 Image Immediately After Failure 93
Figure 6-14: Overall Failure Crack on South Face of S1000-B2 94
Figure 6-15: Horizontal Surface Strains from DIC System 2 on S1000-A3 at a) Stage 3 and b) Stage 4 95
Figure 6-16: Vertical Surface Strains from DIC System 2 on S1000-A3 at a) Peak Load and b) Immediately Before Failure 96
Figure 6-17: Vertical Surface Strain from DIC System 2 on S1000-A3 Immediately After Failure 97
Figure 6-18: Overall Failure Crack on South Face of S1000-A3 97
Figure 6-19: Vertical Surface Strains from DIC System 0 on S1000-A4 at a) 700 kN and b) Peak Load 98
Figure 6-20: a) Horizontal Surface Strains from DIC System 0 on S1000-A4 Immediately Before Failure and b) DIC System 0 Image Immediately After Failure 99
Figure 6-21: Overall Failure Crack on South Face of S1000-A4 100
Figure 6-22: Load-Deflection Curves for a) h = 300 mm and b) h = 1000 mm Specimens 101
Figure 6-23: Relationship between Mid-Span Service Deflection and Reinforcement Ratio 102
Figure 6-24: Final Crack Diagrams for Large Scale Structural Specimens 104
Figure 6-25: DIC Images of the Diagonal Failure Crack After Failure from a) S300-B1 and b) S300-A2 105

Figure 6-26: DIC Images of the Diagonal Failure Crack after Failure from a) S1000-B1, b) S1000-B2, c) S1000-A3 and d) S1000-A4 105
Figure 6-27: Specimen S300-B1 Failure Crack Widths a) Throughout Testing and b) Up to Peak Loads.. 109
Figure 6-28: Failure Crack Widths Throughout Testing for S1000-A3.......................... 110
Figure 6-29: Failure Crack Width Growth at 0.75*h for a) h = 300 mm and b) h = 1000 mm Specimens 111
Figure 6-30: Relationship between Peak Load Crack Width at Effective Depth d and Reinforcement Ratio 113
Figure 6-31: Longitudinal Reinforcement Strains Along Length of S1000-A4 116
Figure 6-32: Relationship between Peak Load Crack Widths and Longitudinal Reinforcement Strain.. 117
Figure 6-33: Relationship between Normalized Shear Stresses and Reinforcement Ratios for a) h = 1000 mm Specimens and b) All Specimens.. 118
Figure 6-34: Relationship between Normalized Shear Stress and a) Peak Load Reinforcement Strain at Mid-Span and b) Peak Load Reinforcement Strain at 2*d.. 120
Figure 6-35: Relationship between Normalized Shear Stresses and Effective Depth 121
Figure 6-36: Size Effect in Shear Comparison between Various Researchers 121
Figure 7-1: Relationship between Shear Capacity Predictions for h = 300 mm Specimens and Reinforcement Ratio... 126
Figure 7-2: Relationship between Shear Capacity Predictions for h = 1000 mm Specimens and Reinforcement Ratio... 126
Figure 7-3: Relationship between Shear Capacity Predictions and Effective Depth 127
Figure 7-4: Comparison of Predicted Flexural Capacities to Peak Moment for h = 300 mm Specimens 130
Figure 7-5: Comparison of Predicted Flexural Capacities to Peak Moment for h = 1000 mm Specimens 131
Figure 7-6: a) Moment-Curvature Relationship for S1000-A4 and b) Curvatures Along Length of Specimen S1000-A4...................................... 134
Figure 7-7: Specimen S1000-A4 Predicted Deflections Based on Curvature 135
Figure 7-8: S1000-A4 Comparison between Predicted and Measured Deflections at the Equivalent Service Load Level... 136
Figure 7-9: Specimen S1000-A4 Measured and Predicted Relationships between Load and Mid-Span Deflection.. 136

List of Abbreviations

AR - aspect ratio of fibers (L_f/D)

CMOD - crack mouth opening displacement (mm)

DIC - digital image correlation

FRC - fiber reinforced concrete

GU - general use

LVDT - linear variable displacement transducer

MCFT - modified compression field theory

MMFX - trade name for ASTM A1035 Grade 690 steel reinforcement manufactured by MMFX Technologies Corporation

MOR - modulus of rupture of concrete (MPa)

SFRC - steel fiber reinforced concrete

3D - three dimensional

List of Symbols

a = shear span (mm)

a_b = distance from the extreme compression face to the bottom of the equivalent concrete stress block at the balanced condition (mm)

a_c = distance from the extreme compression face to the bottom of the equivalent concrete stress block (mm)

a_g = maximum coarse aggregate size (mm)

a/d = shear span to effective depth ratio

A_s = area of longitudinal steel reinforcing (mm^2)

b_w = width of a specimen (mm)

c = distance from the extreme compression fiber to the neutral axis (mm)

c_b = distance from the extreme compression fiber to the neutral axis in the balanced condition(mm)

C_r = concrete compression resistance force (N)

d = effective depth; distance from the extreme compression fiber to the centroid of the tensile force (mm)

d_{CMOD} = change in CMOD (mm)

d_{Δ} = change in mid-span deflection (mm)

d_{θ} = change in rotation angle (°)

d_n = depth from extreme compression fiber to top of notch (mm)

d_v = effective shear depth; defined as the larger of 0.9*d or 0.72*h (mm)

D = fiber diameter (mm)

E_c = modulus of elasticity of concrete (MPa)

E_s = modulus of elasticity of steel reinforcement (MPa)

f_c = compressive stress of concrete (MPa)

f_c' = peak compressive stress of concrete (MPa)

f_r = cracking strength of concrete (also called modulus of rupture or MOR) (MPa)

f_s = axial stress in the longitudinal steel reinforcement (MPa)

f_{test} = residual tensile strength from ASTM C1609-10 flexural prism tests (MPa)

f_y = yield strength of steel reinforcement (MPa)

h = height of member (mm)

I_{cr} = moment of inertia of cracked section transformed to concrete (mm^4)

I_e = effective moment of inertia (mm^4)

I_g = moment of inertia of gross concrete section, neglecting steel reinforcement (mm^4)

L = span length, center to center of supports (mm)

L_c = length of critical diagonal shear crack (mm)

L_f = fiber length (mm)

L_n = clear span length between supports (mm)

M = flexural moment at the critical section of a member (N*mm)

M_a = applied moment (N*mm)

M_{cr} = cracking moment (N*mm)

M_{ext} = moment caused by applied loading (N*mm)

M_{int} = moment based on the compressive and tensile forces (N*mm)

M_n = nominal moment capacity (N*mm)

M_{peak} = moment corresponding to the peak load (N*mm)

M_r = predicted flexural capacity at the critical section of a member (N*mm)

M_{Lf} = applied moment at a mid-span deflection value of $L_f/24$ (N*mm)

P = load applied on a specimen (N)

P_{NL} = load at which non-linear failure crack growth begins (N)

P_{max} = maximum load applied on a specimen (N)

P_{peak} = maximum load applied on a specimen, including self-weight of loading apparatus (N)

P_s = service load on a member (N)

R^2 = coefficient of determination in linear regression

s_{ze} = crack spacing parameter that accounts for the effect of aggregate size (mm)

T_r = tensile resistance force in steel reinforcement (N)

T_{ru} = tensile resistance force due to steel fibers (N)

V = shear force at the critical section of a member (N)

V_c = shear strength of concrete (N)

V_f = fiber volume fraction (%)

V_{cc} = shear force contribution from concrete compression (N)

V_{FRC} = shear force contribution from vertical segment of diagonal tension resistance provided by steel fibers (N)

V_{model} = shear capacity prediction (N)

V_r = shear capacity of a member

V_{test} = maximum shear load applied to a specimen (N)

w_s = failure crack width at service load levels (mm)

w_p = failure crack width at peak load levels (mm)

z = CSA A23.3-04 crack control parameter (N/mm)

α = diagonal failure crack angle with respect to the horizontal axis (°)

α_c = factor defining an equivalent concrete stress block for conditions other than ultimate (Collins & Mitchell, 1997)

α_1 = factor defining an equivalent concrete stress block at the ultimate condition

β_c = factor defining an equivalent concrete stress block for conditions other than ultimate (Collins & Mitchell, 1997)

β_1 = factor defining an equivalent concrete stress block at the ultimate condition

Δ = vertical deflection (mm)

Δ_{max} = mid-span vertical deflection corresponding to the peak load P_{max} (mm)

Δ_s = mid-span vertical deflection corresponding to the service load P_s (mm)

ε_{cf} = concrete strain due to stress (mm/mm)

ε_c' = concrete strain corresponding to peak stress (mm/mm)

ε_s = axial strain in the longitudinal steel reinforcement (mm/mm)

ε_{top} = concrete strain at the extreme compression fiber (mm/mm)

ε_x = axial strain at mid-height of the member (mm/mm)

ε_y = axial strain in the longitudinal steel reinforcement corresponding to f_y (mm/mm)

Ø = curvature of a specimen (mm^{-1})

ρ = ratio of reinforcement area (A_s) to cross-sectional concrete area (b_wd) (%)

σ_{ru} = equivalent uniform tensile stress due to fiber influence (MPa)

ϕ = strength reduction factor for design (ACI 318-08)

ϕ_c = concrete strength reduction factor for design (CSA A23.3-04)

ϕ_s = steel reinforcement strength reduction factor for design (CSA A23.3-04)

1 Introduction

1.1 Steel Fiber Reinforced Concrete Members with ASTM A1035 Longitudinal Reinforcement

As the general state of the national infrastructure in both Canada and the United States ages and deteriorates, alternatives to traditional construction methods are being investigated to increase the durability and consequently the life span of new projects. Two such alternatives are the use of steel fiber reinforced concrete (SFRC) in place of typical plain concrete, and the use of high strength steel reinforcement instead of conventional steel reinforcement. For example, adding randomly distributed fibers to a plain concrete mix has been shown to improve resistance to material deterioration (ACI 544.4R-88) which results in less water and chloride ingress and provides longevity to the steel reinforcement located within the concrete member. In addition, certain types of high strength steel reinforcement have been shown to exhibit improved corrosion resistance compared to conventional reinforcement (NCHRP Report 679, 2011) which can ultimately contribute to structures with longer life spans. Although the durability and performance characteristics of these materials are linked, the structural implications were the primary focus of the current study.

Previous research has been completed separately on the behaviour of SFRC structural members, and on members reinforced with high strength reinforcement. Minimal, if any, research has been completed on members which combine both of these materials.

Adding short, randomly distributed steel fibers into a concrete mix provides an alternative load transfer mechanism at the material scale (e.g. Dinh, Parra-Montesinos, & Wight, 2011; Banthia, 1992; ACI 544.4R-88). Once cracks form, the steel fibers bridge the cracks, thereby reducing crack widths and improving the aggregate interlock action. The post-peak tensile response of the concrete is significantly improved over members constructed with plain concrete (e.g. Minelli & Plizzari, 2010; Nguyen-Minh & Rovnak, 2010; Armelin & Banthia, 1997). At the structural scale, the fibers have been shown to increase the shear capacity significantly over comparable plain concrete members (e.g. Shoaib, Lubell, & Bindiganavile, 2010; Dinh, 2009; Kwak, Eberhard, Kim, & Kim, 2002; ACI 544.4R-88). CSA A23.3-04, the current Canadian design standard for structural concrete design, does not provide any specific provisions for the use of SFRC. ACI 318-08, the current equivalent American design code, acknowledges the benefits of SFRC by permitting the replacement of minimum transverse reinforcement in plain concrete members by the addition of steel fibers, provided that specific materials performance and overall member configuration requirements are met. The elimination of minimum transverse reinforcement creates the potential for structural members with decreased reinforcement congestion, less physical labour requirements and increased durability.

High strength ASTM A1035 Grade 690 reinforcing steel has begun to replace conventional epoxy coated Grade 400 steel reinforcement used in structural members designed for aggressive environments such as bridge decks or underground tunnels. Generally, this replacement is due to the increased corrosion resistance of Grade 690 reinforcement (e.g. NCHRP Report 679, 2011; Williamson, Weyers, Sprinkel, & Brown, 2009). However, this type of reinforcing steel also exhibits an effective yield strength more than double that of Grade 400 reinforcement, while still maintaining the same linear modulus of elasticity at typical service load reinforcement strain levels (e.g. Desalegne & Lubell, 2010; Hassan, Seliem, Dwairi, Rizkalla, & Zia, 2008). Often, this additional strength is neglected due to commonly accepted design limits. The CSA A23.3-04 and ACI 318-08 design provisions currently permit design yield strengths up to 500 MPa and 550 MPa, respectively. The recently published ACI ITG-6R-10 recommended using an equivalent design yield strength limit of 690 MPa for plain concrete members without fibers. In terms of serviceability conditions, the use of ASTM A1035 reinforcement in concrete members at this higher design stress may lead to members with greater deflections and increased crack widths compared to members reinforced with conventional Grade 400 reinforcement (Hassan et al., 2008; Tang & Lubell, 2008). These properties may affect the durability, aesthetic appearance and structural capability of the member and must be taken into consideration during design.

Reinforced concrete members generally experience both flexural and shear forces. While both these forces have to be designed for, their failure mechanisms are very different. A shear failure is typically sudden and brittle, while a flexural failure is often gradual and with prior warning. Extensive research has been completed on one-way, reinforced plain concrete members in both shear and flexure (e.g. Lubell, Bentz, & Collins, 2009; Lubell, 2006; Collins & Kuchma, 1999; Collins, Mitchell, Adebar, & Vecchio, 1996). The shear capacity has been previously found to be influenced by the member depth, the reinforcement ratio and the aggregate size (e.g. Lubell et al., 2009; ACI 445R-99; Collins & Kuchma, 1999; Vecchio & Collins, 1986; Kani, 1967) and can be accounted for through size and strain effect terms in shear design models. Structural members reinforced with high strength longitudinal reinforcement are capable of reaching higher reinforcement strain levels than member reinforced with conventional Grade 400 reinforcement, potentially increasing the strain effect on the shear capacity (Desalegne & Lubell, 2010; Hoult, Sherwood, Bentz, & Collins, 2008). The majority of the research into these size and strain effects has been completed on plain concrete members; minimal attention has been applied in the same areas to SFRC structural members.

1.2 Research Significance

The research presented in the current study has been completed to provide insight into the void of knowledge for structural members containing both SFRC and high strength longitudinal reinforcement. Simply supported shear critical members constructed with 1.0% volume fraction of hooked end steel fibers and with ASTM A1035 Grade 690 longitudinal reinforcement were examined. Specimens with a geometrical size factor of approximately 3.3 were designed with varying reinforcement ratios in order to view the effect on shear capacity from both member size and reinforcement strain parameters. The material properties of the SFRC were also determined through examination of cylinders and prisms with dimensions that varied by a factor of up to 2.

Combined use of these materials was predicted to produce a structural member with acceptable deflections and crack widths, while achieving increased shear capacities compared to members reinforced with plain concrete and conventional reinforcement.

1.3 Project Objectives and Scope

This project encompassed two main phases: analysis of size effects of steel fiber reinforced concrete (SFRC) mechanical properties at the material scale and examination of the shear behaviour of large scale structural members constructed with SFRC and high strength longitudinal reinforcing steel.

In the first phase of the study, the size effect in SFRC in both compression and flexural tension were examined at the material scale. Two sizes of cylinders were tested under compression according to ASTM C39-09a while three sizes of notched prisms were examined in flexure according to ASTM C1609-10. The digital image correlation (DIC) technique was used with the flexural specimens as a non-contact method of measuring three dimensional (3D) surface strains. Specimen deflection and crack growth were measured through the DIC system and were evaluated in relation to specimen size. Size dependent relationships for compressive strength, flexural tensile strength, and equivalent uniform tensile strength were developed.

In the second phase of the study, the shear behaviour of large scale structural members longitudinally reinforced with ASTM A1035 Grade 690 steel and constructed with SFRC was examined. Large scale members of two different overall heights, h = 300 mm and h = 1000 mm, were constructed to include diverse longitudinal reinforcement ratios (ρ) to allow direct consideration of the member behaviour when the reinforcement stress at the time of failure ranged between 450 and 900 MPa. Further, systematically altering both the overall member height and the reinforcement ratio allowed for examination of the so-called size and strain effects on the shear strength of the SFRC members. The failure crack behaviour was analysed throughout the test and size dependent relationships for failure crack widths, mid-span deflections and normalized shear stress at failure were developed. Reinforcement strain dependent relationships were developed for failure crack widths. In addition, the specimens were compared against existing shear, flexural and deflection models.

1.4 Thesis Organization

Chapter 2 provides an overview of background information relevant to this study. The information has been divided into three sections – concrete reinforcement types, previous experimental research and current design models for shear, flexure and deflection.

Chapter 3 reports the mix development process for the SFRC mixes in the study. The methods used to characterize the mechanical properties of these mixes are also explained. The results and discussions of the mechanical properties are described in Chapter 4.

The design and fabrication of the large scale structural specimens are described in Chapter 5, along with the material properties and test procedures. The results and discussions from those tests are detailed in Chapter 6.

The applied shear, moments, and measured deflections of the large scale structural specimens are compared with predictions based on existing design models in Chapter 7.

Chapter 8 summarizes the conclusions from both the materials characterization and large scale structural specimen portions of the study.

Appendix A details the mechanical concrete properties for the cylinders and prisms tested as part of the strength development portion of the materials characterization study, and as companions to the large scale structural specimens. Appendix B contains the material test results from the ASTM A1035 Grade 690 longitudinal reinforcing steel. Appendix C details the behaviour of each large scale specimen as recorded by the various forms of instrumentation.

2 Background

2.1 Overview

In reinforced concrete members without fibers, shear forces are known to transfer through several different mechanisms including aggregate interlock, dowel action of the longitudinal reinforcement, arch action and residual tension forces across cracks (e.g. ACI 445R-99; Vecchio & Collins, 1986; ASCE-ACI 426, 1973). Figure 2-1 demonstrates these shear transfer mechanisms as described by Dinh (2009) where V_{cc} represents the shear contribution from the concrete compression zone, V_{ay} is the shear carried by aggregate interlock and V_d is the shear force due to dowel action. To increase the shear capacity, transverse reinforcement such as stirrups are typically included in structural members.

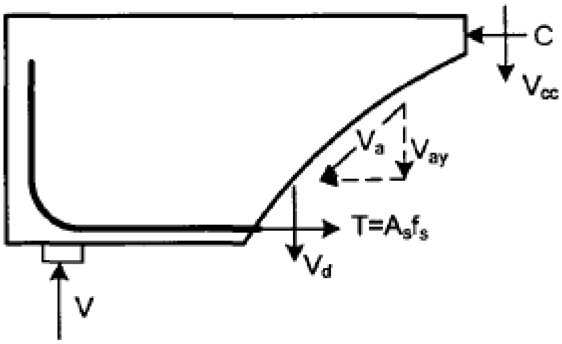

Figure 2-1: Shear Transfer Mechanisms in a Concrete Member without Transverse Reinforcement (Dinh, 2009)

The shear stress at failure of slender reinforced concrete members is known to decrease with an increase in member size (e.g. Bentz, Vecchio, & Collins, 2006; Collins et al., 1996; ACI 445R-99). According to the Modified Compression-Field Theory (MCFT) (Vecchio & Collins, 1986), crack widths in concrete are related to the proximity to the nearest reinforcement layer; therefore as the member depth increases, the diagonal crack widths increase accordingly. These larger widths result in decreased residual tension forces and reduced aggregate interlock action (Walraven, 1981).

The shear stress at failure of slender reinforced concrete members is also known to decrease with an increase in the reinforcement strain (e.g. Lubell et al., 2009; Hoult et al., 2008; Bentz et al., 2006; Collins et al., 1996; ACI 445R-99). The higher reinforcement strain results in higher reinforcement stresses, larger crack widths, reduced aggregate interlock action, smaller compression zones and reduced dowel action.

Several studies have shown the beneficial influence of randomly distributed steel fibers on the shear capacity of a member (e.g. Shoaib et al., 2010; Dinh, 2009; Banthia, 1992; Sharma 1986). The fibers provide an alternate load transfer path across the cracks, reduce the crack widths and spacing, and in turn increase the aggregate interlock action (e.g. Dinh et al., 2011; Minelli & Plizzari, 2010; ACI 544.4R-88). Immediately after cracking occurs, both the fibers and aggregate interlock contribute to the shear carrying capacity of the member. However, as the applied load is increased and the crack widths enlarge, the contribution from aggregate interlock decreases faster than the contribution from the fibers (Dinh et al., 2011).

Slender members with a shear span to depth ratio (a/d) greater than approximately 2.5 (ACI 445R-99), such as the structural members investigated in the current study, generally rely on the aggregate interlock, dowel action and residual tension transfer mechanisms described previously for shear resistance to transverse loads. In flexure, slender members follow the well known plane sections remain plane theorem (MacGregor & Bartlett, 2000). These types of members are designed according to sectional models for shear and flexure, and are the focus of the current study.

Non-slender reinforced concrete members with an a/d ratio generally less than approximately 2.5 (ACI 445R-99) are able to transmit shear forces through direct compression struts formed between the load and support much easier than members with larger ratios (ie. arch action). These members are typically designed according to the strut and tie method but will not be examined in the current study.

2.2 Concrete Reinforcement Types

Plain concrete is well known to be a brittle material; strong in compression and weak in tension. The tensile performance of concrete is typically improved through the addition of reinforcements. Steel, carbon, plastic and even glass have been developed into longitudinal reinforcements that carry the tensile stresses imparted onto concrete members, and also into individual short fibers that can be randomly distributed into the concrete mix to help carry the shear forces and improve the member strength and ductility.

Steel was chosen as the material for both the longitudinal reinforcement and the distributed fibers in the current study. Therefore, the remainder of this section will focus on these two reinforcement types.

2.2.1 Steel Fibers

Adding a moderate volume fraction of steel fibers (V_f = 0.5 to 1.5%) in a random three dimensional (3D) orientation to a concrete mix has been shown to improve the crack distribution and the post peak tensile strength (e.g. Minelli & Plizzari, 2010; Kwak et al., 2002; Banthia, 1992, ACI 544.4R-88) at the material scale compared to plain concrete members. The distributed fibers provide an alternate force transfer path across the cracks, thereby reducing crack widths and improving the aggregate interlock.

Fibers have been shown to have a relatively small impact on the compressive strength compared to the impact on the tensile or flexural strength (e.g. Shah & Ribakov, 2011; Shoaib, Bindiganavile, & Lubell, 2009; ACI 544.4R-88). The strain corresponding to the peak compressive strength however, has been found to be higher in fiber reinforced concrete (FRC) compression tests than in plain concrete tests, and the post-peak slope is less steep. Both these properties are dependent on the type of fiber (Shah, Stroeven, Dalhuisen, & van Stekelenburg, 1978) and indicate the increased toughness of FRC in compression compared to plain concrete without fibers (e.g. Banthia, 1992; ACI 544.4R-88; Shah et al., 1978). The flexural toughness, described as the ability of concrete to absorb energy during deformation, can be estimated by the area under the load-deflection curve (ASTM C1609-10). This property is also increased substantially through the use of fibers (e.g. Minelli & Plizzari, 2010; Banthia; 1992; ACI 544.4R-88; Sharma, 1986).

Various sizes of fibers are available, in terms of both length and diameter. Each size will impart different properties to the concrete – for example, altering the fiber length will change the average fiber embedment length and will affect the width of the inclined cracks before failure (Dinh, Parra-Montesinos, & Wight, 2010) and the member deformations (Adebar, Mindess, St.-Pierre, & Olund, 1997). The ratio of fiber length to diameter (L_f/D) is referred to as the aspect ratio (AR). In general, fiber efficiency increases with the aspect ratio although ratios greater than 100 have typically been found impractical due to low concrete workability and poor fiber distribution (ACI 544.4R-88).

Before deciding on a fiber size, the member layout and quality control testing must also be considered. Using large fibers in a member with a high percentage of longitudinal and/or transverse reinforcement will lead to uneven fiber distribution as the fibers get caught on or around the reinforcement. Voids may be created adjacent to where the fibers get caught, which will then act as flaws in the material (Ozyurt, Mason, & Shah, 2007) and will have a negative impact on the member's performance. For quality control cylinders and prisms, a size factor of 3 between the fiber length and the smallest specimen dimension is generally recommended (ASTM C1609-10) to minimize the influence of fiber alignment along the edges and sides. Thus for 100 mm diameter cylinders and 100 mm cross-sectional prisms, the maximum fiber length recommended would be approximately 30 mm.

Steel fibers are also available in a variety of configurations. The current study used hooked end fibers, but crimped and straight fibers are also readily available. Past studies have shown that hooked end fibers aid in the fiber anchorage into the matrix and can help induce a ductile failure. Shah & Ribakov (2011), Banthia (1992) and ACI 544.4R-88 summarize the results from hooked end, straight and crimped fibers as tested by various researchers and generally conclude that the increased resistance to fiber pullout through deformed surfaces or end anchorage provides increased load carrying capacity compared to straight fibers.

The fiber volume fraction (V_f) will also have an impact on the member's performance (e.g. Shah & Ribakov, 2011; Minelli & Plizzari, 2010; Kwak et al, 2002; Adebar et al., 1997). Shoaib et al. (2009) examined the effects in compression and flexure for fiber volume fractions of 0%, 0.5% and 1.0% with the same hooked end steel fibers used in the current study. In compression, the fiber volume fraction had little effect on the peak strength but the V_f = 1.0% mix showed the greatest post-peak strength improvement. In flexure, the V_f = 1.0% mix showed a 50% increase in the modulus of rupture (MOR) compared to a plain concrete control specimen. The V_f = 0.5% mix showed an 18% increase compared with the control specimen. Other studies have shown that adding fibers over V_f = 1.0% leads to very minimal strength improvements over mixes containing V_f = 1.0% (e.g. Dinh, 2009; Mirsayah & Banthia, 2002; Adebar et al., 1997).

Even with the added benefits of using fibers in a concrete mix, size effects on shear strength are still prominent at the material scale in specimens constructed using fiber reinforced concrete (FRC). Jiang and Banthia (2010) characterized a size effect in flexure on 100 x 100 x 350 mm and 150 x 150 x 500 mm prisms. The prisms were reinforced with hybrid polymeric fibers at three different dosages and tested under ASTM C1609-07. The size effect in flexure was found to decrease with an increase in fiber volume fraction (V_f).

At the structural scale, the enhanced shear capacity benefits from FRC are clear. Adding randomly distributed discrete steel fibers into a structural member will decrease the crack spacing and crack widths, increase the shear capacity and will generally lead to a more ductile failure mode compared to an equivalent plain concrete member (e.g. Shoaib et al., 2010; Dinh, 2009, Adebar et al., 1997; Narayanan & Darwish, 1987). The presence of a size effect in shear however, is still under debate. Minelli and Plizzari (2010) found that although size effects were present in their test specimens with overall nominal heights of 500, 1000 and 1500 mm, these effects had the potential to be mitigated by the presence of steel fibers. Shoaib et al. (2010) compared the normalized shear stress at failure for large scale structural members with V_f = 1.0% of hooked end steel fibers, Grade 400 longitudinal reinforcement and overalls heights of 310 mm and 600 mm. The shear stress at failure was found to decrease as the effective depth increased. Dinh (2009) concluded that the size effect in shear was negligible based on shear tests performed on SFRC specimens with h = 457 and 686 mm. Parra-Montesinos (2006) compiled a database of previously tested large scale structural FRC members with deformed steel fibers containing a wide range of parameters. A plot of the normalized shear stress at failure for the slender members ($a/d \geq 2.8$) in the database versus the effective depth did not show a significant correlation.

2.2.2 ASTM A1035 Steel Reinforcement

ASTM A1035 reinforcement is a low carbon, high chromium alloy steel with no well defined yield point and a tensile strength of approximately 1030 MPa for both Grade 690 and 830 reinforcement (ie. Grade 100 ksi and 120 ksi) (ASTM A1035-11). With conventional steel reinforcement (such as ASTM A615 steel), the stress-strain relationship follows an initial linear-elastic behaviour before reaching a plastic plateau at the yield strength (typically 400 MPa), followed by strain hardening. ASTM A1035 reinforcement exhibits a much higher proportional limit, although the relevant design codes often limit the allowable design strength to much lower values (discussed in

Section 2.4). The modulus of elasticity before the proportional limit is identical to that of conventional reinforcement (E_s = 200,000 MPa) as illustrated in Figure 2-2.

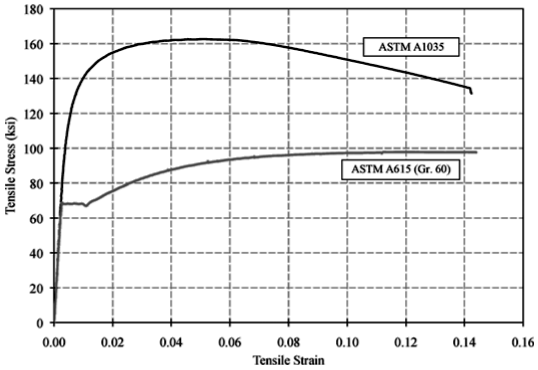

Figure 2-2: Stress-Strain Curves for ASTM A1035 and Conventional ASTM A615 Steel Reinforcement (NCHRP Report 679, 2011)

ASTM A1035 Grade 690 longitudinal reinforcing bars were used in the current study, and will thus be the focus of this section. Further information on Grade 830 reinforcement is available through ASTM A1035-11.

ASTM A1035 reinforcement contains a higher chromium content (8 to 11%) and different microstructure than conventional reinforcement which in turn increases its corrosion resistance (e.g. NCHRP Report 679, 2011; Williamson et al., 2009). This advantage has permitted the replacement of epoxy coated or stainless steel reinforcement with ASTM A1035 steel in corrosive environments although until very recently, the replacement has generally been on par without taking advantage of the higher strength capacity.

ASTM A1035-11 publishes several requirements for the material properties of high strength reinforcement, including a minimum yield strength of 690 MPa as measured by the 0.2% offset method for Grade 690 reinforcement. It also requires a minimum stress of 550 MPa at a strain value of 0.0035 mm/mm to ensure a stiffness at lower strains at least equal to that of lower strength reinforcement such as steel meeting ASTM A615.

ACI ITG-6R-10 provides a recommended lower bound stress-strain curve for Grade 690 reinforcement that accounts for both the initial linear and subsequent non-linear behaviours. The relationship is given as:

$$f_s = \begin{cases} 200{,}000\varepsilon_s & for\ \varepsilon_s \leq 0.0024 \\ 1170 - \dfrac{2.96}{\varepsilon_s + 0.0019} & for\ 0.0024 < \varepsilon_s < 0.02 \\ 1040 & for\ 0.02 < \varepsilon_s < 0.06 \end{cases} \qquad 2\text{-}1$$

Use of a higher strength longitudinal reinforcement generally leads to a smaller reinforcement ratio (ρ) to achieve the same flexural capacity as a comparable member reinforced with conventional Grade 400 steel reinforcement. This reduction in reinforcement will produce a more flexible member with greater deflections (Hassan et al., 2008; Tang & Lubell, 2008). The reinforcement strains will also increase due to the lower reinforcement ratio, leading to greater crack widths and a decrease in the shear capacity – commonly termed as the strain effect (Desalegne & Lubell, 2010; Hoult et al., 2008).

2.3 Previous Experimental Research

2.3.1 Shear Strength of Steel Fiber Reinforced Concrete

The shear behaviour of fiber reinforced concrete (FRC) members has been examined in the past few decades. Dinh (2009) and Adebar et al. (1997) provide extensive summaries of the various parameters examined in research on FRC specimens without transverse reinforcement completed between 1960 and 2004. These summaries list over twenty experimental programs related to shear in FRC but not all of these results will be discussed in this section. The large scale structural members tested in the current study were constructed with steel fiber reinforced concrete (SFRC) and without transverse reinforcement; therefore recent research on rectangular SFRC specimens over a wide range of overall heights and without stirrups will be described in this section.

2.3.1.1 Narayanan and Darwish (1987)

An experimental program was completed consisting of 49 beams with h = 150 mm tested under four point bending. The shear span to effective depth ratio (a/d) ranged between 2.0 and 3.1. Six beams contained no transverse reinforcement, 10 beams contained conventional stirrups and 33 beams contained crimped steel fibers as a method of shear resistance. In the SFRC members, the fiber volume fraction varied between $V_f = 0.25$ and 3.0%. Fiber lengths of 30 and 40 mm were used. The longitudinal reinforcement ratio varied and the concrete compressive strength ranged between 36 and 80 MPa. Conventional steel reinforcement was used.

The shear cracks in the SFRC specimens were similar to those found in the beams with stirrup reinforcement, although the crack spacing did change. In the SFRC beams, a typical crack spacing of 10 mm was observed with no spalling. In the specimens with stirrups, the spacing was closer to 50 mm and concrete spalling occurred.

Increasing the fiber volume fraction was observed to change the mode of failure from a catastrophic shear failure into a more ductile flexural failure. SFRC beams with $V_f <$ 1.0% still experienced sudden shear failures, although the failures were less catastrophic than the specimens without any type of shear reinforcement. A decrease in curvature was also observed with an increase in V_f at similar load levels, confirming the tension stiffening effect from the steel fibers.

A comparison between the peak load deflections in the SFRC beams and the beams with conventional stirrups showed very similar behaviours. The SFRC beams showed only a marginal improvement in ductility compared to the members containing stirrups.

A substantial improvement (up to 170% when V_f = 1.0%) was found in the ultimate shear strength of the SFRC specimens compared to the specimens without any shear reinforcement. The ultimate shear stress increased with an increase in the fiber volume fraction, and with a decrease in the a/d ratio.

2.3.1.2 Adebar et al. (1997)

Adebar et al. (1997) completed 11 large scale shear tests on SFRC beam specimens with h = 610 mm. Three of the beams were subjected to axial tension in addition to shear. All specimens had identical dimensions and conventional longitudinal reinforcement. No transverse reinforcement was used and three control specimens without fibers were constructed for comparison. The amount and size of hooked end steel fibers were the primary test parameters; fibers with lengths of 30 and 50 mm were used at fiber volume fractions (V_f) between 0.4 and 1.5%.

The width of the critical diagonal crack was found to decrease at a specific load level with an increase in fiber volume fraction.

The results from the large scale shear specimens without axial tension containing 30 mm long fibers are summarized in Table 2-1. The peak shear load (V_{test}) has been normalized in terms of the member width, effective depth and the square root of the concrete compressive stress. The normalized peak shear stress showed an increase as the fiber volume fraction increased (Figure 2-3).

Table 2-1: Summary of Large Scale Specimens Tested by Adebar et al. (1997)

Specimen	d (mm)	ρ (%)	f_c' (MPa)	V_f (%)	Fiber Length L_f (mm)	$\frac{V_{test}}{b_w d \sqrt{f_c'}}$
FCI	558	2.15	60.0	0	NA	0.23
FC8	558	2.15	54.8	0.40	30	0.33
FC9	558	2.15	56.5	0.60	30	0.37
FC2	558	2.15	54.1	0.75	30	0.45
FC3	558	2.15	49.9	1.50	30	0.55

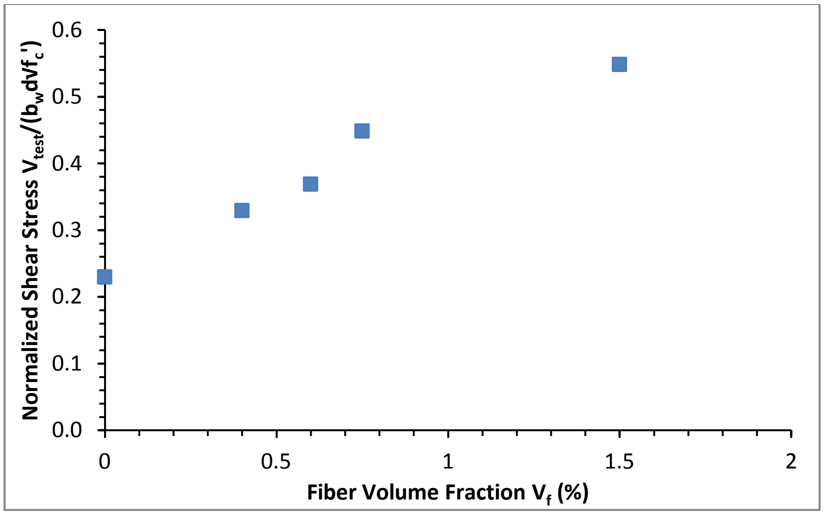

Figure 2-3: Large Scale Specimens Tested by Adebar et al. (1997)

2.3.1.3 Kwak et al. (2002)

Twelve SFRC beams were tested under four-point bending until failure. The fiber volume fraction of hooked end steel fibers was 0, 0.5 or 0.75%. Additionally, three shear span to effective depth ratios (a/d) of 2, 3 and 4 were used. The concrete compressive strengths were between 31 and 65 MPa. All twelve beams had overall heights of h = 250 mm and a longitudinal reinforcement ratio of $\rho = 1.5\%$.

The failure mode in the control specimens with $V_f = 0\%$ was a sudden shear failure. As the V_f increased to 0.50% and 0.75%, the flexural and shear cracks became more closely spaced and the failure mode changed to either a combination of shear and flexure or a full flexural failure. The flexural and shear crack spacing in the beams without fibers was typically 90 to 170 mm but decreased to 70 and 90 mm in the SFRC beams. The ultimate deflection, defined as the point where the load resistance dropped significantly, was found to increase by a factor of up to 5 with an increase in fiber content.

The beams with an a/d ratio of 2 showed significantly higher shear stresses at the ultimate condition than the beams with a/d ratios of 3 and 4 due to the reduced arching and dowel action at larger a/d ratios. The ultimate shear stress in the SFRC beams was noted to increase from 122 to 180% of the strength of the control beams without fibers.

2.3.1.4 Dinh et al. (2011, 2010) and Dinh (2009)

Dinh studied the shear behaviour of SFRC members containing no transverse reinforcement using experimental and analytical techniques (Dinh et al., 2011; Dinh et al., 2010; Dinh, 2009). He considered two series of beams with h = 457 and 686 mm. All specimens were reinforced with conventional Grade 400 steel longitudinal reinforcement. The quantity of longitudinal reinforcement, the fiber type and the fiber volume fraction were the primary test parameters. Control specimens were also constructed using similar dimensions and reinforcement ratios, but with plain concrete instead of SFRC. In addition, one h = 686 mm specimen was cast using plain concrete and 0.17 mm^2/mm of conventional stirrups - 30% greater in area than the minimum requirement in ACI 318-08. The specimens were tested under three point bending until failure, with the majority failing in shear.

The crack pattern was found to improve in the SFRC members compared to the plain concrete members – multiple diagonal cracks formed instead of one large crack. A correlation was subsequently found between the number of flexural and diagonal cracks and the shear strength; members with the highest number of cracks in the critical shear span exhibited higher shear strengths. Dinh also noted that the shear failure modes often differed within a pair of beams with identical properties.

A summary of the large scale beams containing hooked end steel fibers similar to those used in the current study is provided in Table 2-2. The peak shear capacity (V_{test}) has been normalized in terms of the member width, effective depth and square root of the concrete compressive strength and is compared with the fiber volume fraction in Figure 2-4.

Table 2-2: Summary of Large Scale Specimens Tested by Dinh (2009)

Specimen	d (mm)	ρ (%)	f_c' (MPa)	V_f (%)	Fiber Length L_f (mm)	$\frac{V_{test}}{b_w d \sqrt{f'_c}}$
B18-0a	381	2.67	42.8	0	NA	0.17
B18-0b	381	2.67	42.8	0	NA	0.17
B18-1a	381	1.96	44.8	0.75	30	0.44
B18-1b	381	1.96	44.8	0.75	30	0.41
B18-2a	381	1.96	38.1	1.00	30	0.49
B18-2b	381	1.96	38.1	1.00	30	0.50
B18-2c	381	2.67	38.1	1.00	30	0.57
B18-2d	381	2.67	38.1	1.00	30	0.41
B18-3a	381	2.67	31.0	1.50	30	0.46
B18-3b	381	2.67	31.0	1.50	30	0.61
B27-1a	610	2.06	50.8	0.75	30	0.41
B27-1b	610	2.06	50.8	0.75	30	0.38
B27-3a	610	1.56	42.3	0.75	30	0.42
B27-3b	610	1.56	42.3	0.75	30	0.43
B27-5	610	2.06	44.4	1.50	30	0.53
B27-7	610	1.56	37.0	0	NA	0.21
B27-8*	610	1.56	37.0	0	NA	0.30

*Contained minimum shear reinforcement

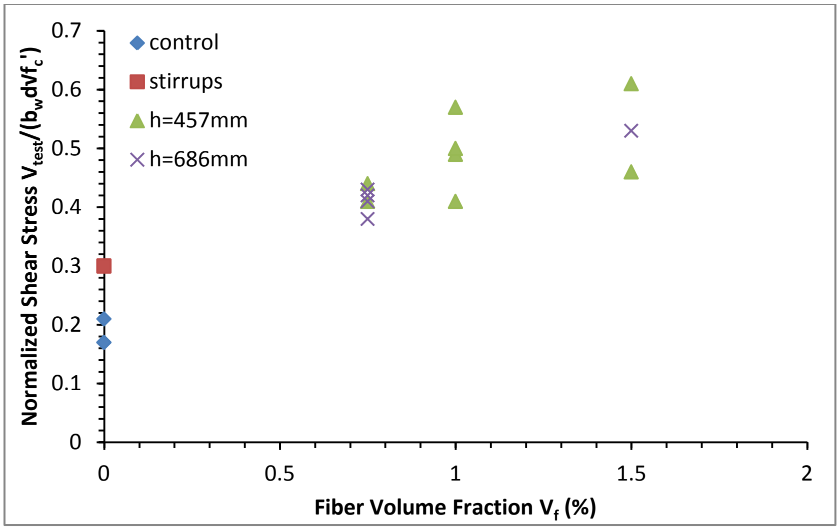

Figure 2-4: Large Scale Specimens Tested by Dinh (2009)

The members containing V_f = 0.75% of hooked end steel fibers exhibited an increase in shear capacity of 159% and 117% compared to the control members without fibers for h = 457 and 686 mm, respectively. The fiber effectiveness was noted to decrease as the fiber content increased beyond V_f = 1.0%. The maximum shear stress in each series occurred in the specimens with the highest fiber volume fraction and largest longitudinal reinforcement ratio. The normalized shear stress at failure for these two SFRC members with the maximum shear strength was 3.2 and 2.5 times larger than the control specimens without fibers for h = 457 and 686 mm, respectively.

A small decrease in shear stress was found related to the member depth, but Dinh considered the size effect to be negligible.

The normalized shear strength of all the h = 686 mm members exceeded that of the member containing ACI 318-08 stirrup reinforcement. The ductility of SFRC members with a fiber volume fraction of hooked end steel fibers greater than or equal to 0.75% was concluded to be greater than the ductility of a geometrically equivalent plain concrete member containing ACI 318-08 minimum stirrups.

In addition to the large scale structural members, Dinh also performed ASTM C1609-10 flexural tests on companion SFRC prisms. The residual strengths of the prisms were compared with the ACI 318-08 requirements (discussed in Section 2.4.1.2) for the use of SFRC as a method of shear resistance. The majority of the prisms did not pass the requirements.

Dinh concluded, based on the strength and ductility of the SFRC beams, that even though the ACI 318-08 requirements for the use of steel fibers as a method of shear resistance were not satisfied, the members containing 0.75% of hooked end steel fibers could be used in place of minimum transverse reinforcement as required by ACI 318-08 for members up to h = 686 mm.

2.3.1.5 Minelli and Plizzari (2010)

Nine large scale SFRC beams with a shear span to effective depth ratio (a/d) of 3 were tested until failure under three point bending. Three fiber volume fractions of hooked end steel fibers were used; 0, 0.64 and approximately 1.0%. The members with V_f = 0% were used as control members for evaluation of the fiber effects. For each of these fiber contents, three beams were cast – one with a nominal overall height of 500 mm, another at 1000 mm and the third at 1500 mm. All beams were constructed with normal strength concrete (f_c' around 30 MPa) and a longitudinal reinforcement ratio of approximately ρ = 1.0% of conventional steel.

Table 2-3: Summary of Large Scale SFRC Specimens Tested by Minelli and Plizzari (2010)

Specimen	d (mm)	ρ (%)	f_c' (MPa)	V_f (%)	Fiber Length L_f (mm)	$\frac{V_{test}}{b_w d \sqrt{f_c'}}$
H500 FRC50	440	1.0	32.1	0.64	50	0.38
H500 FRC75	440	1.0	33.1	1.0	50	0.37
H1000 FRC50	940	1.0	32.1	0.64	50	0.20
H1000 FRC75	940	1.0	33.1	1.0	50	0.26
H1500 FRC50	1440	1.0	32.1	0.64	50	0.24
H1500 FRC75	1440	1.0	33.1	1.0	50	0.27

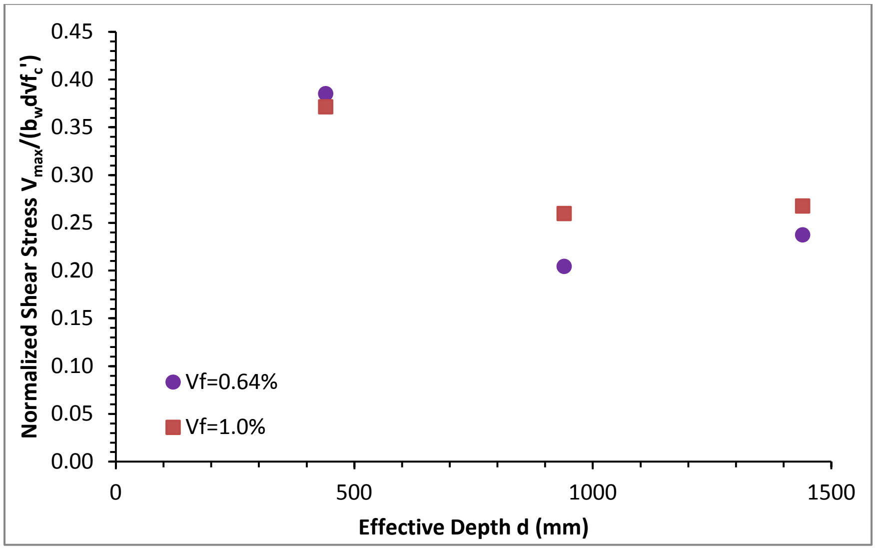

Figure 2-5: Large Scale SFRC Specimens Tested by Minelli and Plizzari (2010)

The post-cracking stiffness in the beams was observed to be enhanced in the SFRC members due to the crack bridging effect of the fibers and the smaller crack spacing compared to the control members. The peak load vertical deflections in the SFRC members were two to three times greater than in the plain concrete members. Shear cracking was observed to begin at a much later load stage in the SFRC members with the steel fibers controlling and stabilizing the ensuing crack propagation. Multi-cracking was observed compared to a single shear crack in the control members. The shear cracks at mid-height were also noted to be at least five times wider in the SFRC members, with shear crack widths between 1 and 2 mm before failure.

The peak shear stresses were normalized by the square root of the concrete compressive strength for comparison (refer to Table 2-3 for a summary of the SFRC members). In the control members, a size effect in shear was visible; the normalized shear stress at failure of the h = 1500 mm member was approximately 53% that of the h = 500 mm member. In the SFRC members of both fiber volume fractions, a size effect was observed between the h = 500 mm and h = 1000 mm members although to a lesser effect with a greater V_f. The normalized shear stresses of the h = 1500 mm members however, were greater than that of the h = 1000 mm members. Minelli and Plizzari attributed this to the crack phenomena experienced by the h = 1500 mm members. The presence of steel fibers in reinforced concrete members was concluded to mitigate the size effects in shear but not eliminate them. The normalized shear stresses are compared with the effective depths in Figure 2-5.

2.3.1.6 **Shoaib et al. (2010)**

Shoaib et al. (2010) studied the shear behaviour of large scale SFRC members reinforced with Grade 400 longitudinal steel reinforcement. Six specimens varying in overall height and longitudinal reinforcement ratio were examined. Two overall member heights were selected in order to examine the size effects in shear; h = 310 and 600 mm. The shear span to effective depth ratio (a/d) was kept constant at 3.0 and 1.0% volume fraction of hooked end steel fibers was used in all mixes. All specimens were tested under three point bending. Four of the members failed in shear, one failed in flexure and another in a combination of flexure and shear.

The maximum diagonal crack width at the level of the longitudinal reinforcement before failure was observed to increase with an increase in member size. Typical diagonal cracks widths before failure were reported as 0.2 and 1.0 mm in the h = 310 mm and h = 600 mm specimens respectively.

Normalizing the shear stress at failure for all the members that failed in shear showed a significant size effect. The h = 600 mm specimens experienced a shear stress at failure approximately 40% less than that of the h = 310 mm specimens.

The average shear capacities of the h = 310 and 600 mm specimens that failed in shear were 3.5 and 2.2 times greater than the ACI 318-08 predicted capacities for plain concrete members, respectively. The average shear capacities of the h = 310 mm and 600 mm specimens were approximately 3.8 and 2.7 times greater than the CSA S6-06 predicted capacities for plain concrete members, respectively.

A summary of the four specimens that failed in shear is provided in Table 2-4. The peak shear capacity (V_{test}) has been normalized in terms of the specimen width, effective depth and square root of the concrete compressive strength and is compared with the effective depth in Figure 2-6.

Table 2-4: Summary of Large Scale SFRC Specimens Tested by Shoaib et al. (2010)

Specimen	d (mm)	ρ (%)	f_c' (MPa)	V_f (%)	Fiber Length L_f (mm)	$\frac{V_{test}}{b_w d\sqrt{f_c'}}$
N31	250	2.67	23.0	1.0	30	0.58
N61	531	1.92	23.0	1.0	30	0.32
N62	523	2.56	23.0	1.0	30	0.32
H62	523	2.56	41.0	1.0	30	0.44

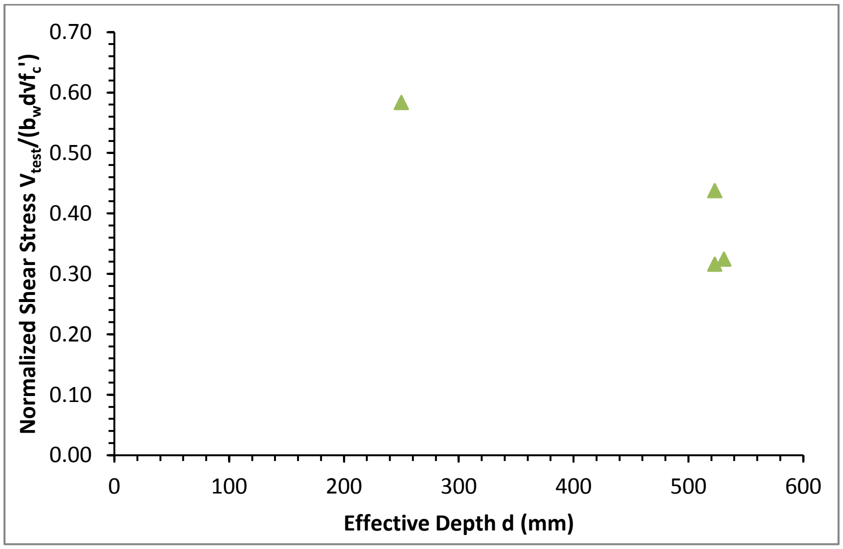

Figure 2-6: Large Scale SFRC Specimens Tested by Shoaib et al. (2010)

2.3.2 Shear Strength of ASTM A1035 Longitudinally Reinforced Specimens

The use of ASTM A1035 steel reinforcement in structural applications is a relatively new technology. The potential for increased reinforcement strains is known to affect the shear capacity of a reinforced concrete member and the lack of experimental data on this subject restricts the level of comfort among design engineers to use higher design strengths. A wide range of research is available on the material characteristics of ASTM A1035 steel reinforcement, but this section will focus on previous research completed on the shear performance of concrete members reinforced with high strength reinforcement.

2.3.2.1 Desalegne and Lubell (2010)

The behaviour of six shear-critical slab strips reinforced with ASTM A1035 longitudinal reinforcement was examined under three-point bending. No transverse reinforcement was included in the slabs. The longitudinal reinforcement ratio, the reinforcement strain at failure and the member depth were the test parameters under consideration. A constant shear span to effective depth ratio (a/d) of 3.5 was used for all specimens and overall heights of h = 305 and 600 mm were examined.

Tensile coupon tests were completed on the ASTM A1035 longitudinal reinforcement. The measured stress-strain relationships were compared with the ACI ITG-6R-10 Appendix B relationship (Equation 2-1) and showed good agreement.

The four slabs with a higher reinforcement ratio (ρ = 0.45%) failed in shear, while the two with ρ = 0.23% failed in a combination of flexure and shear. Linear behaviour was observed in both the load-deflection response and the load-steel strain response up to cracking for all slabs. After cracking, both responses followed linear (or close to linear) behaviour with a reduced slope.

The maximum crack width at an equivalent service load level (determined as $0.6 \cdot P_{max}$) was found to increase with a decrease in the reinforcement ratio. The four slabs with a reinforcement ratio of ρ = 0.45% demonstrated a maximum service crack width of approximately 0.40 mm, which satisfies the ACI 318-08 suggested crack width limit of 0.41 mm. The two remaining slabs with ρ = 0.23% demonstrated maximum service crack widths of 0.50 and 0.60 mm, which exceed the ACI 318-08 limit.

A size effect in shear was observed in the slabs. The h = 600 mm slabs that failed in shear experienced an average 21% decrease in the normalized shear stress at failure compared to the h = 305 mm slabs. A further reduction in the shear stress at failure was observed in the slabs with ρ = 0.23% compared to those with ρ = 0.45%, although it is noted that the lighter reinforced slabs experienced considerably more non-linear behaviour of the reinforcement at failure.

2.3.2.2 **Hassan et al. (2008)**

Six concrete specimens with overall heights of h = 915 mm were tested under three-point bending. The shear span to effective depth ratio (a/d) was set at 1.9 for the first four specimens and 2.7 for the last two. Three concrete compressive strengths were used; f_c' = 32, 38 and 51 MPa. The specimens were constructed in pairs with identical configurations, apart from the reinforcement type and ratio. Within a pair, one specimen was constructed with conventional Grade 400 longitudinal reinforcement with a ratio (ρ) of 0.72% while the other was constructed with ASTM A1035 high strength longitudinal reinforcement at a ratio of 0.44%. The reduction in reinforcement ratio associated with the high strength reinforcement was due to the use of a design yield strength of 690 MPa. No transverse reinforcement was included in any of the specimens.

At failure, the measured deflections of the specimens reinforced with ASTM A1035 steel reinforcement were more than double that of the specimens reinforced with conventional steel reinforcement. This increase was mainly attributed to the lower reinforcement ratio and increased reinforcement strains in the specimens with the high strength reinforcement.

Failure in the Grade 400 steel reinforced specimens was sudden and brittle with relatively little cracking. The specimens reinforced with ASTM A1035 steel experienced a more ductile failure, with considerable deflections and wider cracks. The critical diagonal shear crack in the ASTM A1035 reinforced specimens was almost three times wider than in the equivalent specimen reinforced with conventional reinforcement.

Within each pair of specimens, the shear strength at failure of the specimen reinforced with ASTM A1035 steel reinforcement was significantly higher than in the equivalent specimen reinforced with conventional reinforcement. This discrepancy was more pronounced in the specimens with an a/d ratio of 1.9 that experienced strut and tie behaviour.

2.3.3 Shear Behaviour of Steel Fiber Reinforced Concrete Specimens Containing ASTM A1035 Longitudinal Steel Reinforcement

The previous two sections (2.3.1 and 2.3.2) detailed experimental research previously conducted on the shear behaviour of the two concrete reinforcement types examined in the current study; randomly distributed discrete steel fibers and ASTM A1035 steel reinforcement respectively. There is however no known experimental research that investigates the combination of the two.

2.4 Strength Models

2.4.1 Shear Strength

2.4.1.1 Behaviour

Shear failures tend to be relatively sudden and brittle in the absence of transverse reinforcement. Shear forces acting on a member are typically carried by the concrete itself and by transverse steel reinforcement. Stirrups, the most common form of transverse reinforcement, are designed to intercept tension cracks and resist the shear load to prevent the cracks from opening rapidly – this can allow the member to develop its full flexural capacity and leads to a ductile failure mode.

The shear stress at failure of slender reinforced concrete members without fibers and without transverse reinforcement is known to decrease with an increase in member size and with an increase in the longitudinal reinforcement strain (e.g. Lubell et al., 2009; Bentz et al., 2006; Collins et al., 1996; ACI 445R-99). This leads to the conclusion that for an accurate prediction of a member's shear capacity, both of these parameters should be directly considered.

Randomly distributed discrete steel fibers in a concrete member have been shown to improve the shear capacity compared to a geometrically similar plain concrete member (e.g. Shoaib et al., 2010; Dinh et al. 2010; ACI 544.4R-88). The fibers bridge the diagonal tension cracks and provide an alternative force transfer method (e.g. Dinh et al., 2010 and 2011; Banthia, 1992; Sharma 1986). This benefit has yet to be universally recognized by the North American design codes for reinforced concrete construction, although ACI 318-08 does allow the use of steel fibers as a replacement for minimum shear reinforcement requirements in certain cases.

The shear capacity models from both ACI 318-08 and CSA A23.3-04 are discussed in this section, along with two other models that were developed to take into consideration the increased reinforcement strains of high strength longitudinal steel reinforcement. These four models were developed for plain concrete members and do not take into account the fiber contribution to shear capacity. A fifth model, proposed by Dinh et al. (2011), was developed specifically for SFRC beams without transverse reinforcement but does not take into account the potentially high reinforcement strains associated with use of ASTM A1035 steel reinforcement.

2.4.1.2 **ACI 318-08**

The basic ACI 318-08 shear model for members without transverse reinforcement is:

$$V_{C,ACI} = \phi 0.17\sqrt{f_c'}b_w d \qquad \text{2-2}$$

The model is based on the concrete compressive strength and the member cross-sectional dimensions but does not contain factors accounting for the size effect in shear or for the strain effect caused by the reinforcement strain. Commentary R11.2.2.1 of ACI 318-08 indicates that research has shown the shear strength to reduce with an increase in member size but no further recommendations are provided.

In reinforced concrete flexural members with applied shear loads exceeding 0.5*$V_{C,ACI}$, ACI 318-08 requires a minimum area of shear reinforcement in order to utilize the full $V_{C,ACI}$ shear capacity. Footings, solid slabs and beams with overall heights not greater than 250 mm are excluded from this requirement.

If steel fiber reinforced concrete meeting defined performance specifications is used, the full value of $V_{C,ACI}$ can be used in the absence of stirrups rather than 0.5*$V_{C,ACI}$ (ACI 318-08 Section 11.4.6.1). This provision is applicable for a) a concrete compressive strength of no more than 40 MPa, b) an overall member depth not exceeding 600 mm and c) an applied shear force less than $V_{C,ACI}$. The ACI 318-08 performance specification places limitations based on the volume fraction of steel fibers used as well as residual strengths at various deflection stages under ASTM C1609 flexural tests (ACI 318-08 Section 5.6.6.2). A minimum of 60 kg/m^3 (approximately V_f = 0.76%) of deformed steel fibers must be used in the mix. The residual strength (f_{test}) obtained through ASTM C1609 flexural tests at a mid-span deflection of L/300 must be greater than or equal to 0.9*MOR (modulus of rupture). Additionally, the residual strength at a mid-span deflection of L/150 must be greater than or equal to 0.75*MOR. According to ASTM C1609-10, the MOR is calculated as:

$$MOR = \frac{P_{max}L}{b_w d^2} \tag{2-3}$$

2.4.1.3 **CSA A23.3-04**

The General Method for shear in CSA A23.3-04 (Equation 2-4) is based on the Modified Compression Field Theory (MCFT) (Bentz et al., 2006; Vecchio & Collins, 1986). A so-called strain effect term is provided in the first set of parenthesis of Equation 2-4 to represent the influence on shear strength from the longitudinal reinforcement strain, based on an estimate of the axial strain at mid-height of the member (ε_x) from Equation 2-5. Equation 2-4 assumes that parameter ε_x will not exceed a value of 0.001 mm/mm in the majority of design cases using conventional (ie. Grade 400) steel longitudinal reinforcement. In Equation 2-5, ε_x is simplified as one half of the reinforcement strain (ε_s) at the critical section, and the steel is assumed to follow a linear stress-strain behaviour through use of the modulus of elasticity (E_s). A so-called size effect term is also included by way of the second set of parenthesis of Equation 2-4 to represent the influence on shear strength from the aggregate size (a_g) and effective depth (d_v) of the member. Parameter s_{ze} represents the effective crack spacing of the member, and is described in Equation 2-6. The effective shear depth (d_v) is taken as the greater of 0.9*d or 0.72*h.

$$V_{C,CSA} = \phi_c \left(\frac{0.4}{1+1500\varepsilon_x}\right)\left(\frac{1300}{1000+s_{ze}}\right)\sqrt{f_c'}\,b_w d_v \tag{2-4}$$

$$\varepsilon_x = \frac{\frac{M}{d_v} + V}{2E_s A_s} \leq 0.003 \tag{2-5}$$

$$s_{ze} = \frac{35d_v}{a_g + 15} \geq 0.85d_v \tag{2-6}$$

2.4.1.4 **Hoult et al. (2008)**

Hoult et al. (2008) provided a modified version of the CSA A23.3-04 General Method for shear capacity (see Section 2.4.1.3) that was developed to better account for the higher strains often present in concrete members longitudinally reinforced with high strength steel or fiber reinforcing polymers (Equation 2-7). The strain effect term included in the first set of parenthesis of Equation 2-8 is calculated using the CSA A23.3-04 model (Equation 2-5). The reinforcement is assumed to follow a linear stress-strain behaviour through use of the modulus of elasticity (E_s). The size effect term included in the second set of parenthesis of Equation 2-7 is also calculated based on the CSA A23.3-04 model (Equation 2-6).

$$V_{C,H} = \left(\frac{0.3}{0.5 + (1000\varepsilon_x + 0.15)^{0.7}}\right)\left(\frac{1300}{1000 + s_{ze}}\right)\sqrt{f_c'}\,b_w d_v \qquad \text{2-7}$$

2.4.1.5 **Desalegne and Lubell (2010)**

For concrete specimens reinforced with high strength longitudinal reinforcing steel that does not exhibit a well defined yield point (ie. ASTM A1035 steel), Desalegne and Lubell (2010) proposed modifications to the Hoult et al. shear model (refer to Section 2.4.1.4). The equation for axial strain at mid-height of the member in CSA A23.3-04 (Equation 2-5) is replaced with one that directly accounts for the non-linear stress-strain behaviour of ASTM A1035 steel reinforcement. This model is herein termed as the Desalegne and Lubell General model.

The stress in the longitudinal reinforcement at the critical section is estimated using Equation 2-8 based on the shear and flexural force components. The corresponding reinforcement strain can be found using the lower bound stress-strain curve suggested by ACI ITG-6R-10 for ASTM A1035 Grade 690 reinforcement (Equation 2-1). The axial strain at mid-height of the member (ε_x) is assumed to be one half of the reinforcement strain (ε_s). The modified strain parameter can subsequently be used with the Hoult et al. shear model (Equation 2-7) to account for non-linear stress-strain behaviour of the longitudinal reinforcement and axial strains up to 0.006 mm/mm.

$$f_s = \frac{\frac{M}{d_v} + V}{A_s} \qquad \text{2-8}$$

Desalegne and Lubell also developed a Simplified model by assuming a maximum reinforcement design stress of 690 MPa for ASTM A1035 steel – consistent with the ACI ITG-6R-10 Simplified flexural model. This method was adopted by ACI ITG-6R-10 for the shear design of one-way slabs with ASTM A1035 steel reinforcement. When used in combination with the stress equations noted above, a stress of 690 MPa corresponds to a reinforcement strain of 0.00427 mm/mm. Taking half this value as the mid-height axial strain and using $a_g = 0$ in Equations 2-6 and 2-7 produces a lower bound estimate of the shear capacity, described in Equation 2-9.

$$V_{C,D\&L,S} = \left(\frac{154}{1000 + 2.1d}\right)\sqrt{f_c'}\,b_w d \qquad \text{2-9}$$

2.4.1.6 **Dinh et al. (2011)**

A shear capacity model for steel fiber reinforced concrete (SFRC) beams without transverse reinforcement was developed by Dinh (2009) and refined in Dinh et al. (2011). The model detailed in this section was adapted from Dinh et al. (2011) with background information provided by Dinh (2009).

The model considers the shear capacity of a SFRC member as two separate components (Equation 2-10); the shear force acting in the concrete flexural compression region (V_{cc}) and the vertical component of the tension resistance provided by the steel fibers across the diagonal cracks (V_{FRC}). The contribution to shear capacity from aggregate interlock was neglected due to widening of the critical diagonal crack before failure which reduces or eliminates aggregate interlock. The shear contribution from dowel action was assumed to be minor and was also neglected. The Dinh et al. model is given as:

$$V_{C,Dinh} = V_{cc} + V_{FRC} \tag{2-10}$$

To determine V_{cc}, the member is assumed to be under-reinforced in flexure as required by ACI 318-08. A longitudinal reinforcement stress equal to the yield stress is assumed. A reinforcement ratio limit within calculations of $\rho \leq 2.0\%$ was suggested by Dinh (2009) to avoid over-estimating the tensile force in the longitudinal reinforcement (T_r) in beams with larger amounts of flexural reinforcement. The depth to the neutral axis (c) can be determined based on force equilibrium as detailed in Equation 2-11, where $\beta_{1,ACI}$ is the same as in the ACI 318-08 flexural model described later in Equation 2-20.

$$c = \frac{A_s f_y}{0.85\beta_{1,ACI} f_c' b_w} \tag{2-11}$$

A uniform stress block with stress intensity of $0.85{*}f_c$' was assumed in the concrete compression zone. The uniform shear stress was derived as $0.11{*}f_c$' acting over a stress block depth of $\beta_{1,ACI}c$ (ie. $\alpha_{1,ACI} = 0.11$ in Figure 2-9 in Section 2.4.2). Thus, the shear force from the concrete flexural compression region can be calculated based on Equation 2-12.

$$V_{cc} = 0.11 f_c' \beta_1 c b_w = 0.11\frac{T_r}{0.85} = 0.13 A_s f_y \tag{2-12}$$

The tensile force transmitted across the diagonal cracks by the steel fibers was approximated through an equivalent uniform tensile stress parameter (σ_{ru}). The tension contribution across the crack from fibers located below the longitudinal reinforcement was neglected for simplicity. The diagonal crack angle was approximated at $\alpha = 45°$. The component of shear force resistance attributed to the steel fibers was determined from Equation 2-13.

$$V_{FRC} = T_r \cos\alpha = (\sigma_{ru}) b_w (d - c) \cot\alpha \tag{2-13}$$

The equivalent uniform tensile stress (σ_{ru}) was derived from ASTM C1609 four point bending tests on 150 x 150 x 500 mm un-notched prisms. Once a crack had formed, the flexural behaviour was modelled as two rigid blocks rotating at angle θ away from each other (Figure 2-7).

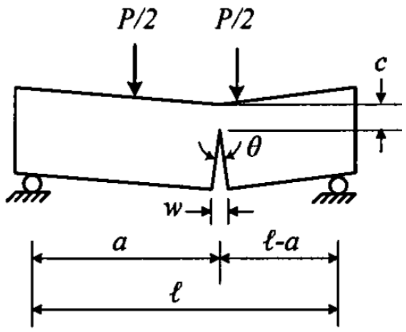

Figure 2-7: Model of ASTM C1609 Un-Notched Flexural Prism Behaviour from Dinh (2009)

A uniform compressive stress of 0.85*f_c' was assumed over the entire compression zone while σ_{ru} acted over the entire tension zone (refer to Figure 2-8). For force equilibrium, the compressive (C_r) and tensile (T_r) forces must be equal. Based on the geometry illustrated in Figure 2-8, both C_r and T_r experience internal lever arms equal to h/2. The applied moment (M_a) can be obtained from the ASTM C1609 flexural tests and used to calculate the depth to the neutral axis (c). Refer to Equations 2-14 and 2-15.

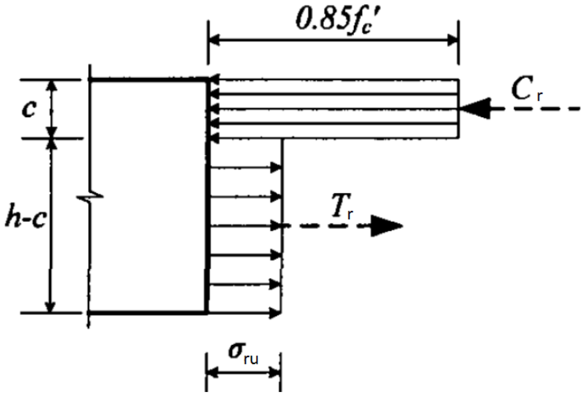

Figure 2-8: Stress Blocks at the Cracked Section (Adapted from Dinh (2009))

$$M_a = \begin{cases} C_r\left(\frac{h}{2}\right) = 0.85f_c' b_w c(\frac{h}{2}) \\ T_r\left(\frac{h}{2}\right) = (\sigma_{ru}) b_w (h-c)(\frac{h}{2}) \end{cases} \quad 2\text{-}14$$

$$c = \frac{2M_a}{0.85f_c' b_w h} \quad 2\text{-}15$$

To further simplify the model based on Dinh's test results, c was taken as 10% of the prism height and Equation 2-14 was rearranged to solve for σ_{ru} (Equation 2-16). A strength reduction factor of 0.8 was arbitrarily selected and recommended for the equivalent uniform tensile stress to account for differences in the behaviour of SFRC prisms and large scale beams.

$$\sigma_{ru} = 0.8(\frac{2M_a}{0.9b_w h^2}) \quad 2\text{-}16$$

The diagonal crack widths in the large scale test specimens examined by Dinh were measured as approximately 5% of the fiber length immediately before failure. Using geometry from the ASTM C1609 flexural prism tests, the estimated crack width before failure was converted to an equivalent mid-span deflection. Based on the previous assumption of c = 0.1*h, the mid-span deflection of the flexural prisms corresponding to the large scale beam crack widths was $L_f/24$, where L_f = the fiber length. Two methods were suggested for obtaining the value of the moment (M_{Lf}) at this deflection point. Dinh suggested obtaining M_{Lf} directly from the fiber manufacturer and/or through the load-deflection curves obtained from ASTM C1609 flexural prism tests.

2.4.1.7 Steel Fiber Reinforced Concrete and ASTM A1035 Reinforcement

As previously discussed in Sections 2.2.1 and 2.4.1.1, the addition of randomly distributed discrete steel fibers to a concrete mix is well known to substantially increase the shear capacity of the member. Several shear models have been proposed to account for the tension stiffening from the fibers but there is currently no widely accepted shear model for steel fiber reinforced concrete (SFRC). Further, there are no shear models suggested for the specific combination of SFRC and ASTM A1035 steel reinforcement.

2.4.2 Flexural Strength

2.4.2.1 Behaviour

Flexure-critical slender reinforced concrete beams with conventional (ie. Grade 400) steel reinforcement can be classified as failing in one of three ways (MacGregor & Bartlett, 2000). Tension controlled failures (also called under-reinforced) occur when the reinforcement yields in tension before the concrete crushes in compression. Compression controlled failures (also called over-reinforced) occur when the concrete crushes before the reinforcement yields. Balanced failures occur when the reinforcement yields simultaneously as the concrete crushes. Each design code has a different approach to flexural design, but the goal is ultimately the same – designing under-reinforced structural members that provide advance warnings of impending failures through large deflections.

Following the well-known plane sections remain plane theory, the strain profile through the cross-section of a reinforced plain concrete member will be linear (MacGregor & Bartlett, 2000). However, the variation in concrete stresses will be non-linear due to the parabolic stress-strain relationship in concrete. The Hognestad Parabola is often accepted as a representative model for plain concrete with $f_c' < 45$ MPa (Collins & Mitchell, 1997) and is described in Equation 2-17.

$$f_c = -f_c'\left(2\left(\frac{\varepsilon_{cf}}{\varepsilon_c'}\right) - (\frac{\varepsilon_{cf}}{\varepsilon_c'})^2\right) \qquad 2\text{-}17$$

To simplify the design procedures, most design codes allow use of an equivalent, rectangular stress block with a uniform stress intensity. The general format is illustrated in Figure 2-9. The height of the actual stress block (shown shaded in Figure 2-9a) and defined by parameter c, represents the distance from the extreme compression face to the neutral axis. In the equivalent stress block at the ultimate condition, this distance is factored by β_1. The equivalent uniform intensity of the stress block is represented as $\alpha_1 f_c'$. The equations for α_1 and β_1 are described individually in the following sections for each design model.

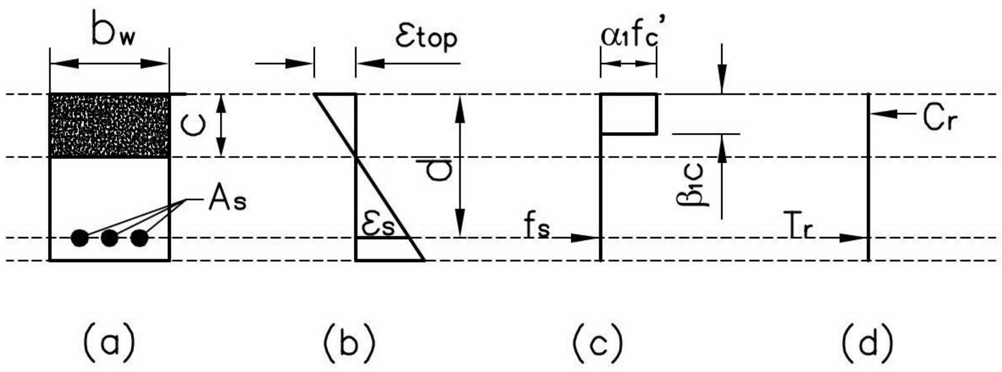

Figure 2-9: Reinforced Plain Concrete Member a) Cross-Section b) Strains c) Equivalent Stress Blocks and d) Forces

The equivalent internal compressive force on the section (C_r) can be determined from the equivalent stress block and corresponding cross-sectional area (Equation 2-18). The tensile resistance (T_r) is determined from the longitudinal reinforcement area and stress (Equation 2-19). To satisfy equilibrium, the compression force (C_r) and the tension force (T_r) must be equal.

$$C_r = \alpha_1 \beta_1 f_c' b_w c \qquad 2\text{-}18$$

$$T_r = A_s f_s \qquad 2\text{-}19$$

The depth of the equivalent concrete stress block, $\beta_1 c$, is found by equating 2-18 and 2-19. The flexural strength is found by the force (C_r or T_r) multiplied by its moment arm ($d-0.5\beta_1 c$ as illustrated in Figure 2-9).

An iterative approach to the entire flexural response can be solved using different cross-sectional strain values. In most cases, the strain at the extreme compression face (ε_{top}) and at the reinforcement layer (ε_s) are either known or assumed. Using these strains with the appropriate material stress-strain curves for both the concrete and the steel reinforcement will determine the compressive and tensile forces (Equations 2-18 and 2-19). For the general case of a flexural member with no axial load, the depth to the neutral axis is found once the sum of the forces equal zero. The corresponding internal moment and curvature can then be found using the internal forces, their respective level arms and the configuration of the strain diagram.

2.4.2.2 **ACI 318-08**

At the ultimate limit state (ULS) condition, ACI 318-08 specifies an average stress of 0.85*f_c' to create the equivalent concrete stress block shown in Figure 2-9 (ie. $\alpha_1 = 0.85$). The depth of the equivalent compression stress block is defined by $\beta_{1,ACI}$ in Equation 2-20.

$$\beta_{1,ACI} = \begin{cases} 0.85 & for\ 17 \leq f_c' \leq 28 \\ 0.85 - 0.05\dfrac{(f_c' - 28)}{7} \geq 0.65 & for\ f_c' \geq 28 \end{cases} \qquad \text{2-20}$$

ACI 318-08 specifies the maximum strain at the extreme compression face as 0.003 mm/mm for design at the ULS. The stress in the longitudinal reinforcement (f_s) cannot exceed f_y although the strain can exceed ε_y. The maximum permissible design yield strength is 550 MPa in flexure (ACI 318-08 Section 9.4).

ACI 318-08 defines a tension controlled section as one where the net tensile strain in the extreme tension reinforcement (ε_s) is greater than or equal to 0.005 mm/mm when the concrete reaches its ultimate compression strain value of 0.003 mm/mm (ACI 318-08 Section 10.3.4). A compression controlled section is defined when the net tensile strain in the extreme tension reinforcement is less than 0.002 mm/mm. ACI 318-08 varies the strength reduction factor ($M_r = \phi M_n$) based on the reinforcement strain at the ultimate load as per Equation 2-21, although all strength reduction factors in the current study were set to 1.0.

$$\begin{array}{cc} \varepsilon_s \leq 0.002 & \phi = 0.65 \\ 0.002 < \varepsilon_s < 0.005 & \phi = 0.65 + (\varepsilon_s - 0.002)(250/3) \\ \varepsilon_s \geq 0.005 & \phi = 0.90 \end{array} \qquad \text{2-21}$$

2.4.2.3 **CSA A23.3-04**

CSA A23.3-04 specifies an equivalent concrete compression stress block at the ultimate limit state using the factors $\alpha_{1,CSA}$ and $\beta_{1,CSA}$ which vary with f_c'. At the ultimate condition, these factors are as described in Equations 2-22 and 2-23.

$$\alpha_{1,CSA} = 0.85 - 0.0015 f_c' \geq 0.67 \qquad \text{2-22}$$

$$\beta_{1,CSA} = 0.97 - 0.0025f_c' \geq 0.67 \qquad 2\text{-}23$$

A maximum concrete crushing strain of 0.0035 mm/mm is defined for the extreme compression face at the ultimate limit state. The reinforcement stress cannot exceed f_y (which is limited to 500 MPa), although the strain can surpass ε_y and there is no limit placed on the strain in the reinforcement steel. CSA A23.3-04 also specifies a concrete resistance factor of $\phi_c = 0.65$, applied directly to C_r in Equation 2-18. A steel reinforcement resistance factor of $\phi_s = 0.85$ is applied directly to T_r in Equation 2-19. These factors were set to 1.0 for the current study.

To ensure an under-reinforced design where the longitudinal steel reinforcement yields before the concrete crushes, a section containing conventional Grade 400 steel reinforcement should be proportioned such that:

$$\frac{c}{d} \leq \frac{700}{700 + f_y} \qquad 2\text{-}24$$

2.4.2.4 ACI ITG-6R-10 and NCHRP 679 (2011)

The recently published ACI ITG-6R-10 and NCHRP 679 (2011) provide recommendations for the design of structural members reinforced with ASTM A1035 Grade 690 steel reinforcement. Both publications recommend increasing the reinforcement design yield strength limit to 690 MPa.

ACI ITG-6R-10 recommends two stress-strain relationships for the high strength reinforcement; the so-called Appendix B model based on the full non-linear behaviour of the high strength reinforcement and the Simplified model based on elastic-plastic behaviour similar to that of conventional reinforcement.

The Appendix B stress-strain relationship is described in Equation 2-1 and shown in Figure 2-10. ACI ITG-6R-10 recommends a limiting strain of 0.015 mm/mm in the longitudinal reinforcement for designs following ACI ITG-6R-10 Appendix B. It is also suggested that serviceability checks should be performed and minimum shear reinforcement be provided due to the lack of experimental data for members designed by this method.

Adjustments to the tension controlled strain limits to ensure a ductile design and strength reduction factors (ϕ) are as recommended by Mast, Dawood, Rizkalla, & Zia (2008). Due to the higher strength of ASTM A1035 reinforcement, it is not required to yield to in order to obtain the high strain levels on the tension face required for a tension controlled member, and thus an increase in the tension controlled strain limits is recommended. Compression reinforcement is restricted to the existing limit of 550 MPa to ensure compatibility with the maximum concrete compression strain of 0.003 mm/mm. The revised strain limits and strength reduction factors for members designed with the Appendix B reinforcement stress-strain relationship are provided in Equation 2-25.

$$\begin{array}{cc} \varepsilon_s \leq 0.0042 & \phi = 0.65 \\ 0.0042 < \varepsilon_s < 0.0067 & \phi = 0.23 + 100\varepsilon_s \\ \varepsilon_s \geq 0.0067 & \phi = 0.90 \end{array} \qquad 2\text{-}25$$

To expedite the design process, ACI ITG-6R-10 also recommends a Simplified elastic-plastic stress-strain relationship (Figure 2-10) that does not require a non-linear analysis. The relationship is based on Mast et al. (2008) and uses an elastic-perfectly plastic stress-strain relationship with initial modulus of elasticity of 200,000 MPa and a yield strength of 690 MPa. The modified strain limits and strength reduction factors to ensure compatibility with ACI 318-08 are as suggested by Mast et al. (2008) and provided in Equation 2-26.

$$\begin{array}{cc} \varepsilon_s \leq 0.004 & \phi = 0.65 \\ 0.004 < \varepsilon_s < 0.009 & \phi = 0.45 + 50\varepsilon_s \\ \varepsilon_s \geq 0.009 & \phi = 0.90 \end{array} \qquad 2\text{-}26$$

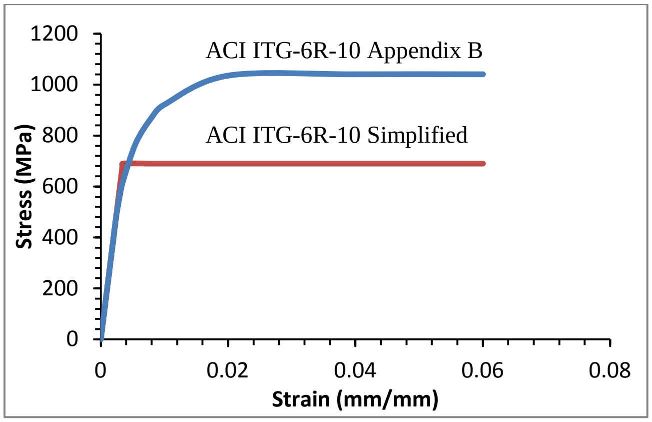

Figure 2-10: ACI ITG-6R-10 Stress-Strain Curves for ASTM A1035 Grade 690 Reinforcement

NCHRP 679 (2011) suggests following the same elastic-perfectly plastic stress-strain behaviour from Mast et al. (2008) up to a yield strength of 690 MPa for both tension and compression controlled members. To ensure adequate ductility in flexure, it recommends increasing the tension controlled strain limit of 0.005 mm/mm for conventional reinforcement to 0.008 mm/mm for ASTM A1035 steel. The compression controlled strain limit is proposed to increase from 0.002 mm/mm to 0.004 mm/mm. These recommendations are based on a study of 286 cases with several different grades of reinforcing steel, concrete strengths and test configurations and are only slightly different than those suggested by Mast et al. (2008). To keep deflections and crack widths within acceptable limits, a maximum steel stress of 400 MPa at the serviceability limit state is recommended.

Mast et al. (2008) examined the predicted capacity of a prototype beam with a longitudinal reinforcement ratio of 1.0% through the various proposed material models. It was found that using high strength steel reinforcement increased the flexural capacity by 95% compared to a similar beam with Grade 400 reinforcement when the Appendix B non-linear stress-strain behaviour of the ASTM A1035 Grade 690 steel was considered. This value decreased to 60% using the Simplified stress-strain model with a design yield strength of 690 MPa. If the behaviour was predicted based on the ACI 318-08 design yield strength limit of 550 MPa, the improvement over the conventional reinforcement was calculated as 31%. Mast concluded that increasing the design limit to 690 MPa would result in more efficient designs while still maintaining adequate reserve capacity.

2.5 Serviceability Models

The serviceability limit states of a structure or structural member must be considered alongside the strength during design. Poor performance at the serviceability condition, including large crack widths and substantial deflections, may hinder the use of a structure or the comfort of the occupants. The service load levels in the current study are estimated at 50% of the peak load, as discussed later in Section 6.1.

The α_1 and β_1 equivalent stress block factors defined previously in Section 2.4.2 are applicable at the ultimate limit states conditions. At all other load conditions (ie. at the serviceability limit states), these factors are defined by Collins & Mitchell (1997) in Equations 2-27 and 2-28.

$$\alpha_c \beta_c = \frac{\varepsilon_{top}}{\varepsilon_c'} - \frac{1}{3}(\frac{\varepsilon_{top}}{\varepsilon_c'})^2 \qquad \text{2-27}$$

$$\beta_c = \frac{4 - \varepsilon_{top}/\varepsilon_c'}{6 - 2\varepsilon_{top}/\varepsilon_c'} \qquad \text{2-28}$$

2.5.1 Crack Control

Control of excess cracking or crack widths is accomplished indirectly in many design models. In CSA A23.3-04, a crack parameter (z) is provided to limit the crack widths occurring in the region adjacent to longitudinal reinforcement for interior and exterior exposures. For members with overall heights exceeding 750 mm, CSA A23.3-04 requires skin reinforcement distributed near the sides of the members between the neutral axis and the main longitudinal tension reinforcement to prevent wide cracks from forming in this area. In members with transverse reinforcement, a maximum stirrup spacing is specified. The spacing limit ensures that diagonal cracks are crossed by at least one stirrup, and crack widths are controlled. In members without transverse reinforcement, crack spacing and crack widths are a function of the member depth (Collins & Kuchma, 1999; Vecchio & Collins, 1986). Members with larger depths will typically experience larger crack widths. Smaller crack widths at the service condition will result in less water ingress, and increase the durability of the member (Banthia, 1992).

ACI 318-08 follows similar principles to CSA A23.3-04 to provide adequate crack control at the service condition. Maximum spacing requirements for longitudinal reinforcement are provided, and skin reinforcement is required in members with overall heights exceeding 900 mm.

2.5.2 Deflection Control

Deflection control requirements are established in design codes to ensure the use of a structure is not compromised and to prevent damages to attached materials. Both ACI 318-08 and CSA A23.3-04 provide deflection limits for structural members under various configurations, generally provided as a fraction of the span (or clear span) length. The deflected behaviour of a member changes along its length, and depends on whether the material at that location has cracked. Both ACI 318-08 and CSA A23.3-04 provide two different methods to control deflection in structures at the serviceability limit state; the first is the deemed-to-comply method and the second is through direct deflection calculations. Only the latter approach will be discussed in this section.

The behaviour of reinforced concrete members in terms of curvature and deflection is complex. Slender members follow the plane sections remain plane hypothesis and the strain distribution over a certain cross section is linear. As detailed by Collins & Mitchell (1997), concrete is able to carry small amounts of tensile stresses before cracking. Once a crack has formed, there is no longer any tension carried by the concrete at that location, instead those forces are transferred into the longitudinal reinforcement. Therefore, at a crack location, the tensile stress in the longitudinal reinforcement will be highest. In between cracks however, the concrete is able to carry tensile stresses when bonded to the longitudinal steel reinforcement. This effect, termed tension stiffening, stiffens the member and reduces deflections (e.g. Bischoff & Scanlon, 2007; Bischoff, 2003; Collins & Mitchell, 1997).

In regions where the concrete member remains uncracked, the change in curvature increases proportionally with the applied moment. In regions where the concrete member has cracked, the moment-curvature relationship is no longer linear. The curvature will increase faster than the applied moment and is highest at crack locations (Collins & Mitchell, 1997). The curvatures along the length of a member can be integrated using moment-area theorem (MacGregor & Bartlett, 2000) to obtain the expected deflections along the length of the member.

The stiffness of a plain concrete member reinforced with conventional Grade 400 steel reinforcement is related to the reinforcement ratio (ρ) (e.g. Lubell et al., 2009; Tang & Lubell, 2008). Increasing the area of steel reinforcement will reduce the strain in the reinforcement and increase the cracked moment of inertia (I_{cr}) leading to an increased effective stiffness of the member.

Members reinforced with high strength longitudinal reinforcement will typically require a smaller reinforcement ratio (ρ) compared to a similar member with conventional steel reinforcement and the same flexural strength. However, the strain in the reinforcement will be higher for the member with the high strength reinforcement. The reduced ρ will lower the cracked moment of inertia (I_{cr}) and decrease the stiffness of the member (Tang & Lubell, 2008). Adding discrete steel fibers into the concrete mix will increase the tensile capacity of the concrete by carrying tension at the cracks in addition to the tension already present between the cracks (Bischoff, 2003). The fibers will increase I_{cr}, enhance the effective stiffness, reduce the crack spacing and widths, and decrease the deflection of a member (Bischoff, 2007; Bischoff, 2003).

2.5.3 Curvature and Deflection Models

Currently, there is no standard method to predict the curvature or deflection of a member reinforced with both steel fibers and high strength longitudinal steel although recommendations are available when only one of these two materials is considered.

For direct deflection calculations of reinforced plain concrete members without fibers, ACI ITG-6R-10 and Tang and Lubell (2008) recommend the use of Bischoff's 2005 equation for effective moment of inertia (I_e) (Equation 2-29). This model accounts for tension stiffening in the concrete between cracks, but not the influence from the steel fibers. Previous research (Bischoff & Scanlon, 2007; Bischoff, 2005) indicates that this model correlates well with short term deflections found in laboratory testing for a range of reinforcement ratios but specifically for low reinforcement ratios.

$$I_e = \frac{I_{cr}}{1-\left(1-\frac{I_{cr}}{I_g}\right)(\frac{M_{cr}}{M_a})^2} \leq I_g \qquad \text{2-29}$$

Several methods have been suggested for direct deflection calculations of fiber reinforced concrete (FRC). Armelin and Banthia (1997) used a plastic hinge model in combination with ASTM C1018 flexural tests to suggest a layered approach. The cracked region of the prism cross section is divided into several layers and the tensile resistance of the fibers on each layer is estimated. Bischoff (2007) proposed an alternative method for calculating the effective moment of inertia of FRC members. The post-cracking tensile strength contribution from the fibers is accounted for by assuming a uniform tensile resistance across the cracked cross section. The revised effective moment of inertia can be used with the ACI 318-08 deflection calculation approach based on an effective moment of inertia.

An additional approach is to calculate the moment-curvature relationship for a FRC member, and integrate the curvature values to obtain the deflections. A method similar to that described by Collins & Mitchell (1997) for tension stiffening in concrete between cracks can be applied to FRC. Collins and Mitchell describe an equivalent uniform tensile stress (simplified as $0.5*f_{cr}$) applied over an effective embedment zone around the longitudinal reinforcement in reinforced concrete members without fibers. As a possible extension to the technique investigated in this study, the tensile stress can be replaced by an equivalent uniform tensile stress carried by the fibers bridging the cracks in FRC members. The tensile stress can determined from ASTM C1609-10 flexural tests (refer to Section 4.2.3) and applied over the entire cracked cross section of the prism. Once force equilibrium is determined through iteration of the neutral axis depth (c), the curvature and deflection can be calculated.

2.6 Summary

In reinforced plain concrete members without transverse reinforcement, shear forces are known to transfer across diagonal cracks through aggregate interlock, dowel action of the longitudinal reinforcement, arch action and residual tension forces. These mechanisms were detailed in Section 2.1. The addition of randomly distributed discrete steel fibers has been previously shown to add an additional force transfer mechanism across cracks. This alternate force transfer path reduces diagonal crack widths, improves aggregate interlock action and increases the post-peak tensile strength compared to a plain concrete member. At the structural scale, steel fiber reinforced concrete (SFRC) has been observed to have substantially larger shear capacities than equivalent concrete members without fibers. Section 2.2.1 summarized these behaviours based on the work by several researchers.

ASTM A1035 Grade 690 steel reinforcement is a high strength material that lacks a distinct yield plateau and exhibits a proportional limit higher than the yield strength of conventional Grade 400 steel reinforcement. A higher chromium content and different microstructure increases the material’s corrosion resistance compared to conventional reinforcement. Use of the higher strength of the steel reinforcement can reduce the quantity of material required in reinforced concrete members for a similar flexural strength, but could increase the reinforcement strain levels as described by several researchers. Reinforced concrete members are known to exhibit a strain effect in shear; the shear stress at failure decreases with an increase in longitudinal reinforcement strain. Therefore, appropriate models must be used to account for the increased reinforcement strains.

Laboratory results are available on the shear behaviour of large scale structural SFRC members longitudinally reinforced with Grade 400 steel reinforcement. Limited experimental data is available for plain concrete members reinforced with ASTM A1035 Grade 690 steel reinforcement. Results from Desalegne & Lubell (2010) and Hassan et al. (2008) were discussed. No known data is available for structural members containing both SFRC and high strength longitudinal steel reinforcement. Nonetheless, the available results examining each of the materials individually provide a basis for comparison with the specimens in the current study.

Current shear strength models consider the influence of SFRC and ASTM A1035 steel reinforcement separately. While there is no widely accepted shear capacity model for SFRC, limited shear and flexural capacity models for plain concrete members with high strength longitudinal reinforcement have recently been developed. ACI 318-08 provisions allow for the replacement of minimum transverse reinforcement with SFRC as a method for shear resistance in specific cases but CSA A23.3-04 provides no guidance for the structural use of SFRC.

Current serviceability models exist that take into account the influence of larger reinforcement strains experienced by high strength longitudinal reinforcement, and separate models exist to account for tension stiffening due to discrete, randomly distributed steel fibers. No known model exists that accounts for the influence from both SFRC and high strength steel reinforcement.

3 Materials Characterization – Experimental Program

3.1 Introduction

The global response of steel fiber reinforced concrete (SFRC) members is known to be influenced by the force transfer mechanisms occurring at cracks, including the contributions from bridging fibers. These transfer mechanisms depend in part on the width of the cracks, which can vary with overall specimen size and the fiber volume fraction (e.g. Shoaib et al., 2010; Dinh, 2009; Adebar et al., 1997).

The first phase in the current study was to develop a unique SFRC mix design that provided consistent and reliable properties and that could be reproduced in large scale batches at a commercial ready-mix facility. A nominal 28 day compressive strength of 40 MPa and a slump after the addition of fibers of approximately 100 mm were the strength and rheological targets. Normal weight aggregate and a volume fraction of 1.0% steel, hooked end fibers were included in all trial and final mix designs.

Materials characterization testing of the developed mixes was performed to examine the response in flexure for notched specimens. Nominal specimen dimensions that varied by a factor of up to 2 were used to allow for the quantification of size dependent influences on the response. Instrumentation based on the digital image correlation (DIC) technique allowed for a detailed study of the variation of crack width over the member depth and its relation to the specimen size and loading. Materials characterization tests for the compression response were conducted using cylinders over a size factor of 1.5.

The specimen configurations used in the materials characterization tests are presented in Section 3.2. The trial mixes and final production mix are described in Section 3.3. The test setup and instrumentation is explained in Section 3.4 for both the compression and flexure tests conducted with the production mix. A description of the test procedures is also provided in Section 3.4.

3.2 Specimen Configurations

Laboratory trial batches up to 0.05 m^3 in volume were used to develop a SFRC mix that could be commercially replicated in a ready mix plant with consistent results. A Gilson drum mixer (model #59015C) with 0.16 m^3 of capacity and drum rotation of 20 rpm was used for the laboratory trials. The trials aimed for a nominal 28 day compressive strength close to 40 MPa, and a slump near 100 mm after the addition of fibers. Once the strength, rheology and durability properties of a trial mix were deemed satisfactory, production on a larger trial scale was completed to determine if any modifications were required to mass produce the mix. After these alterations were completed, the final trial mix became the design used for the structural specimens tested in the current study and was subsequently classified as the production mix. The large scale mixes, both the final trial and production mixes, were produced in a BMH trunion type mixer with a horizontal rotary at the Inland Concrete Ltd. plant in Strathcona County, Alberta.

Cylinders were cast for testing according to ASTM C39-09a, while prisms were cast for testing according to ASTM C1609-10. The strength results reported in the current study are based on the average of three cylinders or prisms, unless otherwise noted. During casting, all slump tests were performed according to ASTM C143-10 and all air content tests were performed according to ASTM C231-09b. The slump test values reported are for the mixes after the steel fibers had been added, unless otherwise noted.

All cylinders and prisms were compacted in two layers with a vibrating table, save for the largest prisms which were compacted with internal vibration. Immediately after casting, the specimen tops were covered in plastic to prevent water evaporation and cured in their moulds under wet burlap and a plastic covering. After 48 hours, all specimens were de-moulded and curing was continued under wet burlap and a plastic covering for the appropriate time period before testing.

3.2.1 Trial Mixes

In each trial mix casting, a total of six 100 mm diameter x 200 mm long cylinders were cast for ASTM C39-09a compressive strength tests at 7 and 28 days. In addition, between four and six 100 x 100 x 300 mm span prisms were cast for the ASTM C1609-10 flexural tests at 7 and 28 days.

3.2.2 Production Mixes

In order to determine the size effects in compression and flexure, geometrically scaled cylinders and prisms were cast for each production mix. For the cylinders, both 100 mm diameter x 200 mm long and 150 mm diameter x 300 mm long sizes were used. For the prisms, three sizes were examined: 100 x 100 x 300 mm span, 150 x 150 x 450 mm span and 200 x 200 x 600 mm span.

Two 5.5 m^3 castings were completed with the production mix, labelled as Casting A and Casting B. In each casting, three cylinders of both sizes mentioned above were cast for the ASTM C39-09a compressive strength tests at 28 days. Nine prisms were cast for the ASTM C1609-10 flexural tests at 28 days - three of each of the three sizes described above. These specimens were used to provide information on the strength development properties of the concrete mix.

Additional cylinders and prisms were also cast for testing alongside the large scale structural specimens described in Chapter 5 to provide information on their specific material properties. Three 150 mm diameter cylinders were cast for each of the large scale structural specimens (referred to as structural companion cylinders), along with a total of six 100 x 100 x 300 mm and three 150 x 150 x 450 mm prisms (referred to as structural companion prisms) in each casting. Figure 3-1 illustrates the size variation in both the cylinders and prisms.

The test setup and procedures for the production mixes are detailed in Section 3.4.

a) b)

Figure 3-1: Production Mix Specimen Size Variation in a) Cylinders and b) Notched Prisms

3.3 Mix Development

The compression and flexural tests completed as part of the trial mixes were intended to provide an overall idea of the concrete strength in compression and in tension, without considering the full load-displacement relationship. A Forney Testing Machine model FX700 was used to perform the trial mix tests at a standard loading rate of 250 kPa/s for both the cylinders and the prisms. All cylinders were compression tested with un-bonded neoprene caps.

3.3.1 Trial Mixes

Hooked end steel fibers (Figure 3-2a) with a length of 30 mm, aspect ratio of 55 and yield strength of 1100 MPa were used in the current study. All mixes contained a fiber volume fraction of V_f = 1.0%. As detailed in Section 2.2.1, volumes of fibers above 1.0% have been shown to have minimal strength improvements over mixes containing 0.75% or 1.0% fibers. For this reason, 1.0% was chosen to provide desired strength enhancement benefits without using an excessive amount of fibers that could increase the likelihood of fiber balling (Figure 3-2b).

a) b)

Figure 3-2: a) Hooked End Steel Fibers and b) Fiber Balling During Casting

Trial Mix #1 was based on the SFRC mix developed by Shoaib et al. (2009), and used Type GU Portland Cement and no admixtures. For subsequent trials, the mix proportions were adapted from a standard mix design from Inland Concrete Ltd. with a nominal 28 day compressive strength of 35 MPa. The cement type was changed to Type HS to increase the suitability of the developed concrete for specific industrial applications. The aggregates (14 mm coarse aggregate and Villeneuve fine aggregate) were obtained from the stockpiles of Inland Concrete Ltd. The material properties and grading information for both the coarse and fine aggregates are listed in Table 3-1 and illustrated in Figure 3-3. The fine and coarse aggregates were used in a saturated, surface dry condition in Trial Mix #2. WRDA 64 water reducer (Grace Concrete Products, 2007b) was added in order to improve the rheology without compromising the strength. The resulting high slump and low strengths of Trial Mix #2 were indications of excess water in the mix which was attributed to the water absorbed by the aggregates. Trial Mix #3 was completed with the same mix proportions as Trial Mix #2, but the aggregates were left in sealed containers prior to use to prevent any water absorption or evaporation. Subsequently, the water state was expected be similar to that used in the ready mix plant. The results at this stage were promising – Trial Mix #3 resulted in a slump of 90 mm while the nominal 28 day compressive strength and MOR increased 9% and 17% respectively compared to Mix Trial #2. Refer to Table 3-2 for details.

Table 3-1: Coarse and Fine Aggregate Properties (Adapted from EBA Report E12201546 June 18, 2010)

14 mm Coarse Aggregate		Fine Aggregate	
Sieve Size (mm)	Percent Passing (%)	Sieve Size (mm)	Percent Passing (%)
28	100		
20	99		
14	91		
10	56	10	100
5	3	5	93
2.5	0	2.5	78
1.25	0	1.25	70
0.630	0	0.630	65
0.315	0	0.315	34
0.160	0	0.160	7
0.080	0.1	0.080	1.2
		FM	2.54
Moisture Content (%)	2.7	Moisture Content (%)	8.3
Bulk Relative Density	2.53	Bulk Relative Density	2.59
Absorption (%)	1.7	Absorption (%)	1.1

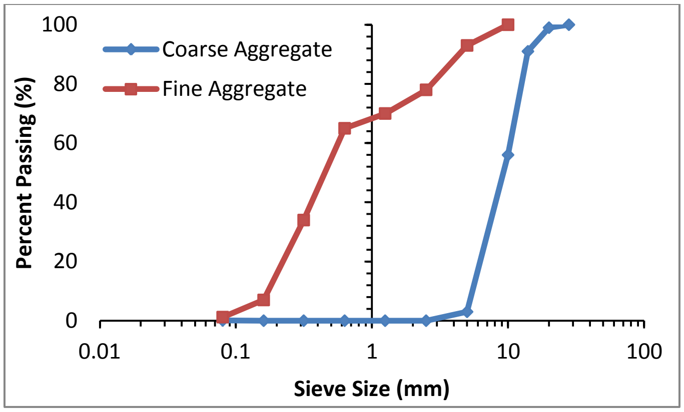

Figure 3-3: Coarse and Fine Aggregate Grading Chart (Adapted from EBA Report E12201546 June 18, 2010)

The mix proportions of Trial #4 were identical to Trial #3 but the cement type was switched to InterCem™, a pre-blended product of Type GU Portland cement and Class F fly ash, in order to develop a product with increased sulphate resistance. Although this change in cement type reduced the 28 day compressive strength and MOR, it was acknowledged that further modifications would be required to produce the mix on a larger scale.

Details of the five trial mixes are provided in Table 3-2.

Table 3-2: Trial Mix Development Details and Results

	Trial Mixes				
	1	2	3	4	5
Target 28 Day Strength (MPa)	40	40	35	35	35
Cement Type	GU	HS	HS	InterCem™	InterCem™
Cement (kg/m^3)	391	391	391	391	391
Fine Aggregate (kg/m^3)	665	785	785	785	796
14 mm Coarse Aggregate (kg/m^3)	993	1048	1048	1048	990
Mixing Water (L/m^3)	235	157	157	157	157
WRDA 64 Water Reducer (L/m^3)	NA	0.98	0.98	0.98	0.25
Steel Fibers (kg/m^3)	78.6	78.6	78.6	78.6	78.6
ADVA 140M Super Plasticizer (L/m^3)	NA	NA	NA	NA	1.33
Final Slump (mm)	60	205	90	60	85
Air Content (%)	2.3	4.4	2.4	NA	6
7 Day Compressive Strength (MPa)	32.6	21.4[B]	29.2[B]	21.6	28.2
7 Day MOR (MPa)	5.64[B]	5.51[AB]	5.22[B]	4.11[C]	4.61
28 Day Compressive Strength (MPa)	41.0	37.1[B]	40.5[B]	37.7	38.1
28 Day MOR (MPa)	6.05	5.78[B]	6.71[B]	5.84[B]	5.43

[A] 14 day results [B] Based on the average of two specimens [C] Based on one specimen

Based on the relative success of Trial Mix #4 with InterCem™ cement, a fifth and final trial mix was completed at a larger scale (3.0 m^3) in the BMH trunion type mixer at Inland Concrete Ltd. A slump of 80 mm was measured before the fibers were added into the back of the mixing truck. The steel fibers reduced the slump to 60 mm, prompting the addition of 1 L of Grace Construction Chemicals ADVA 140M super plasticizer (Grace

Concrete Products, 2007a). Although the slump increased to 85 mm, significant fiber balling was observed (Figure 3-2b). An additional 3 L of super plasticizer was added to minimize the issue. An average 28 day compressive strength of 38.1 MPa was obtained, along with an average MOR of 5.43 MPa.

3.3.2 Production Mix

The concrete mix proportions used for the production mix in the current study were based on Trial Mix #5. The concrete was supplied by Inland Concrete Ltd. within two 5.5 m^3 batches. In each of these batches, three large scale structural specimens were cast along with cylinders and prisms designated for concrete strength development analysis and separate cylinders and prisms designated as companion specimens to the large scale members. Specimens from the first casting are referred to as ‘Casting A’, while ‘Casting B’ designates the second casting. The mix proportions used for both castings are shown below in Table 3-3. Note that the super plasticizer was switched to Grace Construction Chemicals ADVA 195 (Grace Concrete Products, 2008) to provide an increased flow compared to the previous super plasticizer used in Trial #5. ADVA 195 was added both at the mixing plant (6 L) and on site (4 L) to reduce fiber balling and to ensure an even distribution of fibers.

Table 3-3: Production Mix Proportions For Castings A and B

Ingredients	Quantity
InterCem™ Cement (kg/m^3)	391
Fine Aggregate (kg/m^3)	796
14 mm Coarse Aggregate (kg/m^3)	990
Mixing Water (L/m^3)	157
Steel Fibers (kg/m^3)	78.6
WRDA 64 Water Reducer (L/m^3)	0.25
ADVA 195 Super Plasticizer (L/m^3)	1.8

The slump measured at the laboratory according to ASTM C143-10 after the addition of the fibers was 130 mm in Casting A and 150 mm in Casting B. The air contents according to ASTM C231-09b were measured as 1.7% and 3.5% for Castings A and B, respectively.

The strength development specimens from Casting B were cured in the typical wet burlap and plastic covering methods described above (Section 3.2) for 28 days, but were subsequently transferred into a moist curing room until testing. The companion cylinders and prisms from both castings were cured under the same conditions as the large scale structural specimens (Section 5.3).

3.4 Production Mix Test Setups and Procedures

3.4.1 Compression

A 2600 kN capacity MTS Universal Loading Frame was used to perform the compression tests on the cylinders from the production mix (Castings A and B). All cylinders were sulphur capped prior to testing and outfitted with a yoke containing three linear variable displacement transducers (LVDTs) at 120° separation to measure the vertical deformation at mid-height. The LVDTs were connected to a data acquisition system along with the MTS output. The compression tests were performed according to ASTM C39-09a. The test setup is shown in Figure 3-4.

A series of three compression tests was performed for both cylinder sizes. The data presented is the average of three tests, unless otherwise noted. The overall yoke height on the 100 mm diameter cylinders was 110 mm, and 210 mm on the 150 mm diameter cylinders. LVDTs with ±2.5 and ±25.0 mm of travel were used with the small and large yokes respectively.

Figure 3-4: Compression Test Setup on a 100 mm Diameter Cylinder

A displacement controlled loading rate of 0.2 mm/min was used for both cylinder sizes, allowing capture of the full load-displacement relationship in compression including the post-peak response.

3.4.2 Flexure

A 1000 kN capacity MTS Universal Loading Frame was used to perform the flexural tests from Castings A and B according to ASTM C1609-10. A notch was saw cut into the tension face of each prism at mid-span. The purpose of the notch was to pre-determine the crack location and prevent multiple small cracks from forming. The current study used a notch depth equal to 25% of the specimen height. Digital callipers were used to measure the average actual height of each notch. Strength calculations were based on the average height of the prisms after accounting for the notch (d_n), as listed in Appendix A.

A digital image correlation (DIC) system was used during the flexural tests as a method of measuring the surface strains. A single LVDT was also employed at mid-span as verification of the DIC data. Further details on the instrumentation are provided in Section 3.4.2.1.

A displacement controlled loading rate of 0.075 mm/min was used for the prisms with heights of 100 mm and 150 mm, while a rate of 0.1 mm/min was used on the 200 mm prisms. The MTS load and stroke data and the LVDT output were captured by the DIC control computer to allow for time synchronization. The tests were stopped after the MTS stroke reached a deflection limit of L/100, where L represents the prism span.

3.4.2.1 **Instrumentation**

Data acquisition methods during typical flexural prism tests involve cumbersome instrumentation and physical measurements. Recently, the digital image correlation (DIC) technique has been developed as a non-contact method to accurately measure 3D surface strains during testing without the need for additional instrumentation (e.g. Alam & Loukili, 2010; Sutton, Wolters, Peters, Ranson, & McNeill, 1983).

A DIC measurement system was used to track the crack growth and specimen deformation throughout the load history for the production mix prisms. One face of each prism was painted with flat white interior latex paint, and subsequently speckled with black acrylic paint to create a random pattern of dots of varying size up to approximately 3 mm (Figure 3-5a), which corresponded with the ideal dot size of at least 3-4 pixels through the software (Correlated Solutions Inc., 2007, 2009 and 2010). Two 5.0 megapixel digital cameras (Point Grey Research GRAS-50S5M-C) with 35 mm focal length lenses (Fujinon Corporation 1:1.4/35mm HF35SA-1) were placed at a distance of approximately 2.8 m from the prisms and at a converging angle of approximately 4.5° in order to view the entire prism face. Vic-Snap software (Correlated Solutions Inc., 2007 and 2009) recorded pairs of images every 1 second during the test on the 100 mm and 150 mm prisms from Casting A. For the 100 mm and 150 mm prisms from Casting B, images were recorded every 2 seconds. Images for the 200 mm prisms from Casting A were recorded every 3 seconds for the initial linear portion of the load-stroke diagram, then every 2 seconds after reaching approximately 75% of the peak load. After the peak load was reached, the timing was set to 3 seconds. The data from the 200 mm prisms from Casting B was recorded every 2 seconds throughout the entire test.

Vic-3D software (Correlated Solutions Inc., 2007 and 2009) was used to process the recorded images to determine surface deformations by comparing the grey value pattern in each image with the initial reference image (Correlated Solutions Inc., 2010). Rigid body motion was analytically removed by the software to account for any support settlement during testing. Data extracted from the software included horizontal and vertical displacements.

A single LVDT was placed below each prism to one side of the notch. An aluminum plate was epoxied on the underside of the prism as the contact point and a magnetic base attached to the frame supported the LVDT body. Due to the setup restrictions with the prisms from Casting A, only a LVDT with ±2.5 mm of travel could be used. For the prisms from Casting B, a LVDT with ±12.5 mm of travel was used. Figure 3-5b illustrates the test setup and LVDT location.

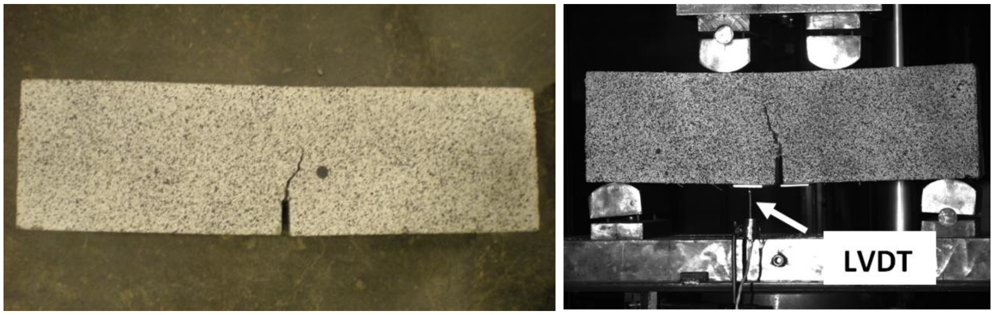

a) b)

Figure 3-5: a) Prism Speckling for DIC System and b) ASTM C1609-10 Flexural Test Setup with LVDT

4 Material Characterization – Test Results and Discussion

The trial mixes were completed to develop an adequate mix design used for the production castings, and as such, the results from the trial mixes are not discussed in this chapter. Rather, this chapter focuses on the strength development and companion test results from the cylinders and prisms in Castings A and B.

A summary of the cylinder and prism test results is provided in this section, generally as the average values of three specimens. Complete data is provided in Appendix A.

The specimens from the strength development phase are referred to based on their size and casting. Cylinders are labelled beginning with a ‘C’ while prisms are labelled beginning with a ‘P’. These letters are followed by three numbers to indicate the size; for example, 100 represents either 100 mm diameter cylinders or 100 x 100 x 300 mm prisms. The letter after the dash represents which casting the specimen was produced from, either Casting A or Casting B. The last number represents the specimen replicate number within its series. Cylinders and prisms used for strength development are numbered 1 through 3. Figure 4-1 provides an illustration of the labelling system.

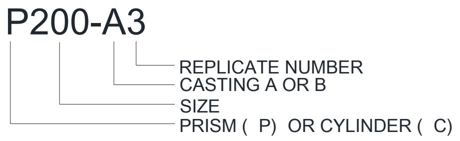

Figure 4-1: Materials Characterization Specimen Labelling System

The structural companion cylinders and prisms were tested alongside their large scale structural specimen companion and are labelled in a similar fashion. The first letter after the dash again corresponds to the casting, and the following number indicates the replicate number within the series. Three cylinders were cast for each of the three large scale structural members, resulting in a total of nine 150 mm diameter companion cylinders in each casting. Following the mix development numbering system, these cylinders are numbered 4 through 12. The response of the companion prisms was determined after all large scale member tests were completed. Therefore, only three 100 x 100 x 300 mm and three 150 x 150 x 450 mm prisms from each casting were tested as companion prisms. These prisms are labelled 4 through 6. To further distinguish the structural companion specimens from the strength development specimens, a ‘C’ is added to the end of the label to represent companion.

Table 4-1 provides a summary of the labelling system described above. The specimens shown in the table are all from Casting A but those from Casting B follow the same labelling system, save for a ‘B’ in the identifying name instead of an ‘A’.

Table 4-1: Cylinder and Prism Labels for Strength Development and Structural Companion Specimens

Label	Casting	Purpose
C100 - A1, A2, A3	A	Strength Development
C150 - A1*, A2, A3	A	Strength Development
C150 - A4C, A5C, A6C	A	Companion 1
C150 - A7C, A8C, A9C	A	Companion 2
C150 - A10C, A11C, A12C	A	Companion 3
P100 - A1, A2, A3	A	Strength Development
P150 - A1, A2, A3	A	Strength Development
P200 - A1, A2, A3	A	Strength Development
P100 - A4C, A5C, A6C	A	Companion 1, 2 and 3
P150 - A4C, A5C, A6C	A	Companion 1, 2 and 3

*Results excluded due to a faulty sulphur cap.

Often, the average response of three cylinders or prisms is detailed instead of the individual responses. In this case, the specimens will be labelled without the replicate numbers. For example, P150B will refer to the average from the 150 x 150 x 450 mm strength development prisms from Casting B and P150BC will refer to those same prisms from the structural companion specimens.

4.1 Compression Response

4.1.1 Strength Development Results

As part of the mix development process, 100 mm and 150 mm cylinders from the production mixes were tested for compressive strength based on ASTM C39-09a. From Casting A, the 150 mm diameter cylinders were tested at 28 days while the 100 mm diameter cylinders were tested at 29 days. The 150 mm diameter cylinders from Casting B were tested at 34 days and the 100 mm cylinders were tested at 107 days.

Table 4-2 summarizes the key properties from the strength development cylinders. It is observed that the compressive strengths decreased as the specimen size increased for both Castings A and B. In Casting A, the 150 mm diameter cylinders exhibited a 12% lower average compressive strength compared to the 100 mm diameter cylinders tested at similar ages. In Casting B, the 150 mm cylinders produced an average compressive strength 21% lower than the 100 mm cylinders; however some of the discrepancy in strength for the Casting B results is likely from the age difference between the two cylinder sizes.

The strain corresponding to the peak stress (ε_c') is also provided in Table 4-2. These strains, especially those from Casting A, are larger than would be expected for plain concrete specimens and can likely be attributed to the expected increase in toughness for FRC specimens as detailed in Section 2.2.1. The average ε_c' increased with an increase in cylinder size, although to varying degrees in each casting as detailed in Table 4-2.

The compressive modulus of elasticity (E_c) was calculated based on the initial linear portion of the stress-strain diagrams, specifically located between the origin and a stress of approximately $0.4{*}f_c'$. The average E_c was 20% lower in the 150 mm cylinders than the 100 mm cylinders from Casting A, and 26% lower in Casting B.

Table 4-2: Summary of Strength Development Compression Test Results

Casting	Cylinder Diameter (mm)	Code	Number of Cylinders	Age at Testing (Days)	f_c'		ε_c'		E_c	
					AVG (MPa)	COV	AVG (mm/mm)	COV	AVG (MPa)	COV
A	100	C100A	3	29	36.6	0.05	0.0032	0.05	19,578	0.08
A	150	C150A	2	28	32.3	0.04	0.0042	0.05	15,605	0.12
B	100	C100B	3	107	39.5	0.01	0.0028	0.07	26,745	0.02
B	150	C150B	3	34	31.0	0.01	0.0029	0.04	19,811	0.06

The average compressive stress-strain curves from both specimen sizes and both castings are compared in Figure 4-2. The code indicated in Table 4-2 for each set of cylinders corresponds to the curve labelling in Figure 4-2.

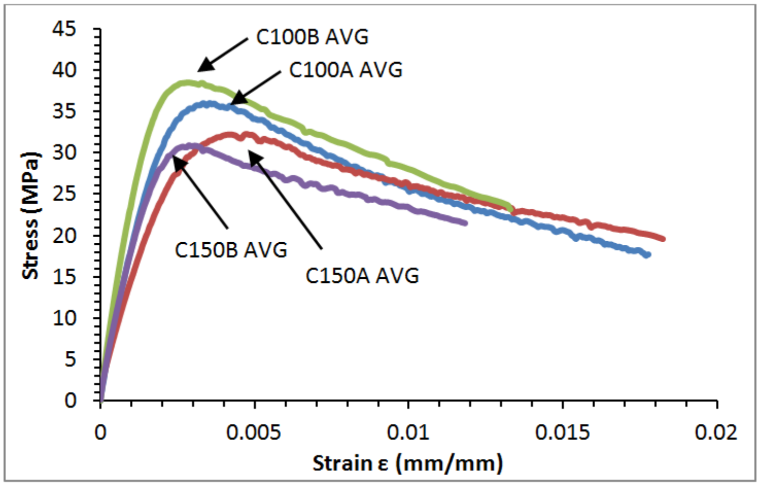

Figure 4-2: Average Compressive Stress-Strain Curves from Casting A and B Strength Development Cylinders

4.1.2 Large Scale Structural Companion Results

Three 150 mm diameter cylinders were cast along with each large scale structural specimen. These cylinders were tested immediately after the associated large scale specimen test in order to provide representative stress-strain curves for the concrete in each specimen. A summary of the relevant information obtained from these tests is provided in Table 4-3.

Table 4-3: Summary of Structural Companion Compression Test Results

Casting	Companion Specimen	Number of Cylinders	Age at Testing (Days)	f_c’		ε_c’		E_c	
				AVG (MPa)	COV	AVG (mm/mm)	COV	AVG (MPa)	COV
A	S1000-A4	3	104	40.1	0.02	0.0039	0.15	19,334	0.06
A	S1000-A3	3	119	41.2	0.02	0.0043	0.12	18,929	0.04
A	S300-A2	2	161	37.9	0.00	0.0043	0.04	17,648	0.04
B	S1000-B1	3	56	30.4	0.04	0.0036	0.11	21,035*	0.13
B	S1000-B2	3	65	31.2	0.03	0.0042	0.11	19,400	0.05
B	S300-B1	3	97	29.9	0.03	0.0040	0.06	17,330	0.06

*C150-B5C measured between origin and 0.5*fc’

The stress-strain curves for S1000-B2, based on the three companion cylinders C150-B7C, C150-B8C and C150-B9C, are shown in Figure 4-3. The stress-strain curves for the remaining large scale specimens showed similar trends and are provided in Appendix A.

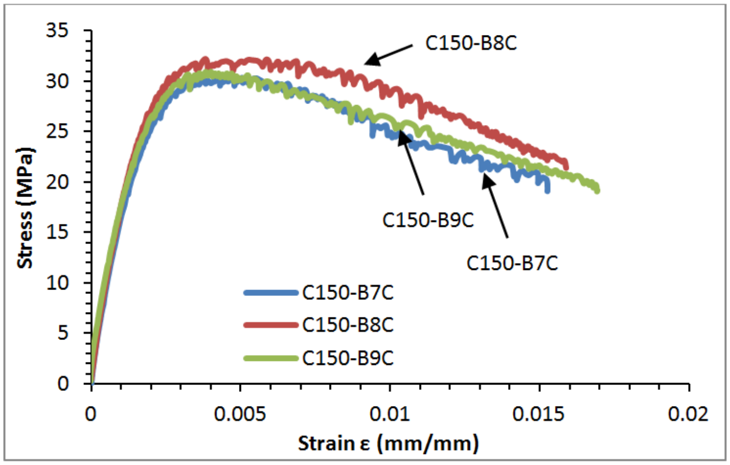

Figure 4-3: Specimen S1000-B2 Structural Companion Cylinder Stress-Strain Curves

4.2 Flexural Response

For both Castings A and B, prisms were produced for testing with the strength development compression cylinders described in Section 4.1.1 and are designated as strength development prisms. Those from Casting A were tested at ages between 31 and 37 days while all prisms from Casting B were tested at ages between 110 days and 131 days due to scheduling restrictions. Each casting included three 100 x 100 x 300 mm, 150 x 150 x 450 mm and 200 x 200 x 600 mm prisms.

Prisms were also tested as companions to the large scale structural specimens (along with the structural companion compression cylinders described in Section 4.1.2) in order to gain a better understanding of the material properties within these structure-scale tests. These prisms are designated as structural companion prisms. A set of three prisms, in both the 100 x 100 x 300 mm and 150 x 150 x 450 mm sizes, were cast and cured alongside each of the large scale specimens. Due to a limited number of forms, the 200 x 200 x 600 mm prisms were only cast for the strength development stage, and not as structural companion prisms. The structural companion prisms were tested at ages exceeding 119 days and the material properties were assumed to have stabilized, therefore three prisms for each size and each casting were tested after all large scale specimens had been tested. A summary of all structural companion specimen prisms is provided in Table 4-4. The prism age indicated in the table is the average age at the time of testing of the prisms.

Table 4-4: Structural Companion Prism Details

Prisms	Size (mm)	Associated Large Scale Structural Companions	Average Prism Age (Days)
P100-A4C, P100-A5C, P100-A6C	100 x 100 x 300	S1000-A3, S1000-A4 and S300-A2	187
P150-A4C, P150-A5C, P150-A6C	150 x 150 x 450	S1000-A3, S1000-A4 and S300-A2	193
P100-B4C, P100-B5C, P100-B6C	100 x 100 x 300	S1000-B1, S1000-B2 and S300-B1	119
P150-B4C, P150-B5C	150 x 150 x 450	S1000-B1, S1000-B2 and S300-B1	124

The digital image correlation (DIC) system was used to measure the surface deformations of the prisms, and the Vic-3D software (Correlated Solutions Inc., 2009) was used to obtain the corresponding surface strain fields. Figure 4-4a shows the horizontal strain components for prism P150-A1 at the end of testing, highlighting the crack location at mid-span. The image is provided here to emphasize the location and extent of cracking, therefore the colour scale has been omitted.

Figure 4-4b shows the eight locations selected using the Vic-3D software and used to evaluate the relative movement of these locations on the prisms. These eight locations correspond to a point immediately above the LVDT location, on each side at the base and top of the notch, at mid-height of mid-span and immediately above each support. Rigid body motion removal was completed in the software (Correlated Solutions Inc., 2009) using an average transformation, resulting in locations at approximately the quarter spans of the prisms that were fixed against movement. Due to the upward motion of the 1000 kN capacity MTS Universal Loading Frame to create the applied load, it was necessary to combine the vertical deflection at the supports with the vertical deflections at mid-span to obtain the total mid-span deflection relative to the supports in the DIC system.

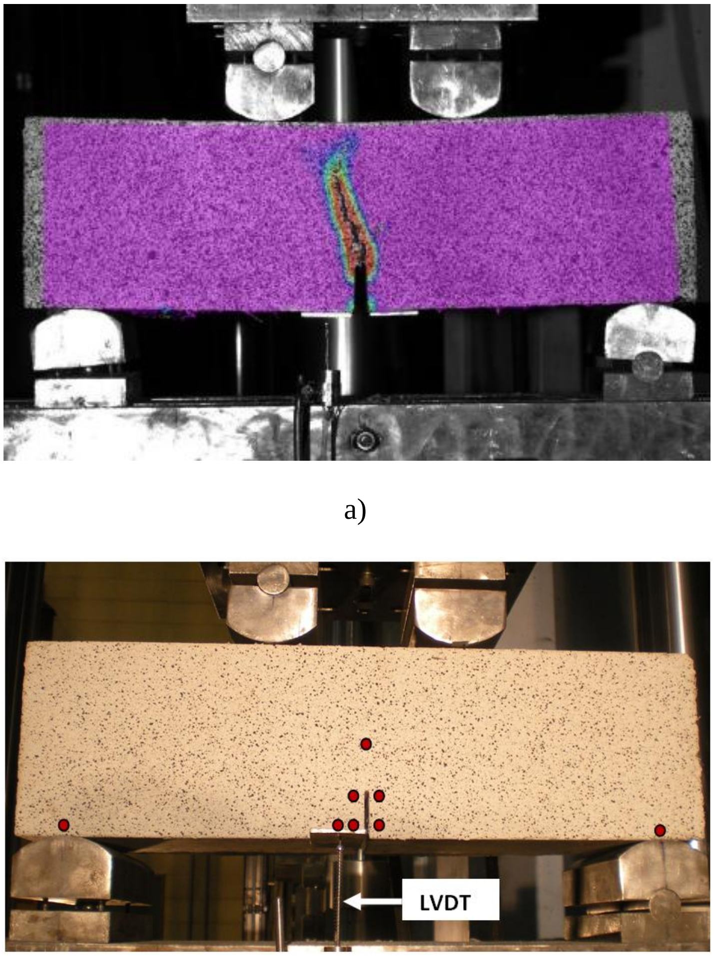
a)

b)

Figure 4-4: a) Horizontal Strain Field for P150-A1 and b) DIC Data Extraction Points

Calculations of the modulus of rupture (MOR) were based on Equation 4-1 (ASTM C1609-10), where d_n represents the height of the prism after accounting for the notch. Results for individual prisms are available in Appendix A.

$$MOR = \frac{P_{max} L}{b_w d_n^2} \tag{4-1}$$

4.2.1 Strength Development Results

The mid-span vertical deflection was calculated at the top and bottom of the notch by using the average reading from the DIC measurement points located on both sides of the notch with the average reading from the measurement points located immediately above both supports (Figure 4-4b). These two mid-span deflections were then compared with the vertical deflection obtained through the mid-height measurement point at mid-span. In each of the three specimen sizes, the deflections at all three locations were comparable.

Figure 4-5a indicates the variation as the average of three 100 mm prisms from Casting A; in this representative case the variation between locations was less than 7%.

The mid-span LVDT measured larger deflections to the DIC system in many of the specimens. This is shown in Figure 4-5b for P100-B2 but the comparison is representative of the majority of prisms. Discrepancies between the two sources of data were attributed to two main factors. The DIC data was corrected by the Vic-3D software for all rigid body motion including support settlement whereas no correction was made to the LVDT data. Due to the nature of the LVDT setup and the rotation of the concrete specimen under increasing loads, the LVDT reading was influenced by both horizontal and rotational components of movement experienced by the specimen during loading and cannot be considered as a valid indicator of vertical deflection. In contrast, the DIC analysis process provides each deformation component (e.g. vertical, horizontal) separately. All subsequent references to the member mid-span deflection refer to the DIC deflection calculated at the bottom of the notch.

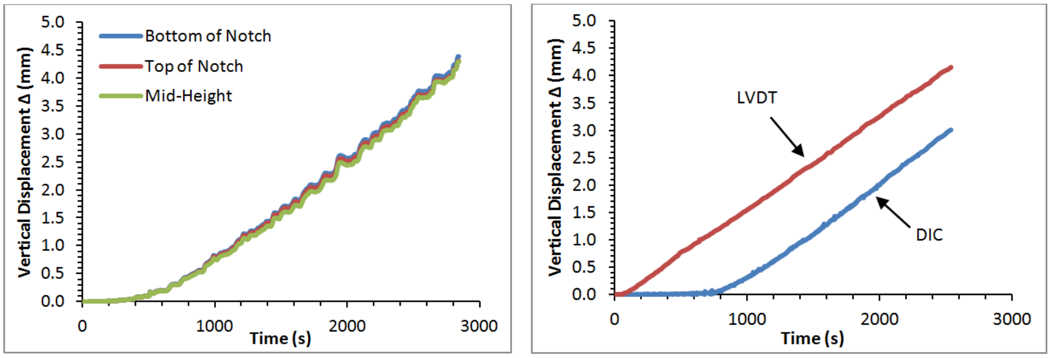

a) b)

Figure 4-5: a) P100A Average Prism Vertical Displacement and b) Comparison of P100-B2 DIC and LVDT Measurements

The crack width expansion at the base of the notch is defined as the crack mouth opening displacement (CMOD). The horizontal expansion between the two DIC measurement points at the bottom of the notch was used to determine the CMOD.

The change in CMOD is plotted against the change in mid-span deflection (d_{CMOD}/d_{Δ}) for all nine strength development prisms from Casting A (three of each of the three sizes) in Figure 4-6a. This same ratio is compared again in Figure 4-6b, but with all eighteen prisms from both Castings A and B. Using a linear regression technique, the results produced d_{CMOD}/d_{Δ} ratios of 1.32 ($R^2 = 1.00$) and 1.29 ($R^2 = 0.99$) for Castings A and B, respectively.

The trend from all three specimen sizes and both castings confirmed that the d_{CMOD}/d_{Δ} relationship is size-independent, and also strength independent. As previously summarized in Table 4-2, the average compressive strength from the 150 mm cylinders from Casting A was 32.3 MPa and 31.1 MPa from Casting B.

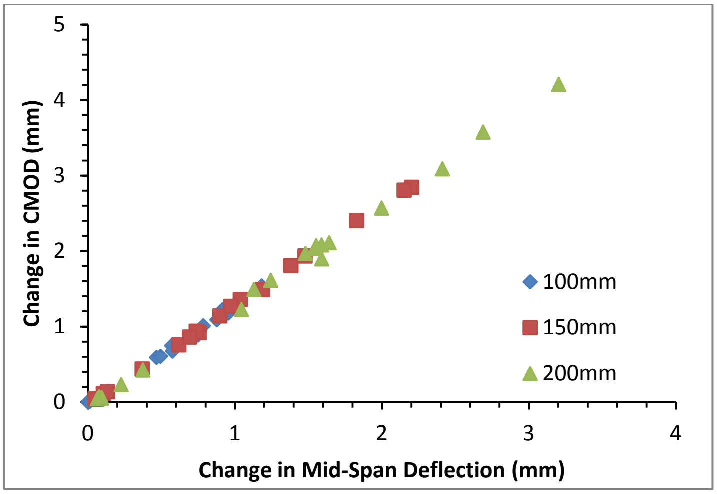

a)

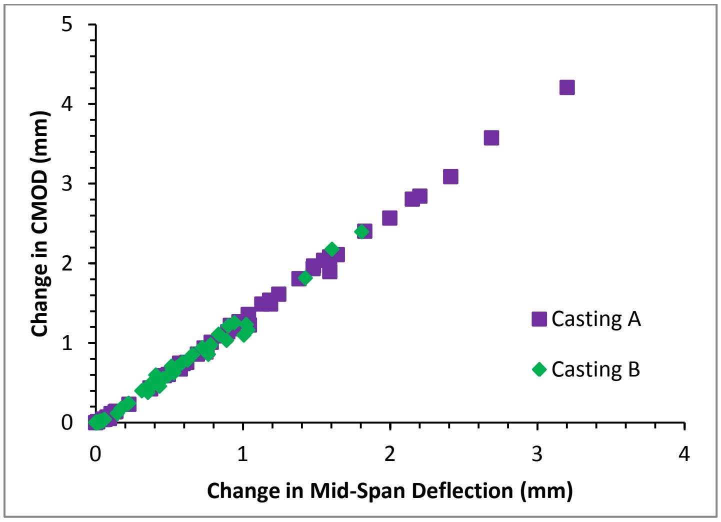

b)

Figure 4-6: Relationship between CMOD and Mid-Span Deflection for Strength Development Prisms from a) Casting A and b) Castings A and B

Armelin and Banthia (1997) predicted the d_{CMOD}/d_{Δ} ratio to be size independent, based on their analytical model and the assumption that geometric similarity is maintained between the prism sizes. They reported on six previously tested 75 x 75 x 250 mm un-notched FRC prisms with f_c' = 50 MPa and containing 0.75% hooked end steel fibers. A d_{CMOD}/d_{Δ} ratio of approximately 1.50 was observed, which they deemed to be reasonably close to their analytical model result of 1.33. The d_{CMOD}/d_{Δ} ratios found for the strength development prisms from Casting A and Casting B in the current study were within 3% of the Armelin and Banthia analytical result of 1.33, even considering that the prisms in the current study were notched.

Figure 4-7a illustrates the average load-deflection curves for all three prism sizes from Casting A while Figure 4-7b shows the modulus of rupture (MOR) for each prism from Castings A and B with their respective member depths. As expected, as the prism size increased, the tensile strength decreased. The average load-deflection curve from the 100 mm prisms from Casting A demonstrated a maximum applied load of 12.9 kN at a vertical displacement of 0.66 mm, which corresponds to a MOR of 6.88 MPa. This correlates well with the flexural response obtained for members of similar size, compressive strength and fiber volume fraction reported by Shoaib et al. (2009). The MOR for the 150 mm and 200 mm prisms from Casting A decreased by 30% and 39% respectively, as compared to the 100 mm prisms. The specimens from Casting B followed a similar trend; those results are available in Appendix A.

The CSA A23.3-04 model for MOR based on the compressive strength of plain concrete without fibers is also shown in Figure 4-7b for comparison. The model is size independent and is described in Equation 4-2. The compressive strength used in this case was taken as the average of the 150 mm diameter strength development cylinders from Casting A (f_c' = 32.3 MPa). The CSA A23.3-04 model is observed to generally underestimate the MOR for SFRC prisms, although the discrepancy decreases as the member size increases.

$$MOR = 0.6\sqrt{f_c'} \tag{4-2}$$

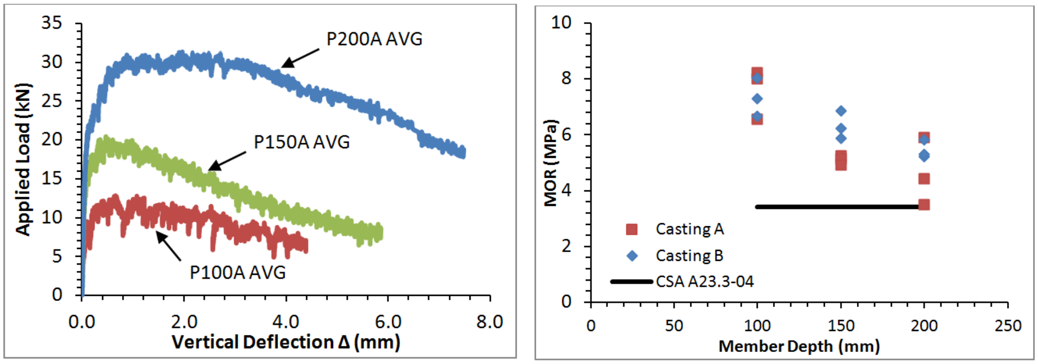

a) b)

Figure 4-7: a) Average Load-Deflection Curves for Casting A Strength Development Prisms and b) Relationship between MOR and Member Depth for Strength Development Prisms

Figure 4-8 plots the peak tensile strength (MOR) against the corresponding CMOD for each specimen from Castings A and B. In general, as the specimen size increased, so did the CMOD at peak load although there were a few exceptions (most notably one 200 mm prism from Casting A).

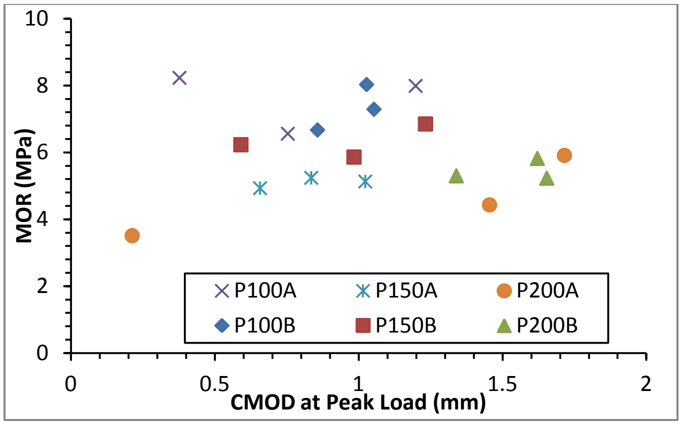

Figure 4-8: Relationship between MOR and CMOD at Peak Load for Strength Development Prisms

The flexural toughness of each prism to a post-peak deflection limit of L/150 was determined using the area under the load-deflection curve (ASTM C1609-10). Table 4-5 summarizes the average flexural toughness values for each prism size from both Casting A and Casting B. Individual results are provided in Appendix A. The equivalent flexural strength ratio ($R_{T,150}$) was determined according to Equation 4-3 using the calculated flexural toughness and the modulus of rupture (MOR) (ASTM C1609-10). The MOR calculation was previously defined in Equation 2-3.

$$R_{T,150} = \frac{150\, T_{150}}{MOR\ bd_n^2} \tag{4-3}$$

Figure 4-9a illustrates the variation in flexural toughness with respect to the member depths. The results indicate a size effect when considering the toughness of a prism; as the prism size increases, the flexural toughness increases. The prisms from Casting B indicate average flexural toughness values higher than those from Casting A except in the 100 mm prism size.

Figure 4-9b demonstrates the variation in equivalent flexural strength ratio with respect to the member depths. A large decrease in $R_{T,150}$ is observed between the 100 mm prisms and the 150 mm prisms, but the overall relationship between all member sizes remains unclear.

Table 4-5: Average Flexural Toughness Values for Strength Development Prisms

		Flexural Toughness		Eq. Flexural Strength Ratio	
Casting	Size	T_{avg} (J)	COV	$R_{T,150}$ (%)	COV
A	100	23,574	0.12	84.0	0.02
A	150	50,398	0.05	79.0	0.04
A	200	114,459	0.37	80.7	0.10
B	100	22,862	0.11	88.8	0.03
B	150	70,730	0.09	85.9	0.02
B	200	139,965	0.07	85.9	0.01

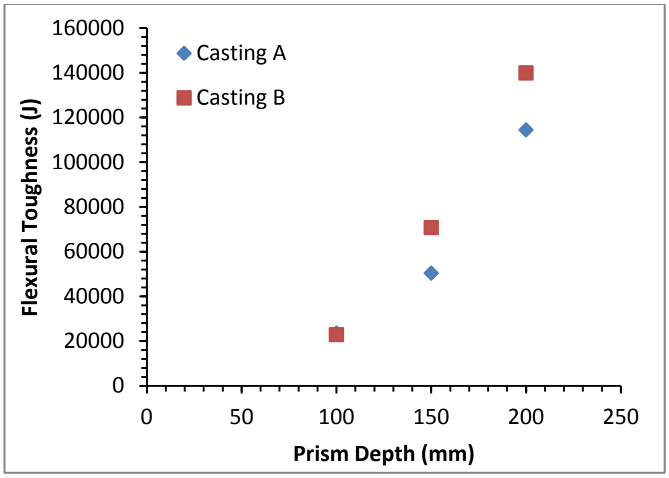

a)

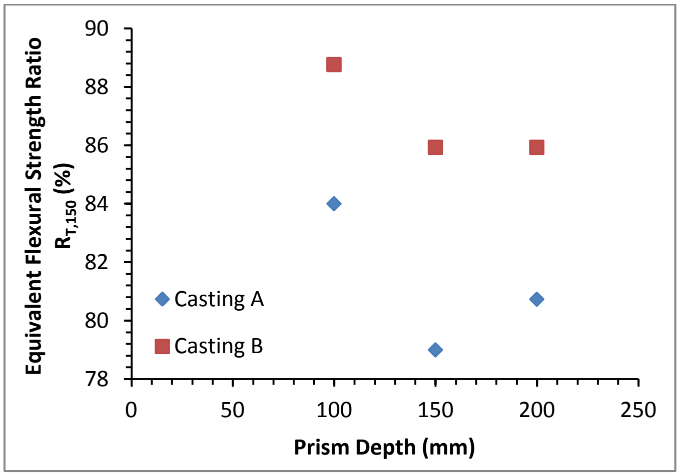

b)

Figure 4-9: Relationship between a) Average Flexural Toughness and Member Depth and b) Average Equivalent Flexural Strength Ratio and Member Depth for Strength Development Prisms

4.2.2 Large Scale Structural Companion Results

The variation of measured deflection throughout the prism height was found to be minimal, as observed previously in Section 4.2.1 for the strength development prisms. The vertical LVDT consistently measured greater deflections than the DIC system, reinforcing the observation in Section 4.2.1 that the LVDT in the current study was not an accurate measure of vertical displacement.

The ratio of change in CMOD to change in mid-span deflection (d_{CMOD}/d_{Δ}) for the companion prisms followed a similar linear trend to the strength development prisms and was once again size independent. Figure 4-10a illustrates the results from both prism sizes in Casting A while Figure 4-10b shows the same trend when both castings are considered. Using linear regression techniques, d_{CMOD}/d_{Δ} ratios of 1.33 (R^2 = 1.00) and 1.31 (R^2 = 1.00) were produced in Castings A and B, respectively. The ratios were within 1.6% of those found with the strength development prisms.

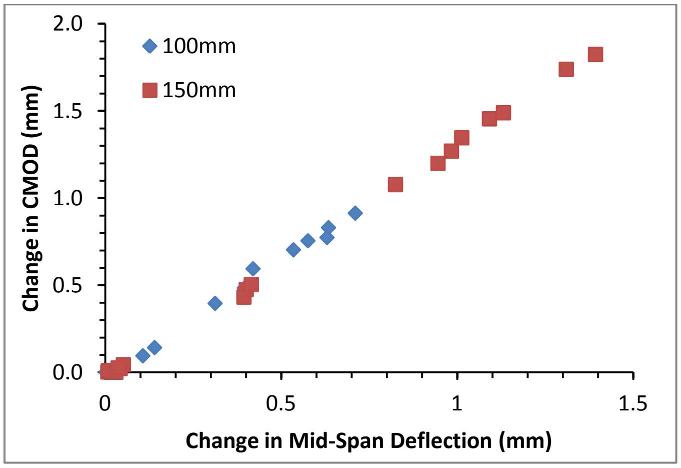

a)

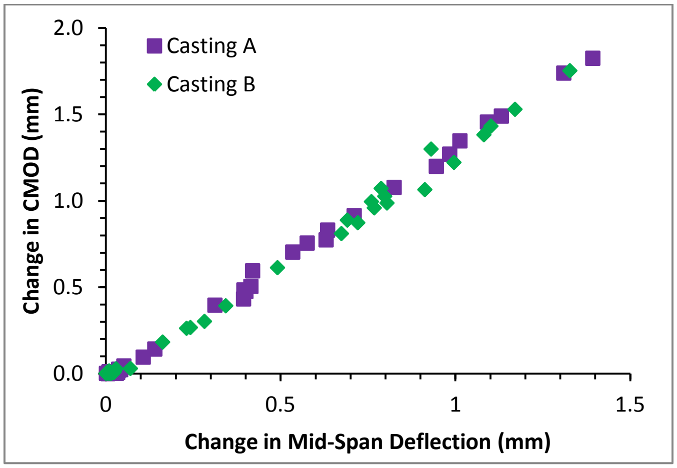

b)

Figure 4-10: Relationship between CMOD and Mid-Span Deflection for Structural Companion Prisms from a) Casting A and b) Castings A and B

The average load-deflection curves for each prism size from Casting A are illustrated in Figure 4-11a. P100AC refers to the average of the 100 x 100 x 300 mm structural companion prisms from Casting A, while P150AC refers to the average of the 150 x 150 x 450 mm structural companion prisms from the same casting. A plot of the individual prism MORs against the overall member depths is shown in Figure 4-11b for the structural companion prisms. Both plots show similar trends to those in Figure 4-7 for the strength development prisms. A maximum applied load of 11.4 kN was observed in the average load-deflection curve from the 100 mm structural companion prisms from Casting A, 12% lower than that of the strength development prisms from the same casting. The average MOR for the 150 mm structural companion prisms from Casting A was 11% lower than the average for the 100 mm prisms (6.08 MPa for the 100 mm prisms and 5.42 MPa for the 150 mm prisms). This suggests that the trend of decreasing MOR with increasing member size reported in Section 4.2.1 continues as the specimens age.

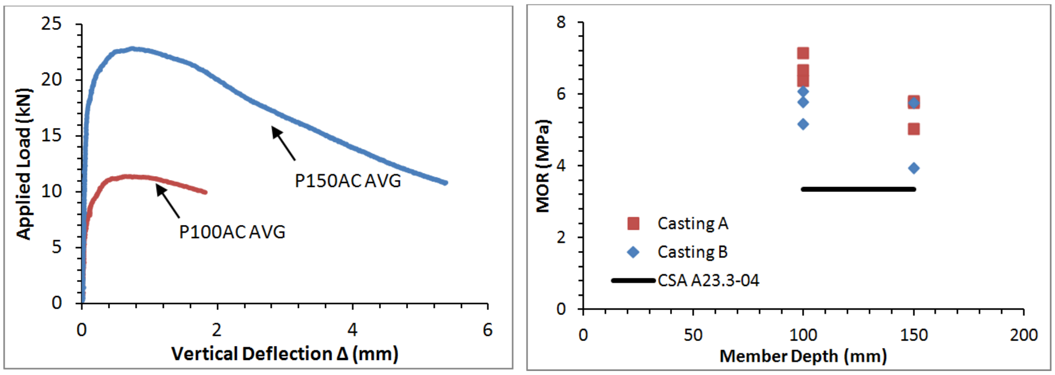

a) b)

Figure 4-11: a) Average Load-Deflection Curves for Casting A Structural Companion Prisms and b) Relationship between MOR and Member Depth for Structural Companion Prisms

Similar to Figure 4-8 for the strength development prisms, Figure 4-12 plots the peak tensile strength (MOR) against the corresponding CMOD for each specimen size from Castings A and B. Once again, a general trend of an increase in the CMOD at peak load with an increase in member size is observed in the specimens from Casting A. No trend is obvious in the specimens from Casting B.

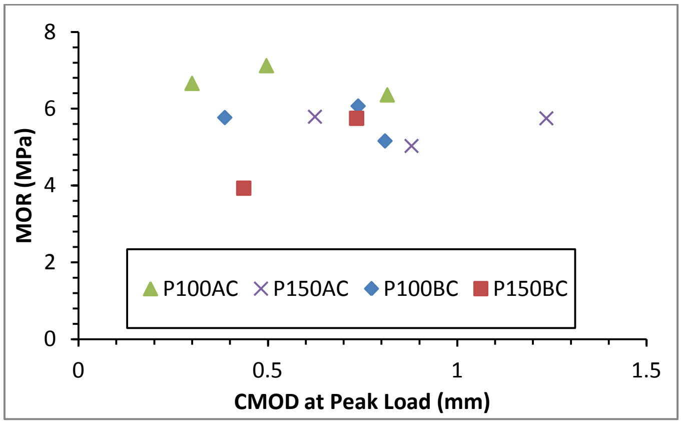

Figure 4-12: Relationship between MOR and CMOD at Peak Load for Structural Companion Prisms

The flexural toughness as defined by ASTM C1609-10 was calculated using the area under the load-deflection curve up to a deflection limit of L/150. Table 4-6 summarizes the average flexural toughness values for each prism size from both Castings A and B, along with the average equivalent flexural strengths ratios as calculated according to Equation 4-3.

Figure 4-13a illustrates the flexural toughness compared to the respective member depths. The results reinforce the size effect demonstrated with the strength development prisms in Figure 4-9. The prisms from Casting A indicate an average higher flexural toughness than those from Casting B.

Figure 4-13b demonstrates the variation in equivalent flexural strength ratio with member depth. A decrease in the $R_{T,150}$ ratio is observed with an increase in member size.

Table 4-6: Average Flexural Toughness Values for Structural Companion Prisms

Casting	Size	Flexural Toughness		Eq. Flexural Strength Ratio	
		T_{avg} (J)	COV	$R_{T,150}$ (%)	COV
A	100	21,900	0.03	89.3	0.03
A	150	62,006	0.06	86.7	0.02
B	100	19,622	0.10	90.6	0.03
B	150	53,258^{A}	0.26	84.0^{A}	0.02

^{A}Average of two prisms

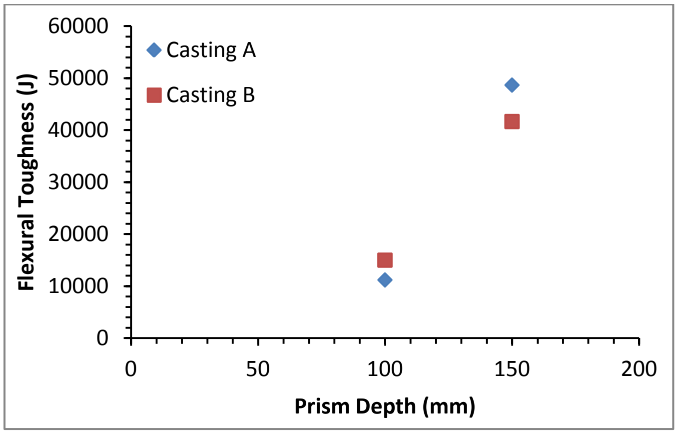

a)

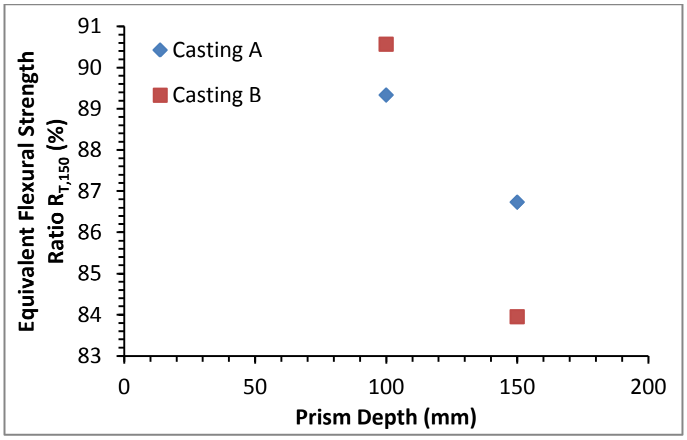

b)

Figure 4-13: Relationship between a) Average Flexural Toughness Values and Member Depth and b) Average Equivalent Flexural Strength Ratio and Member Depth for Structural Companion Prisms

4.2.3 Equivalent Uniform Tensile Stress Across Cracks

Crack widths can provide an indication of the behaviour and performance of a reinforced concrete member. In SFRC, the fibers that bridge these cracks provide a tensile resistance to restrain the rate of crack opening, thereby increasing the load carrying capacity of a member. Recent research (e.g. Shoaib, 2012; Dinh, 2009) examined methods to estimate the force transferred by the fibers across diagonal shear cracks through an equivalent tensile stress parameter. Although the tensile stress distribution along the crack length is non-linear, use of an equivalent uniform stress allows a simplified analytical approach. The equivalent uniform stress can be determined from the ASTM C1609-10 material bending tests described in Section 3.4.2 and related to the shear failure cracks of the large scale structural specimens described in Chapter 6. This relationship can then be used within a prediction model to estimate the shear capacity of FRC members (Dinh, 2009).

The hinge model proposed by Armelin and Banthia (1997) for flexural prisms with a crack location at mid-span was modified to include a notch at mid-span. The deformation model shown in Figure 4-14 was produced. Based on the ASTM C1609-10 specimen configuration in four point bending, the overall prism length L is divided into three equal spans of length a. The middle segment is a constant moment region and it is assumed that the axial strains follow a linear distribution over the height of the cross-section.

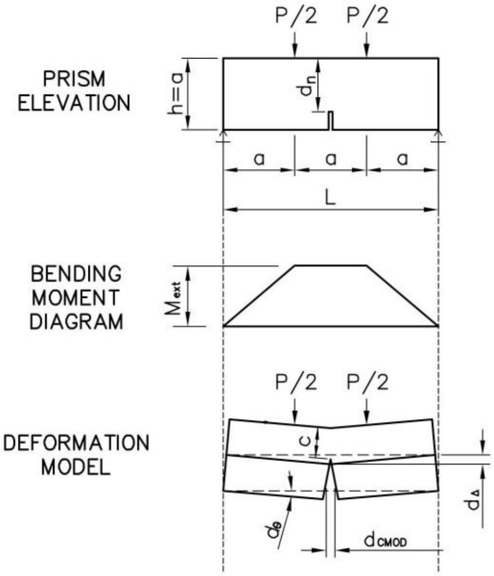

Figure 4-14: ASTM C1609-10 Flexural Prism Layout and Deformation Model (Adapted from Armelin and Banthia, 1997)

The cross section of a flexural prism through the notch location at mid-span is illustrated in Figure 4-15a. The distance between the extreme compression fiber and the neutral axis is defined by c. The region above the neutral axis represents the concrete compression stress zone, which can be represented by the CSA A23.3-04 equivalent rectangular stress block shown in Figure 4-15b. The region below the neutral axis represents the tension stress zone, with an equivalent uniform stress of σ_{ru}. The cross-sectional area along with the corresponding compression and tension stress blocks can be used to obtain the equivalent forces C_r and T_{ru} from the average compression and tension stresses, respectively.

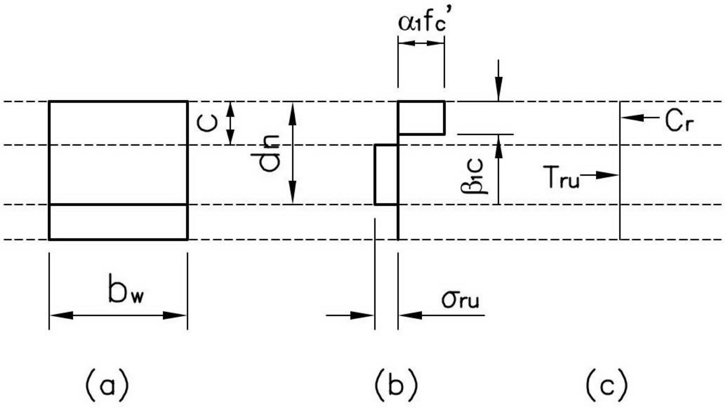

Figure 4-15: Flexural Prism a) Cross Section at Notch Location, b) Stress Diagram, and c) Force Diagram

The compression and tension forces, as defined by CSA A23.3-04 and the methods described above, are detailed in Equations 4-4 and 4-5.

$$C_r = \alpha_1 f_c' \beta_1 c b_w \qquad 4\text{-}4$$

$$T_{ru} = \sigma_{fu}(d_n - c)b_w \qquad 4\text{-}5$$

To satisfy force equilibrium, the sum of the compressive force (C_r) and the tensile force (T_{ru}) must be zero. The depth to the neutral axis can be established at each stage of the test by equating the moment from the applied loading (M_{ext}) to the internal moment (M_{int}) calculated from the compressive and tensile forces, and the internal lever arm which is a function of dimension c. The equations for M_{ext} and M_{int}, applicable to the configuration used in the current study, are detailed in Equations 4-6 and 4-7. Once the depth to the neutral axis is known, the equivalent uniform tensile stress σ_{ru} can be solved (Equation 4-8).

$$M_{ext} = \frac{P}{2}a \qquad 4\text{-}6$$

$$M_{int} = \alpha_1 f_c' \beta_1 c b_w \left(\frac{d_n + c(1 - \beta_1)}{2}\right) \qquad 4\text{-}7$$

$$\sigma_{ru} = \frac{\alpha_1 f_c' \beta_1 c}{d_n - c} \qquad 4\text{-}8$$

Shoaib (2012) used the ratio between the change in CMOD to change in mid-span deflection (d_{CMOD}/d_{Δ}) as 1.33 from Armelin and Banthia (1997) to determine the corresponding crack width for each measured displacement value throughout the test. The crack width was then compared with the equivalent uniform tensile stress from Equation 4-8 for each mix composition examined. In the current study, the d_{CMOD}/d_{Δ} ratio was found to be within 3% of the Armelin and Banthia value (refer to Sections 4.2.1 and 4.2.2). Since the crack widths were directly measured through the use of the DIC system, these values were used for comparing the results from the current study.

The equivalent uniform tensile stresses were determined based on the prisms tested as part of the strength development phase (Section 4.2.3.1), and also on the structural companion prisms (Section 4.2.3.2). Individual values are provided in Appendix A.

4.2.3.1 **Equivalent Uniform Tensile Strength from Strength Development Prisms**

The method described in Section 4.2.3 was used to determine the equivalent uniform tensile stress for the strength development prisms based on the CMOD data extracted through the DIC system.

For each casting, the average equivalent uniform tensile stress curve was determined for all three specimen sizes based on the corresponding CMODs. The average curves for each specimen size from Casting A are compared in Figure 4-16a and those from Casting B are compared in Figure 4-16b. A size effect in tension is observed – as the specimen size increased, the peak equivalent uniform tensile stress decreased. The peak values obtained as the average of the 150 and 200 mm prism curves from Casting A were 32 and 43% lower than the average value from the 100 mm prism curve respectively. From Casting B, the peak values obtained as the average of the 150 and 200 mm prism curves were 20 and 27% lower than the average value from the 100 mm prism curve respectively.

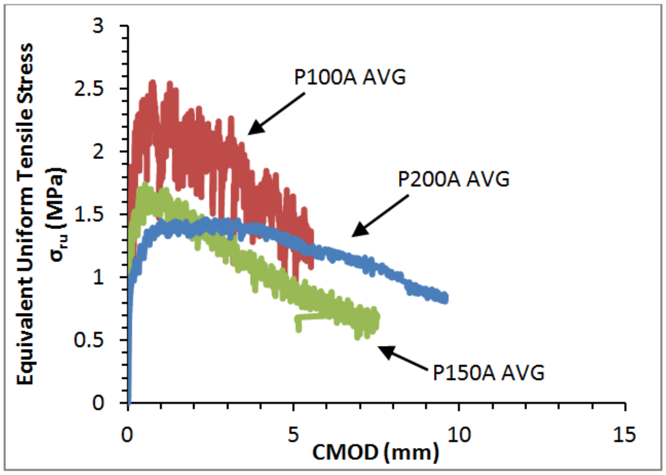

a)

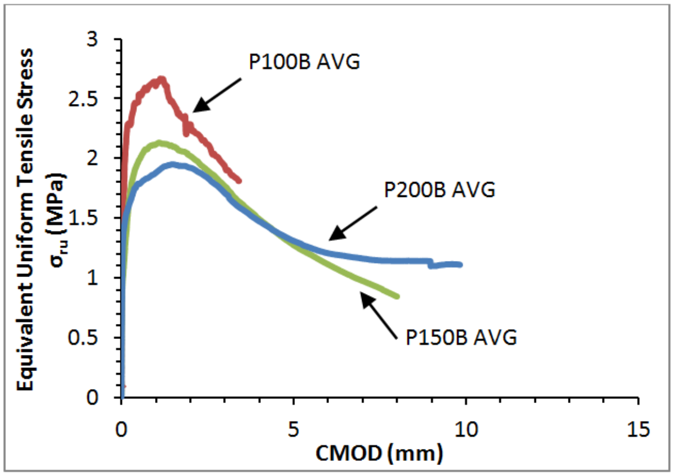

b)

Figure 4-16: Average Equivalent Uniform Tensile Stress-CMOD Curves for Strength Development Prisms from a) Casting A and b) Casting B

Figure 4-17 compares the peak uniform tensile stress with the three specimen sizes. The specimens from Casting B showed a decrease in peak uniform tensile stress with an increase in specimen size. While the 100 mm specimens were relatively close in their peak equivalent uniform tensile stress values, the 150 mm and 200 mm prisms from Casting A showed lower values than those from Casting B. It is possible that the 150 and 200 mm prisms from Casting A received inadequate consolidation during casting, or perhaps an uneven fiber distribution. An analysis of the prisms' cross sections would perhaps provide a better understanding, but was not completed as part of this study.

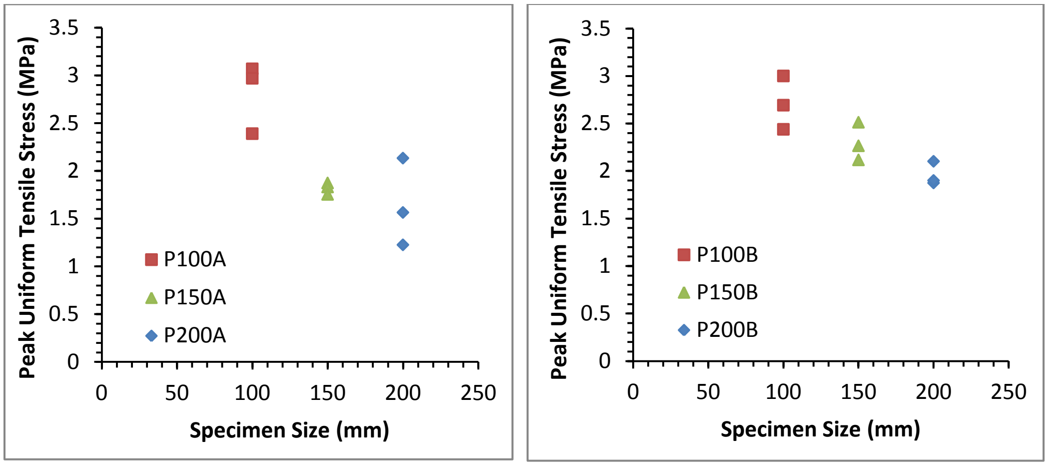

a) b)

Figure 4-17: Peak Uniform Tensile Stresses for Strength Development Prisms from a) Casting A and a) Casting B

Shoaib (2012) normalized the equivalent uniform tensile stresses by the square root of the concrete compressive strength and the fiber volume fraction V_f (Equation 4-9). The fiber volume fraction is used in decimal format rather than as a percentage. Shoaib showed that normalization by this equation provided similar σ_{ru} – CMOD relationships for all compressive strengths and fiber volume fractions in his study. Based on his 100 x 100 x 300 mm notched prisms with an average f_c' = 44 MPa and containing 1.0% volume fraction of fibers (which were tested sometime after 78 days), an average normalized stress of approximately 2.91 MPa was found at a CMOD of approximately 0.6 mm.

$$\sigma_{ruN} = \frac{\sigma_{ru}}{\sqrt{(\frac{V_f}{100})f_c'}} \qquad \text{4-9}$$

Dinh (2009) performed a similar analysis to determine the equivalent uniform tensile stress from un-notched 150 x 150 x 450 mm SFRC companion prisms to his large scale beams. The fibers used by Dinh were of identical length, aspect ratio, end condition and yield strength to those used in the current study. With 0.75% volume fraction of fibers, Dinh tested companion prisms to his B18-1a and b beams with f_c' = 45 MPa, and his B27-1a and b beams with f_c' = 51 MPa. The B18-1a and b prisms had average peak uniform tensile stresses of approximately 360 psi (2.5 MPa) at a CMOD of approximately 0.1 mm. The B27-1a and b prisms experienced an average peak uniform tensile stress of approximately 400 psi (2.8 MPa) at a CMOD of approximately 0.1 mm. The normalized values of these stresses can be found in Table 4-7.

For comparison, the average peak equivalent uniform tensile stresses from the current study were normalized based on the average compressive strength from the 150 mm diameter strength development cylinders from the respective casting. Refer to Table 4-7. The average of the 100 mm prisms from both castings in the current study showed a normalized stress approximately 70% larger than that found by Shoaib and an average CMOD approximately 50% larger. The normalized stresses from the 150 mm prisms in the current study were comparable to those found by Dinh, but the CMODs were much larger. The discrepancy between CMOD sizes could be partially attributed to the notch in the current study. The normalized stresses for the three prism sizes in the current study are compared with those from Shoaib and Dinh in Figure 4-18a. The prisms from Dinh appear to follow the same size effect trend as the ones from the current study although the average from Shoaib does not.

Table 4-7: Comparison of Average Peak Equivalent Uniform Tensile Stresses and CMOD from Strength Development Prisms with Various Researchers

Source	Prism Height h (mm)	f_c’ (MPa)	V_f (%)	Average Peak σ_{ru} (MPa)	$\frac{\sigma_{ru}}{\sqrt{V_f f_c'}}$	Average Peak CMOD (mm)
Shoaib (2012)	100	44.0	1.0	1.9	2.91	0.6
Dinh (2009)^C	150	45.0	0.75	2.5	4.30	0.1
Dinh (2009)^C	150	51.0	0.75	2.8	4.53	0.1
Current Study	100^A	32.3	1.0	2.8	4.94	0.8
Current Study	100^B	31.1	1.0	2.7	4.86	1.0
Current Study	150^A	32.3	1.0	1.8	3.20	0.8
Current Study	150^B	31.1	1.0	2.3	4.12	0.9
Current Study	200^A	32.3	1.0	1.6	2.89	1.1
Current Study	200^B	31.1	1.0	2.0	3.51	1.5

^{A}Strength Development Prisms from Casting A ^{B}Strength Development Prisms from Casting B ^{C}Un-notched prisms

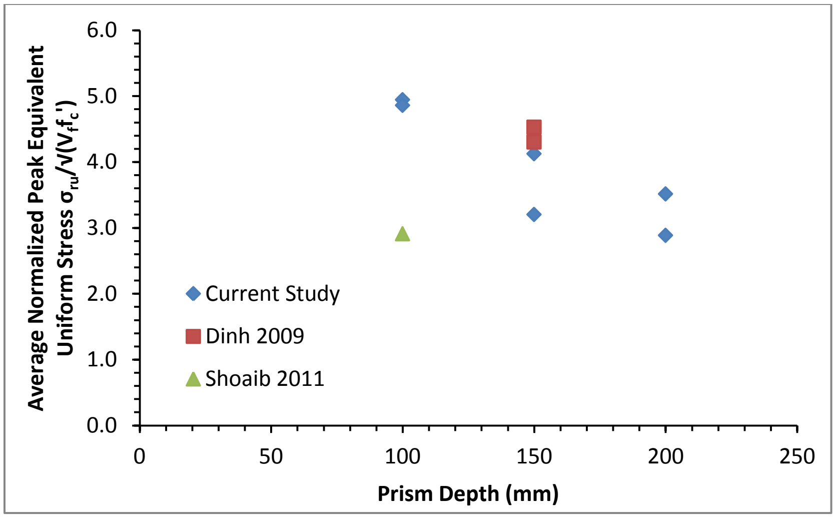

Figure 4-18: Comparison of Average Normalized Peak Equivalent Uniform Tensile Stresses from Various Researchers

4.2.3.2 Equivalent Uniform Tensile Strength from Structural Companion Prisms

A similar analysis to that described in Section 4.2.3.1 was completed for the structural companion prisms. Figure 4-19 shows the average σ_{ru}-CMOD curves for the prisms from both Castings A and B. Similar to the strength development results, a size effect is apparent with the peak equivalent uniform tensile stress. The average peak values for the 150 mm prisms were 17 and 19% lower than the average peak values for the 100 mm prisms from Casting A and B respectively.

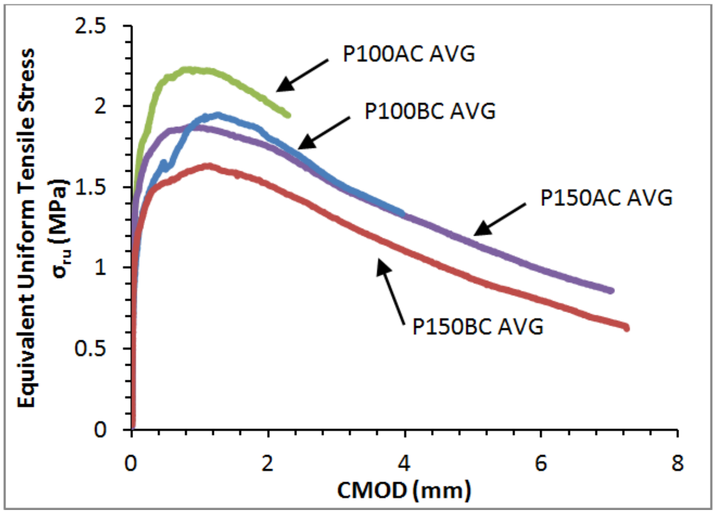

Figure 4-19: Average Uniform Tensile Stress-CMOD Relationships from Casting A and B Structural Companion Prisms

Plotting the peak tensile stresses against the respective prism sizes in Figure 4-20 shows a trend similar to that shown in Figure 4-17; as the specimen size increased, the peak tensile stress generally decreased.

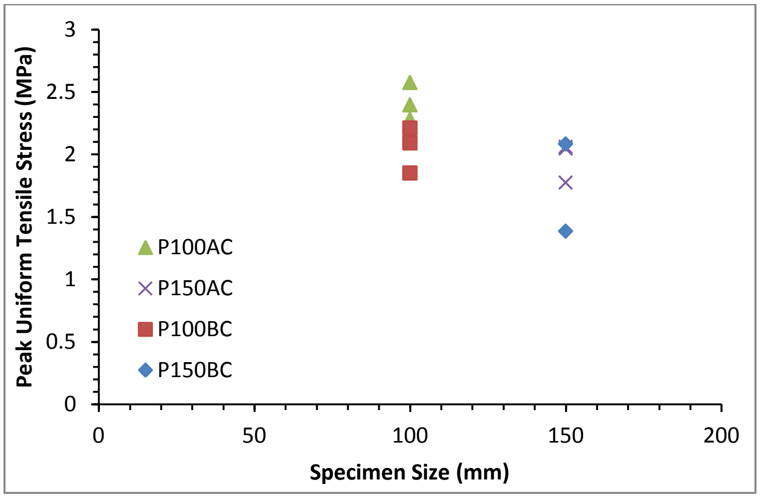

Figure 4-20: Peak Uniform Tensile Stresses for Structural Companion Prisms

A summary of the average equivalent uniform tensile stresses from the structural companion prisms is available in Table 4-8. The 100 mm structural companion prisms exhibited an average normalized equivalent uniform tensile stress approximately 21% lower than that found in the strength development prisms and an average CMOD approximately 33% smaller. The 150 mm structural companion prisms exhibited an average normalized equivalent uniform tensile stress approximately 14% lower than that found in the strength development prisms and an average CMOD approximately 12% smaller. The discrepancies could be due in part to the difference in curing methods between the strength development and structural companion prisms; the former were moist cured until testing while the latter were only moist cured for the first 7 days and were tested at an older age.

Table 4-8: Summary of Average Peak Equivalent Uniform Tensile Stresses and CMODs from Structural Companion Prisms

Code	Prism Height h (mm)	f_c' (MPa)	V_f (%)	Average Peak σ_{ru} (MPa)	$\frac{\sigma_{ru}}{\sqrt{V_f f_c'}}$	Average Peak CMOD (mm)
P100AC	100^A	37.9	1.0	2.4	3.90	0.5
P100BC	100^B	29.9	1.0	2.1	3.84	0.7
P150AC	150^A	37.9	1.0	2.0	3.25	0.9
P150BC	150^B	29.9	1.0	1.7	3.11	0.6

^{A}Companion Prisms from Casting A ^{B}Companion Prisms from Casting B

4.2.4 ACI 318-08 Fiber Reinforced Concrete Performance Requirements

ACI 318-08 provisions permit the use of steel fiber reinforced concrete (SFRC) as a method for shear resistance in structural members for an alternative to minimum transverse reinforcement, provided several configuration and performance criteria are met. Members must be constructed with a concrete compressive strength not exceeding 40 MPa and with an overall member height not greater than 600 mm (ACI 318-08 Clause 11.4.6.1). In addition, the factored shear force cannot exceed Equation 2-2 (ACI 318-08 Clause 11.4.6.1). According to Clause 5.6.6.2, a minimum of 60 kg/m^3 (approximately V_f = 0.76%) of deformed steel fibers must be included in the concrete mix. The current study used 1.0% volume fraction of steel fibers in the concrete mix, which is equivalent to 78 kg/m^3.

A performance requirement in ACI 318-08 Clause 5.6.6.2 also indicates that the residual strength (f_{test}) at a mid-span deflection of L/300 (where L represents the span length) from SFRC prisms tested according to ASTM C1609 must be greater than or equal to 90% of the first peak strength. For all the prisms tested in the current study, the first peak strength equalled the modulus of rupture (MOR). Out of all 29 prisms tested, 62% passed this requirement but only by a maximum of 10% greater residual strength. An additional requirement is for a residual strength at a mid-span deflection of L/150 greater than or equal to 75% of the first peak strength. Only 45% of the prisms passed this requirement, and 31% out of those did not pass the L/300 residual strength requirement. Individual values for the residual strengths are provided in Appendix A.

Based on these guidelines, the SFRC mix used in the current study would not be considered adequate to meet the ACI 318-08 Clause 5.6.6.2 requirements for steel fibers used in place of minimum transverse reinforcement.

4.3 Summary

4.3.1 Compression Response Summary

Compression tests completed on two strength development cylinder sizes from Castings A and B demonstrated a size effect in the compression response – as the specimen size increased, the compressive strength decreased. The stiffness of the members also decreased with an increase in cylinder size; the 100 mm cylinders generally showed a greater modulus of elasticity than the 150 mm cylinders.

Companion cylinders were tested in order to provide accurate stress-strain curves for each of the large scale structural specimens described in Chapter 5. These cylinders produced higher strains at peak load than the strength development samples. The companion cylinders from Casting A produced higher peak stresses than the strength development samples of the same size, while the companions from Casting B produced lower peak stresses than their respective strength development samples.

4.3.2 Flexural Response Summary

Combining both sets of prism data, i.e. both the strength development prisms and the companions to the large scale structural specimens, provided a well-founded indication of the SFRC behaviour under different curing conditions and as it ages.

While the LVDT data proved to be inaccurate, the DIC system provided information to analyze vertical deflections and crack widths. The CMOD was confirmed to increase at a faster rate than the vertical deflection. Comparing the change in CMOD to change in vertical deflection (d_{CMOD}/d_{Δ}) demonstrated an average ratio of approximately 1.31 when all testing ages were considered for the notched specimens from Castings A and B. This ratio is within 1.5% of the 1.33 value published by Armelin and Banthia (1997) for un-notched specimens. The results confirmed that the relationship is size and strength independent.

The member strength was shown to decrease with an increase in member size, indicating a size effect in flexure. The MOR was found to be lower in the structural companion prisms than the strength development prisms, with the exception of two 150 mm prisms from Casting A. While the concrete is expected to gain a moderate amount of strength as it ages, the difference in curing methods between the two sets likely induced additional shrinkage stresses in the structural companion prisms. The CSA A23.3-04 model for MOR based on plain concrete without fibers was found to underestimate the SFRC strength, although the discrepancy decreased as the member size increased.

The CMOD at peak load was found to generally increase with an increase in member size. This trend had exceptions in both the strength development and structural companion prisms, indicating that an additional factor is affecting the CMOD – a physical analysis of the fiber content and orientation at the crack mouth location may have provided further clues but was not investigated in the current study.

The average flexural toughness values were calculated from all prism sizes in both the strength development and structural companion prisms. A size effect was apparent – as the specimen size increased, the flexural toughness increased with it. The equivalent flexural strength ratio was also calculated for all prisms but no overall trend was observed in relation to the specimen size.

The equivalent uniform tensile stress acting across the cracks during testing was determined for each specimen. A size effect was established – increasing the specimen size decreased the peak uniform tensile stress. The average equivalent uniform tensile stress was normalized by the square root of the compressive strength and the fiber volume fraction to allow for comparison with recently published research. The comparisons showed some similarities but also significant differences.

The flexure results were also compared with the ACI 318-08 guidelines to consider SFRC as an accepted method of shear resistance. While the amount of steel fibers included in the mix was adequate, the residual strength requirements based on the ASTM C1609-10 tests were not satisfied.

5 Large Scale Structural Specimens – Experimental Program

5.1 Introduction

Large scale tests of shear critical specimens were conducted to establish the influences of the mechanical properties of the steel fiber reinforced concrete (SFRC) and the passive deformed ASTM A1035 reinforcement on the response of structural members. Four specimens with overall nominal heights of 1000 mm were cast along with two specimens with overall nominal heights of 300 mm. Previous research by Minelli and Plizzari (2010) and Shoaib et al. (2010) has shown a size effect in shear for steel fiber reinforced concrete structural members, but few tests have been completed on members over 600 mm in height. The two overall heights in the current study were chosen to provide data on the size effect in shear over a size factor of approximately 3.3. The longitudinal reinforcement ratios in the specimens varied between 0.40 and 2.61% while all other test parameters remained relatively constant. All specimens were tested under three point bending until failure. Instrumentation measured the vertical and horizontal deflections, the longitudinal reinforcement strains, the concrete surface strains and the crack patterns and widths. The behaviour, both pre and post peak, was analyzed and compared within both size ranges.

Section 5.2 provides a rationalization of the design configurations selected for each specimen. Details of the fabrication process are described in Section 5.3, followed by the material characteristics and the test setup in Sections 5.4 and 5.5 respectively. The instrumentation scheme is provided in Section 5.6, including use of the digital image correlation (DIC) system and a photogrammetry based measurement system. The test procedure is described in Section 5.7.

5.2 Specimen Configurations

The large scale structural specimens were designed with a constant shear span to effective depth ratio (a/d) of 3.0 in order to encourage sectional behaviour in shear rather than forming direct compression struts between the loading point and the support reactions (ACI 445R-99). A constant width of 300 mm was used for all members as Sherwood, Lubell, Bentz & Collins (2006) and Kani (1967) showed that the shear stress at failure for plain reinforced concrete members is not influenced by the specimen width. Two overall heights were designed; h = 300 and 1000 mm. The specimens contained ASTM A1035 Grade 690 steel longitudinal reinforcement but no transverse reinforcement and were designed to fail in shear. The flexural capacities were determined based on the ACI ITG-6R-10 Appendix B recommendations for members with ASTM A1035 Grade 690 longitudinal reinforcement where the full non-linear stress-strain relationship of the steel is considered (refer to Section 2.4.2.4 for details). The fibers are not considered in the Appendix B flexural model. The Desalegne and Lubell (2010) General shear model (Section 2.4.1.5) was used to estimate the shear capacity of the large scale structural specimens based on equivalent plain concrete members reinforced with high performance steel reinforcement. Based on previous work completed by Shoaib (2012) on SFRC members of a similar scale, the preliminary shear estimate of the SFRC specimens was taken as four times larger than the equivalent member without fibers.

A clear cover of 40 mm between the reinforcing steel and concrete face was used on both the sides and soffit. A 40 mm clear spacing between reinforcement layers and a minimum of 40 mm between adjacent longitudinal reinforcement bars were also used. These covers ensured the typical CSA A23.3-04 design standards for plain concrete with interior exposure were met, and also ensured that all spaces were larger than the fiber length of 30 mm to minimize uneven fiber distribution. A target concrete compressive strength of 35 MPa with maximum aggregate size of 14 mm was assumed for design purposes.

In the h = 1000 mm specimens, the longitudinal reinforcement ratios were selected to produce mid-span reinforcement stresses between approximately 600 and 900 MPa at the peak load condition, in order to observe the influence on shear capacity from reinforcement stresses above the CSA A23.3-04 and ACI 318-08 maximum allowable reinforcement design stresses. The resulting longitudinal reinforcement ratios were 0.40, 0.61, 0.83, and 1.03%.

The h = 300 mm specimens were also designed to fail in shear. The longitudinal reinforcement ratios were selected to produce mid-span reinforcement stresses similar to those in the h = 1000 mm specimens. Ratios of 1.51 and 2.61% were predicted to produce peak load stresses of approximately 625 MPa and 450 MPa in the longitudinal reinforcement at mid-span, respectively.

The longitudinal reinforcement was fabricated with ACI 318-08 standard 90° hooks at both ends to enhance the anchorage into the concrete. The distance from the centerline of each support to the end of the specimen was 700 mm in the h = 300 mm specimens and a minimum of 450 mm in the h = 1000 mm specimens. Refer to Appendix C for individual layouts.

A summary of the specimen configurations is provided in Table 5-1 and illustrated in Figure 5-1 and Figure 5-2. The first set of numbers in the specimen name refers to the nominal overall member height, while the letter after the dash (‘A’ or ‘B’) refers to which casting the member was constructed in, as explained in Section 5.3. The number at the end of the name refers to the replicate number within that series. For example, S1000-B2 refers to the second member in the h = 1000 mm series, and was produced in Casting B.

Table 5-1: Large Scale Structural Specimen Configuration Details

Specimen	h (mm)	d (mm)	L (mm)	a/d ratio	ρ (%)	f_c' (MPa)	V_f (%)
S300-B1	300	248	1488	3.0	2.61	29.9	1.0
S300-A2	300	252	1512	3.0	1.51	37.9	1.0
S1000-B1	1000	924	5544	3.0	1.03	30.4	1.0
S1000-B2	1000	924	5544	3.0	0.83	31.2	1.0
S1000-A3	1000	933	5598	3.0	0.61	41.2	1.0
S1000-A4	1000	952	5712	3.0	0.40	40.1	1.0

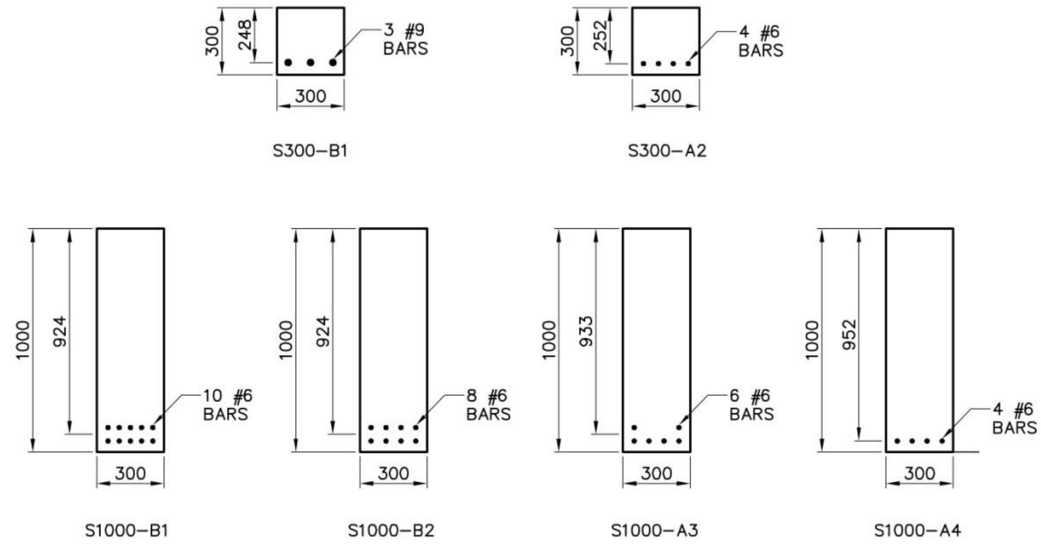

Figure 5-1: Large Scale Structural Specimen Cross-Sections

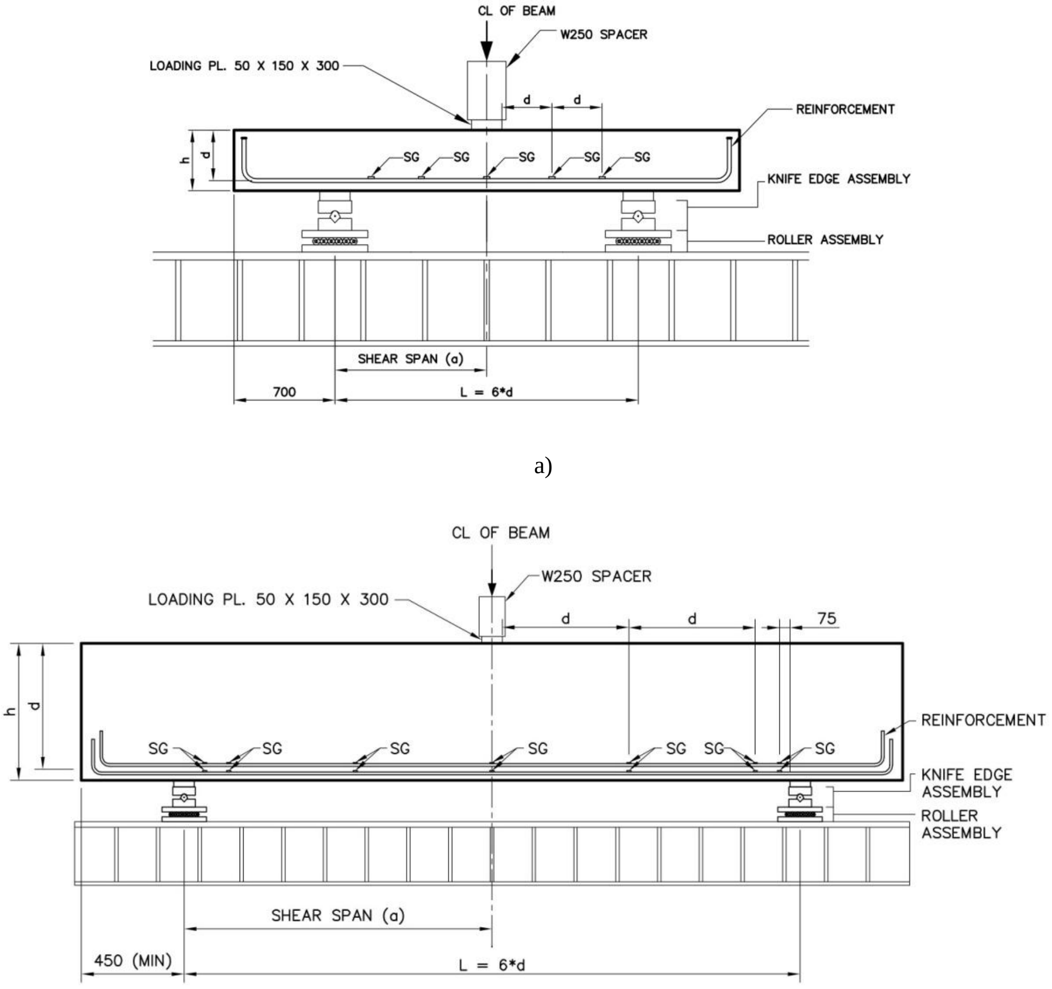

a)

b)

Figure 5-2: Typical Layout for a) h = 300 mm and b) h = 1000 mm Specimens

5.3 Specimen Fabrication

Two SFRC castings were completed (refer to Chapter 3), each one producing one small (h = 300 mm) and two large (h = 1000 mm) specimens. The concrete was supplied by Inland Concrete Ltd., following the SFRC mix design previously developed and described in Section 3.3. Specimens S300-A2, S1000-A3 and S1000-A4 were produced first in Casting A while S300-B1, S1000-B1 and S1000-B2 were produced in Casting B (see Table 5-1).

Plastic chairs were used below and between the reinforcing steel layers to achieve the 40 mm clear cover and spacing requirements. Grade 400 steel 10M framing bars were tied perpendicular to the longitudinal reinforcement in order to maintain appropriate spacing between the bars. The transverse framing bars were approximately 5 mm shorter than the width of the formwork to minimize lateral movement of the reinforcement during casting.

Grade 400 steel 15M lifting hooks were provided perpendicular to the longitudinal steel at each end of the h = 300 mm specimens (Figure 5-3a) and 35M lifting hooks were provided parallel to the longitudinal steel at each end of the h = 1000 mm specimens (Figure 5-3b). The 15M lifting hooks were produced with CSA A23.3-04 standard 90° hooks on each leg and were tied to the longitudinal steel beyond the supports and outside the test region. In the 35M lifting hooks, the outer leg had a CSA A23.3-04 standard 90° hook extending beyond the supports at the end of each specimen. The inner leg was cut at approximately mid-height with a 100 x 100 mm steel plate welded to the end in order to provide anchorage of the lifting hook without interfering with the test region near the supports. In all cases, the lifting hooks were located outside the testing region and did not interfere with the crack distributions.

The h = 300 mm specimens were cast in a steel form composed of channel sections with 19 mm thick plywood end walls (Figure 5-3a). The h = 1000 mm specimens were cast in 1000 mm high wooden forms made from 19 mm thick plywood supported on the outside by wooden 2x4's and a built up steel angle on the lower half. Wooden braces and metal clamps were used across the top of the forms to minimize lateral expansion during casting (Figure 5-3b).

a) b)

Figure 5-3: Formwork and Reinforcement Layout for a) h = 300 mm and b) h = 1000 mm Specimens

The concrete truck chute was used to place the concrete directly in the forms. The concrete was placed in two layers for the h = 300 mm specimens and three layers for the h = 1000 mm specimens (Figure 5-4a). In between each layer, the concrete was consolidated by internal vibration. The top surface was screeded to a smooth finish (Figure 5-4b). Specimens were cured under wet burlap and plastic for 7 days and subsequently removed from the forms between 8 and 37 days after casting.

a) b)

Figure 5-4: a) h = 1000 mm Specimen Cast in Layers and b) After Screeding

5.4 Material Properties

5.4.1 Steel Fiber Reinforced Concrete

The steel fiber reinforced concrete (SFRC) was supplied in two 5.5 m^3 batches. Three specimens were cast simultaneously with cylinders and prisms used for material characterization (refer to Chapter 4). The cylinder results, including peak stress and stress-strain curves as both strength development samples and as large scale structural companions, are reported in Section 4.1. The prism results including deflection, crack growth and flexural strength are reported in Section 4.2 for both strength development and structural companion results.

5.4.2 ASTM A1035 Reinforcing Steel

The ASTM A1035 Grade 690 reinforcing steel was provided by MMFX Technologies in #6 (19 mm) and #9 (29 mm) diameters.

Tension coupon tests based on ASTM A370-11 were performed for three samples from each of the #6 and #9 bar sizes used in the current study. The three samples were randomly chosen from three separate bars of the same batch as the longitudinal reinforcement used in the large scale structural specimens.

Each coupon had an overall length of approximately 600 mm which included a 200 mm gauge length, a minimum distance of two bar diameters on each end between the gauge and the grips, and approximately 125 mm on each end to fill the grips. The requirement for excess length protruding beyond each grip specified in ASTM A370-11 could not be accommodated due to the configuration of the MTS test equipment used. Punch marks were placed every 50 mm along the gauge length. These marks were measured with digital callipers before and after testing, and are detailed in Appendix B.

An extensometer with an initial gauge length of 50 mm was fixed to each coupon at mid-height during testing, but removed after the ultimate load had been reached to avoid possible damage. The extensometer provided continuous readings of the coupon strain throughout the test until removal. Figure 5-5a illustrates a #9 coupon test with the attached extensometer.

In accordance with Section 7.4.3 of ASTM A370-11, the #6 bars were tested at a machine travel rate of 1.0 mm/min to an applied load of approximately 300 kN (past the proportional limit) when the rate was increased to 2.0 mm/min. Similarly, the #9 bars were tested at a machine travel rate of 0.5 mm/min to an applied load of approximately 550 kN (past the proportional limit) when the rate was increased to 4.0 mm/min. The #6 coupons were tested until rupture, while the #9 coupon tests were stopped after visible necking but before rupture had occurred. Data was recorded at 2 Hz. Necking in all cases occurred within the 200 mm test region (Figure 5-5b).

a) b)

Figure 5-5: ASTM A1035 Reinforcement #6 Coupon Test a) With Extensometer and b) After Rupture

Figure 5-6 illustrates the average stress-strain curves obtained for each coupon size. The stress values are based on the nominal cross-sectional area of the bar, and the extensometer data was used to determine the strain values based on the initial gauge length. The ACI ITG-6R-10 lower bound stress-strain curve for ASTM A1035 Grade 690 reinforcing steel (Equation 2-1) has been included on both graphs for comparison.

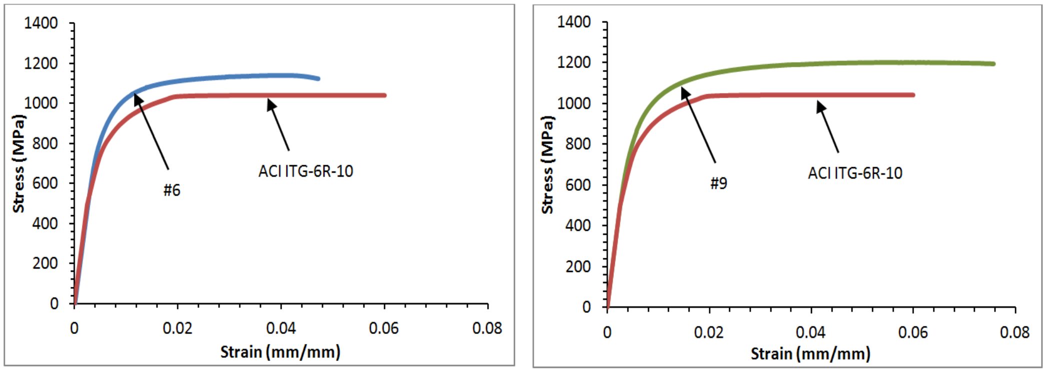

a) b)

Figure 5-6: Average Stress-Strain Curves for a) #6 and b) #9 ASTM A1035 Reinforcing Steel Coupons

The modulus of elasticity (E_s) of the reinforcement was measured using the initial linear portion of the stress-strain response, defined for this purpose as the region between the origin and a point at approximately 40% of the peak stress. The measured modulus of elasticity was found to be within 2.5% the 200,000 MPa design value specified by CSA A23.3-04.

Since this material exhibits no well defined yield point, the 0.2% offset method was used to determine an effective yield stress (σ_y). The stress of each sample at a strain of 0.0035 mm/mm ($\sigma_{0.0035}$) was also extracted for verification with the ASTM A1035-11 requirements noted in Section 2.2.2. The ASTM A1035-11 requirements for a minimum yield strength of 690 MPa and a minimum stress of 550 MPa at a strain value of 0.0035 mm/mm were both satisfied. Table 5-2 summarizes the average results for each bar size.

The measured effective yield strengths were at least 33% higher than the newly recommended 690 MPa design limit stated by the ACI ITG-6R-10 and 83% higher than the CSA A23.3-04 design code limit of 500 MPa.

Table 5-2: Properties of ASTM A1035 Reinforcing Steel Coupons

Bar Size	Area* (mm^2)	E_s (MPa)	$\sigma_{0.0035}$ (MPa)	σ_y (MPa)	ε_y (mm/mm)	σ_{peak} (MPa)	ε_{peak} (mm/mm)
#6	284	195,196	660	946	0.0068	1141	0.0423
#9	645	197,185	650	915	0.0066	1200	0.0554

*Cross-sectional areas taken from ASTM A1035-11

Considering that the moduli of elasticity found through these tests are very close to the 200,000 MPa design value from CSA A23.3-04 and that practical design cases will be based on the design value, all calculations presented are based on E_s = 200,000 MPa unless otherwise noted.

5.5 Test Setup

A MTS 6000 test frame with a compressive capacity of 6200 kN was used for the large scale structural specimens. Supports consisted of a combination of rollers and knife edges to allow horizontal translation and rotation (as illustrated in Figure 5-7) sitting on a steel distributing beam. The bearing plates directly beneath the specimen measured 300 mm wide to match the width of the specimens and 150 mm along the length of the specimens. To ensure uniform contact, a thin layer of plaster was used between the bearing plates and the concrete soffit of the member.

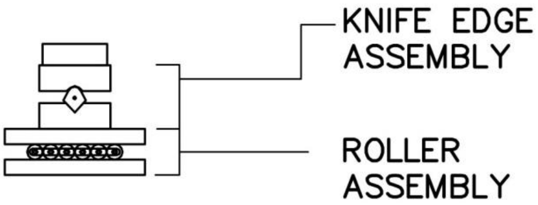

Figure 5-7: Large Scale Structural Specimen Support Details

The loading plate measured 300 mm by 150 mm and was oriented in the same direction as the bearing plates. A thin layer of plaster was also used between the loading plate and concrete face to ensure full contact and a level loading surface. A W250 steel stub column was used between the loading plate and the MTS loading head to provide adequate working space around the specimens. Figure 5-8 shows the MTS frame around S1000-A4 and the overall setup on S300-B1.

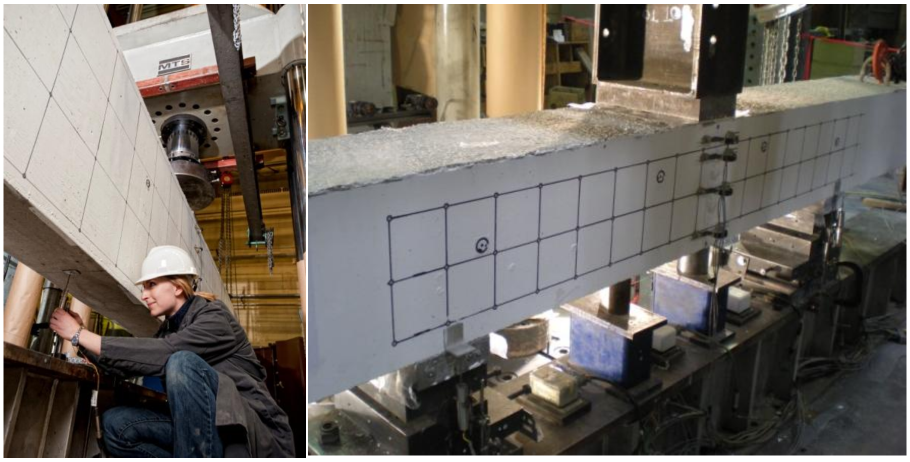

a) b)

Figure 5-8: a) MTS Frame Around S1000-A4 and b) Specimen S300-B1 Setup

5.6 Instrumentation

5.6.1 Physical Instruments

Electrical resistance strain gauges were affixed at selected locations along the length of select steel reinforcement bars prior to casting. A combination of gauges from Kyowa Electronic Instruments Co. Ltd. (Type KFG-5-120-C1-11) and Showa Measuring Instruments Co. Ltd. (Type N11-F4-5-120-11) were used. Each strain gauge had a length of 5 mm and electrical resistance of 120 Ohms. Prior to the strain gauge installation, the steel reinforcing bar was ground to a smooth surface, sanded and degreased. Every effort was made to minimize the amount of material removed during grinding so as to lessen the influence on the reinforcing bar properties. The surface was then conditioned and neutralized before the gauge was applied with a catalyst and M-Bond 200 adhesive. Gauges were typically located at mid-span and at distances of d and 2*d to each side of the centerline, as measured from the face of the loading plate (refer to Figure 5-2). The two h = 1000 mm specimens with the smallest reinforcement ratios (S1000-A3 and S1000-A4) also had strain gauges placed at 75 mm in from the face of each bearing plate (Figure 5-2). Complete details are available in Appendix C for each individual large scale structural specimen.

A vertical LVDT with ±12.5 mm of range was placed at each support to measure the support settlement during testing. A similar LVDT was placed horizontally on the east support in order to measure the horizontal displacement of the east span. During the first test (S1000-A4), LVDTs were also placed under the centerline of the specimen at mid-span and at both quarter span points. Due to the sudden and dramatic failure of the specimen, these three LVDTs were replaced with cable potentiometers for subsequent tests. All vertical displacement data stated in this report has been corrected for the average measured support settlement unless otherwise noted.

A cable potentiometer was placed between the two supports to measure the relative horizontal movement between the supports. The combination of this sensor and the horizontal LVDT on the east support allowed for analysis of the horizontal displacement in each shear span individually.

Four PI gauges were placed on the south face of each specimen to measure the concrete surface strains during testing. In the h = 300 mm specimens, the top PI gauge was placed 35 mm down from the top of the specimen. Three other PI gauges were placed at approximately 0.25*h, 0.5*h and effective depth d from the top. In the h = 1000 mm specimens, the top gauge was placed approximately 75 mm down from the top while the remaining three gauges were maintained at the same locations (0.25*h, 0.5*h and d) as the smaller specimens. The PI gauges had an initial length of 100 mm and were screwed into brass brackets epoxied onto the concrete surface.

A summary of the typical specimen layouts, showing all exterior instrumentation, is provided in Figure 5-9. The layout is shown for both the h = 300 and 1000 mm specimens.

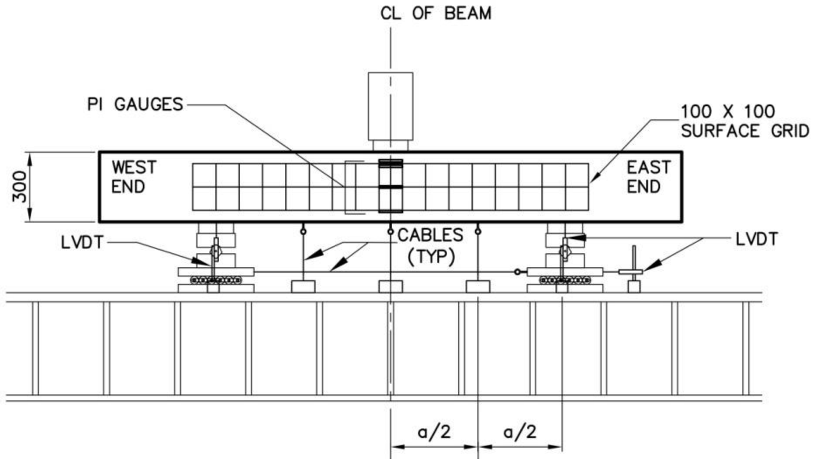

a)

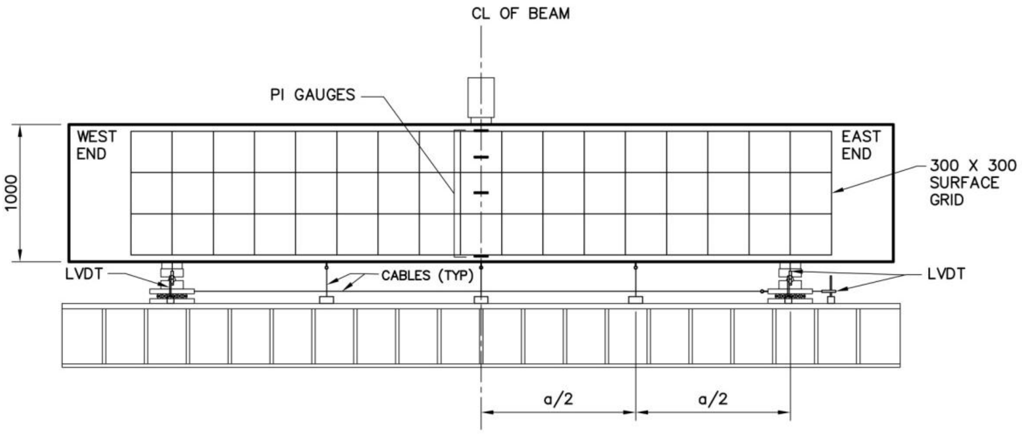

b)

Figure 5-9: Typical Instrumentation Layouts for a) h = 300 mm and b) h = 1000 mm Specimens

The applied load was measured through a load cell integrated in the MTS test frame and does not include the self-weight of the member, the loading plates or the W250 stub column spacer. The weight of the loading plate and W250 stub column spacer was estimated at 0.47 kN while the self-weight of the specimens varied individually.

All the instrumentation was connected into a single data acquisition system, which recorded data every 10 seconds throughout the test. The data acquisition system was operated continuously, even when the loading was paused.

The south face of each specimen was painted with white latex paint to increase the visibility of the cracks and aid in crack tracing and measuring. A 100 x 100 mm grid was drawn on the south face of the h = 300 mm specimens for use with a photogrammetry system. In the h = 1000 mm specimens, the grid measured 300 x 300 mm. The photogrammetry system is explained further in Section 5.6.2 while the grids are illustrated in Figure 5-9.

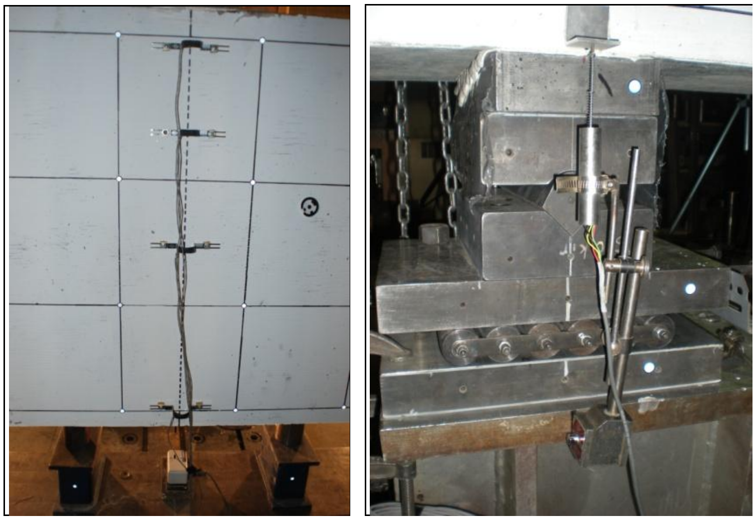

a) b)

Figure 5-10: a) PI Gauges and Mid-Span Cable Potentiometer on a h = 1000 mm Specimen and b) LVDT Setup at Support

5.6.2 Photogrammetry

A square grid was drawn on the south face of the specimens for photogrammetry purposes (Figure 5-9a and Figure 5-10). The h = 300 mm specimens had a 100 x 100 mm grid while a 300 x 300 mm grid was used on the h = 1000 mm specimens. At every grid intersection, small round reflective stickers were placed. Larger coded identifying circles were positioned at arbitrary locations along the length of the specimens. A series of photographs were taken along the length of the specimens before testing began, and subsequently at each load stage using a fixed focal length camera. The reflection of the small stickers along with the position of the identifying circles allows for a software analysis of the images, capable of determining the specimen deflection throughout the test. Due to time restraints, the photogrammetry data was not analysed as part of the current study.

5.6.3 DIC System

The north face of the specimens was also painted white with latex paint, and subsequently speckled with black latex paint. Similar to the setup used for the flexural prism tests (Section 3.4.2), the speckles were typically sized between 3-4 pixels through the Vic-Snap 2009 digital image correlation (DIC) software (Correlated Solutions Inc., 2009 and 2010). Three pairs of cameras were used with the DIC system. Systems 0 and 2 were used to record images of the west and east shear spans, respectively. These cameras had 35 mm focal length lenses (Fujinon Corporation 1:1.4/35mm HF35SA-1). System 1 was placed at mid-span with 12.5 mm focal length lenses (Fujinon Corporation 1:1.4/12.5mm HF12.5SA-1). Systems 0 and 2 were set up at a distance of approximately 3.25 m perpendicular from the specimen and System 1 was placed approximately 1.0 m perpendicular to the specimen.

In the h = 300 mm specimens, Systems 0 and 2 focused on the entire height of the specimens and a horizontal distance of approximately 600 mm situated between the supports and approximately 200 mm from mid-span. System 1 focused on the entire height of the specimens and a horizontal distance of approximately 300 mm to the east and west of mid-span. Figure 5-11a illustrates the three system locations. The 12.5 mm lenses used in System 1 experienced severe distortion around the perimeter of the lenses which limited the accurate viewing area to the center portion.

In the h = 1000 mm specimens, System 0 focused on the lower portion of the specimens. The viewing area extending vertically to approximately 650 mm from the bottom of the specimens and horizontally to approximately 2.2*d, as measured from the face of the loading plate. The horizontal recorded distance on the specimens was approximately 800 mm. This location was chosen based on previous work by Shoaib (2012) on similar SFRC specimens that varied by the reinforcement type and concrete strength. Shoaib's results indicated that the critical shear crack location typically intercepted the level of the longitudinal reinforcement at a distance of 2*d away from the face of the loading plate. The location of System 0 in the current study was chosen to provide DIC data on the critical shear cracks as they reached the longitudinal reinforcement layer. The second system (System 1) was focused on the bottom of the specimens at mid-span in order to capture the mid-span strains and deflections. The 12.5 mm cameras viewed an overall area that spanned approximately 300 mm to the east and west of the centerline, and vertically to approximately 410 mm from the bottom of the specimens. Again, only the center portion of this area was considered to be accurate. The third pair of cameras (System 2) was set up identical to System 0 but placed on the east shear span of the specimens. Figure 5-11b illustrates the three system locations.

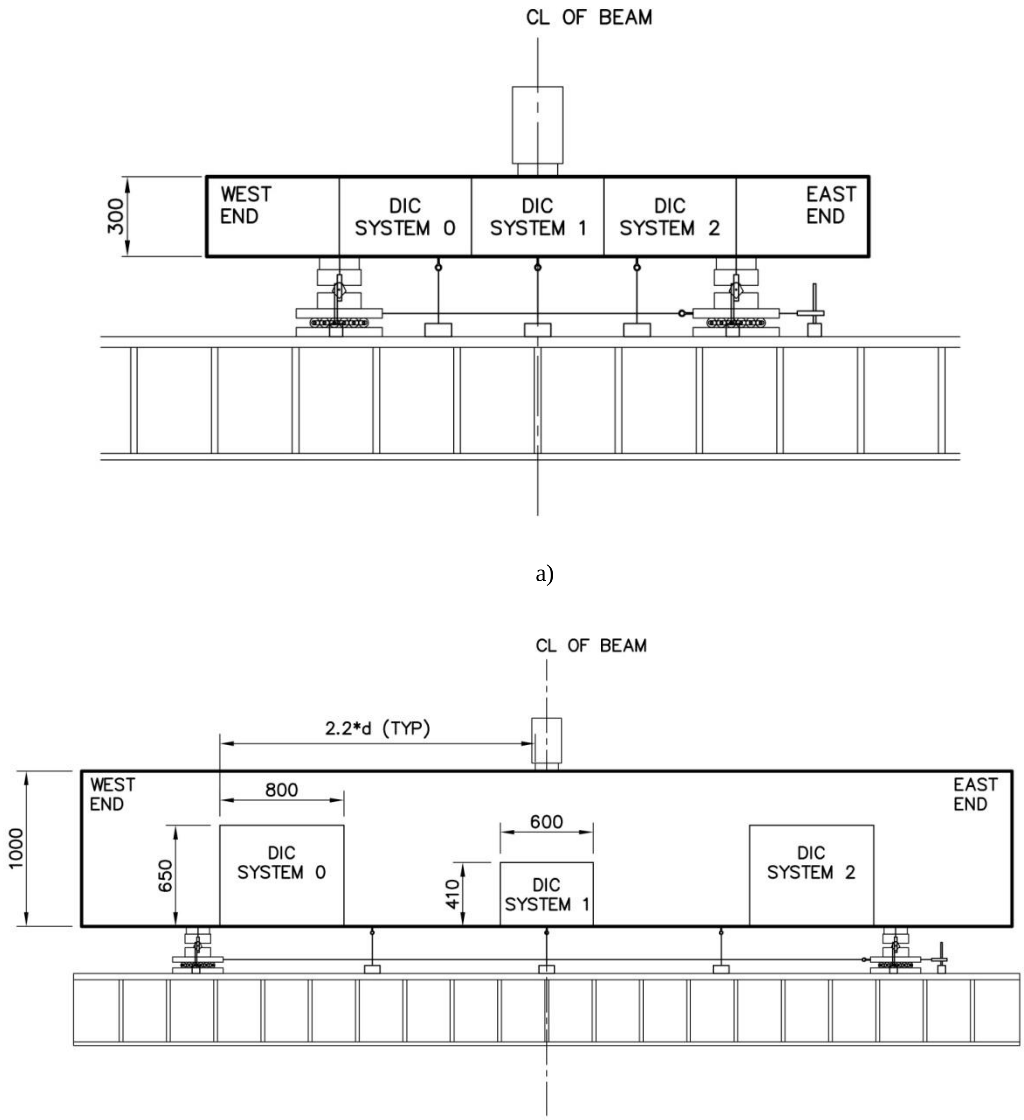

a)

b)

Figure 5-11: Typical DIC System Locations on a) h = 300 mm and b) h = 1000 mm Specimens

A grid was superimposed on the speckled area in order to aid in spatial recognition during the analysis of the DIC images. A dotted line was marked along the length of the specimens at the longitudinal reinforcement layer level(s). In the h = 300 mm specimens, a 200 x 200 mm grid was marked above the reinforcement layer over the entire specimen length. On the east and west shear spans of the h = 1000 mm specimens, a 300 x 300 mm grid was laid out above the reinforcement. At mid-span, a 150 x 150 mm grid was used because of the smaller focus area.

The DIC system was set to record images every 10 seconds throughout the test, in order to allow for synchronization with the data acquisition system. It was stopped when the loading was paused in order to minimize the total quantity of data recorded.

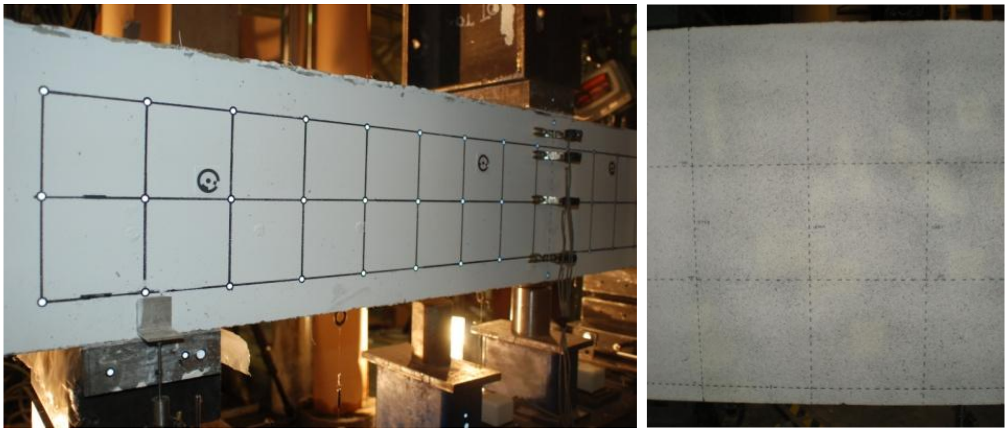

a) b)

Figure 5-12: a) Photogrammetry Setup on S300-B1 and b) DIC Speckling with Grid on a h = 1000 mm Specimen

5.7 Test Procedure

All loading was conducted under displacement control with loading rates determined individually for each specimen based on the predicted stiffness. Loading rates ranged from 0.2 mm/min up to 0.4 mm/min and each test took approximately four hours. Refer to Appendix C for individual specimen loading rates.

Each test was split into 6 load stages (1 through 6) and 4 half load stages (A through D). Stages 1 through 6 were determined by splitting the predicted failure load into 5 equal segments. Stages A through D were located midway between each of the numbered stages. At each numbered stage, the displacement was held to allow for manual measurements along the south face of the specimens. All visible cracks were traced, measured using a crack comparator gauge and photographed. Photographs were also taken to allow for future photogrammetery analysis. No manual measurements were taken after Stage 5 due to safety restrictions. At Stages A through D, the displacement was held but only photographs were taken. If the crack widths approached 1.5 mm prior to the last load stage, the subsequent stages were skipped until failure for safety reasons.

The large scale structural specimens were loaded under displacement controlled loading until failure in order to observe the post peak behaviour. In all cases, failure was defined as a very sudden drop in load carrying capacity, along with a large increase in vertical deflection.

6 Large Scale Structural Specimens – Test Results and Discussion

6.1 General

Prior to testing, the large scale structural specimen dimensions were measured at mid-span and at both supports. The average measured widths and overall heights from those three locations are provided in Table 6-1. The specimens continue to be labelled according to their nominal dimensions, but all calculations were based on these measured values unless otherwise noted. The effective depth however was kept at the design value since this distance could not be measured after casting.

The large scale structural specimens were loaded under displacement controlled loading until failure in order to observe the pre and post peak behaviour. In all cases, failure was defined as a very sudden drop in load carrying capacity, along with a large increase in vertical deflection.

The peak load and mid-span deflections for both h = 300 mm and all four h = 1000 mm specimens are reported in Table 6-1, along with the equivalent service load and subsequent mid-span deflection. The loads reported are based on the applied load from the MTS and include the 0.47 kN weight from the loading plate and the W250 stub column. The self-weight of the specimens is not included. The vertical deflections reported are based on measurements at mid-span and have been corrected for support settlement.

The equivalent service load levels were approximated by using CSA A23.3-04 load and resistance factors. Assuming a ratio of dead to live load between 1 and 3 in combination with the CSA A23.3-04 dead load factor of 1.25 and live load factor of 1.5 produces an average load factor between 1.313 and 1.375. The resistance factor for concrete taken from CSA A23.3-04 is $\phi_c = 0.65$. Combined, these two factors indicate that the service load level is approximately 50% of the peak load level (ie. nominal capacity).

Table 6-1: Large Scale Structural Specimen Properties and Results Summary

Specimen	d (mm)	Measured Height h (mm)	Measured Width b_w (mm)	ρ (%)	f_c' (MPa)	Age at Testing (Days)	Peak Load		Service Load	
							P_{peak} (kN)	Δ_{peak} (mm)	P_s[A] (kN)	Δ_s (mm)
S300-B1	248	310	310	2.61	29.9	93	606	8.7	303	2.5
S300-A2	252	310	310	1.51	37.9	156	445	7.5	222	2.3
S1000-B1	924	1005	303	1.03	30.4	54	973	21.7	487	6.3
S1000-B2	924	1005	303	0.83	31.2	64	918	23.8	459	6.8
S1000-A3	933	1000	305	0.61	41.2	114	739	21.7	369	6.5
S1000-A4	952	1000	311	0.40	40.1	100	729	33.8	364	8.6

[A] $P_s = 0.5 * P_{peak}$

6.2 Failure Mechanisms

All six large scale structural specimens tested in the current study failed in shear. To further characterize the shear failure mechanisms with a moderate level of consistency to previously published work, attempts have been made to follow descriptions provided by ASCE-ACI 426 (1973) and Dinh (2009).

Three failure modes were observed. Specimens S1000-B1 and S1000-A3 were characterized as a combination of diagonal-tension and shear-tension failures (Dinh, 2009). The failure cracks began as web shear cracks (ASCE-ACI 426, 1973) before propagating towards the compression region at mid-span and the support. Minimal or no concrete crushing was observed in the compression zone. Secondary cracks along the reinforcement levels propagated from the failure cracks to the inside face of the support plates after the peak load was reached.

Specimens S300-A2 and S1000-B2 were characterized as a combination of shear-compression and shear-tension failure modes (Dinh, 2009). The failure cracks began as flexural cracks (ASCE-ACI 426, 1973) before extending towards the compression region at mid-span. The opening of the critical diagonal failure crack caused concrete crushing in the compression zone adjacent to the loading plate. Secondary cracks formed along the reinforcement levels after the peak load was reached.

Specimens S300-B1 and S1000-A4 were characterized as diagonal tension failures (Dinh, 2009). The failure cracks began as web shear cracks (ASCE-ACI 429, 1973) before propagating through the compression zone without causing crushing. The failure crack reached the inside face of the support plate with no formation of secondary cracks.

Details of the behaviour of each specimen as it approached peak load and failure are provided in Sections 6.2.1 through 6.2.6 below. DIC images analysed through Vic-3D 2009 (Correlated Solutions Inc., 2009) are provided to highlight the crack and member behaviours. Some of these images are provided with the surface strain shadings although the values associated with the colours have been omitted. The purpose of including the shadings was to indicate the extent or location of the strain concentrations and cracks and not to provide data on the exact strain levels. Further to this point, some of the images are provided with the horizontal surface strains and others are provided with the vertical surface strains. Depending on the physical orientation of the strain concentration or crack, these two options showed different results; therefore the most representative image was chosen to allow for a qualitative examination. Figure 5-11 provides spatial reference on the DIC system locations for the h = 300 mm and h = 1000 mm specimens.

6.2.1 Specimen S300-B1

A single small flexural crack was observed at Stage 2 (200 kN), immediately to the west of mid-span. By Stage 3 (300 kN), a few more cracks were observed with widths less than 0.1 mm. Diagonal cracks started to form by the 400 kN loading stage in both shear spans of the specimen (Figure 6-1a illustrates the east end) but by 500 kN, the east crack had reached 1.25 mm in width while the crack in the west shear span remained at a maximum of 1.0 mm.

The specimen reached a peak load of 606 kN. The failure crack widths at this stage were substantial – approximately 2.8 mm at mid-height (Figure 6-1b). The crack had reached the reinforcement level by this stage but had not extended entirely to the inside face of the east support. Based on the gridlines superimposed on the DIC area, no sliding or shifting had occurred.

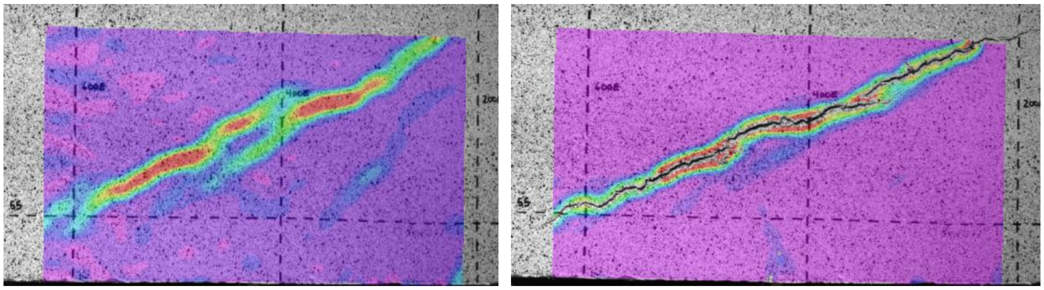

a) b)

Figure 6-1: Vertical Surface Strains from DIC System 2 on S300-B1 at a) 400 kN and b) Peak Load

Failure was characterized by an immediate drop in load carrying capacity, down 47% to approximately 320 kN, along with an increase of approximately 1.6 mm in deflection as measured by the cable potentiometer at the east quarter span point. At this stage, the failure crack had extended almost all the way to the inside face of the east support plate. Based on the gridlines, no visible rotation or horizontal movement had occurred. A small amount of vertical shifting had occurred, with the portion of the member under the failure crack dropping by approximately 2.0 mm. Figure 6-2a provides the Vic-3D DIC image taken immediately after failure.

Under increased applied deformations, the specimen continued to carry a gradually decreasing amount of load. At a load of approximately 229 kN post-peak, the loading rate was increased to 0.15 mm/min from 0.125 mm/min. At approximately 212 kN, the rate was increased to 0.20 mm/min. As the loading progressed, the crack widths and vertical deflection continued to increase and crushing of the concrete in the compression region occurred.

The testing was stopped at a post-peak load of 205 kN (Figure 6-2b). A further 15.5 mm of deflection was measured in the east span between the peak load and the end of the test. During this time, the failure crack widths grew by over six times their size at the peak load and extended past the outside face of the east support. Small amounts of rotation were visible based on the gridlines, as well as vertical and horizontal shifting as the portion of the member under the failure crack was pushed down.

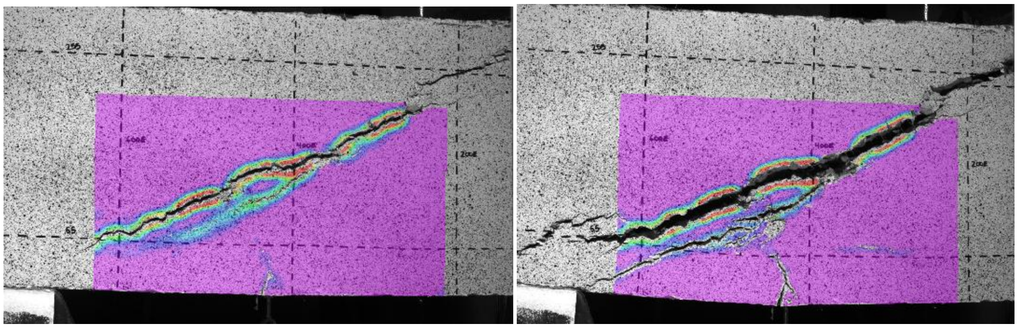

a) b)

Figure 6-2: Vertical Surface Strains from DIC System 2 on S300-B1 a) Immediately After Failure and b) at Approximately 205 kN Post-Peak

The failure crack began as a web shear crack that extended towards both the compression region and the east support. Although large crack widths developed along with significant concrete crushing in the compression zone between the peak load and end of testing, there was minimal to no crushing at failure. The failure crack extended past the east support with significant cracking after failure had occurred. The failure type was therefore classified as a diagonal tension failure. Figure 6-3 provides an overall view of the failure crack on the south face of the specimen.

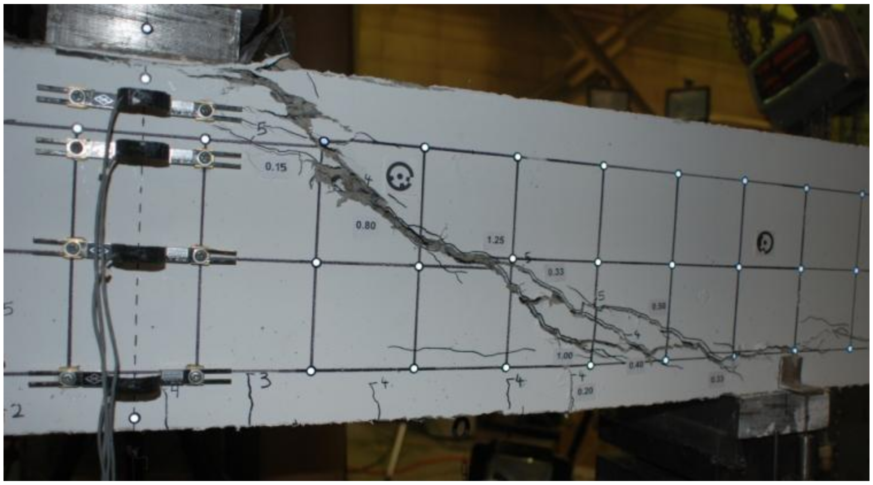

Figure 6-3: Overall Failure Crack on South Face of S300-B1

6.2.2 Specimen S300-A2

At Stage 2 (180 kN), small flexural cracks of negligible width were visible at mid-span. Diagonal cracks had started to form in the east shear span of the specimen by Stage 3 (270 kN) and grew to a maximum width of 0.6 mm around 360 kN. In comparison, the west shear span remained relatively un-cracked. The DIC image at a load of approximately 360 kN is provided in Figure 6-4a; while two main cracks were visible, the left most crack above the reinforcement level began as a flexural crack and ultimately developed into the failure crack.

The specimen reached a peak load of 445 kN before failure. At this stage, the diagonal shear crack had extended towards the compression region and the east support although the crack size at these two extremes was negligible. Based on the vertical and horizontal gridlines, no visible shifting or sliding had occurred.

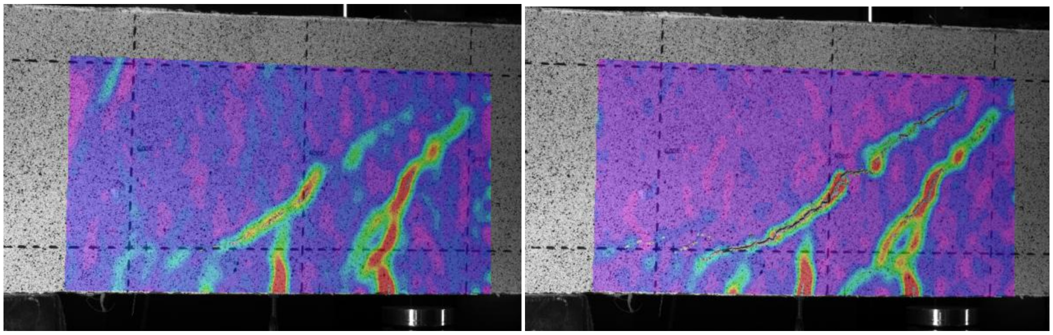
a) b)

Figure 6-4: Horizontal Surface Strains from DIC System 2 on S300-A2 at a) 360 kN and b) Peak Load

Failure was characterized by a sudden 55% drop in load carrying capacity to approximately 200 kN and an increase in vertical deflection of 2.7 mm as measured by the cable potentiometer in the east shear span. The diagonal failure crack extended to the face of the loading plate, causing concrete crushing in the compression region. The diagonal failure crack also extended horizontally approximately 30 mm past the inside face of the east support plate. The gridlines indicated no visible signs of shifting or sliding. Figure 6-5 illustrates the Vic-3D DIC image immediately after failure.

The loading was not continued past the initial failure.

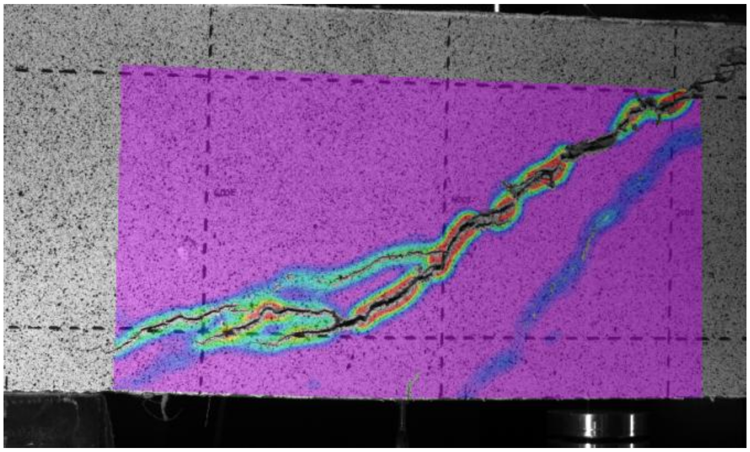

Figure 6-5: Vertical Surface Strains from DIC System 2 on S300-A2 Immediately After Failure

The failure crack began as a flexural crack before propagating towards both the loading plate and the east support. Crushing of the concrete in the compression region occurred, along with splitting cracks along the reinforcement level. This failure was classified as a combination of shear-compression and shear-tension. Figure 6-6 provides an overall view of the failure crack on the south face of the member.

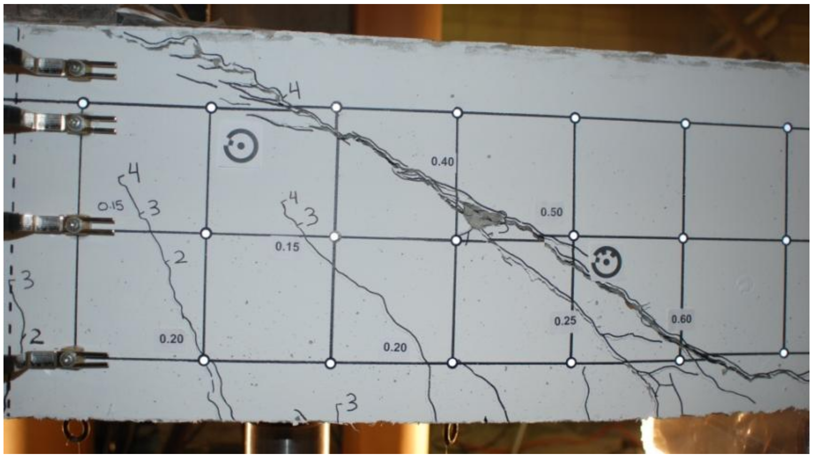

Figure 6-6: Overall Failure Crack on South Face of S300-A2

6.2.3 Specimen S1000-B1

Once the formwork had been stripped away after the casting and curing of S1000-B1, voids in the concrete were revealed near the longitudinal reinforcement layers on the east end of the specimen at approximately 750 mm from mid-span (Figure 6-7). It is believed that the voids were a result of inadequate vibration during casting, either due to the rod not penetrating far enough down into the first layer of concrete or from too large of spacing in between the vibrator penetrations. The largest void had a diameter of approximately 70 mm, extending approximately 50 mm into the specimen to expose the outer faces of the reinforcement. The voids were not repaired before testing.

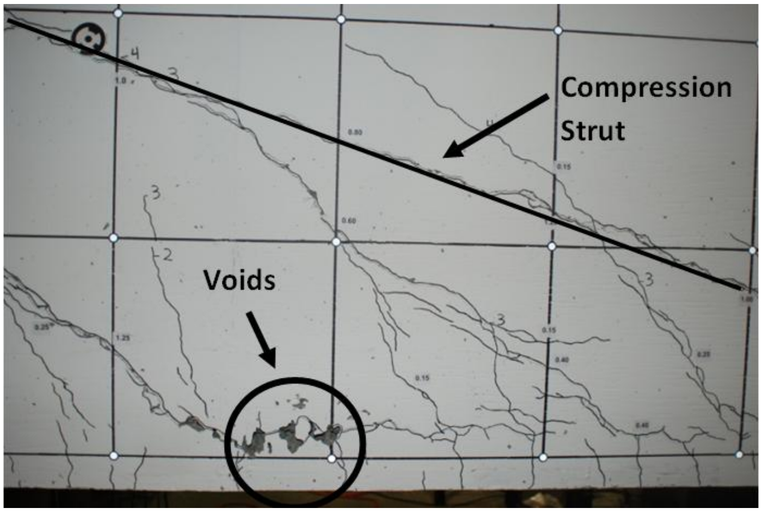

Figure 6-7: Voids and Compression Strut in East End of S1000-B1

It was believed that the voids on the east end of the specimen would result in the smallest and thus weakest cross-sectional area of the specimen, leading to the failure crack location. This end of the specimen experienced the first visible cracks, which were located around the voids, followed by small flexure cracks around mid-span. The flexure cracks started out vertically, before sloping towards the mid-span loading point as the imposed load increased. At a load of approximately 380 kN, the largest crack width measured 0.15 mm. As testing progressed, the cracks in the east shear span continued to dominate over the west shear span. Between the last load stage (856 kN) and failure, a compressive strut appeared to have formed in the east shear span of the specimen, indicated by the nearly linear diagonal crack between the support and the loading point highlighted in Figure 6-7. The presence of this strut forced the failure crack to the west shear span. The reason for the strut formation is unclear.

At the last load stage (Stage D), the largest crack in the west shear span measured approximately 0.33 mm in width. The failure crack was not yet visible on the south face of the specimen although the DIC system did capture high strain concentrations above the upper longitudinal reinforcement layer at approximately 1500 mm to the west of mid-span which would later develop into the failure crack. The location of the crack indicates that it was a web shear crack.

At a peak load of 973 kN, the DIC system captured the failure crack passing through the earlier location of high strain concentrations and extending in both directions towards the loading point and to the upper reinforcement layer. At the upper reinforcement layer, the crack extended approximately 150 mm towards the supports in a primarily horizontal path. Figure 6-8a highlights the failure crack at the peak load. Based on the grid superimposed on the speckling, no visible sliding action between the crack surfaces had occurred at the peak load.

As the loading continued, the failure crack continued to widen. No sliding or shifting was observed on the upper portion of the crack. At the upper reinforcement layer, the failure crack width growth caused the portion of the member under the crack to drop vertically compared to the portion of the member above the crack. The DIC image captured 10 seconds before the final failure, shown in Figure 6-8b, shows the failure crack ending more than 600 mm from the inside face of the west support.

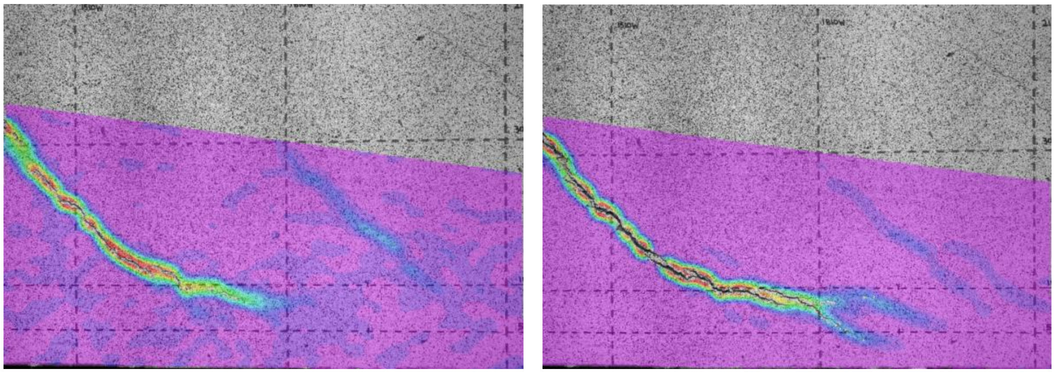

a) b)

Figure 6-8: Vertical Surface Strains from DIC System 0 on S1000-B1 at a) Peak Load and b) Immediately before Failure

Failure was characterized by an immediate and complete loss of load carrying capacity, and an increase of almost 20 mm in vertical deflection as measured by the cable potentiometer at the west quarter span point. The failure crack widths in the DIC area expanded from approximately 4.0 mm in width to greater than 15.0 mm and a high percentage of fiber pull-out was visible. The failure crack also propagated horizontally the remaining distance to the inside face of the west support.

The final image captured by the DIC system (Figure 6-9) shows significant vertical movement where the failure crack reached the upper reinforcement level. The portion of the member below the horizontal segment of the crack is estimated to have shifted approximately 40 mm lower than the section of the member above the crack. Minimal shifting in the horizontal direction was observed.

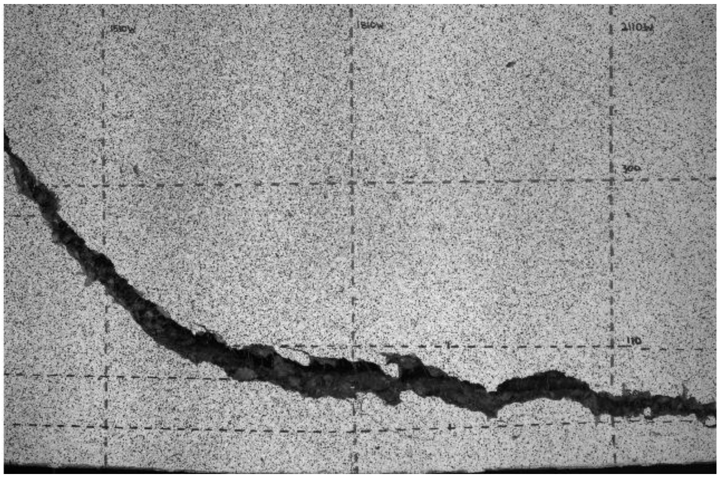

Figure 6-9: Specimen S1000-B1 DIC System 0 Image Immediately After Failure

The failure crack began as a web shear crack before extending towards the compression zone and the longitudinal reinforcement. It followed a bi-linear slope to travel through the west shear span and extended through the top surface of the specimen at the west edge of the loading plate. At failure, the crack propagated horizontally to the inside face of the west support. The failure method was classified as a combination diagonal-tension and shear-tension failure, with an eventual loss of reinforcement bond due to crack propagation along the reinforcement after the peak load was reached. An overall view of the failure crack is provided in Figure 6-10.

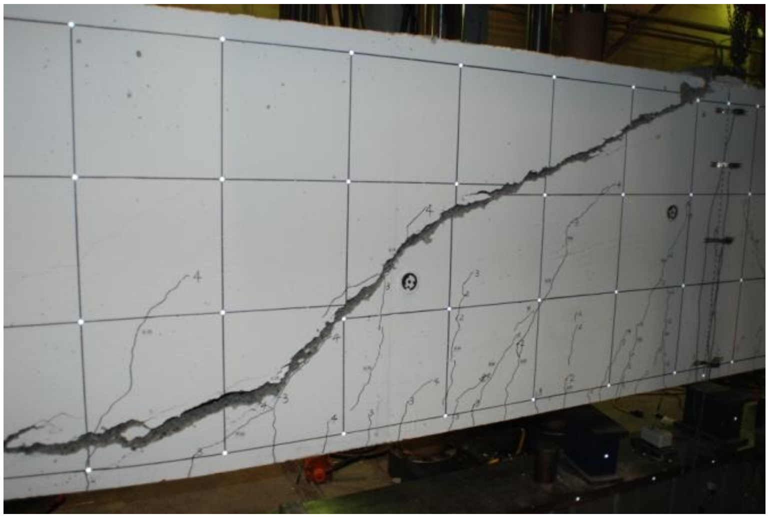

Figure 6-10: Overall Failure Crack on South Face of S1000-B1

6.2.4 Specimen S1000-B2

The first visible flexural cracks were measured at Stage 2 with a load of approximately 340 kN. The cracks were concentrated around mid-span with a maximum width of 0.2 mm. One crack on each side of mid-span extended to approximately mid-height. As the loading increased, cracks began to form along the shear spans on both ends.

In the west shear span, two significant cracks formed. By Stage 3 (510 kN), both cracks had started to grow although the innermost crack was approximately 30% longer and 50% wider. Only the outer crack was captured by the DIC system throughout the loading.

At Stage 5 (850 kN), the outermost crack crossed mid-height of the specimen at approximately 1275 mm west of the specimen mid-span while the innermost crack crossed the same location at approximately 900 mm from the mid-span. The widths of both these cracks in the bottom 350 mm of the specimen were similar, between 1.25 and 1.50 mm. In the 300 mm grid located at mid-height of the specimen, manual measurements indicate that the outer crack varied in width between 0.2 and 0.9 mm, while the inner crack varied between 0.8 and 1.5 mm. Figure 6-11 highlights the two primary cracks as viewed on the south face of the member. The DIC images at this stage show the outer crack reaching the upper reinforcement layer, and extending approximately 100 mm towards the west support.

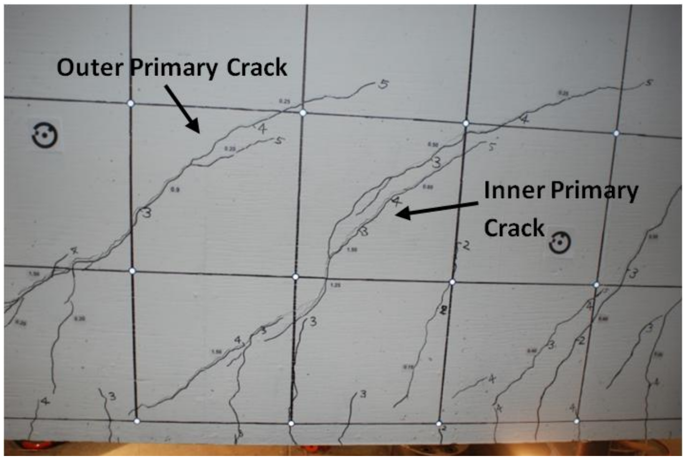

Figure 6-11: Specimen S1000-B2 Primary Cracks on West End

The innermost crack continued to dominate into the final loading stage, and became the primary failure crack of the specimen. At a peak load of 918 kN, the DIC image captured a third crack running almost parallel to the outer crack, and the outer crack extending further towards the west support (Figure 6-12a). Based on the gridlines, sliding or shifting had not occurred. At the lower left corner of the DIC image, a small strain concentration is visible. This represents the tip of the actual failure crack (the inner primary crack) extending west (i.e. to the right) towards the support.

The DIC image taken immediately before failure (Figure 6-12b) illustrates the crack expansion between peak load and failure of the outer primary crack. The main failure crack had propagated slightly since the peak load image but the three distinct cracks remained separate. No shifting or sliding was visible.

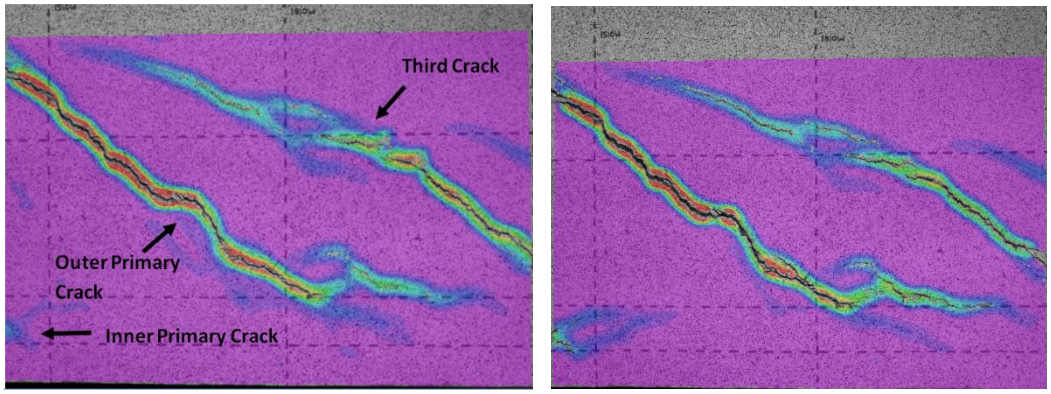

a) b)

Figure 6-12: Vertical Surface Strains from DIC System 0 on S1000-B2 at a) Peak Load and b) Immediately Before Failure

Failure was characterized by an immediate and complete loss of load carrying capacity, and an increase of almost 15 mm in deflection as measured by the cable potentiometer at the west quarter span point. The three primary cracks joined along the length of the horizontal reinforcement and extended to the inside face of the west support (Figure 6-13). The portion of the member under the failure crack dropped by approximately 10 mm compared to the portion above the failure crack. A slight rotation of the member about the crack is visible by comparing the vertical gridlines above and below the failure crack.

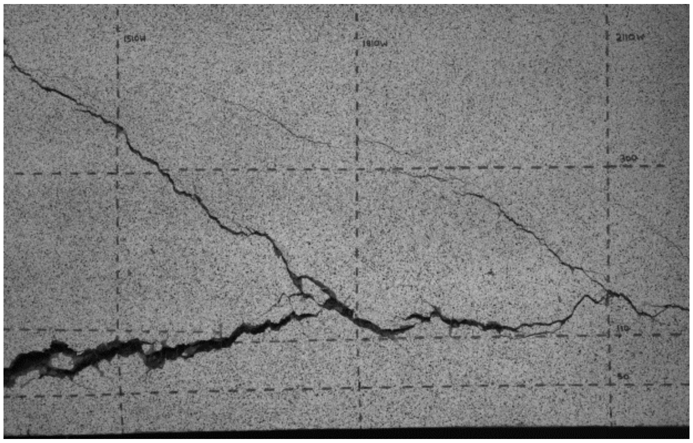

Figure 6-13: S1000-B2 DIC System 0 Image Immediately After Failure

The failure crack began as a flexural crack approximately halfway through the west shear span. It propagated towards the compression region at a steep slope and caused a slight rotation in the member on both sides of the crack. The crack propagation and member rotation caused concrete crushing in the compression zone at the tip of the crack. At the reinforcement level, the crack extended towards the inside face of the west support after the peak load was reached. The failure mode was classified as a combination shear-compression and shear-tension failure, with a secondary crack propagating along the length of the horizontal reinforcing steel. An overall view of the failure crack on the south face of the specimen is provided in Figure 6-14.

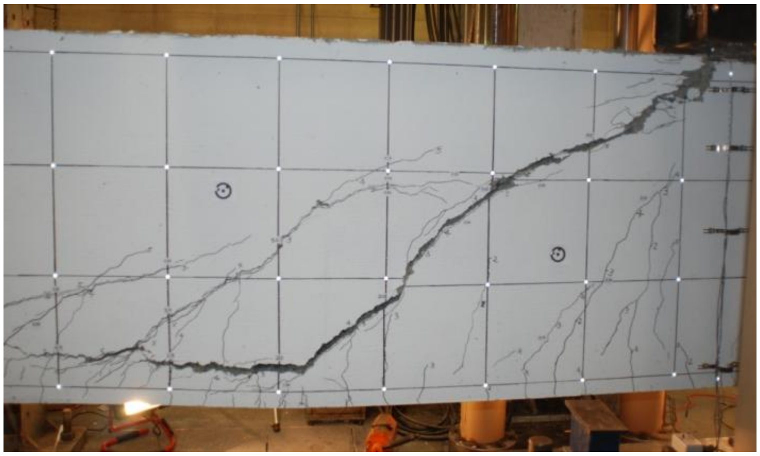

Figure 6-14: Overall Failure Crack on South Face of S1000-B2

6.2.5 Specimen S1000-A3

The first visible flexural cracks were measured at Stage 2 (290 kN). They were concentrated at mid-span, with the largest crack extending just past mid-height at approximately 600 mm west of mid-span. The maximum width of the crack at Stage 2 measured 0.15 mm.

At Stage 3 (435 kN), the failure crack was not yet visible on the south face of the specimen but a strain concentration in the east shear span was captured by the DIC system that spanned from above the upper reinforcement layer to approximately mid-depth (Figure 6-15a). Between Stage 3 and Stage 4 (585 kN), the failure crack had formed in the east shear span. The failure crack followed the path of the earlier noted strain concentrations around mid-height, but branched out to the east (left) in the lower half of the member (Figure 6-15b). By Stage 5 (725 kN), the dominant crack in the east shear span was clearly visible with a maximum width of 1.5 mm. Significant cracking covered the remainder of both shear spans.

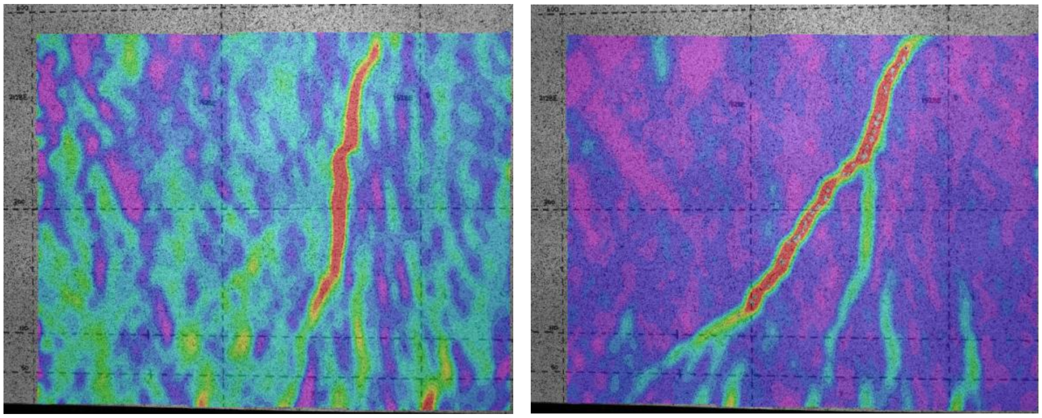

a) b)

Figure 6-15: Horizontal Surface Strains from DIC System 2 on S1000-A3 at a) Stage 3 and b) Stage 4

At a peak load of 739 kN, the DIC system captured the failure crack with a visibly larger width than at Stage 5 and extending to the lower reinforcement layer (Figure 6-16a). Strain concentrations were visible horizontally along a portion of both the upper and lower reinforcement layers, and a small crack was observed within the lower reinforcement strain concentration. This crack ended approximately 600 mm from the inside face of the east support. Based on the gridline markings, no horizontal shifting had occurred at this point. The horizontal gridlines at distances of 110 mm and 300 mm from the soffit of the member indicate that vertical shifting had occurred; the portion of the member under the failure crack had dropped approximately 2 mm at the 110 mm grid and approximately 4 mm at the 300 mm grid.

The DIC image taken immediately before failure (Figure 6-16b) visibly demonstrates the increase in the failure crack width. The crack along the lower longitudinal reinforcement is easily visible at this stage but does not appear to extend to the east support. The gridlines continue to indicate shifting primarily in the vertical direction.

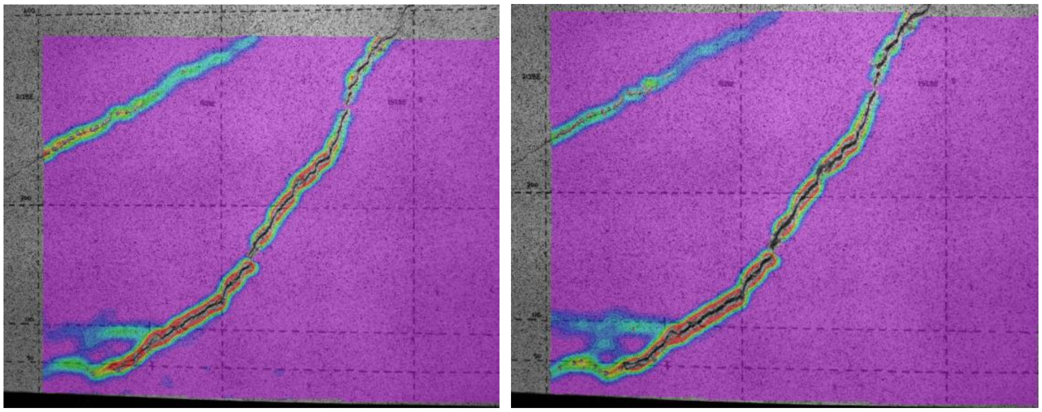

a) b)

Figure 6-16: Vertical Surface Strains from DIC System 2 on S1000-A3 at a) Peak Load and b) Immediately Before Failure

Failure was characterized by an immediate and complete loss of load carrying capacity, and an increase of approximately 14 mm in deflection as measured by the cable potentiometer at the east quarter span point. The failure crack extended horizontally to the inside face of the east support along the longitudinal reinforcement. Significant amounts of fiber pull-out were visible within the failure crack plane. Figure 6-17 illustrates the failure crack immediately after failure.

Immediately before failure, a tension crack also formed from the top of the specimen and connected with the diagonal failure crack at a vertical distance of approximately 250 mm from the top. This crack split the portion of the member above the failure crack into two and allowed these two portions to rotate independently away from the tension crack.

The portion of the specimen under the failure crack experienced a vertical drop of approximately 55 mm as measured at the horizontal gridline located at a distance of 110 mm from the member soffit. Minimal horizontal shifting or sliding is observed, although the portion of the member above the failure crack experienced rotation.

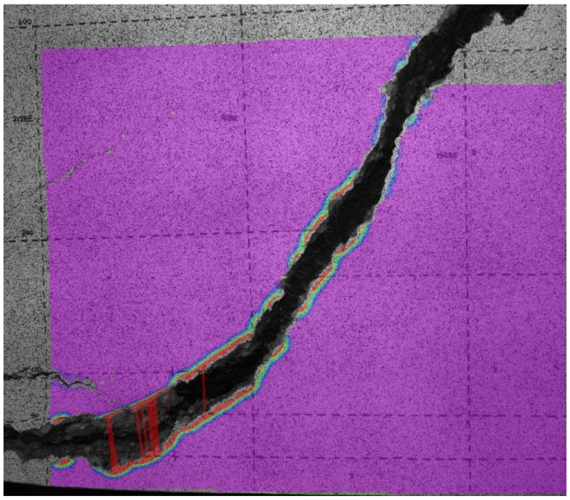

Figure 6-17: Vertical Surface Strain from DIC System 2 on S1000-A3 Immediately After Failure

The failure crack began as a web shear crack before extending towards the compression region and the reinforcement levels. The crack followed a steep slope in the lower half of the specimen. In the upper portion of S1000-A3, the crack propagated horizontally through approximately half of the shear span with a moderate slope towards the loading plate. Once the reinforcement layer was reached, the failure crack extended out horizontally towards the inside face of the support. Figure 6-18 illustrates the failure crack on the south face of the specimen. Failure was classified as a combination of diagonal-tension and shear-tension, with a secondary crack propagating along the length of the longitudinal reinforcement.

Figure 6-18: Overall Failure Crack on South Face of S1000-A3

6.2.6 Specimen S1000-A4

The first flexural crack was traced at Stage 1 (110 kN) with a width less than 0.1 mm at approximately 300 mm to the west of the specimen centerline. By Stage 5 (550 kN), the largest cracks were only 0.6 mm and no definite failure path had been revealed. The DIC image at this stage from the west shear span indicated a strain concentration between the reinforcement layer and mid-height, although it did not develop into the failure crack. The loading rate was subsequently increased to 0.25 mm/min from the initial 0.20 mm/min.

At a load of approximately 700 kN, a strain concentration was visible on the right (west) side of the System 0 DIC images (Figure 6-19a). The lower portion of this concentration appeared to stem from a flexural crack. The upper portion ultimately became part of the failure crack, which then bypassed the lower part of the strain concentration and ran relatively parallel to it.

At a peak load of 729 kN, the failure crack was visible in the DIC images and had extended both towards the loading plate and the west support (Figure 6-19b). Only the mid-height area of the failure crack was captured by the DIC system, therefore the diagonal crack behaviour at the reinforcement level is unknown. At this stage, the vertical gridlines indicate no visible sliding or shifting had occurred. The horizontal gridline at a distance of 350 mm from the member soffit indicate minimal shifting in the vertical direction where the crack crossed it.

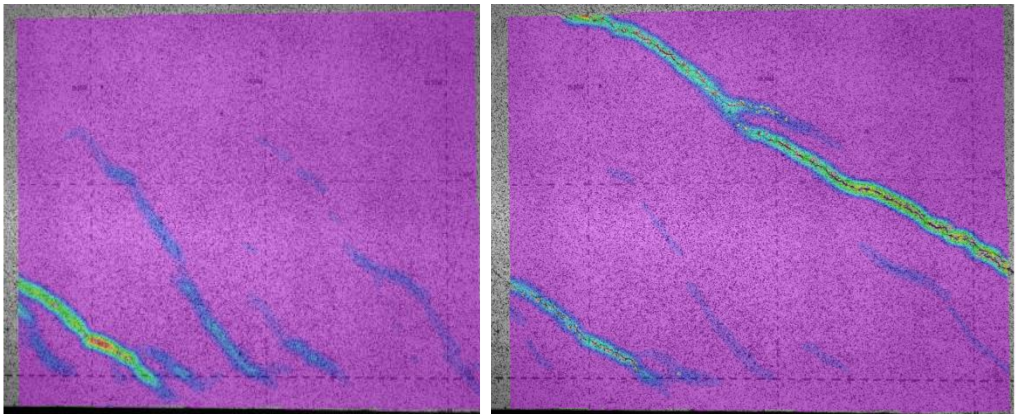
a) b)

Figure 6-19: Vertical Surface Strains from DIC System 0 on S1000-A4 at a) 700 kN and b) Peak Load

Immediately before failure (Figure 6-20a), the failure crack width growth since peak load was apparent. There was no visible rotation or horizontal sliding, and the vertical shifting appears consistent with that at the peak load.

Failure was characterized by an immediate and complete loss of load carrying capacity, and an increase of approximately 16 mm in deflection as measured by the LVDT at the west quarter span point. The failure crack widths increased substantially and significant fiber pullout was observed.

Immediately before failure, a tension crack also formed from the top of the specimen and connected with the diagonal failure crack at a vertical distance of approximately 200 mm from the top. This crack split the portion of the member above the failure crack into two and allowed these two portions to rotate independently away from the tension crack.

Significant rotation and shifting was observed along the failure crack after failure (Figure 6-20b). Approximately 28 mm of horizontal shifting was observed based on the left-most vertical gridline, along with approximately 59 mm in the vertical direction as measured based on the horizontal gridline located a distance of 350 mm from the soffit of the member.

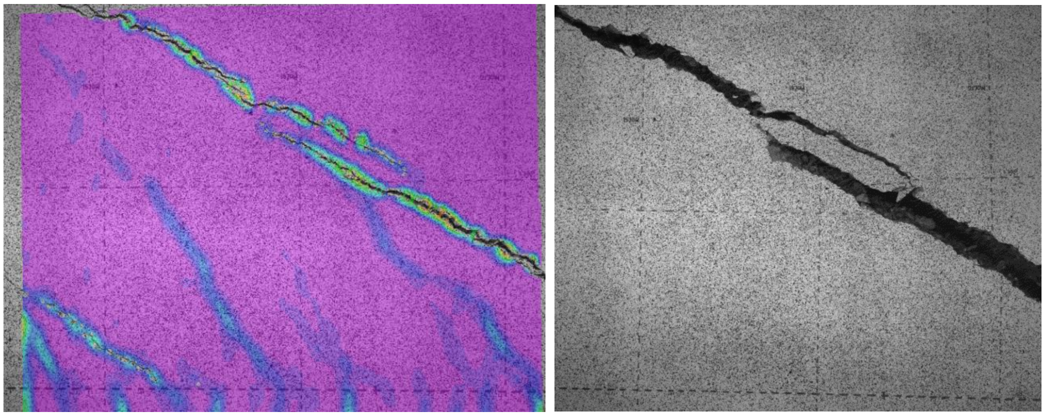
a) b)

Figure 6-20: a) Horizontal Surface Strains from DIC System 0 on S1000-A4 Immediately Before Failure and b) DIC System 0 Image Immediately After Failure

The failure crack began at mid-height as a web shear crack before extending towards the loading plate and to the west support. The slope was bi-linear; relatively steep in the lower half of S1000-A4 before levelling out horizontally to travel to mid-span. The failure crack reached the reinforcement layer at approximately 300 mm to the east of the support plate. The failure mechanism is characterized as a diagonal tension failure. Figure 6-21 provides an overview of the entire failure crack on the south face of the member.

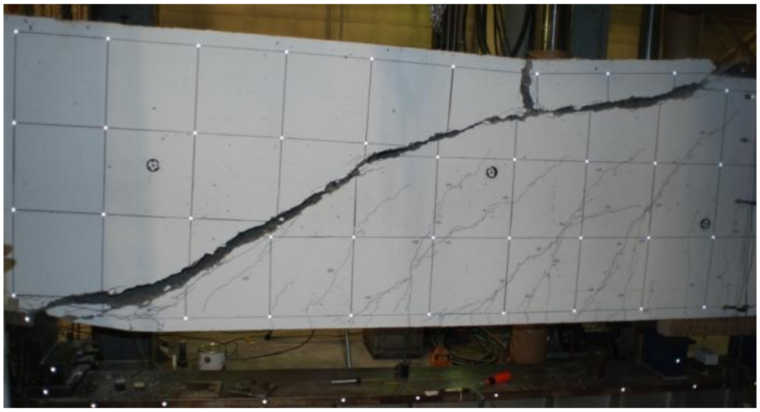

Figure 6-21: Overall Failure Crack on South Face of S1000-A4

6.2.7 Summary

The h = 300 mm specimens failed suddenly in shear. Although these members experienced very large drops in load carrying capacity, both were still able to carry approximately 50% of the peak load with further deflections and deterioration.

All four h = 1000 mm specimens failed suddenly and catastrophically in shear. They experienced sudden, large increases in vertical deflections and a complete loss of load carrying capacity. Some of the specimens experienced concrete crushing in the compression zone, and some experienced a decrease in reinforcement bond due to secondary cracks propagating along the horizontal reinforcement.

The overall failure mechanism for all of these specimens was shear, but the behaviour both before and after failure differed in all six cases. This demonstrates that the behaviour of no two reinforced concrete members is the same, and the exact failure mechanisms are complex and often involve several types of behaviour (Dinh, 2009).

6.3 Load-Deflection Behaviour

Comparing the load-deflection curves of the large scale structural specimens provided an overview of the performance of each member. Since the deflection control requirements of a simply supported member are determined in typical design cases by the maximum mid-span deflection, this location was chosen for comparison purposes instead of the quarter span deflection values from the failed specimen end. The reported mid-span deflection of each specimen was corrected for measured support settlements. Figure 6-22a compares the behaviour of the h = 300 mm specimens while Figure 6-22b compares the h = 1000 mm specimens.

As the reinforcement ratio increased, the stiffness of the specimens increased. The resulting higher stiffness should lead to a decrease in the mid-span deflection at the same applied load. The h = 300 mm specimens followed this behaviour. However, at the peak load, specimen S300-B1 which contained 70% more longitudinal reinforcing steel than

S300-A2 experienced a 17% higher mid-span deflection at peak load (Figure 6-22a) due to the higher nominal strength.

In the h = 1000 mm specimens, the mid-span deflection at both service level and peak load increased with a decrease in reinforcement ratio, save for S1000-A3 (Figure 6-22b). Although S1000-A3 contained 30% less longitudinal reinforcing steel than S1000-B2, it experienced 10% less mid-span deflection at peak load instead of more. The reason for this discrepancy is unclear but is likely related to the difference in failure mechanisms between the two. As expected, the h = 1000 mm specimens showed higher deflections at similar load levels as the reinforcement ratio decreased.

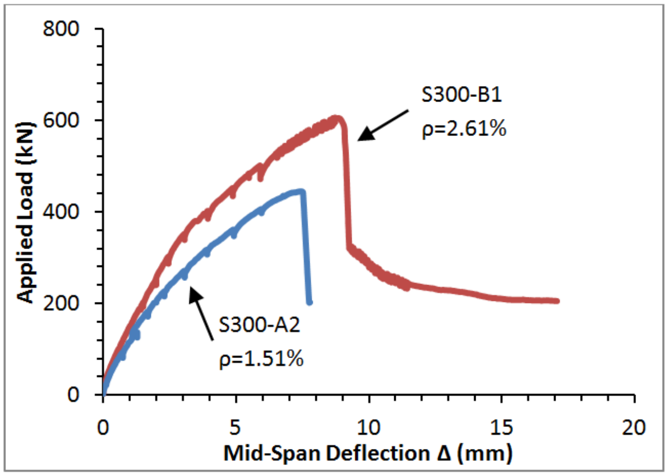

a)

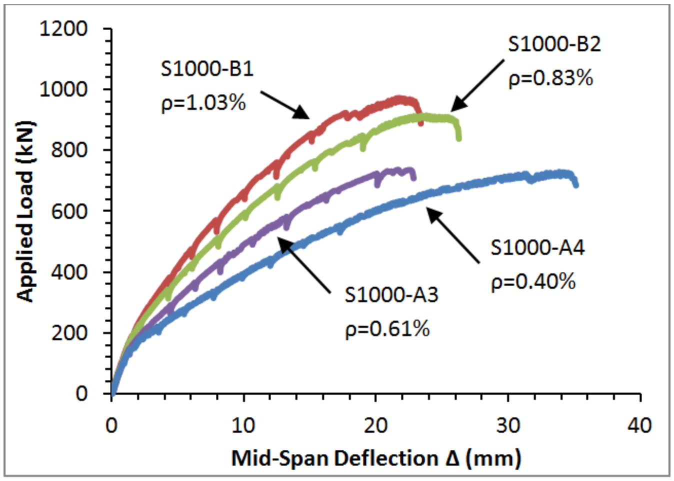

b)

Figure 6-22: Load-Deflection Curves for a) h = 300 mm and b) h = 1000 mm Specimens

The mid-span deflection at the equivalent service load (ie. $P_s = 0.5*P_{peak}$) is compared with the reinforcement ratio in Figure 6-23 for the h = 300 and 1000 mm specimens. A decrease in the service deflection is generally observed with an increase in the reinforcement ratio, similar to the behaviour shown in Figure 6-22 at the peak load.

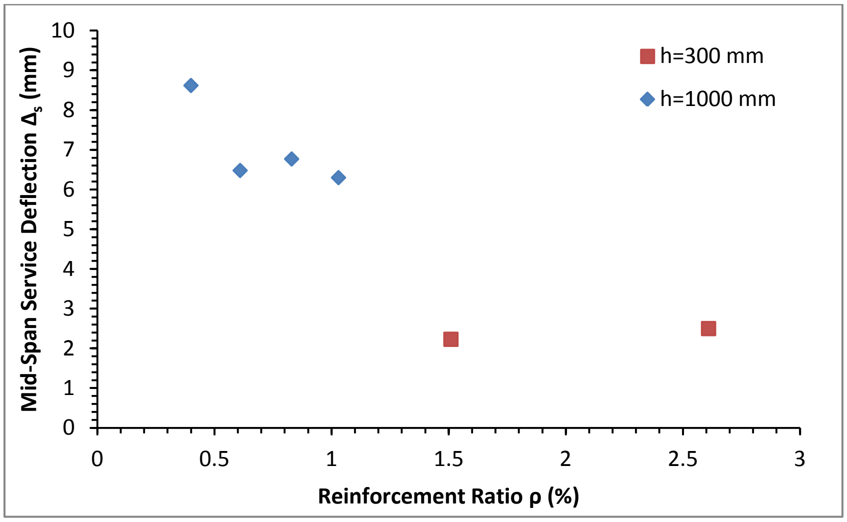

Figure 6-23: Relationship between Mid-Span Service Deflection and Reinforcement Ratio

The potentially larger deflections of structural members reinforced with ASTM A1035 steel compared with members reinforced with conventional Grade 400 steel remain a concern at the serviceability limit states. Both CSA A23.3-04 and ACI 318-08 recommend maximum allowable deflections at the service load levels for plain concrete members of various configurations. The most stringent deflection limit in CSA A23.3-04 is $L_n/480$ for roof or floor construction supporting non-structural elements likely to be damaged by large deflections, where L_n represents the clear span between supports. Similarly in the ACI 318-08 code for the same construction conditions, the deflection limit is L/480 where L represents the span length center to center of supports. Table 6-2 indicates the service deflection for each specimen, along with the ratio of this deflection to the clear span (Δ_s/L_n). Comparing this ratio to the CSA A23.3-04 and ACI 318-08 limit of 0.0021 (i.e. $\Delta_s = L_n/480$) indicates that all specimens satisfied the deflection control limits for plain concrete members.

Table 6-2: Mid-Span Service Deflections for Large Scale Structural Specimens

Specimen	ρ (%)	d (mm)	Δ_s (mm)	Δ_s/L_n
S300-B1	2.61	248	2.5	0.0019
S300-A2	1.51	252	2.3	0.0016
S1000-B1	1.03	924	6.3	0.0012
S1000-B2	0.83	924	6.8	0.0013
S1000-A3	0.61	933	6.5	0.0012
S1000-A4	0.40	952	8.6	0.0016

6.4 Crack Patterns and Crack Widths

As explained in Section 5.7, the cracks on the south face of the specimens were traced and measured through use of a crack comparator gauge at each load stage. A schematic of these crack patterns was drawn for each specimen to give an indication of the extent and location of cracking. The diagonal shear failure crack has also been included with shading to emphasize the extent of the crack widths and any concrete spalling that occurred. Crack diagrams for each specimen at each of the load stages are provided in Appendix C. The final diagrams, after failure, are provided in Figure 6-24.

The failure cracks, as captured by the DIC system, are shown in Figure 6-25 for the h = 300 mm specimens and Figure 6-26 for the h = 1000 mm specimens. The primary objective was to determine the failure crack widths at both the service and peak load levels. The crack widths at these load levels were extracted through the DIC post-processing system (Correlated Solutions Inc., 2009) at distances of 0.5*h, 0.75*h and d from the compression face. Since the failure location of each specimen was not known at the time of setup, capturing all three of these crack locations on each specimen was attempted but not expected.

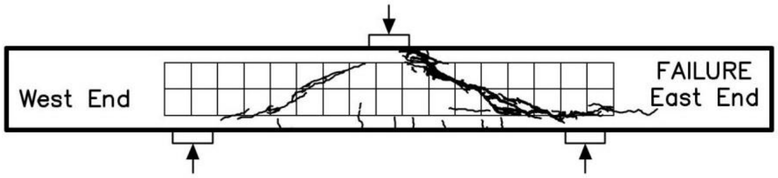

S300-B1: p = 2.61%, fc' = 29.9 MPa

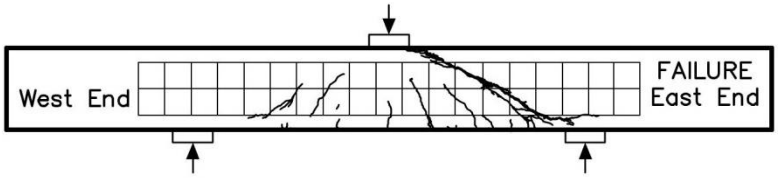

S300-A2: p = 1.51%, fc' = 37.9 MPa

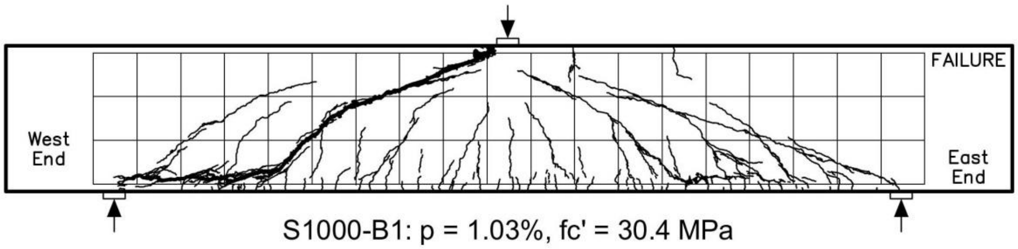

S1000-B1: p = 1.03%, fc' = 30.4 MPa

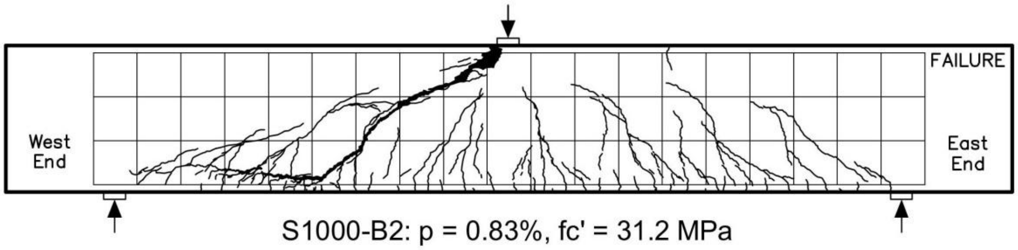

S1000-B2: p = 0.83%, fc' = 31.2 MPa

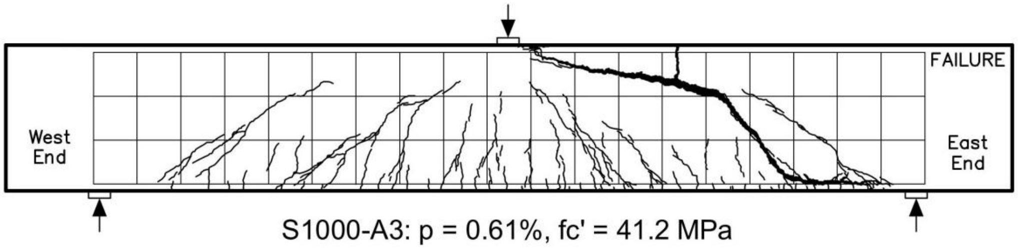

S1000-A3: p = 0.61%, fc' = 41.2 MPa

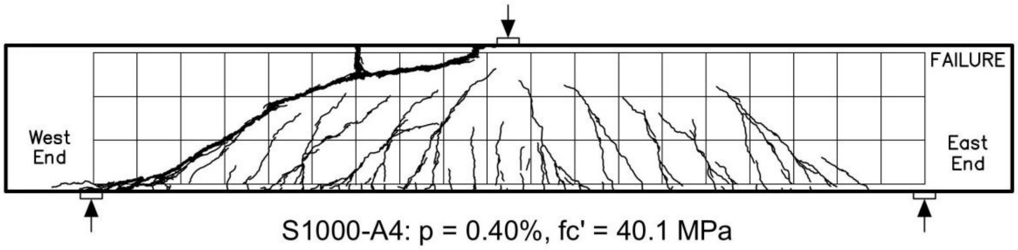

S1000-A4: p = 0.40%, fc' = 40.1 MPa

Figure 6-24: Final Crack Diagrams for Large Scale Structural Specimens

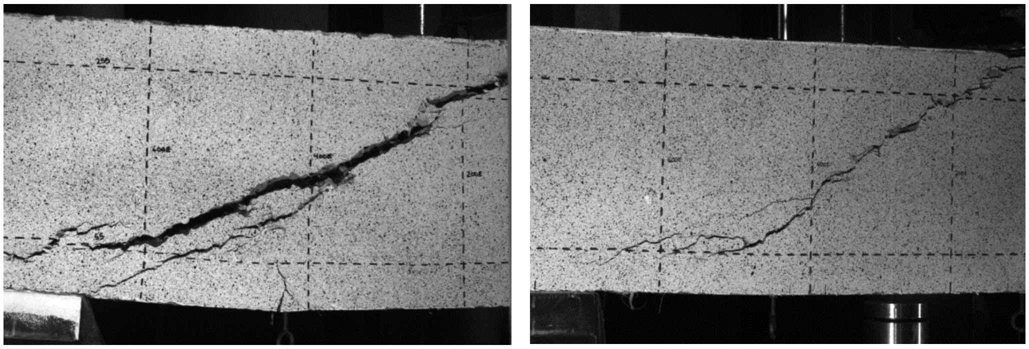

a) b)

Figure 6-25: DIC Images of the Diagonal Failure Crack After Failure from a) S300-B1 and b) S300-A2

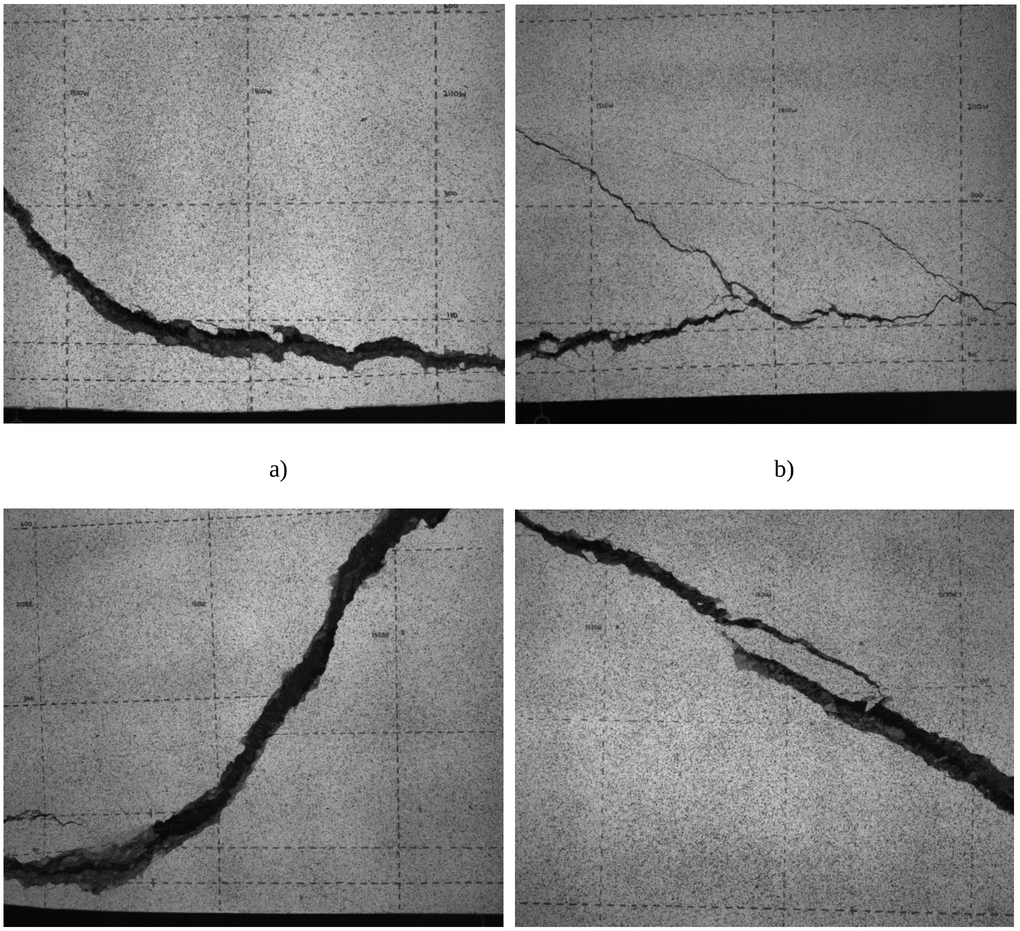

a) b)

c) d)

Figure 6-26: DIC Images of the Diagonal Failure Crack after Failure from a) S1000-B1, b) S1000-B2, c) S1000-A3 and d) S1000-A4

Due to the nature of the material, the exact angle and width of the cracks constantly change along the crack length. In order to obtain a reasonably accurate estimate of the crack size, the angle of the diagonal shear crack was estimated at each of the locations indicated above (0.5*h, 0.75*h and d) based on the DIC images at the peak load. These angles are provided in Table 6-3 and Table 6-4 and are with respect to the longitudinal axis of the specimens. In the image analysis software (Correlated Solutions Inc., 2009), a virtual extensometer perpendicular to this angle was drawn over the crack location on the image corresponding to the peak load. Data output from the extensometer was then used to determine the crack widths shown in Table 6-5.

In addition, an overall crack angle was determined based on the crack behaviour above the reinforcement level and below the concrete crushing zone. Since only portions of the failure cracks were captured by the majority of the DIC setups, the overall crack angles are best estimates based on the information shown in the photogrammetry images and are with respect to the longitudinal axis of the specimen. The length of the critical diagonal crack (L_c) from mid-span to the location where it crossed the longitudinal reinforcement is also recorded and compared with the effective depth in Table 6-3 and Table 6-4.

The crack angles and widths at the three height locations (0.5*h, 0.75*h and d) on S1000-B2 are not based on the failure crack, but are instead of the second primary crack as detailed in Section 6.2.4. The DIC system was only able to capture a horizontal section of the failure crack as it extended towards the support, but it did capture the behaviour of the second crack. The cracks widths presented for S1000-B2 are expected to be lower than the actual failure crack widths, but they are the best estimates available. The overall failure angle for S1000-B2 is based on the actual failure crack from the photogrammetry images.

Table 6-3: Failure Crack Details for h = 300 mm Specimens

		Failure Crack Angles (°)			Overall Failure Crack		
Specimen	ρ (%)	0.5*h	0.75*h	d	Angle (°)	L_c (mm)	L_c/d
S300-B1	2.61	8	29	45	31	650	2.6
S300-A2	1.51	43	38	10	39	500	2.0
AVG		26	34	28	35	575	2.3
COV		0.97	0.19	0.90	0.16	0.18	0.18

Table 6-4: Failure Crack Details for h = 1000 mm Specimens

		Failure Crack Angles (°)			Overall Failure Crack		
Specimen	ρ (%)	0.5*h	0.75*h	d	Angle (°)	L_c (mm)	L_c/d
S1000-B1	1.03	NA	48	15	45	1500	1.6
S1000-B2	0.83	30[A]	40[A]	24[A]	43	1275	1.4
S1000-A3	0.61	58	54	34	51	1950	2.1
S1000-A4	0.40	23	39	NA	35	2400	2.5
AVG		37	45	24	44	1781	1.9
COV		0.50	0.16	0.39	0.15	0.28	0.26

[A] Based on second primary crack

The results from the h = 300 mm specimens from the current study are comparable to the results found by Shoaib (2012). Two h = 300 mm normal strength SFRC specimens tested by Shoaib (N31 and N32) exhibited an average overall crack angle of 33°. The diagonal shear failure cracks crossed the longitudinal reinforcement at an average distance of 2.3*d from mid-span. Comparing Shoaib's results with those from S300-B1 and S300-A2 in the current study shows a similar average overall crack angle (35°) and the same average distance to the longitudinal reinforcement.

In the h = 1000 mm specimens, the estimated overall crack angles are for the most part, significantly higher than those found by Shoaib (2012) although the crack lengths are similar. Two normal strength h = 1000 mm SFRC specimens with conventional longitudinal reinforcement (N10-1 and N10-2) from Shoaib's study showed an average crack angle of 32.0°, 20% lower than the average 44° found in the current study. The average of the crack length to effective depth ratio (L_c/d) from Shoaib produced a value of 2.2. The average from the four h = 1000 mm specimens in the current study produced a crack length of 1.9*d and a larger variation than found by Shoaib.

The DIC system measured negligible crack widths at the equivalent service load level (i.e. 0.5*P_{peak}) for the three measured crack locations (0.5*h, 0.75*h and d) on all large scale structural specimens. However, manual measurements using a crack comparator gauge of the eventual failure crack were recorded on S1000-B2 at Stage 3 (510 kN), which was considered reasonably close to the equivalent service load of 459 kN. Therefore, these manual measurements were used as the service crack width values (w_s) for S1000-B2. Crack widths at the equivalent service load (w_s) and at the peak load level (w_p) are indicated in Table 6-5 where the distances 0.5*h, 0.75*h and d are measured from the compression face.

Table 6-5: Large Scale Structural Specimen Failure Crack Widths at Service and Peak Loads

		0.5*h		0.75*h		d	
Specimen	ρ (%)	w_s (mm)	w_p (mm)	w_s (mm)	w_p (mm)	w_s (mm)	w_p (mm)
S300-B1	2.61	0.01	2.84	0	1.87	0	1.06
S300-A2	1.51	0	1.11	0.01	1.66	0	1.20
S1000-B1	1.03	0	NA	0	2.32	0	1.75
S1000-B2	0.83	0.15^A	2.79	0.30^A	3.55	0	1.90
S1000-A3	0.61	0.11	2.85	0	3.05	0	3.01
S1000-A4	0.40	0	2.09	0	2.32	0	NA

^{A}As measured by manual measurements

The crack widths exhibited by S1000-A4 were smaller than the other h = 1000 mm specimens, both during testing and at peak load. The overall crack angle was also shallower than the other h = 1000 mm members. This behaviour is consistent with the higher than expected load carrying capacity of S1000-A4 (refer to Section 5.2 for design methodology). Smaller crack widths likely resulted in increased aggregate interlock action compared to S1000-A3 and thus a high shear capacity. Specimen S1000-A3 contained 50% more longitudinal reinforcing steel than S1000-A4, yet only reached a shear capacity less than 2% higher. The reason for the smaller crack widths is unclear;

perhaps S1000-A4 experienced a higher than normal fiber volume or better fiber dispersion compared to the other specimens. A physical analysis of a cross section from S1000-A3 and S1000-A4 might have aided in determining the source of the discrepancy, but could not be completed due to time and laboratory constraints.

Figure 6-27 shows the applied load versus failure crack width growth relationships for S300-B1 at the three crack locations discussed (0.5*h, 0.75*h and d from the compression face). Figure 6-27a shows the crack width growth over the full load history, while Figure 6-27b highlights the same crack growth but only to immediately past the peak loads. It is apparent that the failure crack grew at a small, relatively linear rate until a certain stress level was reached. This data reinforces the negligible widths of the eventual failure cracks measured at the equivalent service load levels (detailed in Table 6-5). Once that particular stress level was reached, the crack growth was rapid until failure. The diagonal crack growth behaviour at all three locations was comparable, although the crack widths increased as mid-height was approached. This behaviour was also typical of S300-A2 which is detailed in Appendix C.

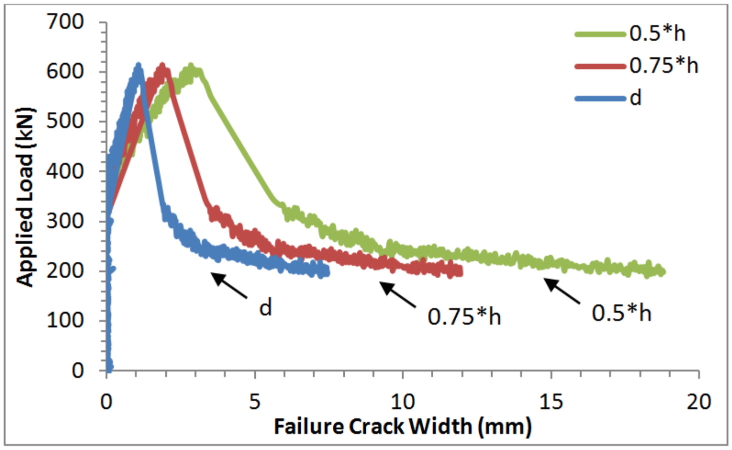

a)

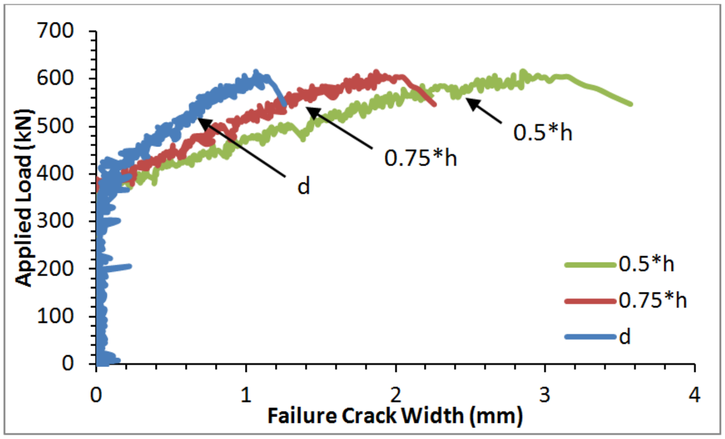

b)

Figure 6-27: Specimen S300-B1 Failure Crack Widths a) Throughout Testing and b) Up to Peak Loads

Figure 6-28 shows the failure crack width growth as the load increased for S1000-A3 at 0.5*h, 0.75*h and d. Similar to the h = 300 mm specimens, the failure crack grew at a small, relatively linear rate until a certain stress level was reached. Once that particular level was reached, the crack growth was rapid until failure. Similar behaviour was observed for all h = 1000 mm specimens, and is detailed in Appendix C.

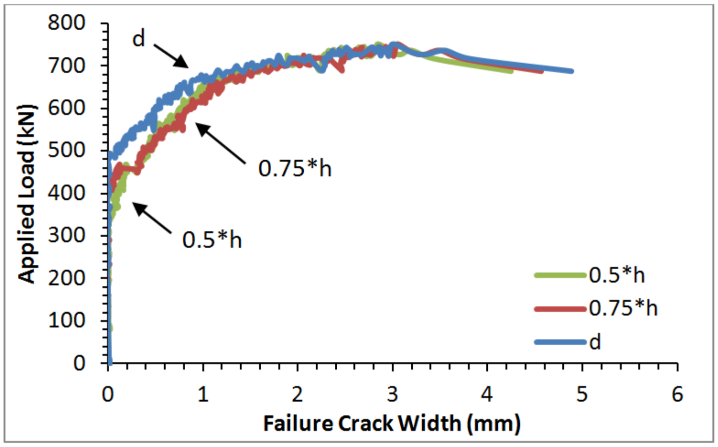

Figure 6-28: Failure Crack Widths Throughout Testing for S1000-A3

Diagonal crack growth data was obtained through the DIC system for all specimens at a distance of 0.75*h from the extreme compression fiber. The crack growth at this location is compared against the applied load for the h = 300 mm specimens in Figure 6-29a. Both specimens exhibit similar behaviours, although the loading on S300-B1 was continued after the initial failure which allowed for increased crack growth. Figure 6-29b compares the same variables for the h = 1000 mm specimens. It is interesting to note that although S1000-A3 and S1000-A4 reached comparable failure loads, the diagonal crack growth in S1000-A3 began much earlier. S1000-A4 appears to have progressed from a negligible crack width immediately into a rapid crack growth.

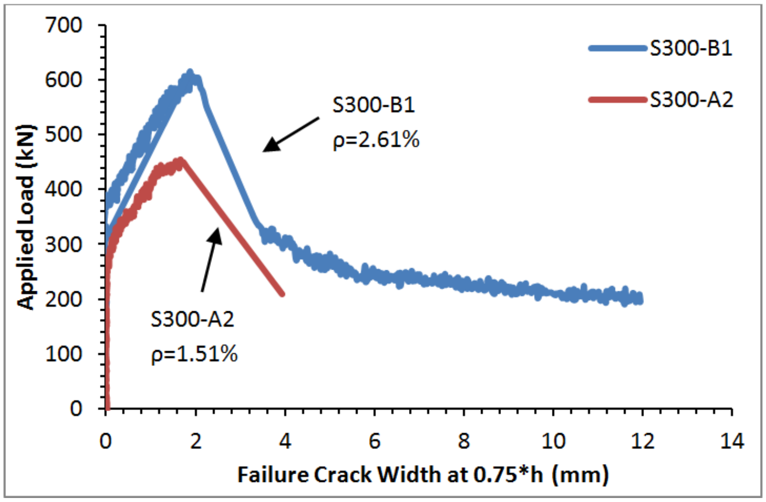

a)

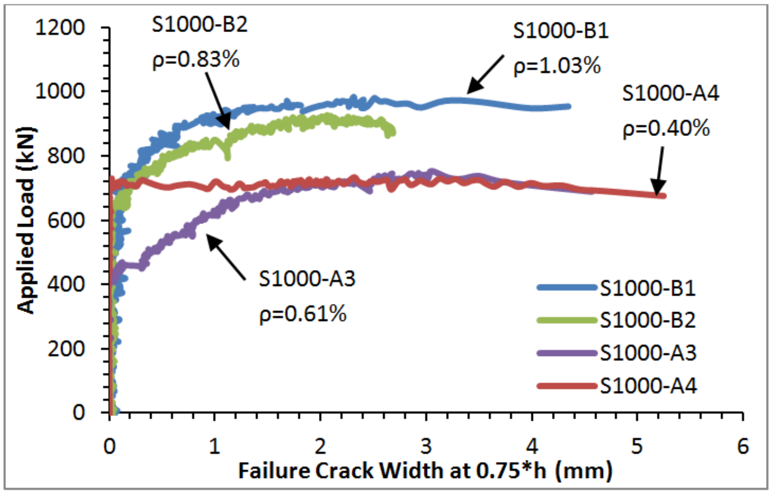

b)

Figure 6-29: Failure Crack Width Growth at 0.75*h for a) h = 300 mm and b) h = 1000 mm Specimens

All the large scale specimens experienced relatively similar failure crack growth behaviour; an initial linear slow growth followed by non-linear behaviour and rapid crack growth. The point at which this crack growth transitioned from linear to non-linear behaviour was determined at the 0.75*h crack location for all specimens. The load at which the non-linear behaviour and rapid crack growth began is defined as P_{NL} and is provided in Table 6-6 as a percentage of the peak load. The load corresponding to the non-linear crack growth in S1000-A4 confirms what was illustrated in Figure 6-29b; rapid crack growth did not being until 96% of the peak load had been reached. This behaviour is vastly different than the other large scale members. The average P_{NL}/P_{peak} ratio for the other members was 55%, indicating that the failure crack growth began to increase just after the equivalent service load was reached.

Table 6-6: Large Scale Structural Specimen Loads Corresponding to Non-Linear and Rapid Failure Crack Growth

Specimen	ρ (%)	P_{NL}/P_{peak} (%)
S300-B1	2.61	58
S300-A2	1.51	49
S1000-B1	1.03	51
S1000-B2	0.83	61
S1000-A3	0.61	54
S1000-A4	0.40	96

Prior to 1999, the ACI design code limited the allowable crack width at service loads for plain concrete members to 0.4 mm (ACI 318-08). In ACI 318-08 and CSA A23.3-04, the maximum crack widths are not explicitly defined but rather a maximum reinforcement spacing and minimum area requirements are used to indirectly achieve adequate crack control. CSA S6-06, the Canadian Highway Bridge Design Code, provides maximum crack widths allowed on plain concrete structures under various types of exposures at the serviceability limit states. For non-prestressed members, the most stringent case of 0.25 mm at the service load level is considered when the member is exposed to de-icing chemicals or salts. For comparison, the loads at which the eventual failure crack in the specimens from the current study were observed to reach crack widths of 0.25 mm were determined through use of the DIC system. These loads are expressed as a percentage of the specimen's peak load in Table 6-7 and Table 6-8. The results for S1000-B2 are based on the second primary crack as DIC data for the actual failure crack is unavailable. As detailed in Section 6.1, the equivalent service state in the current study was determined to be 50% of the peak load. The overall average, based on all three height locations, was at a load of approximately 73% of the peak load for the h = 300 mm specimens. For the h = 1000 mm specimens, the overall average was at approximately 79% of the peak load. Therefore, since the eventual failure crack in all the specimens reached a 0.25 mm crack width at a load larger than 50% of the peak load, the CSA S6-06 cracking control requirements are satisfied.

Table 6-7: Percentage of Peak Load at a Crack Width of 0.25 mm for h = 300 mm Specimens

Specimen	ρ (%)	% of Peak Load at a Crack Width of 0.25 mm		
		0.5*h	0.75*h	d
S300-B1	2.61	64	68	73
S300-A2	1.51	79	74	79
AVG		72	71	76
COV		0.15	0.06	0.06

Table 6-8: Percentage of Peak Load at a Crack Width of 0.25 mm for h = 1000 mm Specimens

Specimen	ρ (%)	% of Peak Load at a Crack Width of 0.25 mm		
		0.5*h	0.75*h	d
S1000-B1	1.03	NA	78	87
S1000-B2	0.83	87^A	64^A	80^A
S1000-A3	0.61	62	62	73
S1000-A4	0.40	98	98	NA
AVG		82	76	80
COV		0.22	0.22	0.09

^{A}Based on second primary crack

The crack widths in the reinforcement region of flexural members are directly related to the strain in the longitudinal reinforcement (e.g. Collins et al., 1996; Vecchio & Collins, 1986), and thus to the reinforcement ratio. As the specimen bends in flexure, the strain in the tension region increases and causes cracks to form. Figure 6-30 illustrates the relationship between the reinforcement ratio and the peak load failure crack width at the reinforcement level (effective depth d) for both specimen sizes. S1000-A4 was excluded since DIC data was not available at the reinforcement level. As expected, the crack widths are smaller on the h = 300 mm specimens than on the h = 1000 mm specimens.

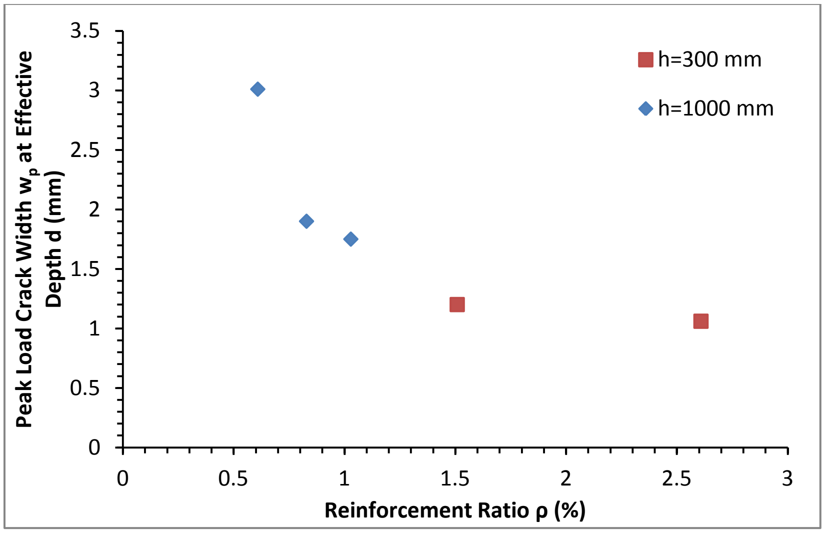

Figure 6-30: Relationship Between Peak Load Crack Width at Effective Depth d and Reinforcement Ratio

Crack widths above the tension reinforcement are related to the distance between the neutral axis and reinforcement – as this distance increases, the average spacing between shear cracks increases in plain concrete without fibers (Collins & Kuchma, 1999). According to Bischoff (2003) and Vecchio & Collins (1986), the crack widths are directly related to the crack spacing. Even in the presence of a moderate volume fraction of fibers, it is expected that the h = 300 mm specimens would experience smaller crack widths above the tension reinforcement than the larger specimens. Specimen S300-B1 proves to be an exception to this case, with a mid-height crack width on par or larger than that of the h = 1000 mm specimens at the peak load (see Table 6-5).

The distance to the neutral axis from the compression face (c) at the peak load was determined in each specimen using the mid-span longitudinal reinforcement strain as recorded by the electrical resistance strain gauges (and for S1000-A4 as predicted in Section 6.5), the concrete strain as measured by the top PI gauge and the plane sections remain plane theorem. In the h = 300 mm specimens, the distance to the neutral axis was determined as c = 70 and 95 mm for S300-B1 and S300-A2 respectively. The distance to the neutral axis in the h = 1000 mm specimens ranged between c = 325 and 495 mm. Therefore, the crack widths measured at mid-height (0.5*h) in the h = 300 mm specimens should be larger than at a distance of 0.75*h from the compression face since the lower location is still in the proximity of the longitudinal reinforcement. While S300-B1 follows this hypothesis, S300-A2 shows a larger crack width at the lower location. The crack widths measured in the h = 1000 mm specimens should be larger at 0.75*h than at 0.5*h and is confirmed by the measured results reported in Table 6-5.

6.5 Longitudinal Reinforcement Strains

Localized reinforcement strains were recorded through use of 5 mm electrical resistance strain gauges applied on the surface of the longitudinal reinforcement. The strains recorded would have been influenced by whether cracks were present at the strain gauge location, and also by the amount of fibers bridging those cracks. If cracks were present, the localized reinforcement strain would increase due to the lack of local tension stiffening in the concrete (Vecchio & Collins, 1986). However, the presence of fibers bridging the cracks would contribute a moderate amount of tension stiffening (e.g. Dinh et al., 2011; Bischoff, 2007).

A PI gauge was mounted on the south face of each specimen at the reinforcement level (specifically at the effective depth d from the top for specimens with two layers of reinforcement as detailed in Section 5.6.1). Over a gauge length of 100 mm, the PI gauge recorded the average surface strains throughout each test. If cracks were present within the recorded length, the influence of the crack width would be smeared over the average rebar strain for the entire gauge length. If no cracks were present, the recorded strains could be lower than adjacent areas with significant cracking.

The DIC system could also be used to extract surface strains at the reinforcement level. Extracting a single point would lead to the same potential complications as the strain gauges, while taking the average over a predetermined length would yield similar results to the PI gauge.

For the purpose of simplicity and for direct comparison with strains experienced along the length of the longitudinal reinforcement, the values recorded by the strain gauges are used in this section.

Although strain gauges were placed at the locations detailed in Section 5.6 (strain gauges adjacent to the supports were only installed on S1000-A3 and S1000-A4) and often in pairs on adjacent reinforcement bars, in some cases one or more strain gauges either debonded from the reinforcement prior to or during testing or failed to work entirely. Further details are provided for individual specimens in Appendix C.

Specimen S1000-A4 was designed to reach a peak load mid-span reinforcement stress above the ACI ITG-6R-10 Simplified flexural design limit of 690 MPa. Two strain gauges were placed at mid-span on adjacent reinforcing bars. One of the gauges was not reading correctly prior to testing and thus was not recorded. The second strain gauge at mid-span reached a strain of 0.00430 mm/mm at an applied load of approximately 600 kN before gradually becoming un-bonded prior to reaching the specimen peak load of 729 kN. A strain gauge at d from the face of the loading plate in the west shear span recorded a strain of 0.00571 mm/mm at the peak load, while a strain gauge at the same location in the east shear span recorded a strain of 0.00449 mm/mm. These strains correspond to stresses of 781 MPa and 707 MPa respectively, according to Equation 2-1. The mid-span reinforcement strain at the peak load for Specimen S1000-A4 was therefore taken from the DIC system. A horizontal strain of 0.00715 mm/mm was recorded through System 1, which corresponds to a stress of 843 MPa according to Equation 2-1.

The mid-span reinforcement strains, as recorded by the electrical resistance strain gauges, are provided in Table 6-9 for all six structural specimens at both the peak load and at the equivalent service load. The corresponding stresses have also been noted, based on the ACI ITG-6R-10 non-linear stress-strain relationship for the steel reinforcement (Equation 2-1).

To provide adequate crack control in members with high strength reinforcement, ACI ITG-6R-10 recommends maintaining a steel stress less than 460 MPa at the service load level. At the equivalent service load level in S300-B1 of 303 kN, the maximum reinforcement strain (as measured by the strain gauges) was 0.00220 mm/mm which corresponds to a stress of 440 MPa (Equation 2-1). As this value is below the recommended limit, and as S300-B1 experienced the largest reinforcement strains out of all specimens at the service level, this indicates that the six specimens in this study satisfied the ACI ITG-6R-10 recommended stress level to ensure adequate crack control.

Table 6-9: Large Scale Structural Specimen Mid-Span Reinforcement Strains Recorded at Peak and Service Loads

		Peak Load		Service Load	
Specimen	ρ (%)	Strain (mm/mm)	Stress (MPa)	Strain (mm/mm)	Stress (MPa)
S300-B1	2.61	0.00342	614	0.00220	440
S300-A2	1.51	0.00307	574	0.00145	290
S1000-B1	1.03	0.00355	627	0.00131	262
S1000-B2	0.83	0.00356	628	0.00145	290
S1000-A3	0.61	0.00360	632	0.00116	232
S1000-A4	0.40	0.00715*	843	0.00201	402

*From DIC System

Figure 6-31 describes the longitudinal reinforcement strains along the length of S1000-A4, as measured by the strain gauges at the load stages indicated in the graph. The distances correspond to the locations shown previously in Figure 5-2. As stated above, the mid-span gauge failed before reaching the 700 kN load level. The strain response of the longitudinal reinforcement is similar in the remaining large scale structural specimens and is detailed individually in Appendix C.

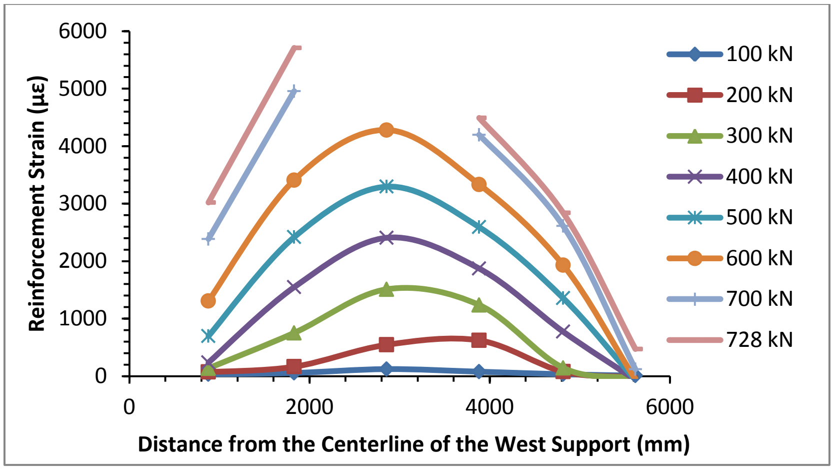

Figure 6-31: Longitudinal Reinforcement Strains Along Length of S1000-A4

It was established in Section 6.4 that the crack widths at the reinforcement level are related to the strain in the longitudinal reinforcement. Figure 6-32 demonstrates the relationship between the diagonal shear critical crack width and the reinforcement strain at peak load for the h = 300 mm and h = 1000 mm specimens. The crack width was taken at the effective depth (distance d in Table 6-5). The length of the critical failure crack was determined in Table 6-3 and Table 6-4 to be an average of 2.3*d for the h = 300 mm specimens and 1.9*d for the h = 1000 mm specimens. Therefore, the electrical resistance strain gauges located on the reinforcing steel at a distance of 2*d from the face of the loading plate (see Figure 5-2 for a visual description of the location) in the shear span that experienced the failure crack provided the most representative strain values. These values are shown in the figures below. The results for S1000-A4 were not included since the DIC system did not capture the failure crack behaviour at the reinforcement level. The critical crack width at the reinforcement level is observed to increase with the reinforcement strain.

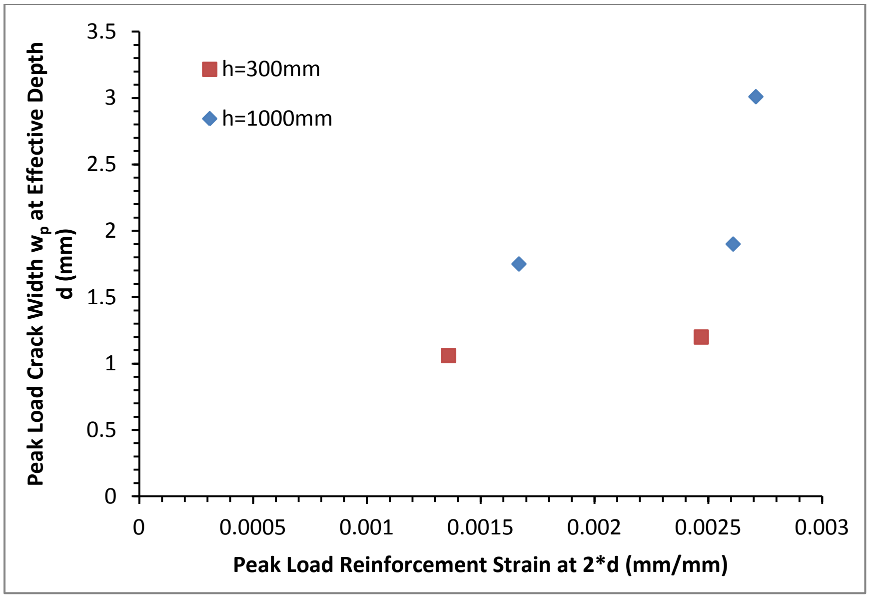

Figure 6-32: Relationship Between Peak Load Crack Widths and Longitudinal Reinforcement Strain

6.6 Shear Capacity Trends

Due to the use of multiple member dimensions in the current study, the shear behaviour of the large scale structural specimens was normalized to allow for direct comparison. The peak load (including the 0.47 kN from the loading plate and W250 stub column spacer) was converted into an equivalent shear stress over the specimen cross-section, using the actual specimen width and design effective depth. Further, the shear stress was also normalized by the square root of the concrete compressive strength, based on the average of the specimen companion cylinders (refer to Table 6-1). This normalized shear stress σ_N is given by:

$$\sigma_N = \frac{P_{peak}}{2b_w d\sqrt{f_c'}} \qquad 6\text{-}1$$

Figure 6-33 compares the normalized shear stress for the specimens with their associated reinforcement ratio. Figure 6-33a shows the h = 1000 mm results while Figure 6-33b combines both sizes. The normalized shear stress at failure is observed to increase with an increase in the reinforcement ratio. The relationship appears to be relatively linear.

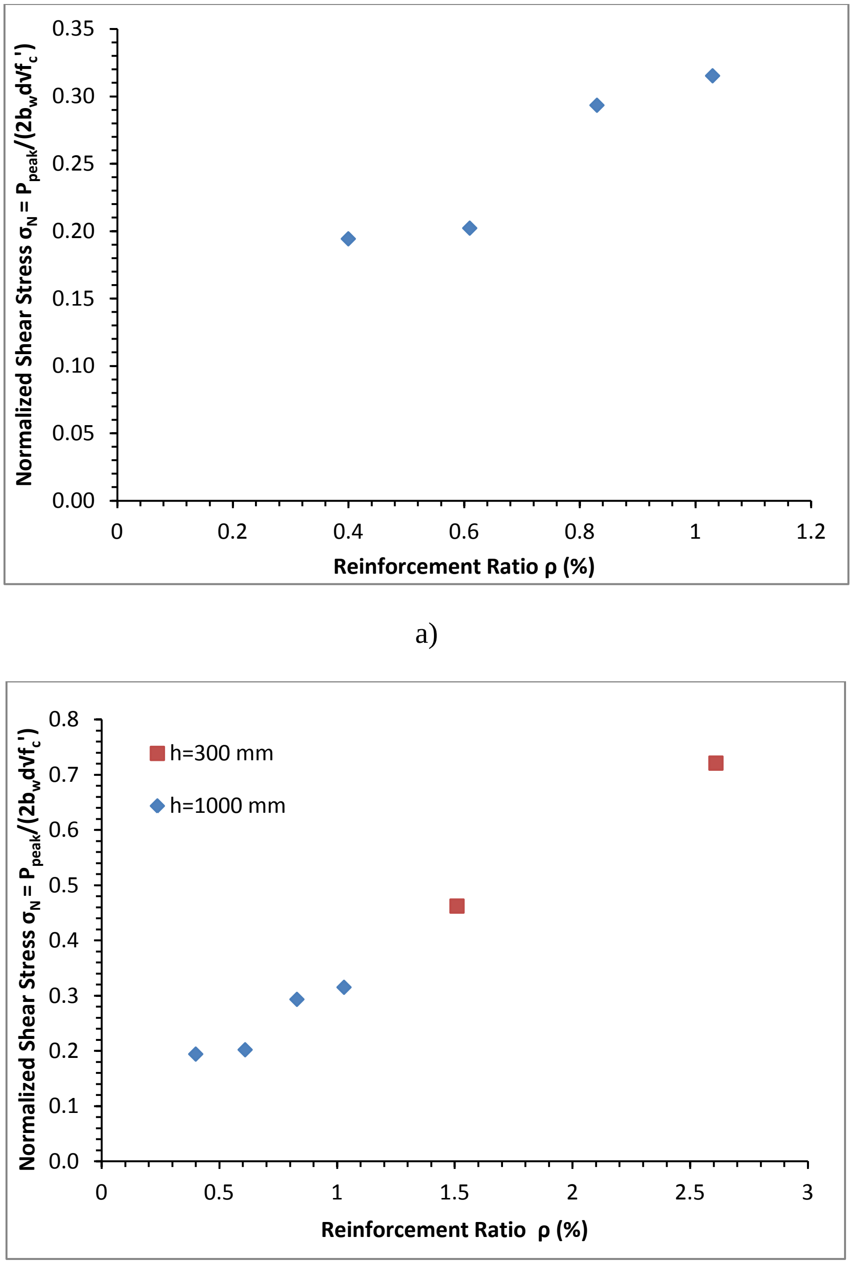

a)

b)

Figure 6-33: Relationship Between Normalized Shear Stresses and Reinforcement Ratios for a) h = 1000 mm Specimens and b) All Specimens

Figure 6-34a illustrates the normalized shear stress for each specimen compared to the measured mid-span steel reinforcement strain at peak load. The measured reinforcement strains were very similar at mid-span in all of the specimens except S1000-A4, which experienced a strain larger than the ACI ITG-6R-10 proportional limit of 0.00427 mm/mm (refer to Table 6-9). These strain values make it difficult to observe a relationship between the normalized shear stress and mid-span reinforcement strain. Figure 6-34b plots the same parameters, but with the measured reinforcement strain located at 2*d from the face of the loading plate in the shear span that experienced the diagonal failure crack. As discussed in Section 6.4, the reinforcement strain is related to the crack widths at the reinforcement level, which in turn influences the shear capacity of a member. In Figure 6-34b, the normalized shear stress is generally observed to decrease with an increase in reinforcement strain, although this relationship is more apparent in the h = 300 mm specimens than the h = 1000 mm specimens.

These relationships (Figure 6-33 and Figure 6-34) provide an indication of the strain effect on the shear strength of SFRC – as the reinforcement ratio increases, the reinforcement strain generally decreases and the shear stress at failure increases. As discussed later in this section, the difference in normalized shear capacity for specimens with similar reinforcement strains in due in part to a size effect on the shear strength of the SFRC.

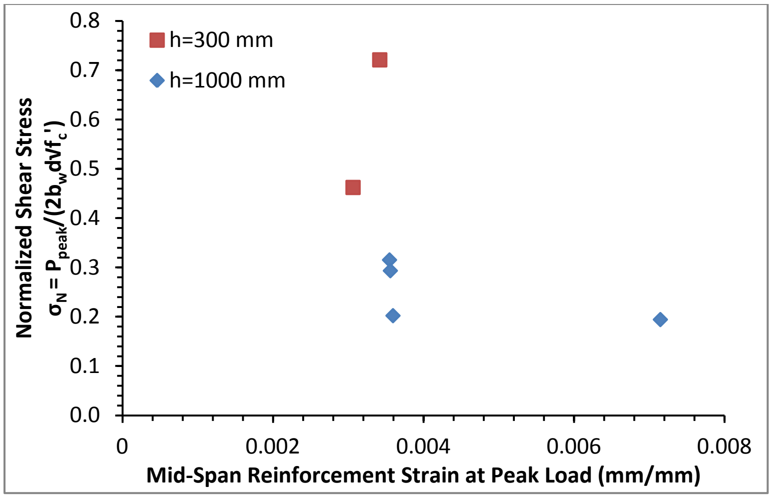

a)

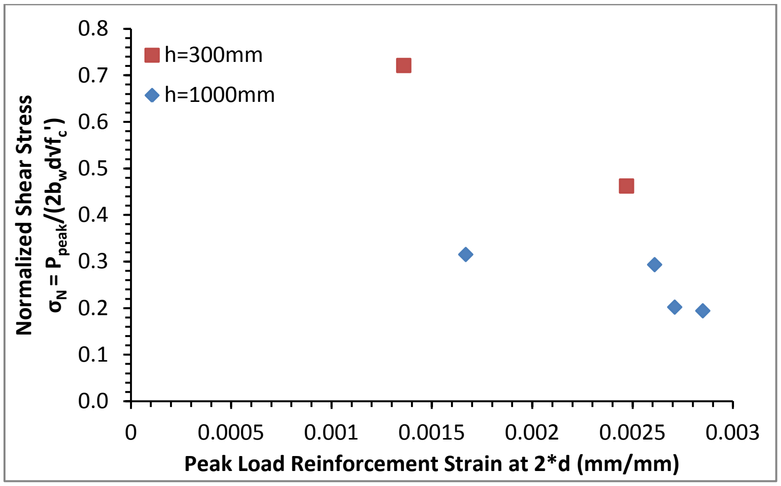

b)

Figure 6-34: Relationship Between Normalized Shear Stress and a) Peak Load Reinforcement Strain at Mid-Span and b) Peak Load Reinforcement Strain at 2*d

The size effect on the shear strength of SFRC can be observed by comparing the normalized shear stresses with the specimen effective depths. Figure 6-35 provides an indication of the size effect in shear when both the h = 300 mm and h = 1000 mm specimens are compared. As noted above, the difference in normalized shear capacity for specimens with similar effective depths is due in part to the strain effect on the shear strength of the SFRC (refer to Figure 6-33 and Figure 6-34).

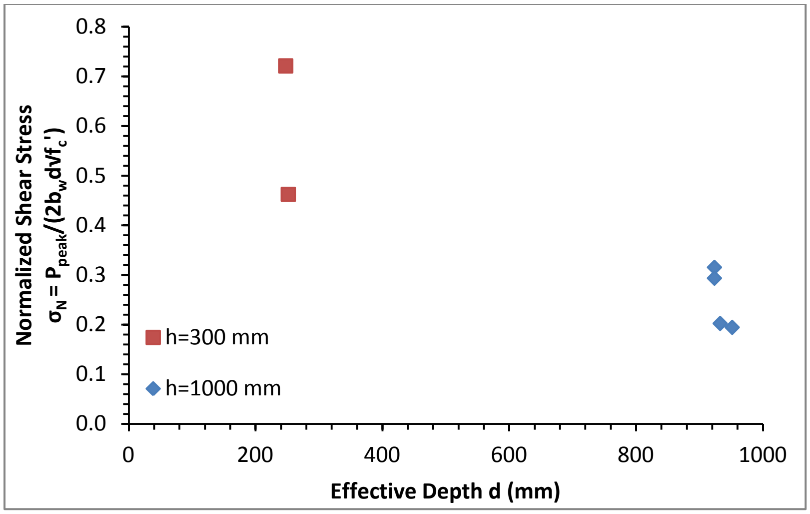

Figure 6-35: Relationship Between Normalized Shear Stresses and Effective Depth

As detailed in Section 2.3.1, Dinh (2009) found the size effect in shear from h = 457 and 686 mm SFRC beams to be negligible. Minelli & Plizzari (2010) and Shoaib et al. (2010) however found a strong correlation between the normalized shear stress at failure and the effective depth in tests of SFRC specimens with nominal overall heights between 300 mm and 1500 mm. For comparison with the specimens in the current study, four of the beams from Dinh and three from Minelli & Plizzari containing V_f = 1.0%, along with four from Shoaib et al. that failed in shear are plotted in Figure 6-36 alongside the h = 300 and 1000 mm specimens from the current study. The strain effect on the shear strength has not been accounted for in Figure 6-36, contributing to the strength differences observed between members with similar effective depths. A visible size effect on the shear strength is observed and is consistent with the trend of the new data developed in this study.

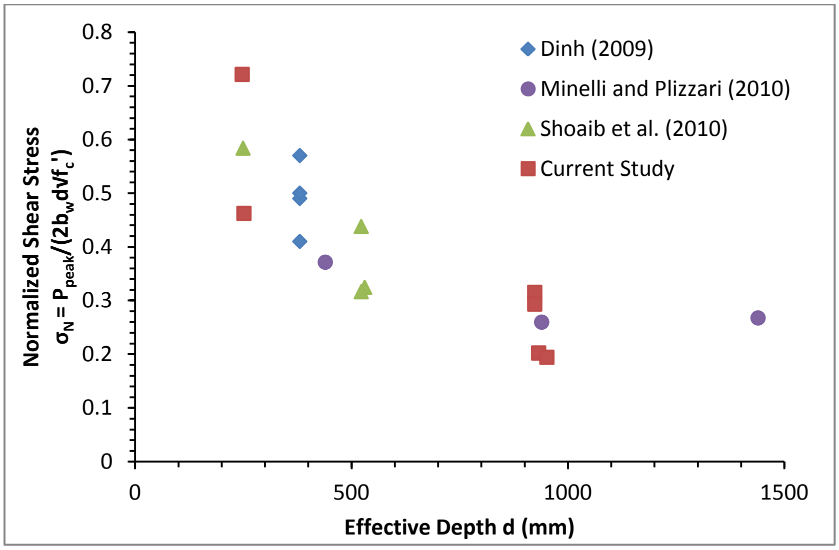

Figure 6-36: Size Effect in Shear Comparison between Various Researchers

6.7 Summary

All six large scale structural specimens examined in the current study failed in shear, although the exact mechanisms leading up to failure differed in all cases. The failure mechanisms were classified similar to the method from ASCE-ACI 426 (1973) and Dinh (2009) and took into consideration the presence or absence of concrete crushing, splitting cracks along the longitudinal reinforcement, rotation or shifting of the member and the origin of the failure crack. Two specimens failed from each of the following mechanisms; a combination of diagonal-tension and shear-tension (S1000-B1 and S1000-A3), a combination of shear-compression and shear-tension (S300-A2 and S1000-B2) and diagonal tension (S300-B1 and S1000-A4).

The key findings found through analysis of the six large scale structural specimens were:

- The mid-span service deflections experienced by all six large scale structural specimens satisfied the span/480 deflection control criteria from ACI 318-08 and CSA A23.3-04 for plain concrete members.
- The average diagonal shear failure crack length, as measured from mid-span, was 2.3*d with an average overall crack angle of 35° for the h = 300 mm specimens.
- The average diagonal shear failure crack length, as measured from mid-span, was 1.9*d with an average overall crack angle of 44° for the h = 1000 mm specimens.
- All six specimens exhibited a failure crack width of 0.25 mm at loads between 71% and 82% of the peak load, satisfying the CSA S6-06 crack width control requirements for plain concrete members.
- The peak load failure crack width at the level of the longitudinal reinforcement was observed to increase with an increase in the reinforcement ratio.
- ACI ITG-6R-10 recommends a maximum reinforcement stress of 460 MPa at the service condition for crack control purposes. The stress at the service load level found in the specimen with the largest reinforcement strains (S300-B1) was approximately 440 MPa, indicating that all six specimens satisfied this condition.
- The normalized shear stress at failure indicated a strain effect when the peak load reinforcement strain at 2*d from the face of the loading plate was compared. As the reinforcement strain increased, the shear stress at failure decreased. This trend was more evident in the h = 300 mm specimens than the h = 1000 mm specimens.
- The normalized shear stress at failure indicated a size effect. As the effective depth of the members increased, the shear stress at failure decreased.

7 Analytical Predictions

The accuracy of accepted design methods for plain concrete members to predict the behaviour of steel fiber reinforced concrete (SFRC) members was examined. Predictions for shear and flexural capacity, along with expected deflections at the equivalent service load level, were compared to the data obtained through the current study. A shear capacity model for SFRC developed by Dinh (2011) was also examined. Detailed descriptions of each design method are provided in Section 2.3.

Although the longitudinal reinforcement strains and the stress-strain response of steel coupons were measured during the overall test program, these values were not used in the predictions since they are not available in a typical design situation. The ACI ITG-6R-10 stress-strain model, although slightly different than the tension coupon results obtained in this study (refer to Figure 5-6), was used as a representative relationship and member strain information used in some of the models are calculated values according to the model.

All resistance factors were set to a value of 1.0 for prediction purposes.

7.1.1 Shear Capacity Predictions

The methods described in Section 2.4.1 were used to predict the shear capacity of the large scale structural specimens reported in Chapter 6. The resulting predicted shear capacities are detailed in Table 7-1. Equation 2-2 was used for the ACI 318-08 predictions of shear capacity; the specimens in the current study contained no transverse reinforcement and were classified as slabs for the purpose of the ACI 318-08 shear capacity distinction (refer to Section 2.4.1.2). Equation 2-4 provided the CSA A23.3-04 prediction with the maximum value of ε_x calculated by Equation 2-5 to be 0.00249 mm/mm in S1000-A4, below the 0.003 mm/mm limit in Equation 2-5. The non-linear behaviour of the ASTM A1035 steel reinforcement was not accounted for in either the ACI 318-08 or CSA A23.3-04 models.

The Hoult et al. (2008) shear model (Equation 2-7) assumes a bi-linear stress-strain relationship for the reinforcing steel but uses a so-called second order approximation for the strain influence captured by parameter ε_x. Similar to the ACI 318-08 and CSA A23.3-04 models, the actual non-linear behaviour of the ASTM A1035 steel reinforcement used in the current study is not accounted for in the Hoult model.

Two shear prediction models for plain reinforced concrete without fibers that directly considered the non-linear stress-strain response of the steel were examined. Both models were developed by Desalegne & Lubell (2010). In the first model, termed the Desalegne and Lubell General model, the stress in the longitudinal reinforcement at the critical section for shear was first determined by Equation 2-8, before being converted into a strain (ε_s) using the ACI ITG-6R-10 idealized stress-strain response (Equation 2-1). The steel reinforcement strain was subsequently divided in half to represent the axial strain parameter (ε_x). This modified axial strain was then used in combination with the Hoult et al. (2008) shear model shown in Equation 2-7. The second prediction method, termed the Desalegne and Lubell Simplified model, uses an assumed ε_x value of 0.00213 mm/mm and was proposed as a lower bound prediction, practical for design purposes when the design yield stress was limited to 690 MPa (Equation 2-9). The Desalegne and Lubell General model has been validated for ε_x values up to 0.006 mm/mm; the maximum ε_x calculated in the specimens from the current study was 0.0076 mm/mm in S1000-A4 and 0.0041 mm/mm in S1000-A3. This indicates that S1000-A4 is beyond the previously validated range of the Desalegne and Lubell General shear model and exceeds the ε_x assumed in the Desalegne and Lubell Simplified model.

The Dinh et al. (2011) model was examined in order to provide a shear capacity prediction for SFRC that accounts for the effect from the fibers. The average equivalent tensile stress (σ_{ru}) was calculated based on Equation 2-16 and the 150 x 150 x 450 mm ASTM C1609-10 large scale companion prism results described in Section 4.2 from Castings A and B. At a mid-span vertical deflection equal to $L_f/24$ = 1.25 mm, the σ_{ru} was determined to be 1.90 MPa and 1.63 MPa from Casting A and Casting B respectively. The shear contribution from the concrete in the flexural compression region (Equation 2-12) was determined based on the assumption of yielding of the longitudinal reinforcement using the ACI 318-08 limit of f_y = 550 MPa. In S300-B1, the area of longitudinal reinforcement was limited to ρ = 2.0% as per the recommendation in Dinh (2009). The shear contribution from the steel fibers was estimated based on the diagonal crack angle of 45° specified in the model.

The peak shear load for each specimen is compared with the predicted shear capacity based on the methods described above. The average ratios of the peak shear load to the predicted shear capacity (V_{test}/V_{model}) in the shear models for plain concrete in Table 7-1 provide an indication of the fiber contribution to the shear capacity. A critical location at a distance of d from the face of the loading plate was chosen for the strength models to provide a level of consistency with all prediction models. V_{test} is defined as $0.5*P_{peak}$ in the current study, based on a simply supported three point bending configuration. Table 7-1 summarizes these results.

Table 7-1: Shear Capacity Prediction Summary

		Ratio of Peak Shear Load to Predicted Shear Capacity (V_{test}/V_{model})					
		Linear Stress-Strain			Non-Linear Stress-Strain		SFRC
Specimen	ρ (%)	ACI 318-08	CSA A23.3-04	Hoult et al.	D and L General	D and L Simplified	Dinh et al.
S300-B1	2.61	4.24	5.26	4.40	4.40	7.12	1.91
S300-A2	1.51	2.72	3.91	3.12	3.20	4.59	1.37
S1000-B1	1.03	1.85	4.04	3.27	3.31	6.02	1.03
S1000-B2	0.83	1.73	4.21	3.28	3.49	5.60	1.01
S1000-A3	0.61	1.19	3.07	2.35	2.58	3.89	0.74
S1000-A4	0.40	1.14	4.00	2.79	5.28	3.78	0.74
AVG		2.15	4.08	3.20	3.71	5.17	1.13
COV		0.55	0.17	0.21	0.26	0.25	0.40

The first five shear models examined were developed for plain concrete members without fibers. Out of these five, the ACI 318-08 model exhibited the lowest V_{test}/V_{model} ratios for both specimen sizes but also the largest coefficient of variation. Considering that the model does not account for the size and strain effects on shear in plain reinforced concrete without fibers, this method is not considered representative of the actual shear behaviour and is likely the reason the ACI 318-08 predictions are much closer for the h = 1000 mm specimens than the h = 300 mm specimens. It is also interesting to note that although the SFRC did not satisfy the ACI 318-08 residual strength requirements for the use of steel fibers as a method of shear resistance (refer to Section 4.2.4), the shear capacity of the h = 300 mm specimens was between 2.7 and 4.2 times the ACI 318-08 prediction for shear capacity based on plain concrete. The h = 1000 mm specimens exceeded the height limit in ACI 318-08 for SFRC members in addition to the residual strength inadequacies. The shear capacity in S1000-B1 and S1000-B2 was between 1.7 and 1.8 times larger than the ACI 318-08 prediction.

The Hoult et al. model provided an average V_{test}/V_{model} ratio of 3.20 and a COV of 0.21. The CSA A23.3-04 model produced an average V_{test}/V_{model} ratio of 4.08 and a COV of 0.17, the lowest out of all the models examined. The low COV values of the Hoult et al. and CSA A23.3-04 models indicate their ability to account for the size and strain effects on the shear strength of a member. It is important to note however that the majority of the peak load reinforcement strains experienced by the specimens in the current study were very close to the initial linear portion of the steel stress-strain relationship (refer to Figure 5-6). While the Hoult et al. model accounts for the higher reinforcement strains associated with high strength steel, use of this model with specimens that exhibit higher levels of non-linear reinforcement behaviour may result in a larger V_{test}/V_{model} ratio and/or a larger COV.

The lower bound Simplified model suggested by Desalegne and Lubell was the most conservative with an average V_{test}/V_{model} ratio of 5.17. The Desalegne and Lubell General model, with the non-linear stress-strain reinforcement relationship, was more effective at considering the size and strain effects in the shear capacity of the member. The average shear capacity was 3.71 times larger than the shear capacity prediction using this method but ranged between 2.58 and 5.28.

The Dinh et al. model for shear in SFRC produced the lowest V_{test}/V_{model} ratio out of all the shear models examined with an average ratio of 1.13. This ratio was considerably lower than the plain concrete model predictions. The COV however was more than double that of the CSA A23.3-04 shear model, likely due to the lack of consideration of the size effects and an increase in the strain effects from the non-linear behaviour of the longitudinal reinforcement. The Dinh model was un-conservative in the h = 1000 mm specimens with the smallest reinforcement ratios (S1000-A3 and S1000-A4) but produced conservative predictions for the h = 300 mm specimens. The predictions for S1000-B1 and S1000-B2 were within 3% of the test capacity.

In general, all the methods considered provided better predictions of shear capacity for specimens with lower reinforcement ratios as observed in Figure 7-1 and Figure 7-2. The exception was the Dinh model which produced un-conservative predictions for large members with small reinforcement ratios. Figure 7-3 illustrates the V_{test}/V_{model} ratio compared with the effective depth of each specimen.

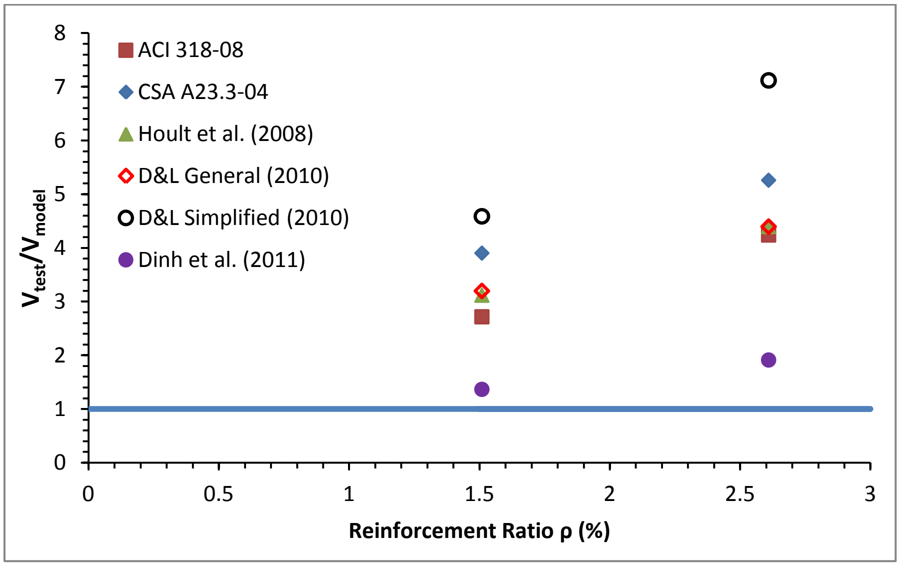

Figure 7-1: Relationship between Shear Capacity Predictions for h = 300 mm Specimens and Reinforcement Ratio

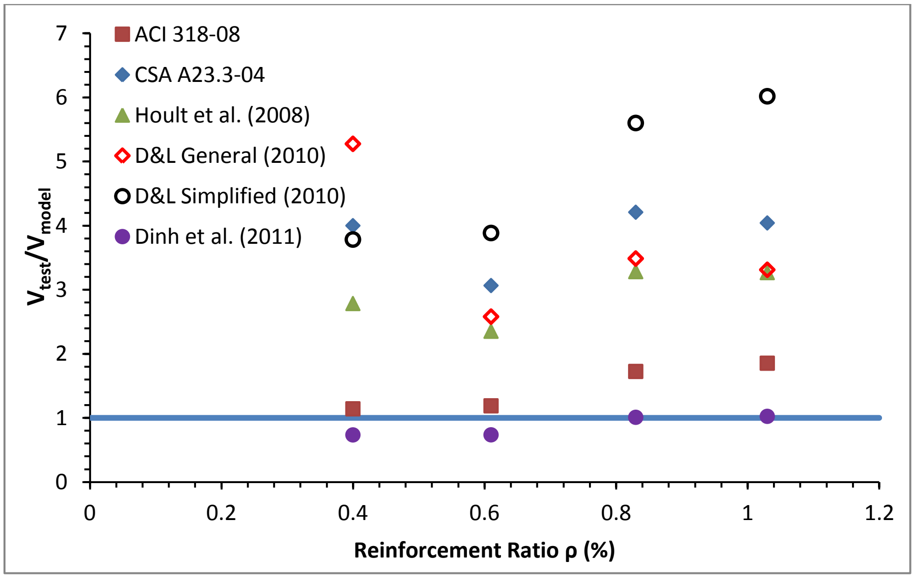

Figure 7-2: Relationship between Shear Capacity Predictions for h = 1000 mm Specimens and Reinforcement Ratio

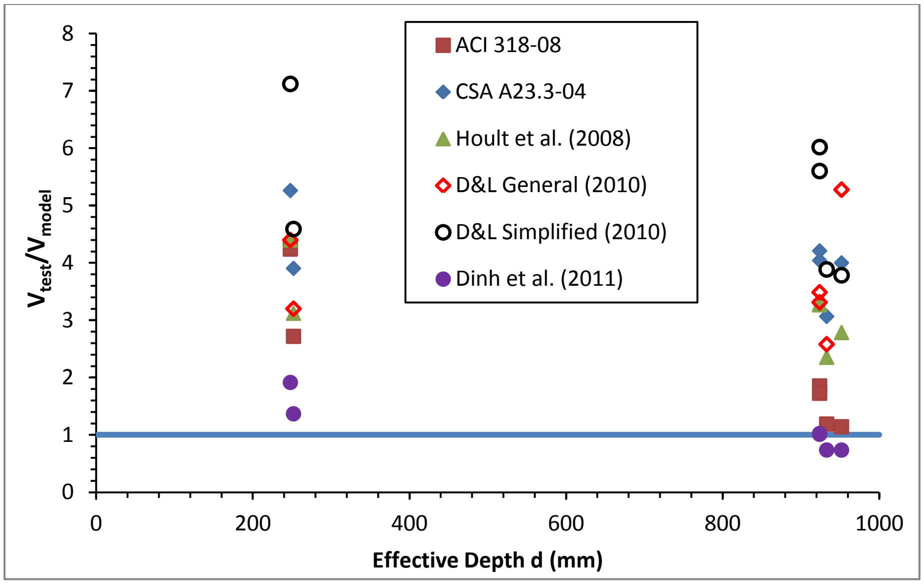

Figure 7-3: Relationship between Shear Capacity Predictions and Effective Depth

7.1.2 Flexural Capacity Predictions

Similar to the shear capacity predictions in Section 7.1.1, flexural capacity predictions were obtained based on models for plain concrete without fibers that used either linear or non-linear stress-strain relationships for the reinforcement. The CSA A23.3-04, ACI 318-08 and ACI ITG-6R-10 flexural models were examined and previously detailed in Section 2.4.2.

The flexural capacity predictions based on the CSA A23.3-04 model were calculated after setting all resistance factors to 1.0 while predictions based on the ACI 318-08 or ACI ITG-6R-10 models represent the nominal flexural capacity predictions. For each prediction method, the members were also classified into their respective categories for failure mode – ie. over-reinforced, tension-controlled, etc (refer to Section 2.4.2). The classifications are based on the assumption that the strain limits between failure types are the same for SFRC as they are for plain concrete members.

The ACI 318-08 predicted flexural capacities were based on the method described in Section 2.4.2.2 using the equivalent concrete stress of $0.85*f_c$', a maximum strain in the extreme compression fiber of 0.003 mm/mm and a yield plateau at the maximum yield strength of 550 MPa. The calculated strain in the longitudinal reinforcement was found to be greater than the strain corresponding to the design yield strength limit of 550 MPa in all cases except for S300-B1, where the calculated reinforcement stress reached 471 MPa. All specimens were classified as tension-controlled members, save for S300-B1 which fell into the transition zone between tension and compression controlled.

The flexural capacity predictions of the specimens based on CSA A23.3-04 provisions for plain concrete were determined using a maximum strain in the extreme compression fiber of 0.0035 mm/mm as described in Section 2.4.2.3. The tensile resistance contributions from the concrete and the steel fibers were ignored. The calculated strain in the longitudinal reinforcement was found to be greater than the strain corresponding to the maximum permissible design yield strength of 500 MPa in all cases except for S300-B1, where the calculated reinforcement stress reached 499 MPa. Thus, all the specimens were categorized as under-reinforced with this approach, except for S300-B1 which fell, albeit marginally, into the over-reinforced category.

The Simplified flexural design method suggested by ACI ITG-6R-10 was also used to predict the flexural capacity of the specimens (refer to Section 2.4.2.4). The design method is similar to that of ACI 318-08 with a bi-linear reinforcement stress-strain relationship and a maximum design yield stress of 690 MPa. All specimens had calculated stresses exceeding the design yield stress, apart from S300-B1 which reached 471 MPa. Due to the increase in tension and compression controlled strain limits for members reinforced with ASTM A1035 reinforcement, S1000-B1, S1000-B2 and S300-A2 were demoted from tension controlled members down into the transition zone between tension and compression controlled. Specimens S1000-A3 and S1000-A4 maintained their tension controlled classification while S300-B1 was re-classified from the transition zone to a compression controlled member. Both S1000-A3 and S1000-A4 experienced reinforcement strains greater than the 0.015 mm/mm recommended limit for deflection control.

Finally, the ACI ITG-6R-10 Appendix B non-linear stress-strain relationship for ASTM A1035 Grade 690 reinforcement (Equation 2-1) was used in combination with the ACI 318-08 flexural model (refer to Section 2.4.2.4). As a result of the changes in the tension and compression controlled strain limits for this model, S1000-B2 was changed to a tension controlled member and S1000-A4 was the only specimen with a calculated reinforcement strain over the 0.015 mm/mm recommended limit.

The predicted nominal moment capacity of the members increased with each increase in design yield stress. The CSA A23.3-04 predicted capacities were generally the lowest, and the values based on the non-linear stress-strain relationship from ACI ITG-6R-10 Appendix B were the highest. The exception was S300-B1, which was unable to reach a calculated reinforcement stress higher than 499 MPa and thus showed similar predicted capacities for all flexural models examined.

The predicted capacities are provided in Table 7-2. It is important to note that although the nominal flexural strength increased using the ACI ITG-6R-10 Simplified and Appendix B methods, once the strength reduction values are imposed, the useable design strength could be reduced to lower than those found using the ACI 318-08 model. The member classifications are also provided in Table 7-2; "under" and "over" refer to under-reinforced and over-reinforced CSA A23.3-04 members respectively. "Tension", "compression" and "transition" refer to ACI 318-08 or ACI ITG-6R-10 tension controlled members, compression controlled members and members in the transition zone in between the two, respectively.

Table 7-2: Flexural Capacity Predictions

Specimen	ρ (%)	Predicted Nominal Flexural Capacity (kN*m) and Member Classification							
		Linear Stress-Strain						Non-Linear Stress-Strain	
		ACI 318-08		CSA A23.3-04		ACI ITG-6R-10 Simplified		ACI ITG-6R-10 Appendix B	
		M_r	Class	M_r	Class	M_r	Class	M_r	Class
S300-B1	2.61	174	Transition	177	Over	174	Compression	174	Compression
S300-A2	1.51	139	Tension	127	Under	168	Transition	169	Transition
S1000-B1	1.03	1297	Tension	1185	Under	1577	Transition	1708	Transition
S1000-B2	0.83	1066	Tension	972	Under	1306	Transition	1527	Tension
S1000-A3	0.61	840	Tension	765	Under	1041	Tension	1386	Tension
S1000-A4	0.40	581	Tension	529	Under	723	Tension	1041	Tension

The CSA A23.3-04 design model provided the most conservative predictions of the flexural capacity. Using these values as the benchmark, Table 7-3 shows the increase in capacity based on the three other methods when compared to the CSA A23.3-04 values. Specimen S1000-A4 experienced an almost 100% increase in predicted capacity between the CSA A23.3-04 model and the ACI ITG-6R-10 model based on the Appendix B non-linear reinforcement relationship. The reinforcement stress in S300-B1 failed to reach the respective yield stresses in all four of the design models discussed. This lower stress in combination with a lower maximum concrete compression strain in the ACI 318-08 model resulted in the slight reduction in capacity when compared to the CSA A23.3-04 model. The average increase for each method is also provided along with the corresponding coefficient of variation, although data from S300-B1 was excluded from these values since reinforcement yield was not reached.

Table 7-3: Nominal Flexural Capacity Increases Compared to CSA A23.3-04 Predictions

Specimen	ρ (%)	Increase in Predicted Flexural Capacity (%)		
		Linear		Non-Linear
		ACI 318-08	ACI ITG-6R-10 Simplified	ACI ITG-6R-10 Appendix B
S300-B1	2.61	-1.9	-1.9	-1.9
S300-A2	1.51	9.6	32.5	33.6
S1000-B1	1.03	9.5	33.1	44.1
S1000-B2	0.83	9.6	34.3	57.1
S1000-A3	0.61	9.9	36.1	81.2
S1000-A4	0.40	9.9	36.8	96.9
AVG*		9.7	34.5	62.6
COV*		0.02	0.05	0.42

*Excluding Specimen S300-B1

Both the ACI 318-08 and the Simplified ACI ITG-6R-10 predictions increased a consistent amount compared to the CSA A23.3-04 model, as noted by the low coefficients of variation in Table 7-3. Based on the ACI ITG-6R-10 Appendix B non-linear reinforcement relationship, the flexural predictions increased substantially more for members with low reinforcement ratios than for the members with high ratios.

Since the specimens all failed in shear prior to reaching their full flexural capacity, a comparison between the predicted flexural capacities and the moment corresponding to the peak load (M_{peak}) cannot be made directly. It is possible however, to examine which design methods predicted capacities above or below the value reached. Table 7-4 indicates the peak applied load for each large scale specimen in the current study, and the corresponding maximum flexural moment. Figure 7-4 and Figure 7-5 demonstrate M_{peak} reached in the h = 300 mm and h = 1000 mm specimens respectively, and where each design model prediction falls in relation.

Table 7-4: Large Scale Structural Specimens Maximum Applied Moment

Specimen	ρ (%)	d (mm)	P_{peak} (kN)	M_{peak} (kN*m)
S300-B1	2.61	248	606	226
S300-A2	1.51	252	445	168
S1000-B1	1.03	924	973	1349
S1000-B2	0.83	924	918	1272
S1000-A3	0.61	933	739	1034
S1000-A4	0.40	952	729	1041

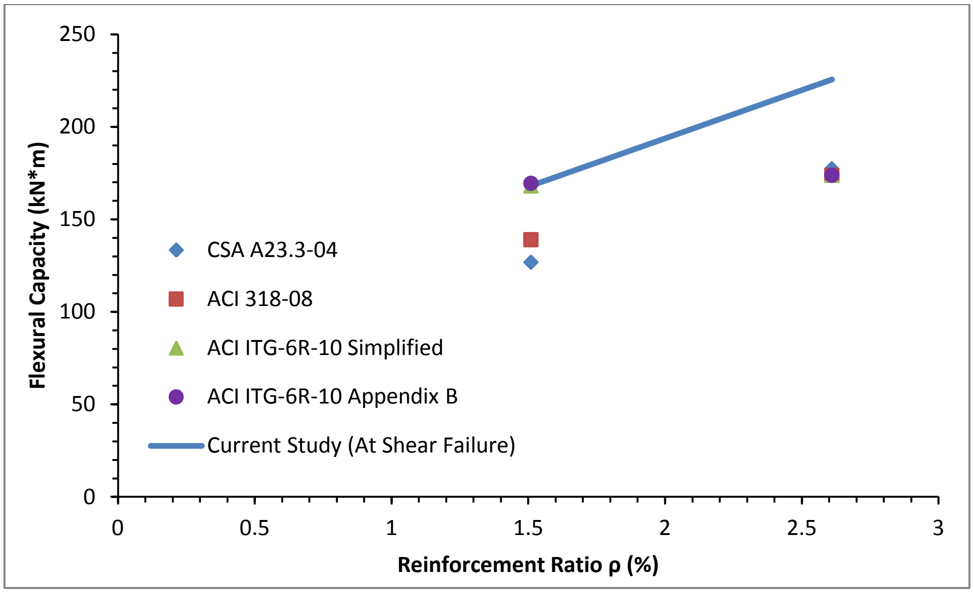

Figure 7-4: Comparison of Predicted Flexural Capacities to Peak Moment for h = 300 mm Specimens

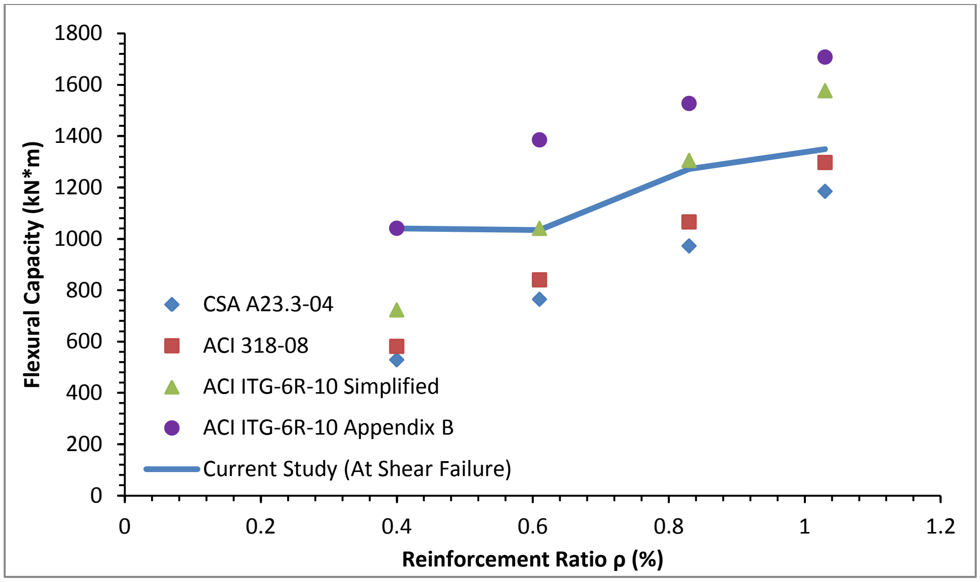

Figure 7-5: Comparison of Predicted Flexural Capacities to Peak Moment for h = 1000 mm Specimens

The ACI 318-08 flexural model, with a design yield strength of 550 MPa, under-predicted the flexural capacity of the specimens in the current study. In the h = 1000 mm specimens, the predicted flexural capacity was closer to the measured flexural moment (M_{peak}) in the members with higher reinforcement ratios. In the h = 300 mm specimens, the reverse was true - the prediction was closer to M_{peak} in S300-A2 with the smaller reinforcement ratio. The predictions varied between 3.8% below M_{peak} in S1000-B1 to 44.1% lower in S1000-A4.

The CSA A23.3-04 flexural design model, used with the maximum allowable design yield strength of 500 MPa, under-predicted the flexural capacity of the specimens. The predicted flexural capacities were closer to M_{peak} in the specimens with higher reinforcement ratios in both the h = 300 mm and h = 1000 mm members. The predicted values ranged between 12.2% below M_{peak} in S1000-B1 to 49.2% lower in S1000-A4.

The ACI ITG-6R-10 Simplified flexural model predicted capacities both above and below M_{peak}. The predicted values were within 2.6% of M_{peak} for S300-A2, S1000-B2 and S1000-A3. In the remaining three specimens, the predictions were much more scattered, varying between 30.5% below M_{peak} in S1000-A4 to 16.9% above M_{peak} in S1000-B1.

The ACI ITG-6R-10 Appendix B non-linear reinforcement stress-strain relationship provided flexural capacity predictions larger than M_{peak} in the h = 1000 mm specimens. The predicted values ranged between 0.1% above M_{peak} in S1000-B4 to 34.0% above M_{peak} in S1000-A3. In the h = 300 mm specimens, the predicted capacity was 22.9% lower on S300-B1 due to the flexural model's prediction of the reinforcement strain. In S300-A2, the predicted capacity was 0.8% above M_{peak}.

The ACI ITG-6R-10 Simplified model takes advantage of an increased design yield strength, and predicted an average 34.5% increase in flexural capacity compared to the CSA A23.3-04 model. The ACI ITG-6R-10 Appendix B model uses the full non-linear behaviour of the Grade 690 reinforcement and predicted an average 62.6% increase in flexural capacity compared to CSA A23.3-04. While this model provides the greatest calculated flexural strength benefit, its ability to enhance the model to account for the fibers can only be examined with specimens that fail in flexure.

7.1.3 Deflection Predictions

Although several methods have been suggested to predict the deflected behaviour of fiber reinforced concrete (FRC) members (refer to Section 2.5.3), the influence from the steel fibers have been ignored in this section in order to understand the validity of using a plain concrete model for steel fiber reinforced concrete (SFRC) members. The predicted load-deflection response of the members, idealized as plain concrete members with high strength longitudinal reinforcement, was determined from the variation in calculated curvatures along the member length.

The cross-section moment-curvature relationship of each specimen was found using the well known theory that plane sections remain plane along with a varying compression strain at the top of the member (ε_{top}). The Collins and Mitchell (1997) stress block parameters (α_c and β_c described in Equations 2-27 and 2-28) and both the Simplified and Appendix B stress-strain relationships for Grade 690 reinforcement as suggested by ACI ITG-6R-10 were used. Between 7 and 10 cross-sections along each shear span of the specimen were examined. The curvature was determined for various loading conditions between the unloaded and peak load states.

Similar to the methods used to determine the flexural capacity predictions (see Section 7.1.2), the distance to the neutral axis (c) was solved iteratively for equilibrium of the internal axial compressive and tensile forces for different strain values ε_{top} at the extreme compression fiber. The corresponding moment was then determined along with the curvature (Ø). The curvature was based on the calculated strain at the extreme compression fiber and the calculated distance to the neutral axis (Equation 7-1).

$$\emptyset = \varepsilon_{top}/c \qquad 7\text{-}1$$

The influence of tension stiffening on the moment-curvature relationship was investigated by applying the approximation from Collins and Mitchell (1997). An equivalent uniform tensile stress of $0.5*f_r$ was used over an effective embedment zone around the tension reinforcement of S300-B1 and S1000-B1. f_r was taken as $0.33*\sqrt{f_c}$’ (Collins & Mitchell,1997) and did not directly include the effect of fibers. The tension stiffening was found to have a minimal affect on the curvature and deflection results. For the remainder of the deflection analysis discussed in the current study, tension stiffening was ignored.

The moment-curvature relationships based on both the Simplified and Appendix B steel stress-strain relationships from ACI ITG-6R-10 are illustrated in Figure 7-6a for S1000-A4. While both M - Ø relationships follow an initially linear response, they differ near the peak loads when the Appendix B non-linear stress-strain relationship allows for increased moment resistance while the Simplified relationship is restricted by a maximum reinforcement stress of 690 MPa. Similar behaviour was observed for the other structural specimens, except for S300-B1 which remained in the linear behaviour region. Refer to Appendix C for individual responses.

The physical location along the length of the specimen corresponding to the moment and curvature values obtained through the iterative process was determined through use of the bending moment diagram. Based on the specimen configurations in simply supported three point bending, the maximum moment occurred at mid-span and no moment was present at the supports. All M - Ø values corresponded with a location along the specimen span, determined using similar triangles. Figure 7-6b illustrates the calculated curvatures along the length of S1000-A4, and highlights the initially linear curvature behaviour, followed by non-linear behaviour near mid-span (x = 2856 mm) where the curvature peaks at the peak load level for both the ACI ITG-6R-10 Appendix B and Simplified stress-strain relationships. The difference between the curvatures obtained through use of the Appendix B and Simplified stress-strain relationships demonstrates the influence on curvature when a non-linear analysis is used. The curvature is also shown as fully linear along the length of the member at the service load level. Specimen S1000-A4 experienced the most non-linear steel reinforcement behaviour, thus the curvature figures shown below are similar for all other specimens but with lesser degrees of non-linear behaviour (detailed in Appendix C).

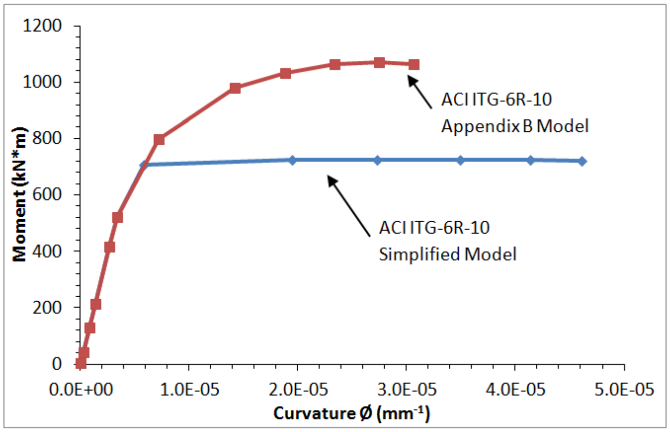

a)

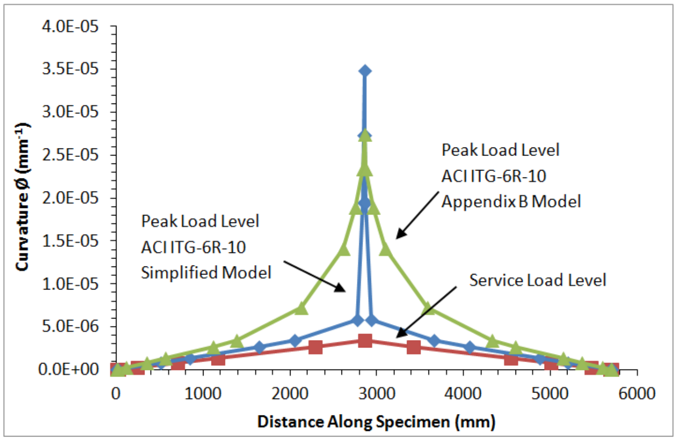

b)

Figure 7-6: a) Moment-Curvature Relationship for S1000-A4 and b) Curvatures Along Length of Specimen S1000-A4

The curvature and moment values found through the process indicated above were used to predict the deflections (Δ) along the length of the specimen at different load levels. Numerical integration of the curvature values was performed through the moment-area theorem (Collins & Mitchell, 1997).

Figure 7-7 demonstrates the deflection behaviour along one half of S1000-A4, based on the Simplified and Appendix B reinforcement stress-strain relationships described above. The calculated deflections are based on the peak moment capacity determined by each stress-strain model. Therefore, the curves shown in the figure are at different load levels, but are used to highlight the difference between using the linear and non-linear reinforcement stress-strain relationships. Using the Appendix B non-linear stress-strain behaviour resulted in a 113% increase in the predicted mid-span deflection when compared to the Simplified stress-strain relationship, and a 48% increase in the predicted mid-span moment capacity. The discrepancy between the predictions based on these two stress-strain models decreased in the other specimens as the amount of non-linear behaviour decreased.

In addition, the predicted deflection behaviour is shown in Figure 7-7 based on the Appendix B reinforcement stress-strain relationship at a mid-span peak load equivalent to that calculated using the Simplified stress-strain relationship (P_{max} = 508 kN). As the strain in the extreme compression fiber continues to increase after the proportional stress limit of 690 MPa has been reached in the longitudinal reinforcement using the Simplified relationship, the depth of the compression block (c) decreases in order to maintain equilibrium between the compressive and tensile forces. Conversely in the Appendix B model at the 508 kN load level, the stress in the longitudinal reinforcement continues to increase past 690 MPa as the strain in the extreme compression fiber increases and the depth of the compression block increases to satisfy force equilibrium. The curvatures and predicted deflections at the 508 kN load level using the Simplified stress-strain relationship are therefore larger than those using the Appendix B relationship.

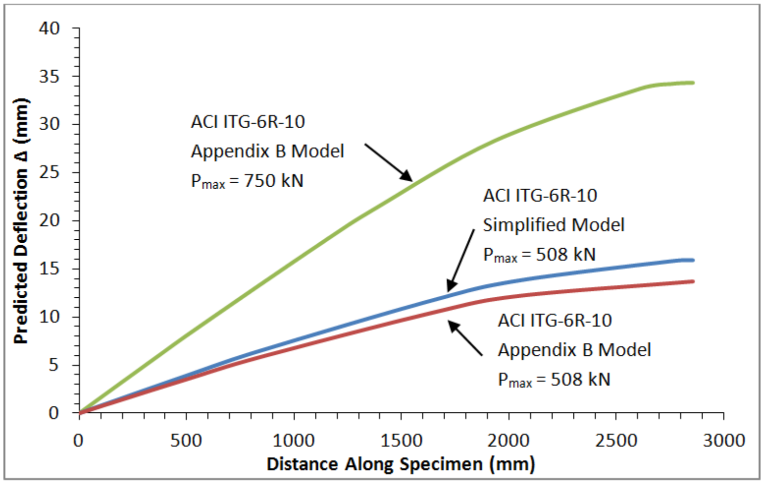

Figure 7-7: Specimen S1000-A4 Predicted Deflections Based on Curvature

The specimen deflections in the current study were recorded at mid-span and both quarter span points through use of cable potentiometers (or LVDTs on S1000-A4). Deflection control limits are typically applied only at the serviceability limit states in design cases, therefore the predicted deflections at the equivalent service load level in the current study are of primary interest. In the large scale structural specimens, the reinforcement strain at the equivalent service load was in the linear portion of the stress-strain relationship, therefore both the Appendix B and Simplified models produced identical deflection results at the serviceability limit states. Comparisons of the measured deflection values from the current study, after correction for measured support settlement, with the predicted values are illustrated in Figure 7-8. The model deflections were approximately 7% higher than the measured deflection at mid-span in S1000-A4. In the h = 300 mm specimens, the predicted mid-span deflections varied between 12 and 20% less than the actual measured values. In the remaining h = 1000 mm specimens, the predicted deflections varied between 1 and 7% less than the actual deflections (refer to Appendix C).

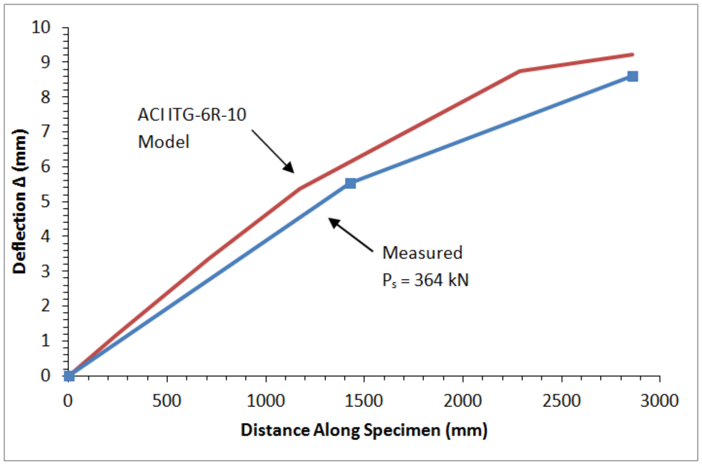

Figure 7-8: S1000-A4 Comparison between Predicted and Measured Deflections at the Equivalent Service Load Level

The predicted mid-span deflection was computed at various imposed load levels using the ACI ITG-6R-10 Appendix B non-linear steel stress-strain relationship. This curve was compared to a similar curve developed from measurements of S1000-A4 during testing in Figure 7-9. The relationship between these two curves confirms what was found above; at small loads, the prediction model estimates larger mid-span deflections than measured. Starting just below the service level however, the prediction model under-estimates the member deflection. This behaviour is typical of all the large scale structural specimens except for S300-B1, where the deflection is under-estimated starting at approximately 30% of the equivalent service load (refer to Appendix C).

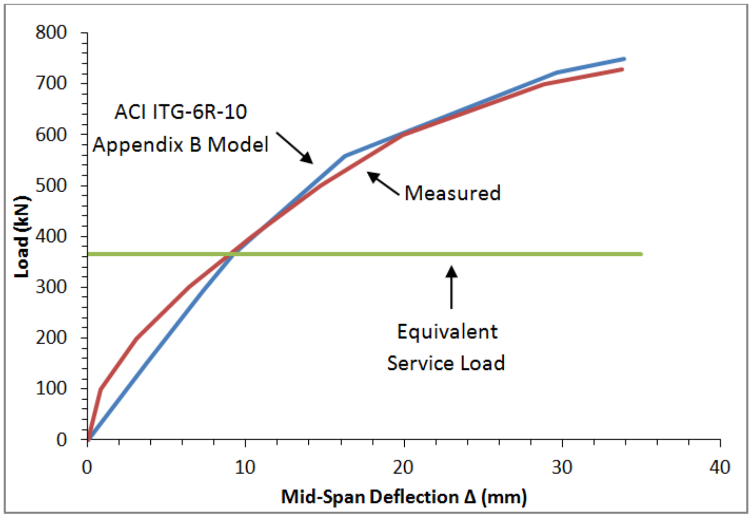

Figure 7-9: Specimen S1000-A4 Measured and Predicted Relationships between Load and Mid-Span Deflection

The deflection predictions in this section were based on plain concrete members reinforced with ASTM A1035 steel reinforcement. The ACI ITG-6R-10 Simplified model for the stress-strain behaviour of high strength steel reinforcement produced vastly different deflection predictions at the ultimate load level than the Appendix B stress-strain relationship. At the service level however, these two models produced identical results since the reinforcement was still in the linear stress-strain region. Design engineers are primarily concerned with a reinforced concrete member's deflection at the service level. The predictions described in this section were within 7% of the measured deflections for the h = 1000 mm specimens at the equivalent service load but a discrepancy up to a 20% was produced in the h = 300 mm specimens. Further investigation into an alternative method for the deflection prediction of SFRC members reinforced with ASTM A1035 steel reinforcement is recommended as additional testing is conducted on members with this material combination. The influence of long duration loading effects also requires further study.

7.1.4 Recommendations

In terms of shear capacity, the Desalegne and Lubell General model combined with the ACI ITG-6R-10 Appendix B non-linear stress-strain reinforcement relationship provides a detailed capacity prediction while taking into consideration both the size and strain effects. For members with both high strength longitudinal reinforcement and steel fibers, this method is recommended along with a fiber factor of 2.0 to provide a conservative estimate of the shear capacity while accounting for both material properties. The fiber factor would be directly applied to the Desalegne and Lubell General shear model ($V_{C,D\&L,G}$) for plain concrete without fibers as shown in Equation 7-2.

$$V_{C,FRC} = 2.0V_{C,D\&L,G} \tag{7-2}$$

The Dinh et al. (2011) shear model for SFRC members was observed to have the lowest V_{test}/V_{model} ratio out of all the models examined, but does not account for size and strain effects on the shear capacity. This model is recommended for structural SFRC members that do not experience significant strain effects, and with overall heights less than 1000 mm.

In order to take advantage of the additional strength of the high-performance reinforcement, use of the ACI ITG-6R-10 Simplified stress-strain reinforcement model with a design yield strength of 690 MPa is recommended for the flexural capacity predictions. Although the Appendix B model provided increased flexural capacity predictions, the structural specimens in the current study were not able to verify its accuracy.

The curvature integration process used without considering the influence from fibers provided relatively accurate mid-span deflection predictions at the equivalent service load levels, but became un-conservative at loads above the service level. Both the ACI ITG-6R-10 Simplified and Appendix B steel reinforcement stress-strain relationships produced the same prediction at the equivalent service load level since the reinforcement stress-strain response was still in the linear region. The predictions were also significantly closer at the service level to the measured deflections in the h = 1000 mm specimens than in the h = 300 mm specimens. Both the ACI 318-08 and CSA A23.3-04 provisions for maximum allowable mid-span deflection in plain concrete members were satisfied.

7.2 Summary

- The Desalegne and Lubell General model (2010) for shear capacity in combination with the ACI ITG-6R-10 Appendix B non-linear steel stress-strain relationship and a fiber factor of 2.0 (refer to Equation 7-2) is recommended for shear predictions of SFRC members reinforced with Grade 690 longitudinal reinforcement. The fiber contribution to the shear capacity was found to range between 2.5 and 5.3 times the predicted capacity for plain concrete members using this model.
- The Dinh et al. (2011) shear model for SFRC members is suggested as a reliable model for members without significant size and strain effects, since these are not accounted for.
- Although it was previously shown that the SFRC mix used in the current study did not meet the ACI 318-08 requirements for use as a method of shear resistance, the shear capacity of the h = 300 mm members in the current study was approximately double the ACI 318-08 prediction for plain concrete members using the full value of $V_{C,ACI}$ in Equation 2-2.
- Using the ACI-ITG-6R-10 Simplified stress-strain relationship in combination with the ACI 318-08 flexural model resulted in an increase in the predicted nominal flexural capacity between 32 and 37% compared to the CSA A23.3-04 flexural model. This method is recommended for flexural capacity predictions of SFRC specimens reinforced with Grade 690 longitudinal reinforcement.
- Using the ACI ITG-6R-10 Appendix B non-linear steel reinforcement stress-strain relationship in combination with the ACI 318-08 flexural model resulted in an increase in the predicted nominal flexural capacity between 34 and 97% of the CSA A23.3-04 model based on the maximum allowable design yield strength of 500 MPa. However, the accuracy of this model could not be assessed based on the specimens in the current study.
- The deflection predictions based on the curvature integration process for plain concrete members was found to be relatively accurate at small load levels in the h = 1000 mm specimens. The predictions were un-conservative in the h = 300 mm specimens (up to a 20% discrepancy), suggesting that alternate methods need to be examined for the prediction of deflections in SFRC specimens reinforced with ASTM A1035 steel reinforcement.

8 Summary and Conclusions

8.1 Summary

A unique steel fiber reinforced concrete (SFRC) mix was developed for the current study. The goal was to create a mix that could be commercially replicated at a ready-mix plant with consistent results, while maintaining satisfactory strength and rheology characteristics. Several trial mixes were completed, initially in small batches at the University of Alberta and later at a larger scale at Inland Concrete Ltd. The final mix contained InterCem™, a pre-blended product of Type GU Portland Cement and Class F fly ash, along with 1.0% volume fraction of hooked end steel fibers. The cylinders, prisms and large scale structural specimens used for materials characterization were produced from two 5.5 m^3 batches. The cylinders and prisms were cast for strength development studies and also as quality control companions to the large scale structural members cast from these batches.

The study initially examined the size effect at the material scale in steel fiber reinforced concrete (SFRC) in both compression and flexural tension. Size effects have previously been established in plain concrete but are less well understood for SFRC. Two sizes of cylinders, 100 and 150 mm diameters, were tested in compression according to ASTM C39-09a. Notched flexural prisms of three different sizes, 100 x 100 x 300 mm, 150 x 150 x 450 mm and 200 x 200 x 600 mm, were tested according to ASTM C1609-10. The digital image correlation (DIC) technique was used during the ASTM C1609-10 flexural tests as a non-contact method to provide continuous data on the prism behaviour and performance without the need for additional instrumentation. The images obtained through the DIC system were post-processed to obtain a quantitative understanding of the crack widths and vertical deflections.

The second phase of the current study examined the shear behaviour of structural members longitudinally reinforced with ASTM A1035 Grade 690 steel and constructed with SFRC. Six large scale specimens of two different overall heights, h = 300 mm and h = 1000 mm, were constructed. A range of reinforcement ratios were selected to examine the specimen behaviour with respect to reinforcement stresses at the time of failure that were below and above the ACI 318-08 and CSA A23.3-04 maximum permitted design yield strengths. All six specimens had widths of 300 mm and a shear span to effective depth ratio (a/d) of 3.0 in order to encourage sectional behaviour. Altering the specimen heights and longitudinal reinforcement ratios allowed for an examination of both the size and strain effects in shear. The DIC system was used along with additional physical instrumentation. All specimens were tested in three point bending under displacement controlled loading until failure, where failure was defined by a sudden, large drop in load carrying capacity.

The shear and flexural performances of each of the large scale specimens were compared with capacity predictions based on current, relevant design models. The majority of the shear capacity prediction models were based on plain concrete members, allowing for an analysis of the fiber contribution towards the overall shear capacity. One shear model for SFRC was also examined for comparison. The flexural capacity predictions were either based on the maximum design yield strength permitted by the model, or based on the Simplified and Appendix B reinforcement stress-strain curves recommended by ACI ITG-6R-10 for structural members designed with ASTM A1035 Grade 690 longitudinal reinforcement. The member deflections were also compared with predictions based on the curvature integration process for plain concrete members.

8.2 Conclusions

The conclusions provided were drawn from the laboratory and analytical components of the current study.

8.2.1 Materials Characterization

- A size effect in compression was apparent through the ASTM C39-09a cylinder tests. The cylinders from Casting A showed an average 12% decrease in the compressive strength of the 150 mm diameter cylinders compared to the 100 mm cylinders. From Casting B, this discrepancy was 21% although a portion of that was likely due to the age difference between the two cylinder sizes.
- The ASTM C1609-10 notched flexural prism tests demonstrated a higher rate of increase in the crack mouth opening than in the vertical deflection. The ratio of change in crack mouth opening displacement (CMOD) to the change in vertical displacement (d_{CMOD}/d_{Δ}) was found to be an average of 1.31 for the strength development prisms, and 1.32 for the companion prisms. The relationship was observed to be size and strength independent.
- A size effect was observed in the tensile strength of the flexural prisms. As the member depth increased, the modulus of rupture (MOR) decreased. The CSA A23.3-04 MOR model for plain concrete members underestimated the strength in the SFRC prisms, although the discrepancy decreased as the member size increased.
- A relationship between the equivalent uniform tensile stress carried by the steel fibers across the cracks of the notched prisms and the CMOD was established. A size effect for the maximum tensile stress in relation to the prism size was observed. In general, as the member depth increased, the peak equivalent uniform tensile stress decreased.
- The SFRC mix used in the current study did not satisfy the ACI 318-08 Clause 5.6.6.2 requirements to allow use of the steel fibers as a method of shear resistance.

8.2.2 Large Scale Structural Specimens

- The h = 300 mm specimens experienced very sudden drops in load carrying capacity at failure, but were still able to maintain approximately 50% of the peak load. One of the specimens experienced a combination of shear-compression and shear-tension failure while the other experienced diagonal tension failure.
- All four h = 1000 mm specimens experienced very sudden, brittle failures with a complete loss of their load carrying capacity. While all specimens failed in shear, the failure mechanism varied between a combination of diagonal-tension and shear-tension, a combination of shear-compression and shear-tension and diagonal tension failure.
- The mid-span deflections at the equivalent service load level satisfied the most stringent of deflection control cases (ie. span/480) as described by both CSA A23.3-04 and ACI 318-08 for plain concrete members. The reinforcement stress limit at the service condition suggested by the ACI ITG-6R-10 for crack control purposes was also satisfied.
- The shear stress at failure showed both size and strain effects, reinforcing the need for shear capacity models that account for both influences. The Desalegne & Lubell General model for shear capacity in combination with the Appendix B non-linear reinforcement stress-strain relationship described by the ACI ITG-6R-10 is recommended for shear predictions of SFRC members reinforced with Grade 690 reinforcement. A fiber factor of 2.0, applied directly to $V_{C,D\&L,G}$, is recommended to conservatively account for the influence on shear capacity from the steel fibres.
- The shear capacity of the h = 300 mm specimens was at least 2.72 times the shear capacity prediction provided by the ACI 318-08 model for plain concrete members, even though the SFRC mix did not satisfy the requirements for use as shear reinforcement in place of minimum transverse reinforcement requirements. The ACI 318-08 shear predictions for the h = 1000 mm specimens were much closer to the measured test values (a maximum of 1.85 times larger in S1000-B1), likely due to the size effects in shear that were un-accounted for.
- Use of the ACI 318-08 flexural model in combination with the ACI ITG-6R-10 Simplified reinforcement stress-strain relationship is recommended for flexural design of SFRC members containing Grade 690 reinforcement. This method acknowledges increased flexural capacity from the higher steel strength while maintaining adequate reserve capacity.
- The deflection predictions according to the curvature integration method for plain concrete provided accurate predictions below the equivalent service load level in the h = 1000 mm specimens. Improvements could be made to the prediction model to account for the tension stiffening effect due to the fiber influence and may improve the prediction accuracy in the h = 300 mm specimens.

8.3 Recommendations for Future Work

The research described in the current study was completed in order to gain a better understanding of the behaviour of steel fiber reinforced concrete members reinforced with high strength reinforcement. The combination of these two materials provides the potential for superior structural members with increased strength and durability. However, further research is required to gain a better understanding of the behaviour. The following are recommendations for additional work to complement the results developed in the current study.

- The SFRC mix was based on InterCem™, a pre-blended product of Type GU Portland Cement and Class F fly ash, to increase the sulphate durability of the final product. Further analysis should be completed on this mix to examine the sulphate durability, shrinkage and creep properties.
- The relationship between the CMOD at peak load and prism size was found to be inconsistent. Further tests could be completed to examine this relationship.
- The equivalent uniform tensile stress approximations were found to differ from those reported by Dinh (2009) and Shoaib (2012). Further refinement of the approximations and analytical or laboratory methods could be completed in order to provide more consistent results.
- Additional large scale structural specimens constructed with the combination of steel fiber reinforced concrete (SFRC) and high strength longitudinal steel should be examined in shear to increase the available data on the behaviour of this combination.
- Although the large scale specimens were designed to encourage sectional behaviour, one member appeared to experience a strut formation at one end before re-distributing the load and failing in sectional behaviour in the opposite shear span. The behaviour of similar members with different a/d ratios should be examined to determine if the transition zone between sectional and arch behaviour is different than that of plain concrete members. This study would also help to identify the influence of reinforcement strains on shear capacity separate from the influence of the reinforcement ratio.
- The fiber contribution to the shear capacity was found to at least double the capacities predicted using the CSA A23.3-04 or Hoult shear models for plain concrete. However, this factor of 2.0 could vary depending on the steel fiber volume fraction used. Similar large scale specimens could be constructed with varying fiber volumes to analyse this relationship.
- The Dinh et al. (2011) shear model for SFRC provided the lowest V_{test}/V_{model} ratios for the specimens tested in the current study. The predictions became un-conservative in members with higher reinforcement strains, and were more conservative in the h = 300 mm specimens. This suggests that the size and strain effects need to be accounted for in this model, and further revisions are recommended.

- A simple and widely accepted shear model is required for SFRC to enable its use in the design industry without the need for analysis of ASTM C1609-10 flexural prisms.
- Analysis of flexure critical specimens should be completed to validate the use ACI ITG-6R-10 Appendix B model with SFRC members.
- A simple deflection model is required for SFRC that can be used by design engineers. The long term deformation behaviour of SFRC should also be examined.

References

ACI Committee 318. (2008). *ACI 318-08 Building Code Requirements for Structural Concrete and Commentary*. Farmington Hills, MI: American Concrete Institute.

ACI Committee 544. (1988, Reapproved 2009). *ACI 544.4R-88 Design considerations for steel fiber reinforced concrete*. Farmington Hills, MI: American Concrete Institute.

ACI Innovation Task Group 6. (2010). *ACI ITG-6R-10 Design guide for the use of ASTM A1035/A1035M Grade 100 (690) steel bars for structural concrete*. Farmington Hills, MI: American Concrete Institute.

ACI-ASCE Committee 445. (1999, Reapproved 2009). *ACI 445R-99 Recent Approaches to Shear Design of Structural Concrete*. Farmington Hills, MI: American Concrete Institute.

ASCE-ACI Task Committee 426. (1973). The Shear Strength of Reinforced Concrete Members. Proceedings from *ASCE, Journal of the Structural Division, 99*(ST6): 1091-1187.

Adebar, P., Mindess, S., St.-Pierre, D., & Olund, B. (1997). Shear tests of fiber concrete beams without stirrups. *ACI Structural Journal, 94*(1), 68-76.

Alam, S. Y., & Loukili, A. (2010). Application of Digital Image Correlation to size effect tests of concrete. Proceedings from *7th International Conference on Fracture Mechanics of Concrete and Concrete Structures*. Jeju, South Korea: Korea Concrete Institute.

Armelin, H. S., & Banthia, N. (1997). Predicting the flexural postcracking performance of steel fiber reinforced concrete from the pullout of single fibers. *ACI Materials Journal, 94* (1), 18-31.

ASTM A370-11. (2011). *Standard test methods and definitions for mechanical testing of steel products*. West Conshohocken, PA: ASTM International.

ASTM A1035/A1035M-11. (2011). *Standard specification for deformed and plain, low-carbon, chromium, steel bars for concrete reinforcement*. West Conshohocken, PA: ASTM International.

ASTM C39/C39M-09a. (2009). *Standard test method for compressive strength of cylindrical concrete specimens*. West Conshohocken, PA: ASTM International.

ASTM C143/C143M-10. (2010). *Standard test method for slump of hydraulic-cement concrete*. West Conshohocken, PA: ASTM International.

ASTM C231/C231M-09b. (2009). *Standard test method for air content of freshly mixed concrete by the pressure method*. West Conshohocken, PA: ASTM International.

ASTM C1609/C1609M-10. (2010). *Standard test method for flexural performance of fiber-reinforced concrete (using beam with third-point loading)*. West Conshohocken, PA: ASTM International.

Banthia, N. (1992). Fibre reinforced concrete. In S. N. Ghosh (Ed), *Progress in cement and concrete (Vol. 1 Part 2)* (pp. 288-320). New Delhi, India: ABI Books Private Ltd.

Bentz, E., Vecchio, F., & Collins, M. (2006). Simplified modified compression field theory for calculating shear strength of reinforced concrete elements. *ACI Structural Journal, 103*(4), 614-624.

Bischoff, P. H. (2003). Tension stiffening and cracking of steel fiber-reinforced concrete. *Journal of Materials in Civil Engineering, 15*(2), 174-182. doi:10.1061/(ASCE)0899-1561(2003)15:2(174)

Bischoff, P. H. (2005). Re-evaluation of deflection prediction for concrete beams reinforced with steel and fiber reinforced polymer bars. *Journal of Structural Engineering-ASCE, 131*(5), 752-767. doi:10.1061/(ASCE)0733-9445(2005)131:5(752)

Bischoff, P. H. (2007). Deflection calculation using an effective moment inertia for FRC. In Bischoff, P. H. & Malhas, F. (Eds), *SP-248-2 Deflection and stiffness issues in FRC and thin structural elements* (pp. 17-30). Retrieved from http://www.concrete.org.

Bischoff, P. H., & Scanlon, A. (2007). Effective moment of inertia for calculating deflections of concrete members containing steel reinforcement and fiber-reinforced polymer reinforcement. *ACI Structural Journal*, *104*(1), 68-75.

Canadian Standards Association. (2004). *A23.3-04 Design of Concrete Structures*. Mississauga, ON: Canadian Standards Association.

Canadian Standards Association. (2006). *CAN/CSA-S6-06 Canadian Highway Bridge Design Code*. Mississauga, ON: Canadian Standards Association.

Collins, M. P., & Kuchma, D. (1999). How safe are our large, lightly reinforced concrete beams, slabs, and footings? *ACI Structural Journal*, 96(4), 482-490.

Collins, M. P., & Mitchell, D. (1997). *Prestressed concrete structures*. Toronto, ON: Response Publications.

Collins, M. P., Mitchell, D., Adebar, P., & Vecchio, F.J. (1996). A general shear design method. *ACI Structural Journal*, *93*(1), 36-45.

Correlated Solutions Inc. (2007). Vic-Snap 2007 and Vic-3D 2007 [computer software]. Available from http://www.correlatedsolutions.com/support.

Correlated Solutions Inc. (2009). Vic-Snap 2009 and Vic-3D 2009 [computer software]. Available from http://www.correlatedsolutions.com/support.

Correlated Solutions Inc. (2010). Vic-3D 2010 Testing Guide. Retrieved from http://www.correlatedsolutions.com/support.

Desalegne, A. S., & Lubell, A. S. (2010). Shear behavior of concrete slabs longitudinally reinforced with high-performance steel. *ACI Structural Journal, 107*(2), 228-236.

Dinh, H. (2009). *Shear behavior of steel fiber reinforced concrete beams without stirrup reinforcement*. (Doctoral dissertation). Retrieved from ProQuest. (3382064)

Dinh, H. H., Parra-Montesinos, G. J., & Wight, J. K. (2010). Shear behavior of steel fiber-reinforced concrete beams without stirrup reinforcement. *ACI Structural Journal, 107*(5), 597-606.

Dinh, H. H., Parra-Montesinos, G. J., & Wight, J. K. (2011). Shear strength model for steel fiber reinforced concrete beams without stirrup reinforcement. *Journal of Structural Engineering, 137*(10), 1039-1051. doi: 10.1061/(ASCE)ST.1943-541X.0000362

Grace Concrete Products. (2007a). ADVA 140M: High-range water-reducing admixture. Retrieved from http://www.na.graceconstruction.com.

Grace Concrete Products. (2007b). WRDA 64: Water-reducing admixture. Retrieved from http://www.na.graceconstruction.com.

Grace Concrete Products. (2008). ADVA 195: High-range water-reducing admixture. Retrieved from http://www.na.graceconstruction.com.

Hassan, T. K., Seliem, H. M., Dwairi, H., Rizkalla, S. H., & Zia, P. (2008). Shear behavior of large concrete beams reinforced with high-strength steel. *ACI Structural Journal, 105*(2), 173-179.

Hoult, N. A., Sherwood, E. G., Bentz, E. C., & Collins, M. P. (2008). Does the use of FRP reinforcement change the one-way shear behaviour of reinforced concrete slabs? *Journal of Composites for Construction, 12*(2), 125-133.

Jiang, Z., & Banthia, N. (2010). Size effects in flexural toughness of fiber reinforced concrete. *Journal of Testing and Evaluation, 38*(3), 332-338.

Kani, G. N. J. (1967). How safe are our large reinforced concrete beams? *ACI Journal Proceedings, 64*(3), 128-141.

Kwak, Y., Eberhard, M., Kim, W., & Kim, J. (2002). Shear strength of steel fiber-reinforced concrete beams without stirrups RID G-5455-2011. *ACI Structural Journal, 99*(4), 530-538.

Lubell, A. S. (2006). *Shear in wide reinforced concrete members*. (Doctoral dissertation). Retrieved from ProQuest. (NR21792)

Lubell, A. S., Bentz, E. C., & Collins, M. P. (2009). Influence of longitudinal reinforcement on one-way shear in slabs and wide beams. *Journal of Structural Engineering-ASCE, 135*(1), 78-87. doi:10.1061/(ASCE)0733-9445(2009)135:1(78)

MacGregor, J. G. & Bartlett, F. M. (2000). *Reinforced concrete: mechanics and design*. Scarborough, ON: Prentice Hall Canada Inc.

Mast, R. F., Dawood, M., Rizkalla, S. H., & Zia, P. (2008). Flexural strength design of concrete beams reinforced with high-strength steel bars. *ACI Structural Journal, 105*(5), 570-577.

Minelli, F., & Plizzari, G. A. (2010). Shear strength of FRC members with little or no shear reinforcement: a new analytical model. In Minelli, F. & Plizzari, G. (Eds), *fib bulletin 57 Shear and punching shear in RC and FRC elements* (pp. 211-225). Lausanne, Switzerland: International Federation for Structural Concrete (fib).

Mirsayah, A., & Banthia, N. (2002). Shear strength of steel fiber-reinforced concrete. *ACI Materials Journal, 99*(5), 473-479.

Narayanan, R. & Darwish, I. Y. S. (1987). Use of steel fibers as shear reinforcement. *ACI Structural Journal, 84*(3), 216-227.

Nguyen-Minh, L., & Rovnak, M. (2010). New formula for the estimation of shear resistance of fibre reinforced specimens. *Canadian Journal of Civil Engineering, 38*(1), 23-35. doi: 10.1139/L10-107

Ozyurt, N., Mason, T. O., & Shah, S. P. (2007). Correlation of fiber dispersion, rheology and mechanical performance of FRCs. *Cement and Concrete Composites, 29*, 70-79. doi: 10.1016/j.cemconcomp.2006.08.006

Parra-Montesinos, G. J. (2006). Shear strength of beams with deformed steel fibers. *Concrete International, 28*(11), 57-67.

Shah, A. A., & Ribakov, Y. (2011). Recent trends in steel fibered high-strength concrete. *Materials & Design, 32*(8-9), 4122-4151. doi: 10.1016/j.matdes.2011.03.030

Shah, S. P., Stroeven, P., Dalhuisen, D., & van Stekelenburg, P. (1978). Complete stress-strain curves for steel fibre reinforced concrete in uniaxial tension and compression. In Swamy, R. N. (Ed), *RILEM Symposium 1978 Testing and test* *methods of fibre cement composites* (pp. 399-408). Lancaster, England: The Construction Press.

Sharma, A. (1986). Shear-strength of steel fiber reinforced-concrete beams. *Journal of the American Concrete Institute, 83*(4), 624-628.

Sherwood, E. G., Lubell, A. S., Bentz, E. C., & Collins, M. R. (2006). One-way shear strength of thick slabs and wide beams. *ACI Structural Journal, 103*(6), 794-802.

Shoaib, A. (2012). *Shear strength of steel fiber reinforced concrete members with longitudinal reinforcement and without stirrups*. (Doctoral dissertation, draft). Private correspondence, February 4, 2012.

Shoaib, A., Bindiganavile, V. S., & Lubell, A. S., (2009). Effect of steel fibers on the shear response of structural lightweight concrete. Proceedings from *CSCE 2009 Annual General Conference*. St. John's, NL: CSCE.

Shoaib, A., Lubell, A. S., & Bindiganavile, V. S. (2010). Size effect in the shear response of steel fiber reinforced concrete members without stirrups. Proceedings from *8th International Conference on Short and Medium Span Bridges*. Niagara Falls, ON: CSCE.

Sutton, M. A., Wolters, W. J., Peters, W. H., Ranson, W. F., & McNeill, S. R. (1983). Determination of displacement using an improved digital correlation method. *Image and Vision Computing, 1*(3), 133-139.

Tang, J., & Lubell, A. S. (2008). Influence of longitudinal reinforcement strength on one-way slab deflection. *Canadian Journal of Civil Engineering, 35*(10), 1076-1087. doi:10.1139/L08-050

Transportation Research Board. (2011). *NCHRP Report 679 Design of concrete structures using high-strength steel reinforcement*. Washington, DC: National Academy of Sciences.

Vecchio, F. J., & Collins, M. P. (1986). The Modified Compression-Field Theory for reinforced concrete elements subjected to shear. *ACI Journal, 83*(2), 219-231.

Walraven, J. C. (1981). Fundamental analysis of aggregate interlock. *Journal of the Structural Division, 107*(ST11), 2245-2270.

Williamson, G. S., Weyers, R. E., Sprinkel, M. M., & Brown, M. C. (2009). Concrete and steel type influence on probabilistic corrosion service life. *ACI Materials Journal, 106*(1), 82-88.

Appendix A : **Steel Fiber Reinforced Concrete Properties**

A.1 General

The data provided in Appendix A covers the results from the materials characterization tests performed in this study and is intended to supplement the information provided in Sections 3 and 4.

In between each test, all instrumentation was checked for accuracy and re-calibrated when necessary. The MTS load and stroke along with all additional instrumentation were zeroed prior to the start of loading.

A.2 Strength Development Compression Test Results

Cylinder compression tests were performed according to ASTM C39-09a and flexural prism tests were performed according to ASTM C1609-10 for each of the trial mixes at 7 and 28 days to provide an indication of the mix strength development. These results are summarized below, along with the batch size, slump as measured according to ASTM C143-10 after the addition of fibers and the air content as measured according to ASTM C231-09b. The cylinders and prisms used for the trial mixes were tested in a Forney Testing Machine at a standard rate of 250 kPa/s. As such, only the peak loads were obtained from these tests. The cylinders were tested with un-bonded neoprene caps.

Table A.2-1: Trial Mix #1 Details

Trial Mix #1

Batch Size = 0.047 m^3
Slump = 60 mm
Air Content = 2.3 %

Specimen	7 Day Results		28 Day Results	
	f_c' (MPa)	MOR (MPa)	f_c' (MPa)	MOR (MPa)
1	31.1	5.65	42.4	6.07
2	34.0	5.63	39.3	5.89
3	32.8	NA	41.4	6.18
AVG	32.6	5.64	41.0	6.05
COV	0.05	0.00	0.04	0.02

Table A.2-2: Trial Mix #2 Details

Trial Mix #2

Batch Size = 0.050 m^3
Slump = 205 mm
Air Content = 4.4 %

Specimen	7 Day Results		28 Day Results	
	f_c' (MPa)	MOR (MPa)*	f_c' (MPa)	MOR (MPa)
1	21.3	5.32	37.2	5.95
2	21.5	5.69	36.9	5.6
AVG	21.4	5.51	37.1	5.78
COV	0.00	0.05	0.01	0.04

*14 Day Results

Table A.2-3: Trial Mix #3 Details

Trial Mix #3

Batch Size = 0.038 m^3
Slump = 90 mm
Air Content = 2.4 %

Specimen	7 Day Results		28 Day Results	
	f_c' (MPa)	MOR (MPa)	f_c' (MPa)	MOR (MPa)
1	29.8	6.24	39.5	6.86
2	28.7	4.19	41.5	6.56
AVG	29.2	5.22	40.5	6.71
COV	0.03	0.28	0.04	0.03

Table A.2-4: Trial Mix #4 Details

Trial Mix #4

Batch Size = 0.038 m^3
Slump = 60 mm
Air Content = NA %

Specimen	7 Day Results		28 Day Results	
	f_c' (MPa)	MOR (MPa)	f_c' (MPa)	MOR (MPa)
1	21.4	4.11	38.1	5.10
2	21.2	NA	39.0	6.59
3	22.1	NA	35.9	NA
AVG	21.6	4.11	37.7	5.84
COV	0.02	NA	0.04	0.18

Table A.2-5: Trial Mix #5 Details

Trial Mix #5

Batch Size = 3.000 m^3
Slump = 85 mm
Air Content = 6 %

Specimen	7 Day Results		28 Day Results	
	f_c' (MPa)	MOR (MPa)	f_c' (MPa)	MOR (MPa)
1	27.6	4.55	39.6	4.90
2	28.7	4.95	38.9	5.13
3	28.4	4.33	35.9	6.25
AVG	28.2	4.61	38.1	5.43
COV	0.02	0.07	0.05	0.13

Once the final mix was obtained, two 5.5 m^3 castings were completed for the construction of the large scale structural specimens; Casting A and Casting B. In each of these castings, two sizes of cylinders were cast for strength development; 100 mm diameter and 150 mm diameter. They were moist cured until testing. These cylinders were tested in a 2600 kN MTS Universal Loading Frame with sulphur caps in order to capture the full stress-strain behaviour. The peak stress and strain values, along with the modulus of elasticity as measured between the origin and a stress of approximately $0.4*f_c$', are provided in the tables below for each casting. The associated stress-strain curves are also included.

Table A.2-6: Casting A Strength Development Cylinder Results

Strength Development Cylinders - Casting A

Cylinder	Diameter (mm)	Age (Days)	f_c' (MPa)	$\varepsilon_{c'}$ (mm/mm)	E_c (MPa)
C100-A1	100	29	35.4	0.0034	17,803
C100-A2	100	29	35.4	0.0032	20,276
C100-A3	100	29	38.8	0.0031	20,656
AVG			36.6	0.0032	19,578
COV			0.05	0.05	0.08

Cylinder	Diameter (mm)	Age (Days)	f_c' (MPa)	$\varepsilon_{c'}$ (mm/mm)	E_c (MPa)
C150-A1	150	28	excluded		
C150-A2	150	28	31.2	0.0040	14,227
C150-A3	150	28	33.3	0.0043	16,983
AVG			32.3	0.0042	15,605
COV			0.04	0.05	0.12

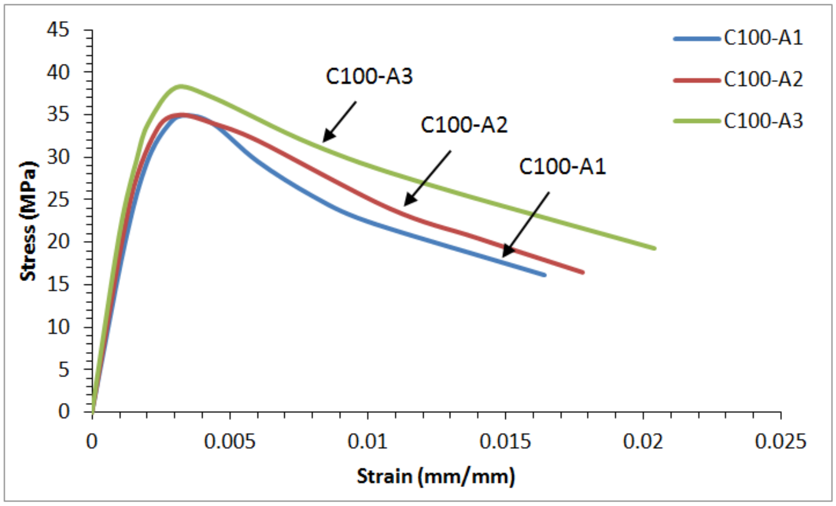

Figure A.2-1: Stress-Strain Curves for 100 mm Diameter Strength Development Cylinders from Casting A

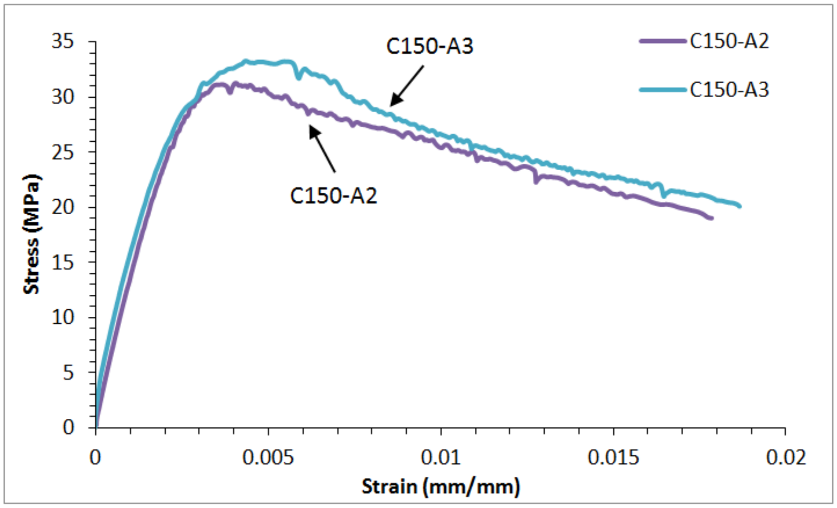

Figure A.2-2: Stress-Strain Curves for 150 mm Diameter Strength Development Cylinders from Casting A

Table A.2-7: Casting B Strength Development Cylinder Results

Strength Development Cylinders - Casting B

Cylinder	Diameter (mm)	Age (Days)	f_c' (MPa)	$\varepsilon_{c'}$ (mm/mm)	E_c (MPa)
C100-B1	100	107	39.3	0.0030	27,005
C100-B2	100	107	39.1	0.0027	27,092
C100-B3	100	107	39.9	0.0027	26,138
AVG			39.5	0.0028	26,745
COV			0.01	0.07	0.02

Cylinder	Diameter (mm)	Age (Days)	f_c' (MPa)	$\varepsilon_{c'}$ (mm/mm)	E_c (MPa)
C150-B1	150	34	30.9	0.0030	18,593
C150-B2	150	34	30.7	0.0030	19,968
C150-B3	150	34	31.5	0.0028	20,872
AVG			31.0	0.0029	19,811
COV			0.01	0.04	0.06

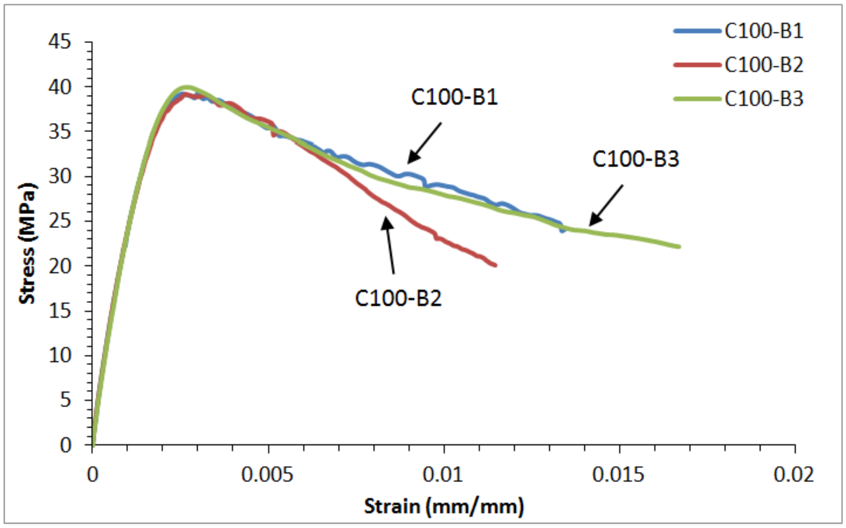

Figure A.2-3: Stress-Strain Curves from 100 mm Diameter Strength Development Cylinders from Casting B

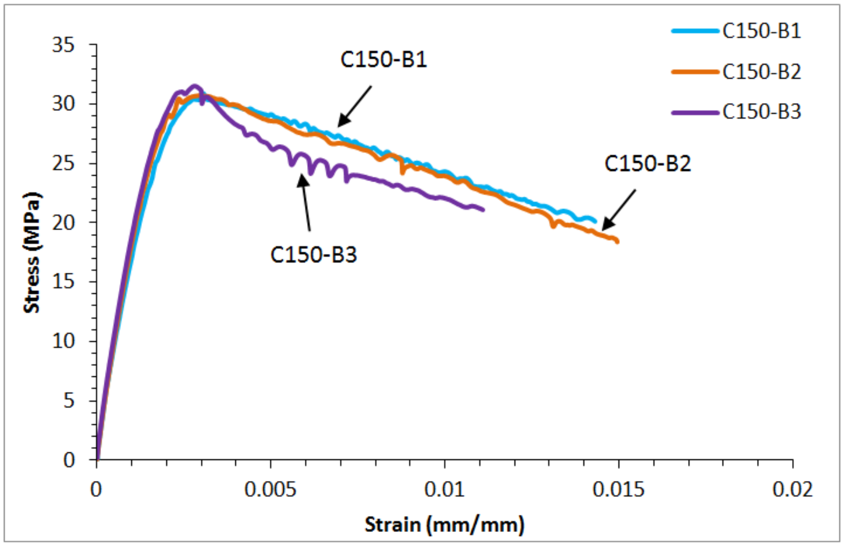

Figure A.2-4: Stress-Strain Curves from 150 mm Diameter Strength Development Cylinders from Casting B

A.3 Large Scale Companion Compression Test Results

In addition to the strength development cylinders, 150 mm diameter cylinders were also produced in Castings A and B and cured alongside the large scale structural specimens as quality control specimens. These cylinders were tested in the MTS Universal Loading Frame after being sulphur capped. A summary of each set of cylinders, along with their full stress-strain curves, is provided below.

Table A.3-1: Specimen S300-B1 Companion Cylinder Results

S300-B1 Companion Cylinders

Cylinder	Diameter (mm)	Age (Days)	f_c' (MPa)	$\varepsilon_{c'}$ (mm/mm)	E_c (MPa)
C150-B10C	150	97	28.8	0.0042	16,269
C150-B11C	150	97	30.1	0.0038	18,274
C150-B12C	150	97	30.6	0.0041	17,446
AVG			29.9	0.0040	17,330
COV			0.03	0.06	0.06

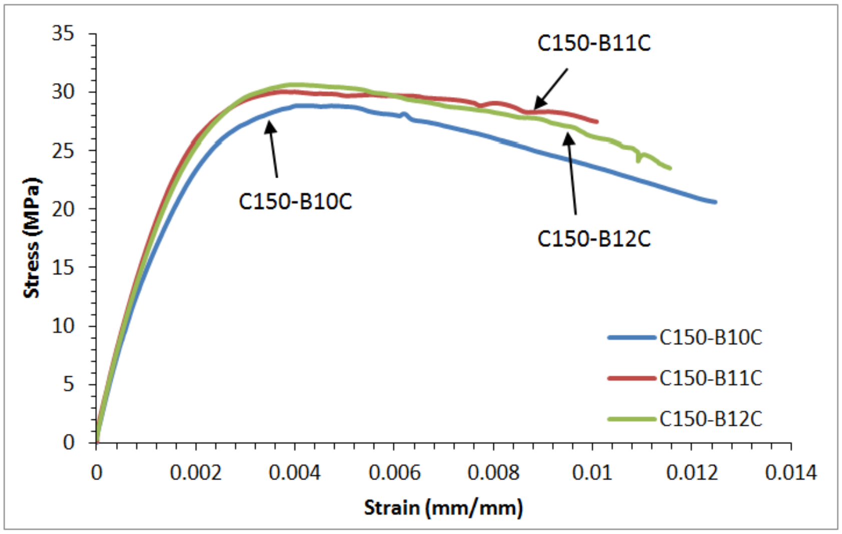

Figure A.3-1: Specimen S300-B1 Companion Cylinder Stress-Strain Curves

Table A.3-2: Specimen S300-A2 Companion Cylinder Results

S300-A2 Companion Cylinders

Cylinder	Diameter (mm)	Age (Days)	f_c' (MPa)	$\varepsilon_{c'}$ (mm/mm)	E_c (MPa)
C150-A10C	150	161	38.0	0.0042	18,090
C150-A11C	150	161	37.7	0.0045	17,207
AVG			37.9	0.0043	17,648
COV			0.00	0.04	0.04

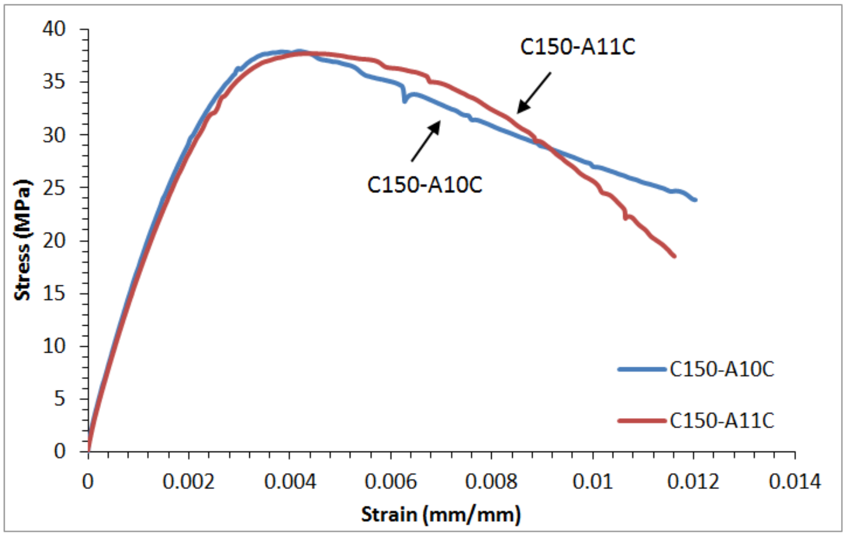

Figure A.3-2: Specimen S300-A2 Companion Cylinder Stress-Strain Curves

Table A.3-3: Specimen S1000-B1 Companion Cylinder Results

S1000-B1 Companion Cylinders

Cylinder	Diameter (mm)	Age (Days)	f_c' (MPa)	$\varepsilon_{c'}$ (mm/mm)	E_c (MPa)
C150-B4C	150	56	29.0	0.0032	18,743
C150-B5C	150	56	31.2	0.0038	20,358*
C150-B6C	150	56	31.0	0.0039	24,003
AVG			30.4	0.0036	21,035
COV			0.04	0.11	0.13

*Measured between the origin and 0.5*f_c’

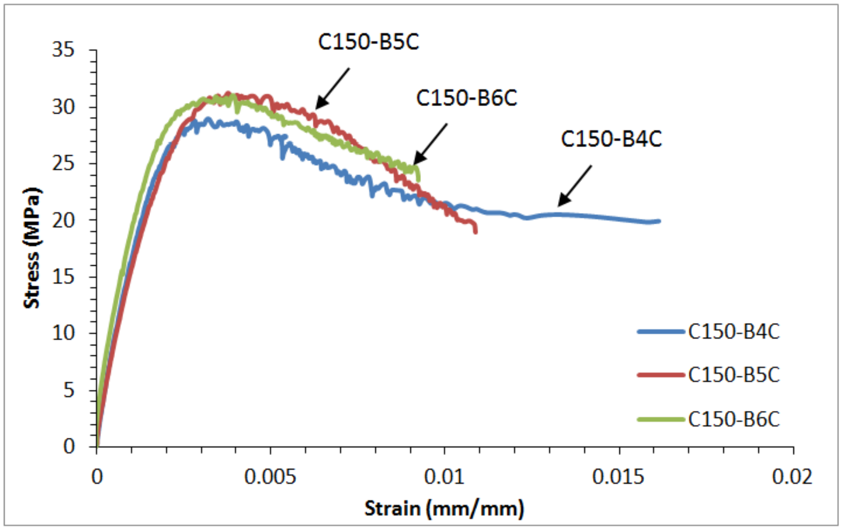

Figure A.3-3: Specimen S1000-B1 Companion Cylinder Stress-Strain Curves

Table A.3-4: Specimen S1000-B2 Companion Cylinder Results

S1000-B2 Companion Cylinders

Cylinder	Diameter (mm)	Age (Days)	f_c' (MPa)	$\varepsilon_{c'}$ (mm/mm)	E_c (MPa)
C150-B7C	150	65	30.5	0.0047	18,373
C150-B8C	150	65	32.2	0.0038	19,473
C150-B9C	150	65	31.0	0.0040	20,353
AVG			31.2	0.0042	19,400
COV			0.03	0.11	0.05

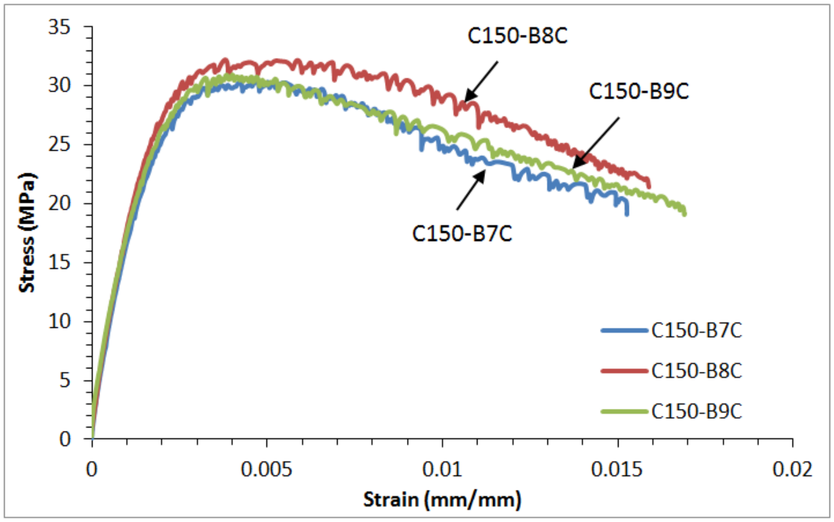

Figure A.3-4: Specimen S1000-B2 Companion Cylinder Stress-Strain Curves

Table A.3-5: Specimen S1000-A3 Companion Cylinder Results

S1000-A3 Companion Cylinders

Cylinder	Diameter (mm)	Age (Days)	f_c' (MPa)	$\varepsilon_{c'}$ (mm/mm)	E_c (MPa)
C150-A7C	150	119	42.1	0.0046	19,731
C150-A8C	150	119	41.0	0.0045	18,189
C150-A9C	150	119	40.5	0.0037	18,866
AVG			41.2	0.0043	18,929
COV			0.02	0.12	0.04

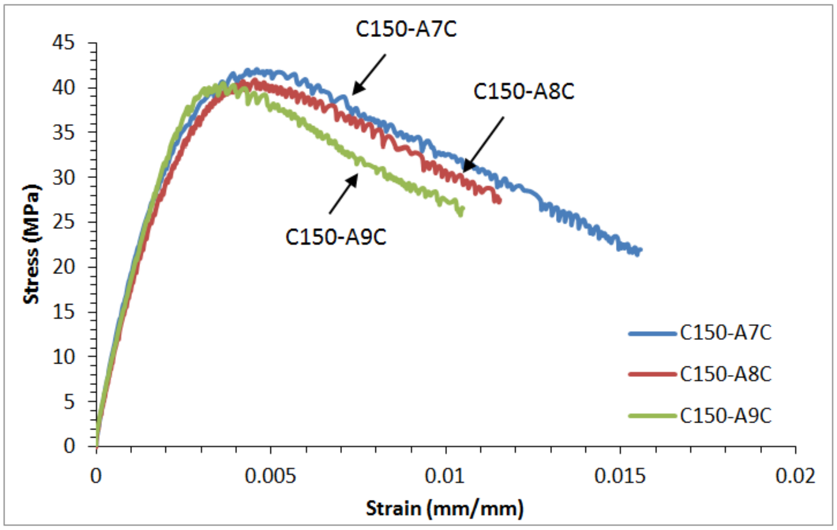

Figure A.3-5: Specimen S1000-A3 Companion Cylinder Stress-Strain Curves

Table A.3-6: Specimen S1000-A4 Companion Cylinder Results

S1000-A4 Companion Cylinders

Cylinder	Diameter (mm)	Age (Days)	f_c' (MPa)	$\varepsilon_{c'}$ (mm/mm)	E_c (MPa)
C150-A4C	150	104	40.7	0.0035	20,580
C150-A5C	150	104	40.2	0.0046	18,420
C150-A6C	150	104	39.3	0.0037	19,003
AVG			40.1	0.0039	19,334
COV			0.02	0.15	0.06

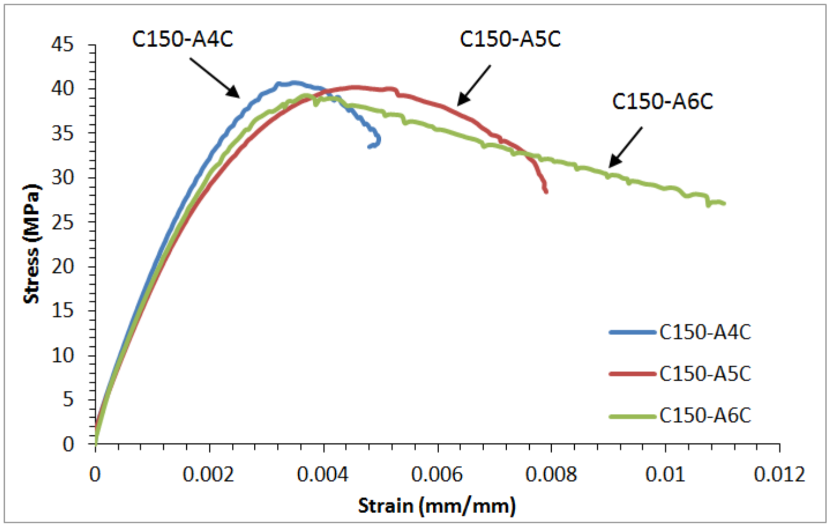

Figure A.3-6: Specimen S1000-A4 Companion Cylinder Stress-Strain Curves

A.4 Strength Development Prisms Flexural Test Results

Flexural tests were performed on notched prisms from Castings A and B according to ASTM C1609-10 to provide an indication of the mix strength development. The prisms were tested in a 1000 kN capacity MTS Universal Loading Frame. A displacement controlled rate of 0.075 mm/min was used for the 100 and 150 mm prisms, while a rate of 0.10 mm/min was used for the 200 mm prisms.

The load-deflection curves, shown as the average for each specimen size, are provided for both Casting A and Casting B. The height of the prisms at the notch location (d_n) are indicated in the tables below as the average of two measurements made using digital callipers. The peak equivalent uniform tensile stress (σ_{ru}) value for each prism, as calculated based on Equation 4-8, are listed in the tables below. A digital image correlation (DIC) system was used in conjunction with the ASTM C1609-10 tests as a non-contact method of measuring surface strains. The vertical deflection (Δ) and CMOD values are based on this system and have been corrected through the software for rigid body motion.

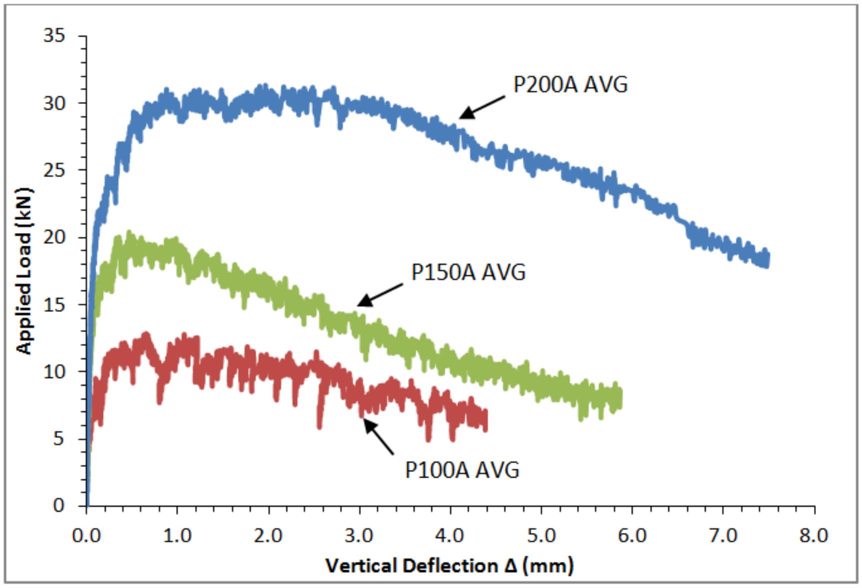

Figure A.4-1: Casting A Strength Development Prisms Average Load-Deflection Curves

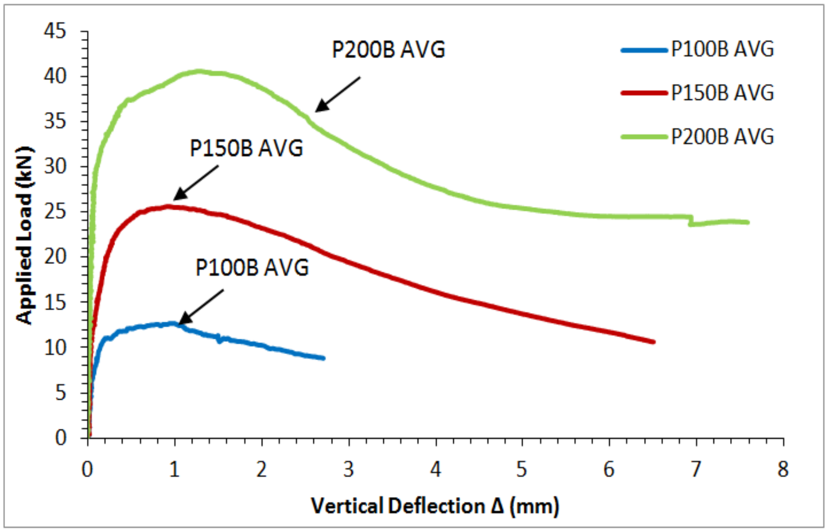

Figure A.4-2: Casting B Strength Development Prisms Average Load-Deflection Curves

Table A.4-1: Casting A Strength Development Prisms Summary of Results

Casting A Strength Development Prisms						
Specimen	d_n (mm)	Peak Load (kN)	MOR (MPa)	CMOD at Peak (mm)	Vertical Δ at Peak (mm)	Peak σ_{ru} (MPa)
P100-A1	75.0	12.31	6.56	0.75	0.64	2.39
P100-A2	73.6	14.84	8.23	0.38	0.37	3.07
P100-A3	74.8	14.90	7.99	1.20	1.04	2.97
AVG	74.5	14.01	7.59	0.78	0.68	2.81
COV	0.01	0.11	0.12	0.53	0.50	0.13
P150-A1	110.2	21.20	5.24	0.84	0.72	1.87
P150-A2	112.1	21.49	5.13	1.02	0.90	1.83
P150-A3	113.4	21.10	4.93	0.66	0.57	1.75
AVG	111.9	21.26	5.10	0.84	0.73	1.82
COV	0.01	0.01	0.03	0.22	0.22	0.03
P200-A1	152.7	45.93	5.91	1.72	1.50	2.13
P200-A2	150.6	33.47	4.43	1.46	1.31	1.56
P200-A3	147.0	25.29	3.51	0.21	0.22	1.23
AVG	150.1	34.89	4.62	1.13	1.01	1.64
COV	0.02	0.30	0.26	0.71	0.68	0.28

Table A.4-2: Casting B Strength Development Prisms Summary of Results

Casting B Strength Development Prisms						
Specimen	d_n (mm)	Peak Load (kN)	MOR (MPa)	CMOD at Peak (mm)	Vertical Δ at Peak (mm)	Peak σ_{ru} (MPa)
P100-B1	71.3	12.34	7.29	1.05	0.84	2.69
P100-B2	72.9	11.79	6.67	0.86	0.75	2.44
P100-B3	73.7	14.53	8.03	1.03	0.86	3.00
AVG	72.6	12.89	7.33	0.98	0.82	2.71
COV	0.02	0.11	0.09	0.11	0.07	0.10
P150-B1	115.2	27.57	6.23	0.59	0.53	2.27
P150-B2	113.9	29.59	6.85	1.23	1.09	2.51
P150-B3	113.5	25.12	5.86	0.98	0.82	2.12
AVG	114.2	27.43	6.31	0.94	0.81	2.30
COV	0.01	0.08	0.08	0.35	0.35	0.09
P200-B1	149.4	43.25	5.82	1.62	1.43	2.10
P200-B2	150.0	39.24	5.23	1.65	1.37	1.88
P200-B3	149.7	39.58	5.30	1.34	1.16	1.90
AVG	149.7	40.69	5.45	1.54	1.32	1.96
COV	0.00	0.05	0.06	0.11	0.11	0.06

The relationship between the equivalent uniform tensile stress (σ_{ru}) and the CMOD is shown in the figures below as the average of each prism size.

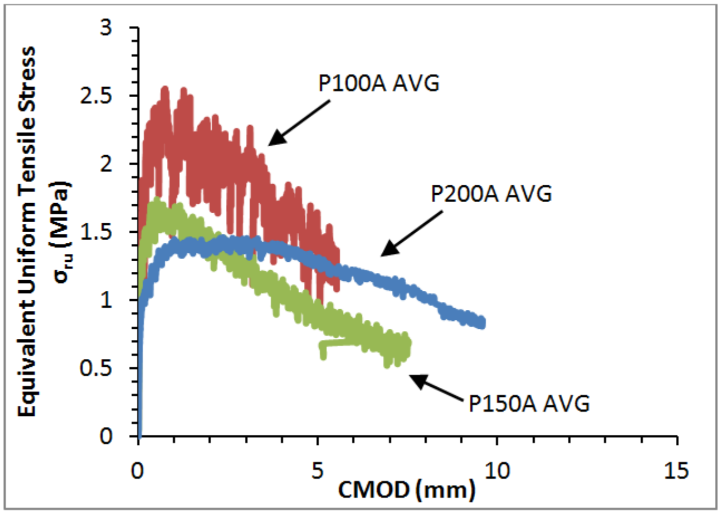

Figure A.4-3: Average Equivalent Uniform Tensile Stress-CMOD Curves for Casting A Strength Development Prisms

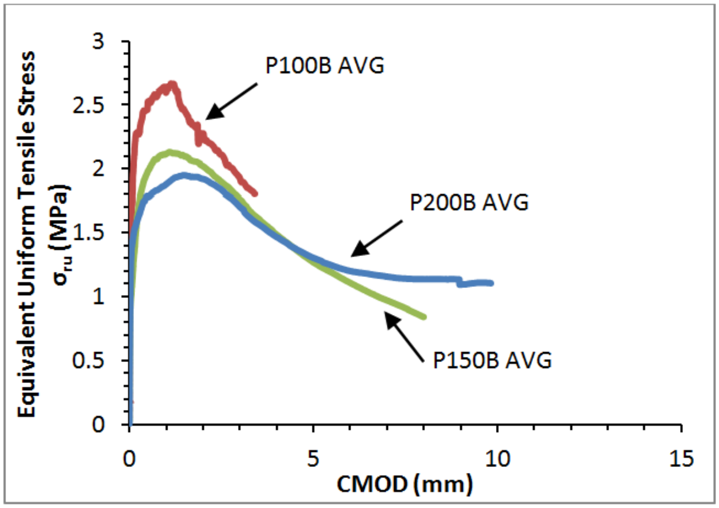

Figure A.4-4: Average Equivalent Uniform Tensile Stress-CMOD Curves for Casting B Strength Development Prisms

A.5 Companion Prisms Flexural Test Results

Flexural tests were performed on notched prisms from Castings A and B according to ASTM C1609-10 as companions to the large scale specimens. The prisms were tested in a 1000 kN capacity MTS Universal Loading Frame. A displacement controlled rate of 0.075 mm/min was used for the 100 and 150 mm prisms, while a rate of 0.10 mm/min was used for the 200 mm prisms.

The load-deflection curves, shown as the average for each specimen size, are provided for both Casting A and Casting B. The height of the prisms at the notch location (d_n) are indicated in the tables below as the average of two measurements made using digital callipers. The peak equivalent uniform tensile stress (σ_{ru}) value for each prism, as calculated based on Equation 4-8, are listed in the tables below. A digital image correlation (DIC) system was used in conjunction with the ASTM C1609-10 tests as a non-contact method of measuring surface strains. The vertical deflection (Δ) and CMOD values are based on this system and have been corrected through the software for rigid body motion.

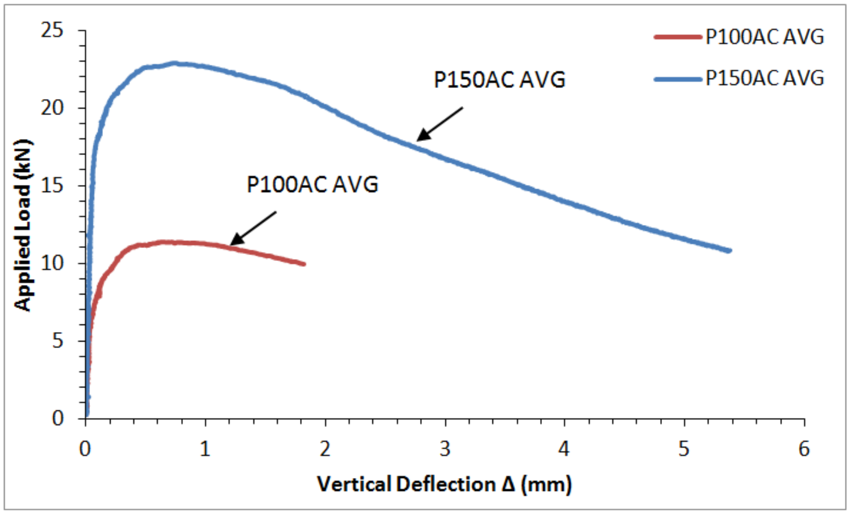

Figure A.5-1: Casting A Companion Prisms Average Load-Deflection Curves

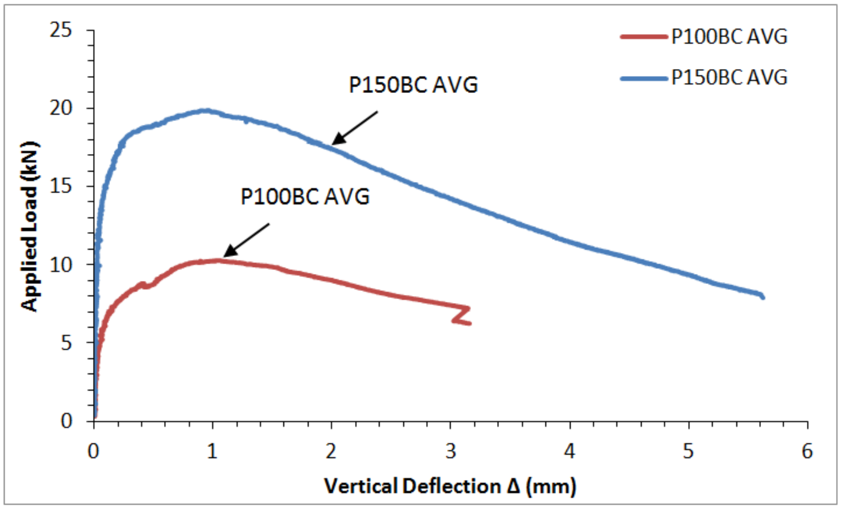

Figure A.5-2: Casting B Companion Prisms Average Load-Deflection Curves

Table A.5-1: Casting A Companion Prisms Summary of Results

Casting A Companion Prisms						
Specimen	d_n (mm)	Peak Load (kN)	MOR (MPa)	CMOD at Peak (mm)	Vertical Δ at Peak (mm)	Peak σ_{ru} (MPa)
P100-A4C	75.0	11.93	6.36	0.82	0.61	2.28
P100-A5C	72.2	12.37	7.12	0.50	0.44	2.58
P100-A6C	75.0	12.49	6.66	0.30	0.34	2.40
AVG	74.1	12.26	6.71	0.54	0.46	2.42
COV	0.02	0.02	0.06	0.48	0.30	0.06
P150-A4C	112.8	24.38	5.75	1.24	1.02	2.05
P150-A5C	115.0	22.14	5.03	0.88	0.78	1.77
P150-A6C	113.8	24.98	5.79	0.63	0.54	2.06
AVG	113.9	23.83	5.52	0.91	0.78	1.96
COV	0.01	0.06	0.08	0.34	0.31	0.08

Table A.5-2: Casting B Companion Prisms Summary of Results

Casting B Companion Prisms						
Specimen	d_n (mm)	Peak Load (kN)	MOR (MPa)	CMOD at Peak (mm)	Vertical Δ at Peak (mm)	Peak σ_{ru} (MPa)
P100-B4C	75.4	10.93	5.77	0.39	0.34	2.09
P100-B5C	75.9	11.66	6.07	0.74	0.67	2.21
P100-B6C	75.9	9.89	5.16	0.81	0.67	1.85
AVG	75.7	10.83	5.67	0.65	0.56	2.05
COV	0.00	0.08	0.08	0.35	0.34	0.09
P150-B4C	115.5	17.46	3.93	0.44	0.37	1.39
P150-B5C	113.6	24.72	5.75	0.74	0.66	2.08
AVG	114.6	21.09	4.84	0.59	0.51	1.73
COV	0.01	0.24	0.27	0.36	0.39	0.28

A.6 Flexural Toughness Values and Residual Tensile Strengths

The flexural toughness (T_{150}) of each prism was determined by the area under the load-deflection curve from the ASTM C1609-10 tests up to a deflection limit of L/150. These toughness values are listed below for both the strength development and companion prisms. The equivalent flexural strength ratio ($R_{T,150}$) was also determined for each specimen as described in Section 4.2.

To compare with the ACI 318-08 residual strength requirements for the use of SFRC as a method of shear resistance, the residual strength of the prisms at deflections of L/300 and L/150 were obtained (f_{test}). These measured strengths are listed in the tables below as a percentage of the ACI 318-08 required strength. Details are provided in Section 4.2.4. In the tables below, $f_{90\%}$ represents 90% of the first peak strength and corresponds to the deflection of L/300. Deflections at L/150 correspond to $f_{75\%}$, which represents 75% of the first peak strength. The tables also indicate whether the specimen passed these two ACI 318-08 residual strength requirements.

Table A.6-1: Casting A Strength Development Prisms Toughness and Residual Tensile Strength Values

Casting A Strength Development Prisms						
Specimen	d_n (mm)	T_{150} (J)	$R_{T,150}$ (%)	$f_{test}/f_{90\%}$ (%)	$f_{test}/f_{75\%}$ (%)	Pass ACI 318-08?
P100-A1	75.0	20,410	82.9	90.9	97.8	No
P100-A2	73.6	24,668	83.1	97.5	104.2	No
P100-A3	74.8	25,644	86.0	99.7	121.4	No
AVG	74.5	23,574	84.0	96.0	107.8	
COV	0.01	0.12	0.02	0.05	0.11	
P150-A1	110.2	48,494	76.3	80.0	74.7	No
P150-A2	112.1	53,402	82.8	97.7	90.4	No
P150-A3	113.4	49,298	77.9	83.3	81.9	No
AVG	111.9	50,398	79.0	87.0	82.3	
COV	0.01	0.05	0.04	0.11	0.10	
P200-A1	152.7	157,249	85.6	105.4	102.3	Yes
P200-A2	150.6	113,521	84.8	100.0	98.2	No
P200-A3	147.0	72,606	71.8	79.3	66.1	No
AVG	150.1	114,459	80.7	94.9	88.9	
COV	0.02	0.37	0.10	0.15	0.22	

Table A.6-2: Casting B Strength Development Prisms Toughness and Residual Tensile Strength Values

Casting B Strength Development Prisms						
Specimen	d_n (mm)	T_{150} (J)	$R_{T,150}$ (%)	$f_{test}/f_{90\%}$ (%)	$f_{test}/f_{75\%}$ (%)	Pass ACI 318-08?
P100-B1	71.3	21,339	86.5	99.0	102.1	No
P100-B2	72.9	21,501	91.2	108.5	104.4	Yes
P100-B3	73.7	25,745	88.6	109.1	111.4	Yes
AVG	72.6	22,862	88.8	105.5	NA	
COV	0.02	0.11	0.03	0.05	NA	
P150-B1	115.2	69,863	84.5	96.7	89.0	No
P150-B2	113.9	77,434	87.2	107.8	99.3	No
P150-B3	113.5	64,894	86.1	103.2	90.3	No
AVG	114.2	70,730	85.9	102.6	92.9	
COV	0.01	0.09	0.02	0.05	0.06	
P200-B1	149.4	151,067	87.3	108.2	101.8	Yes
P200-B2	150.0	133,883	85.3	102.7	86.8	No
P200-B3	149.7	134,944	85.2	104.5	83.0	No
AVG	149.7	139,965	85.9	105.1	90.5	
COV	0.00	0.07	0.01	0.03	NA	

Table A.6-3: Casting A Companion Prisms Toughness and Residual Tensile Strength Values

Casting A Companion Prisms						
Specimen	d_n (mm)	T_{150} (J)	$R_{T,150}$ (%)	$f_{test}/f_{90\%}$ (%)	$f_{test}/f_{75\%}$ (%)	Pass ACI 318-08?
P100-A4C	75.0	21,316	89.4	103.8	100.6	Yes
P100-A5C	72.2	22,761	92.0	107.2	110.4	Yes
P100-A6C	75.0	21,622	86.6	97.5	103.0	No
AVG	74.1	21,900	89.3	102.8	104.7	
COV	0.02	0.03	0.03	0.05	0.05	
P150-A4C	112.8	64,785	88.6	105.1	98.6	No
P150-A5C	115.0	57,394	86.4	101.5	92.8	No
P150-A6C	113.8	63,839	85.2	100.5	86.6	No
AVG	113.9	62,006	86.7	102.4	92.7	
COV	0.01	0.06	0.02	0.02	0.06	

Table A.6-4: Casting B Companion Prisms Toughness and Residual Tensile Strength Values

Casting B Companion Prisms						
Specimen	d_n (mm)	T_{150} (J)	$R_{T,150}$ (%)	$f_{test}/f_{90\%}$ (%)	$f_{test}/f_{75\%}$ (%)	Pass ACI 318-08?
P100-B4C	75.4	19,316	88.4	104.7	101.1	Yes
P100-B5C	75.9	21,800	93.5	109.9	121.5	Yes
P100-B6C	75.9	17,751	89.8	106.6	105.9	Yes
AVG	75.7	19,622	90.6	107.1	NA	
COV	0.00	0.10	0.03	0.02	121.50	
P150-B4C	115.5	43,311	82.7	92.7	87.5	No
P150-B5C	113.6	63,204	85.2	101.9	90.6	No
AVG	114.6	53,258	84.0	97.3	NA	
COV	0.01	0.26	0.02	0.07	NA	

Appendix B **: ASTM A1035 Reinforcement Details**

B.1 ASTM A1035 Reinforcing Steel Coupon Test Results

Tension coupon tests were performed according to ASTM A370-11 on the #6 and #9 ASTM A1035 steel reinforcing bars used in the current study. The data provided in Appendix B is intended to complement Section 5.4.2, and has been previously been summarized in that section.

Punch marks were placed every 50 mm along the gauge length of each test specimen. The initial and final lengths between the notches are compared below, as measured by digital callipers.

Table B.1-1: ASTM A1035 Reinforcing Steel Coupon Punch Mark Measurements

Notch		Distance Between Notches (mm)					
		6-1	6-2	6-3	9-1	9-2	9-3
1-2	Initial	50.60	50.68	50.23	49.56	49.85	49.50
	Final	54.28	52.73	52.33	52.39	52.92	51.73
2-3	Initial	50.24	49.90	49.85	49.54	50.02	50.14
	Final	Fracture	51.95	Fracture	57.7	58.02	52.47
3-4	Initial	50.21	50.64	50.39	50.58	49.78	49.78
	Final	51.99	52.89	52.16	54.29	55.08	52.31
4-5	Initial	50.70	50.45	49.45	49.95	50.05	50.28
	Final	52.34	Fracture	51.25	52.61	52.92	59.3

Table B.1-2: ASTM A1035 #6 Reinforcing Steel Coupon Test Results

Coupon	E_s (MPa)	$\sigma_{0.0035}$ (MPa)	σ_y (MPa)	ε_y (mm/mm)	σ_{peak} (MPa)	ε_{peak} (mm/mm)
6-1	196,336	661.2	941.0	0.0068	1130.0	0.0435
6-2	192,923	653.2	958.1	0.0070	1136.9	0.0424
6-3	196,329	666.1	939.4	0.0068	1155.8	0.0409
AVG	195,196	660.2	946.2	0.0068	1140.9	0.0423
COV	0.01	0.01	0.01	0.01	0.01	0.03

Table B.1-3: ASTM A1035 #9 Reinforcing Steel Coupon Test Results

Coupon	E_s (MPa)	$\sigma_{0.0035}$ (MPa)	σ_y (MPa)	ε_y (mm/mm)	σ_{peak} (MPa)	ε_{peak} (mm/mm)
9-1	203,066	659.2	922.3	0.0065	1204.2	0.0574
9-2	190,395	635.7	918.7	0.0068	1203.2	0.0602
9-3	198,095	654.5	903.8	0.0066	1191.6	0.0486
AVG	197,185	649.8	914.9	0.0066	1199.7	0.0554
COV	0.03	0.02	0.01	0.02	0.01	0.11

Appendix C : **Large Scale Structural Specimen Details**

C.1 General

Appendix C deals with the individual responses of each of the large scale structural specimens and is intended to complement the data summarized in Sections 5 and 6.

The external instrumentation was initially calibrated prior to testing of Specimen S1000-A4, which was the first large scale structural specimen tested. In between each test, all instrumentation was checked for accuracy and re-calibrated when necessary. The MTS load and stroke and all additional instrumentations were zeroed prior to the start of loading.

The load values stated are based on the MTS applied load, and do not account for the self weight of the specimen, the W250 stub column spacer or the loading plate. Deflection measurements at the quarter span points and at mid-span have all been corrected for average support settlement, as measured by the LVDTs at each support.

In general, the following items are discussed for each specimen:

- The overall setup and electrical resistance strain gauge locations. The strain gauges have been labelled A to G as recorded during each test, with strain gauge D located at mid-span in all specimens. Strain gauges A and G were located adjacent to the supports, and were only installed on S1000-A3 and S1000-A4.
- The load history response showing each load stage.
- The load-deflection response at both the mid-span and as the average of the quarter span points.
- The crack patterns and widths as measured by the crack comparator gauge at each numbered load stage.
- The failure crack growth during loading.
- The concrete surface strains as measured by the four PI gauges.
- The longitudinal reinforcement strains along the length of the specimens, as measured by the electrical resistance strain gauges at various load levels.
- The predicted moment-curvature relationships as determined through both the Simplified and Appendix B steel reinforcement stress-strain relationships provided in ACI ITG-6R-10.
- The predicted curvature along the length of each specimen.
- A comparison between the predicted and measured mid-span deflections at the service load level.
- A comparison between the predicted and measured relationships between the applied load and the mid-span deflection.

All references to Simplified refer to the ACI ITG-6R-10 Simplified model for ASTM A1035 Grade 690 steel reinforcement, while Appendix B refers to the ACI ITG-6R-10 Appendix B model.

C.2 Specimen S300-B1

Specimen S300-B1 was the third specimen from Casting B to be tested and the last specimen overall. A displacement controlled loading rate of 0.125 mm/min was used to start the test. At a post-peak load of approximately 229 kN, the loading rate was increased to 0.15 mm/min. At a post-peak load of approximately 212 kN, the loading rate was again increased to 0.20 mm/min. Failure occurred in the east end of the specimen.

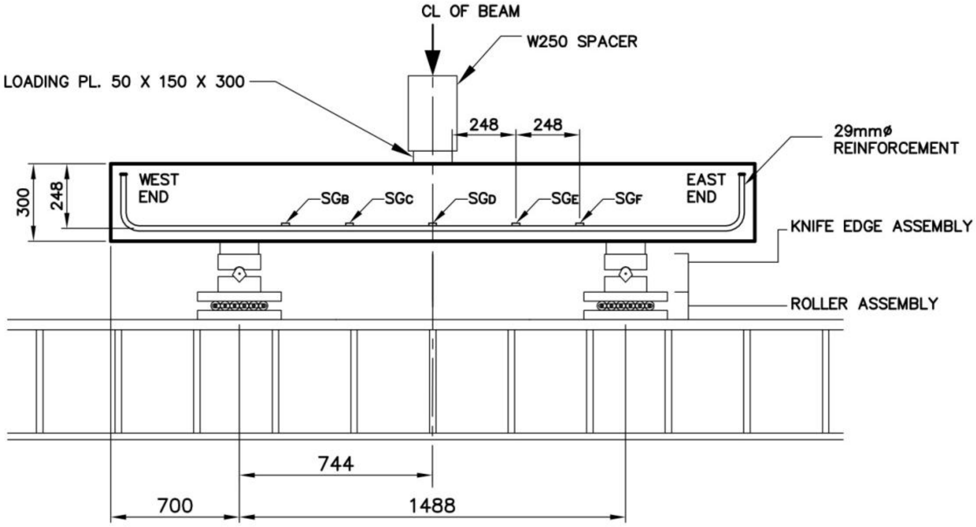

Figure C.2-1: Specimen S300-B1 Test Setup and Configuration

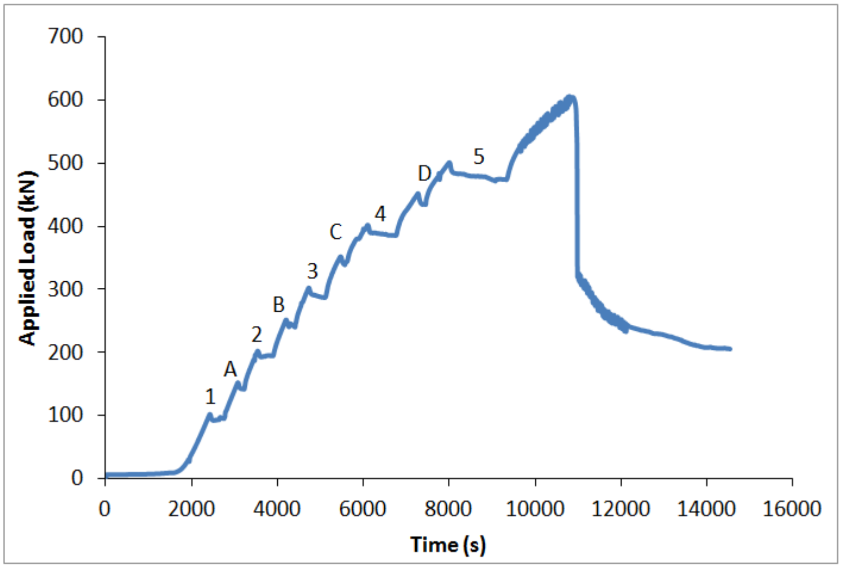

Figure C.2-2: Specimen S300-B1 Load Stages

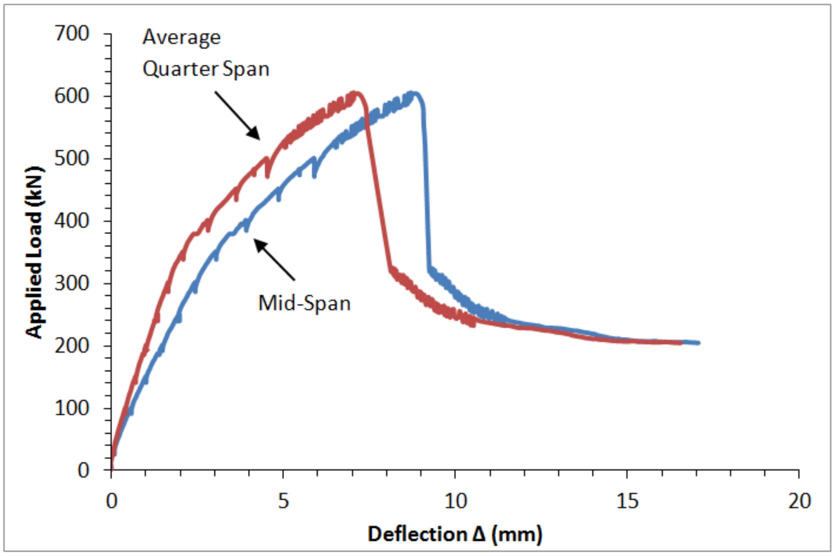

Figure C.2-3: Specimen S300-B1 Load-Deflection Relationships

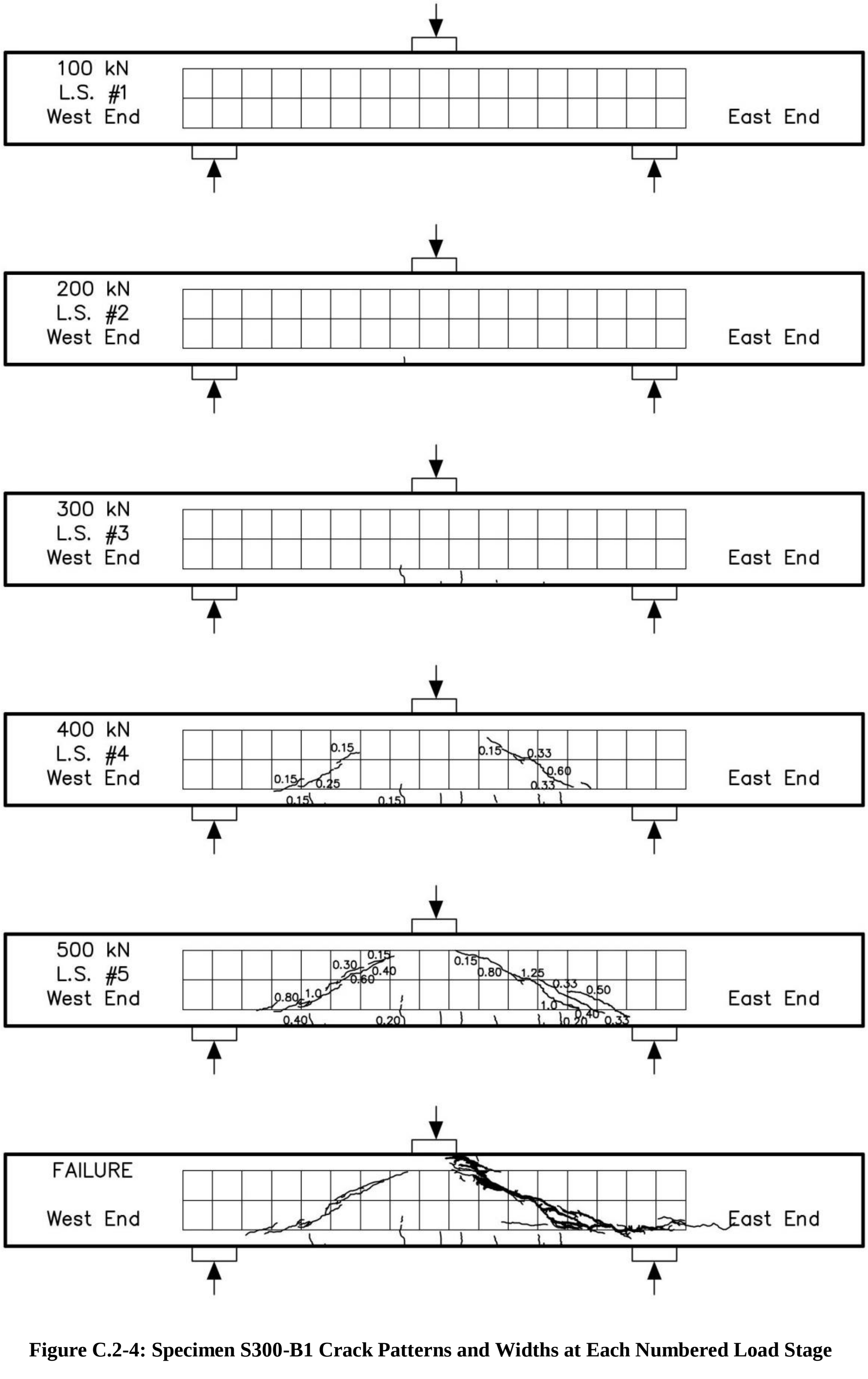

Figure C.2-4: Specimen S300-B1 Crack Patterns and Widths at Each Numbered Load Stage

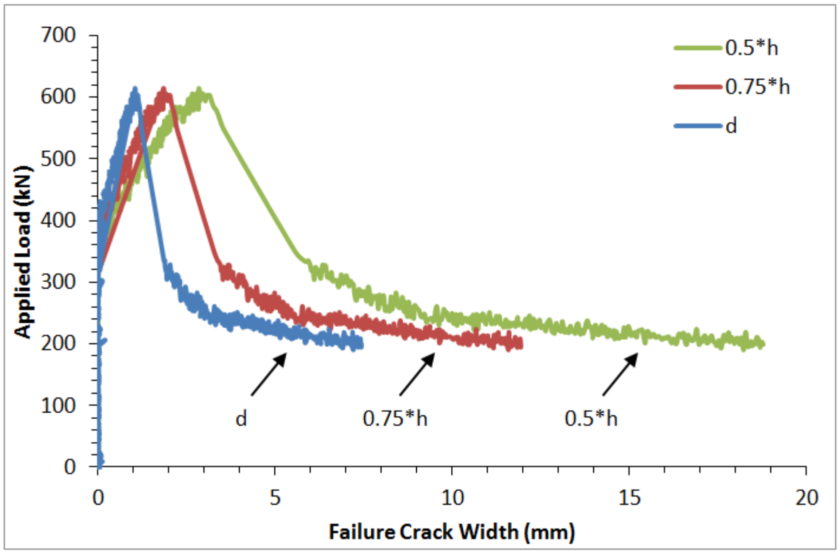

Figure C.2-5: Specimen S300-B1 Failure Crack Growth Throughout Testing

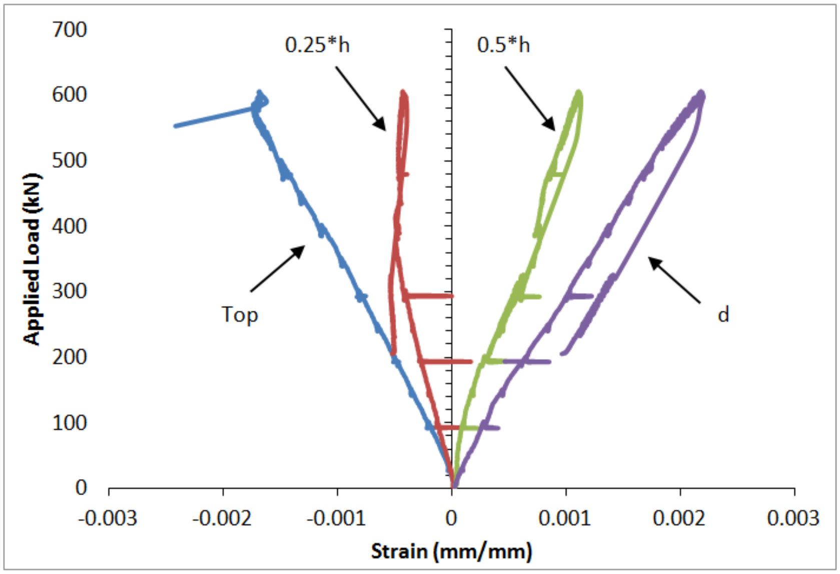

Figure C.2-6: Specimen S300-B1 Concrete Surface Strains as Measured by PI Gauges Throughout Testing

The strain gauge located at d from the face of the loading plate in the east span did not function during testing and has not been included in Figure C.2-7.

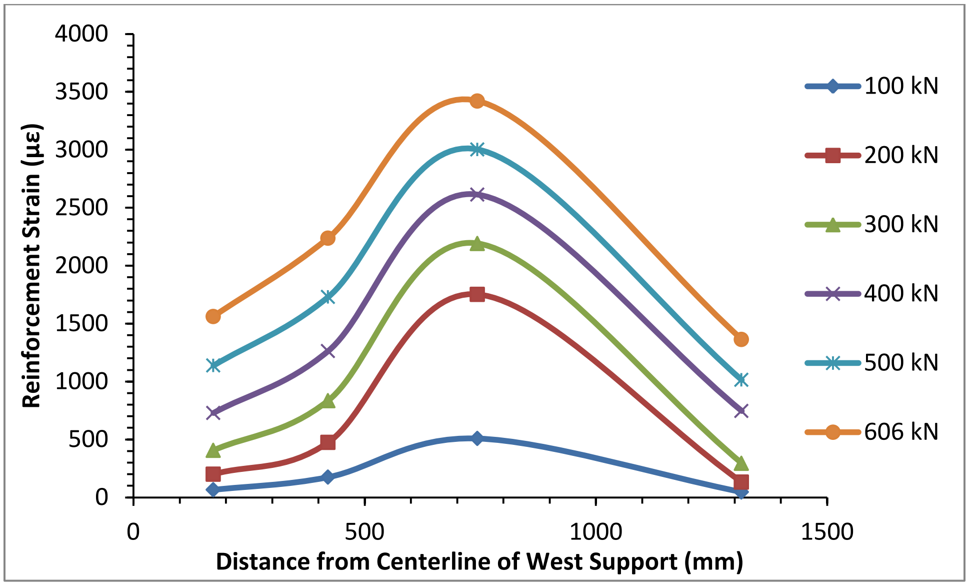

Figure C.2-7: Specimen S300-B1 Longitudinal Reinforcement Strains at Various Load Stages

The longitudinal reinforcement in Specimen S300-B1 did not exceed the 690 MPa design yield strength from the ACI ITG-6R-10 Simplified method in the deflection prediction calculations, as illustrated in Figure C.2-8. The predicted moment-curvature relationship is therefore identical based on both the Simplified and Appendix B stress-strain relationships.

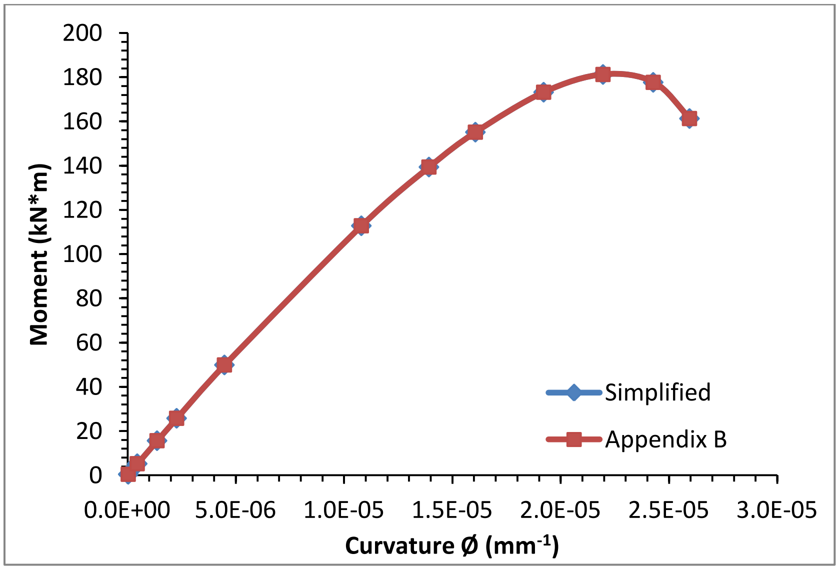

Figure C.2-8: Specimen S300-B1 Predicted Moment-Curvature Relationships

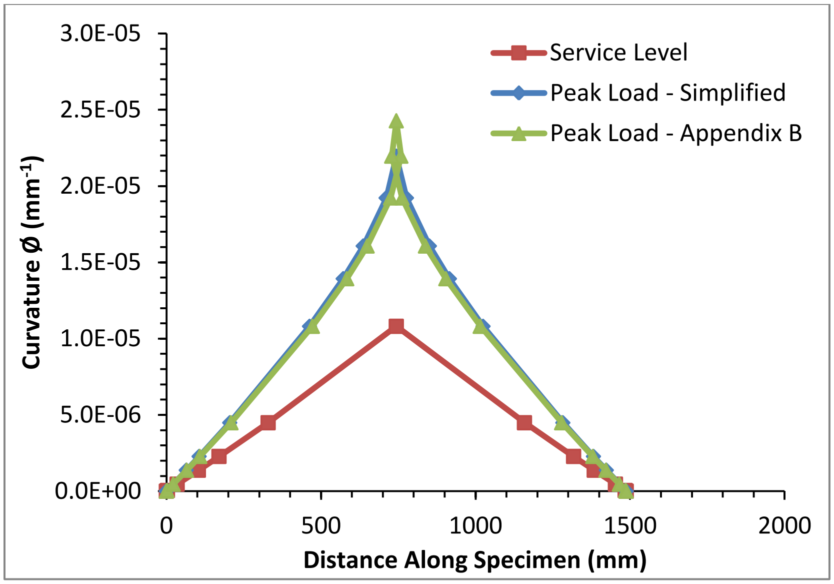

Figure C.2-9: Predicted Curvatures Along the Length of Specimen S300-B1

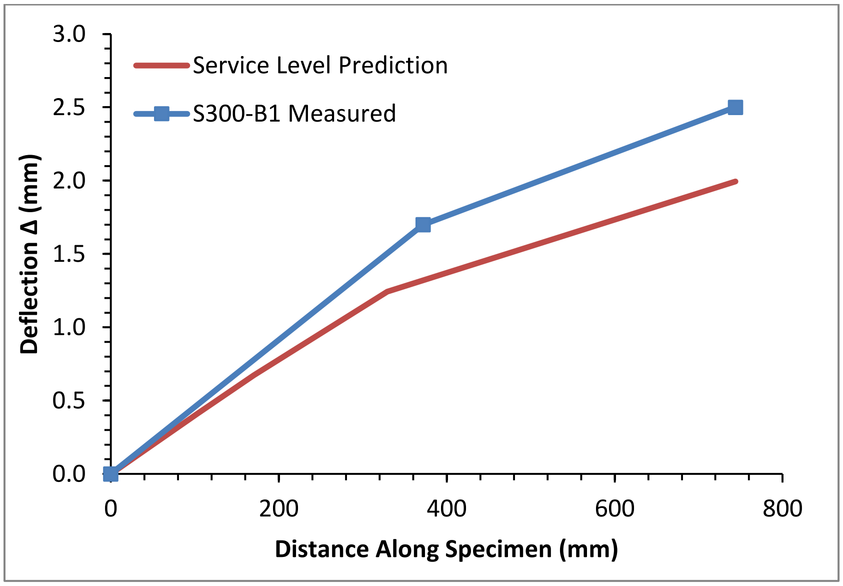

Figure C.2-10: Comparison of Predicted and Measured Service Load Deflections Along the Length of Specimen S300-B1

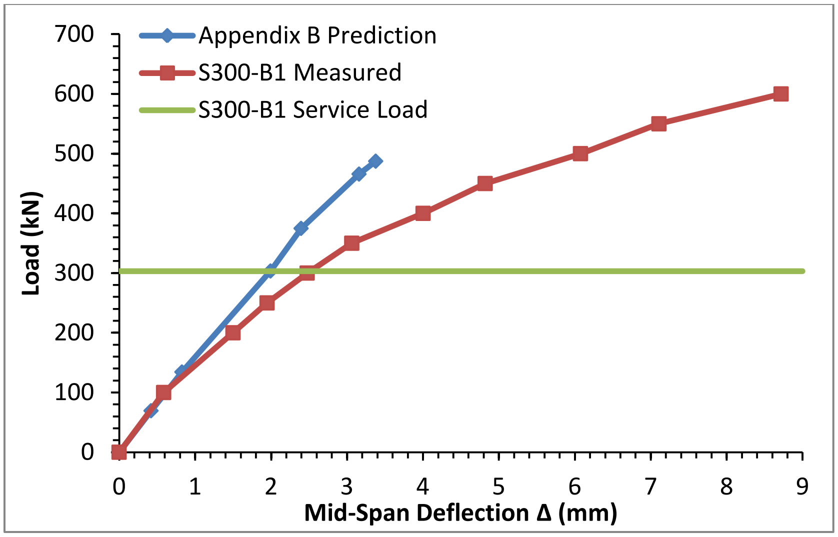

Figure C.2-11: Comparison of Predicted and Measured Load-Mid-Span Deflection Relationships for Specimen S300-B1

C.3 Specimen S300-A2

Specimen S300-A2 was the third specimen from Casting A to be tested and the fifth specimen overall. The displacement controlled loading rate was 0.15 mm/min. Failure occurred on the east end of the specimen.

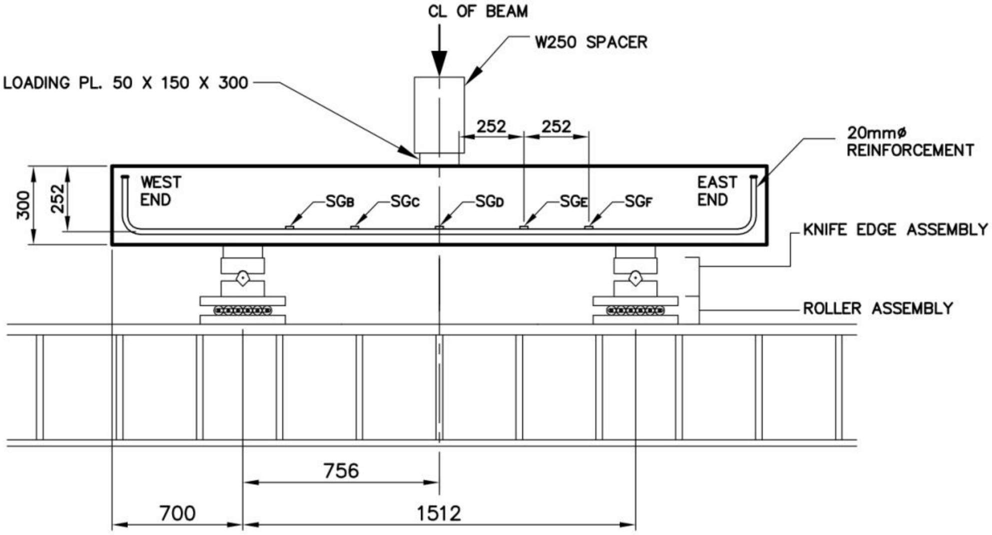

Figure C.3-1: Specimen S300-A2 Test Setup and Configuration

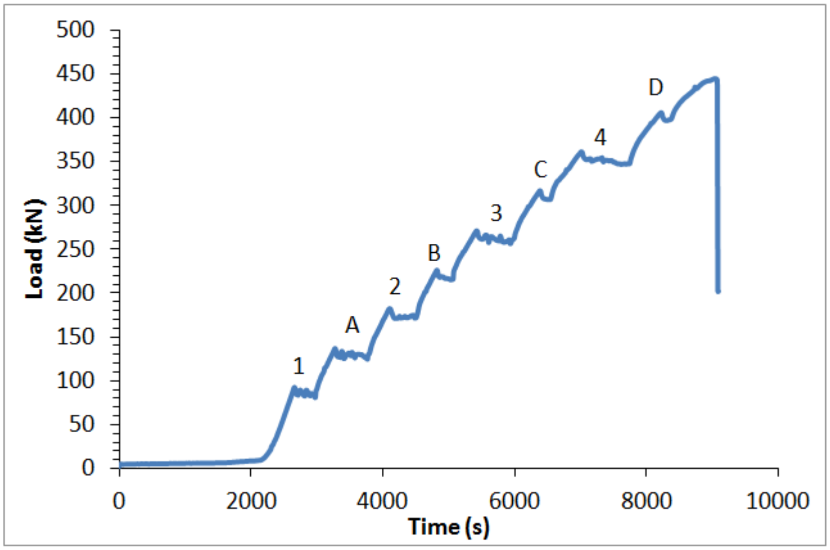

Figure C.3-2: Specimen S300-A2 Load Stages

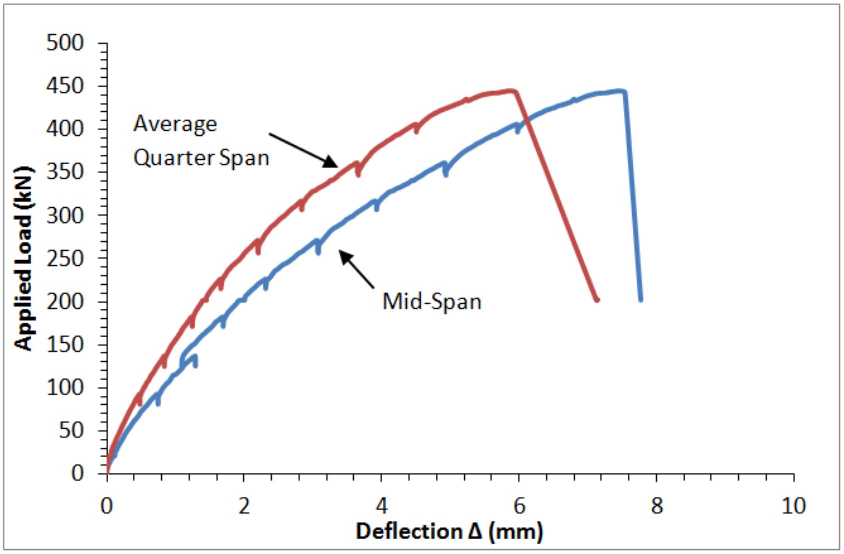

Figure C.3-3: Specimen S300-A2 Load-Deflection Relationships

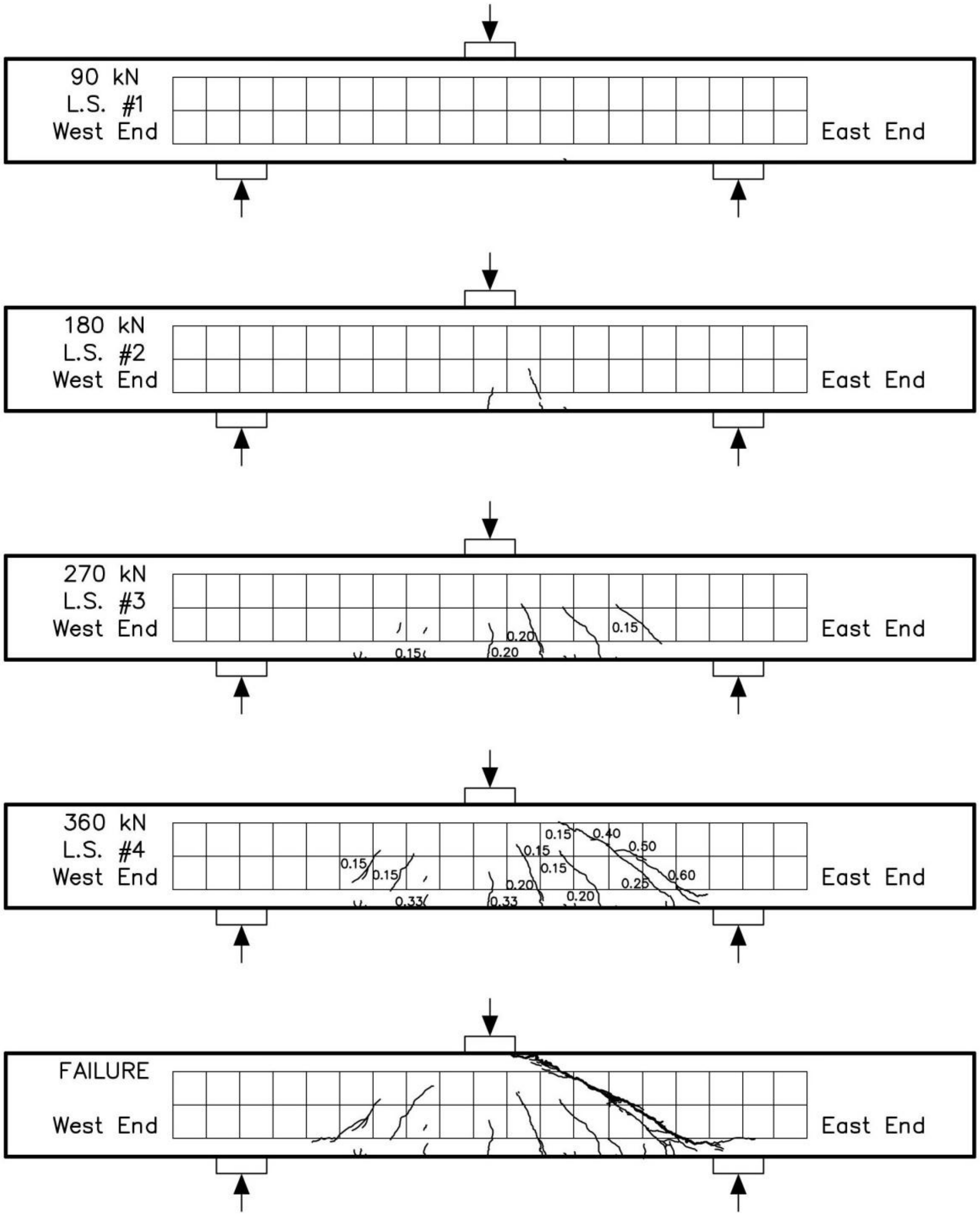

Figure C.3-4: Specimen S300-A2 Crack Patterns and Widths at Each Numbered Load Stage

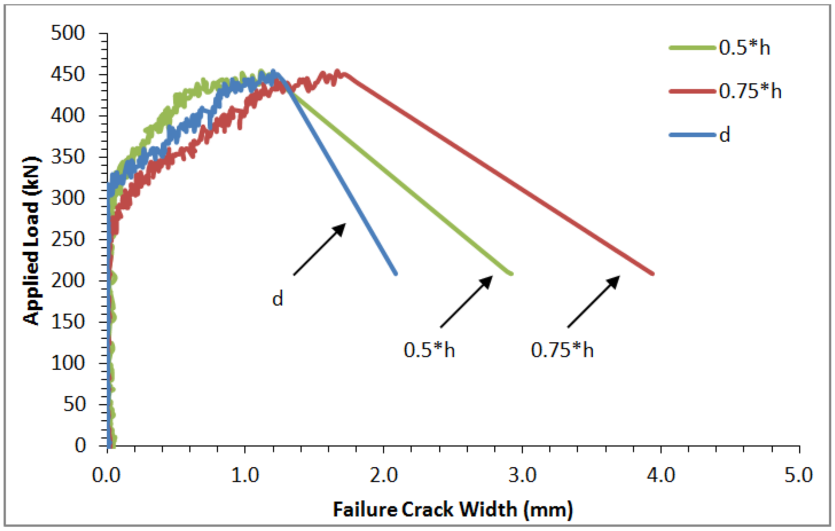

Figure C.3-5: Specimen S300-A2 Failure Crack Growth Throughout Testing

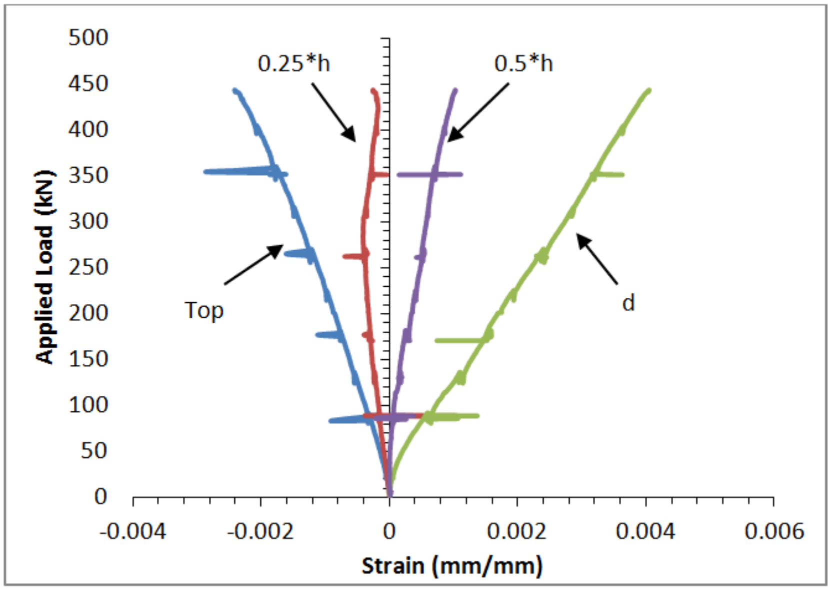

Figure C.3-6: Specimen S300-A2 Concrete Surface Strains as Measured by PI Gauges Throughout Testing

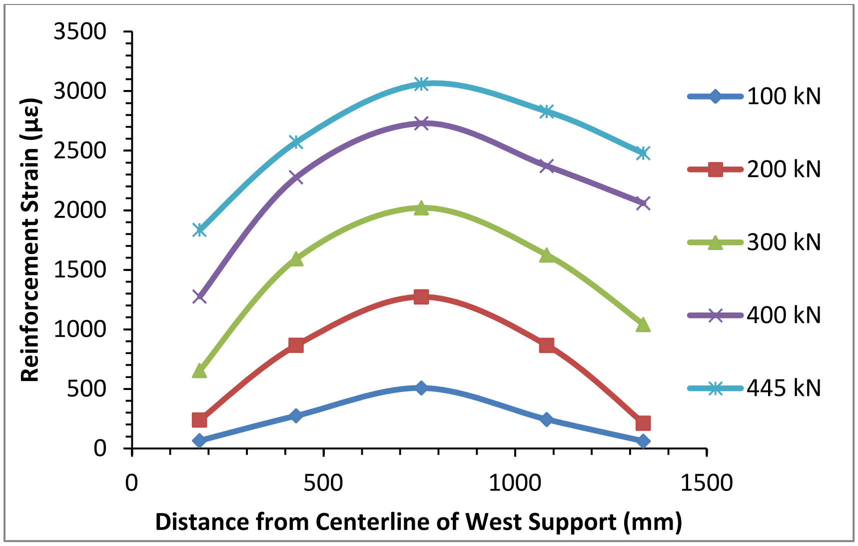

Figure C.3-7: Specimen S300-A2 Longitudinal Reinforcement Strains at Various Load Stages

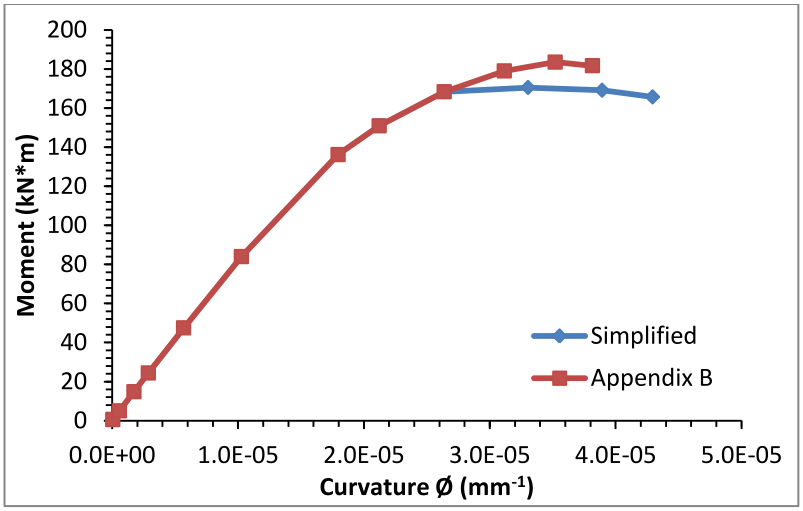

Figure C.3-8: Specimen S300-A2 Predicted Moment-Curvature Relationships

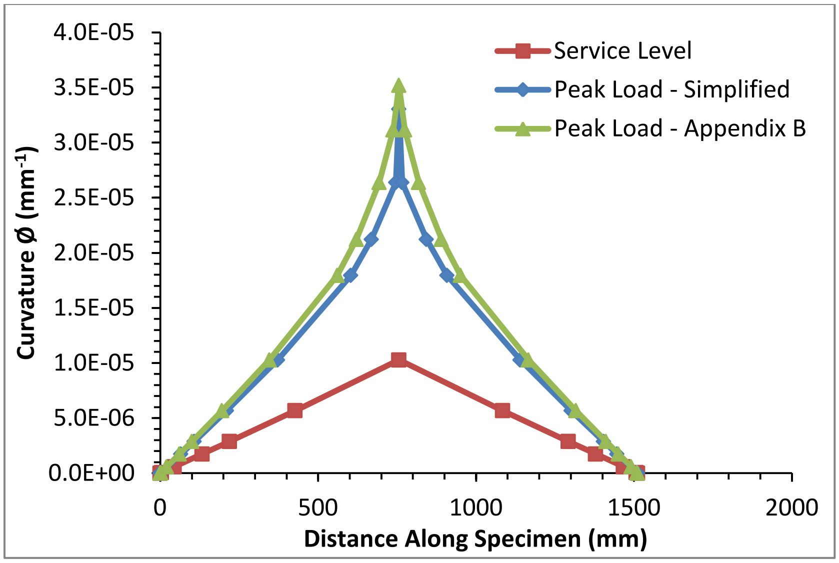

Figure C.3-9: Predicted Curvatures Along the Length of Specimen S300-A2

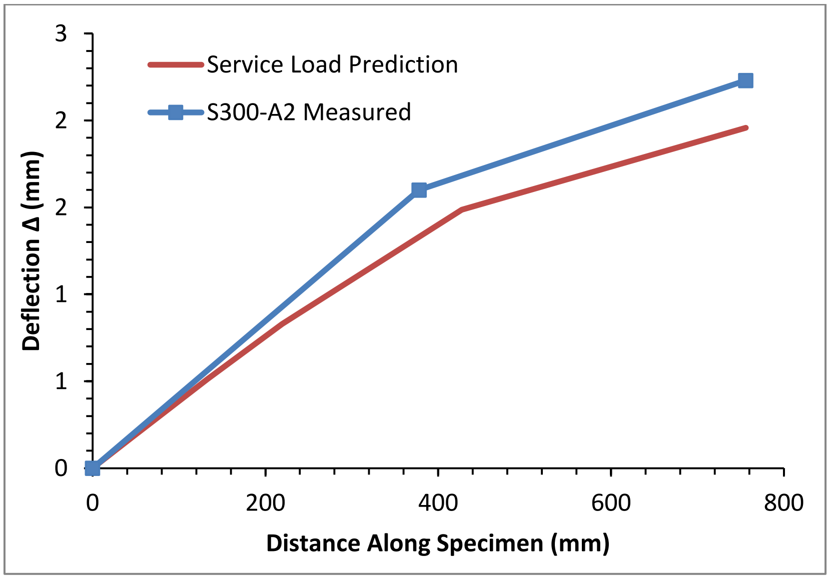

Figure C.3-10: Comparison of Predicted and Measured Service Load Deflections Along the Length of Specimen S300-A2

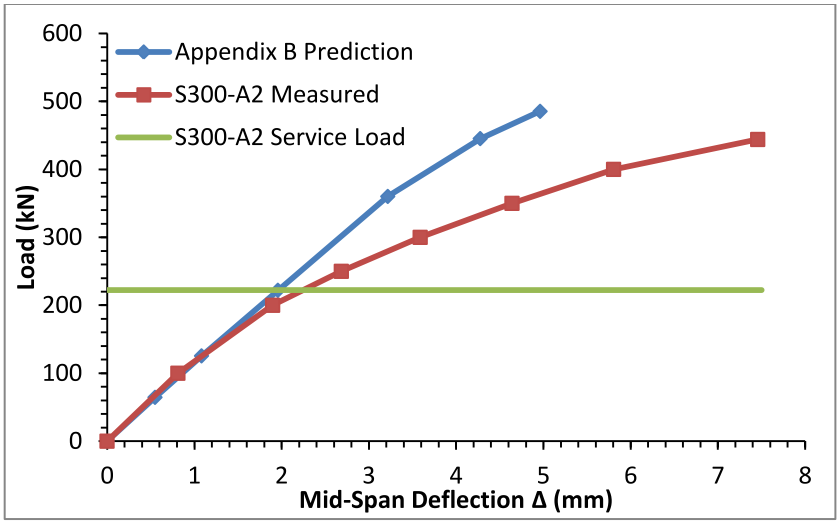

Figure C.3-11: Comparison of Predicted and Measured Load-Mid-Span Deflection Relationships for Specimen S300-A2

C.4 Specimen S1000-B1

Specimen S1000-B1 was the first specimen from Casting B to be tested, and the third overall. A displacement controlled loading rate of 0.3 mm/min was used. Failure occurred in the west end of the specimen.

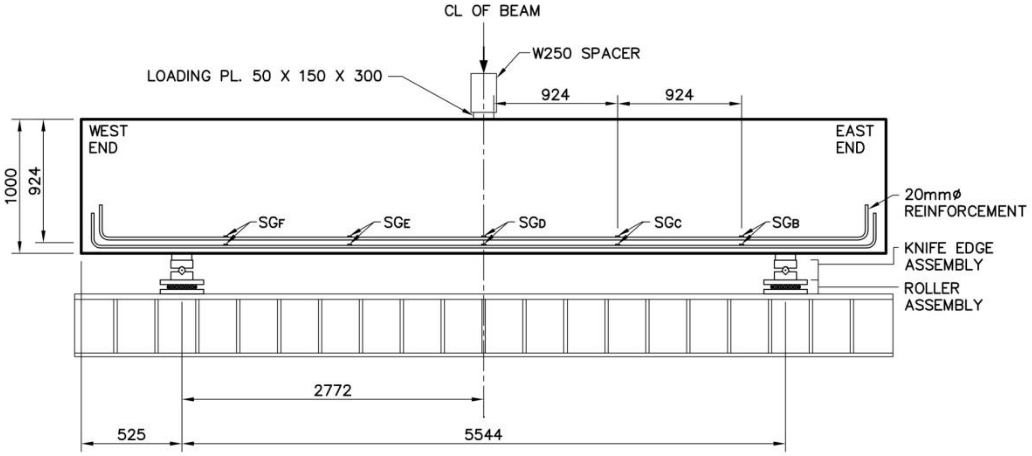

Figure C.4-1: Specimen S1000-B1 Test Setup and Configuration

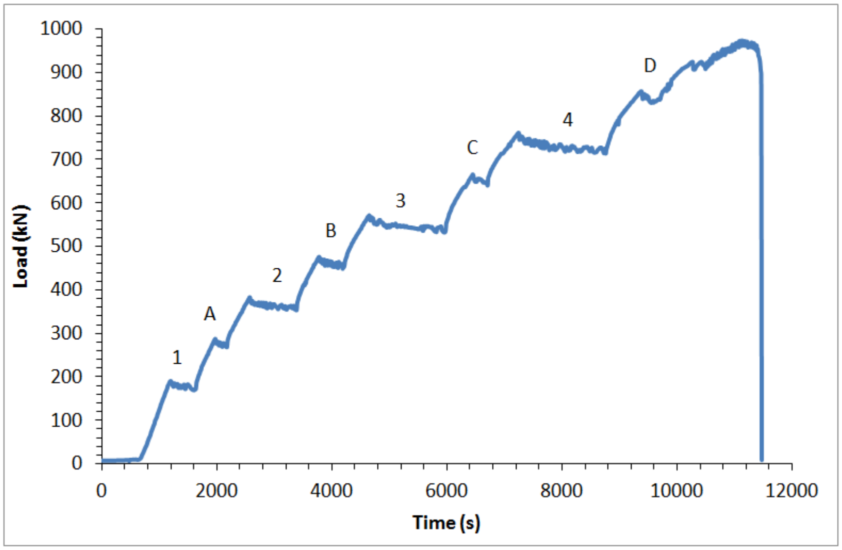

Figure C.4-2: Specimen S1000-B1 Load Stages

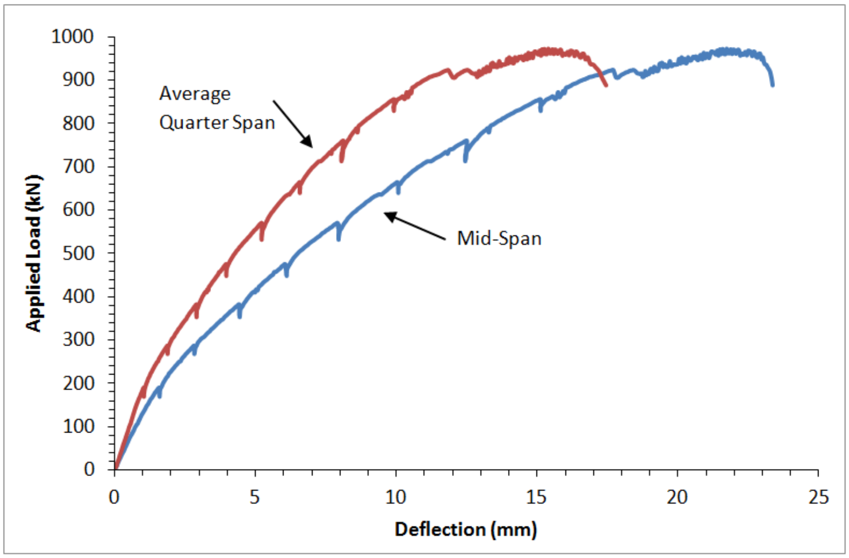

Figure C.4-3: Specimen S1000-B1 Load-Deflection Relationships

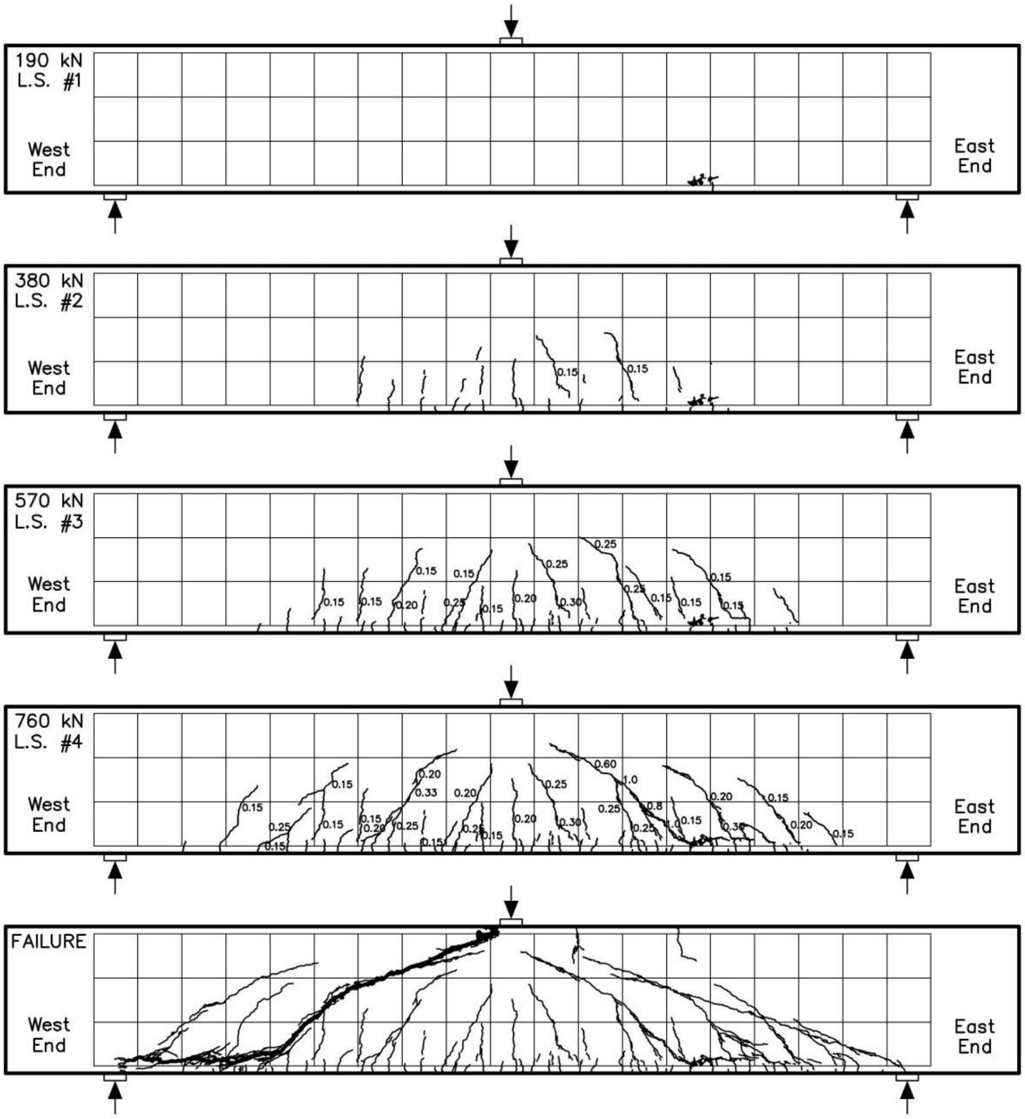

Figure C.4-4: Specimen S1000-B1 Crack Patterns and Widths at Each Numbered Load Stage

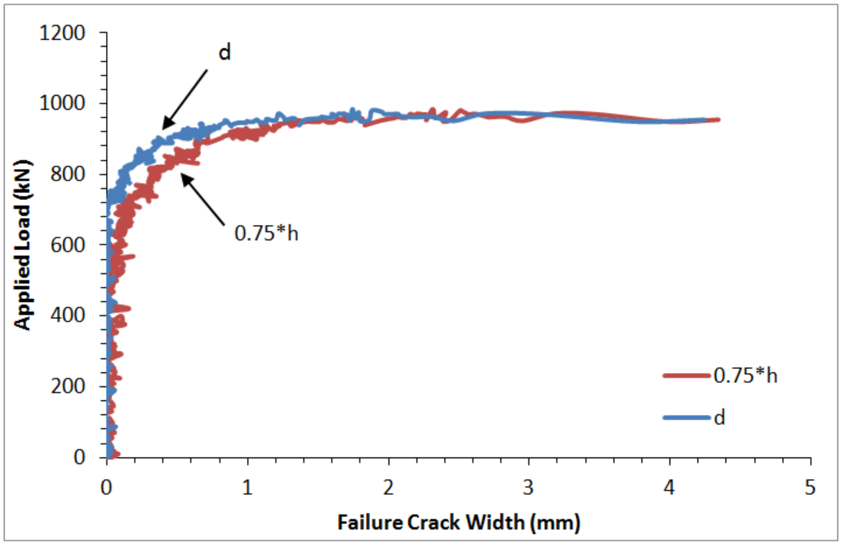

Figure C.4-5: Specimen S1000-B1 Failure Crack Growth Throughout Testing

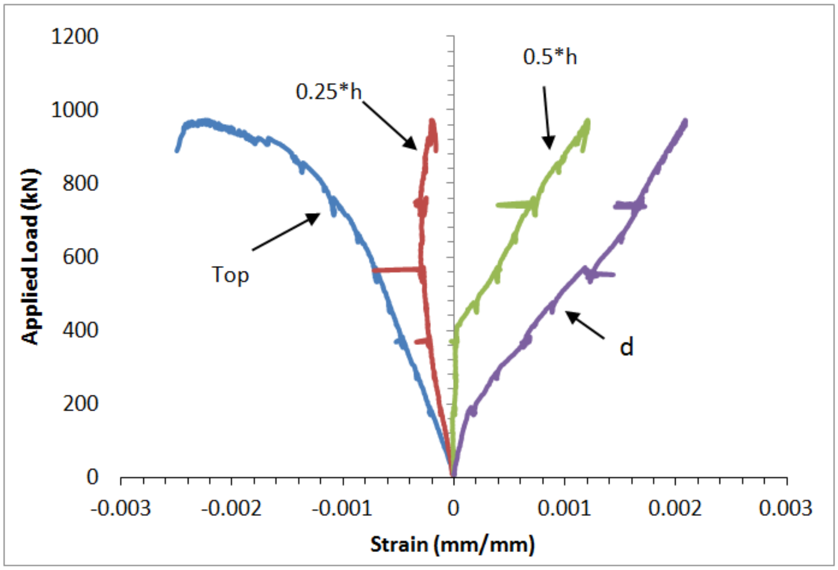

Figure C.4-6: Specimen S1000-B1 Concrete Surface Strains as Measured by PI Gauges Throughout Testing

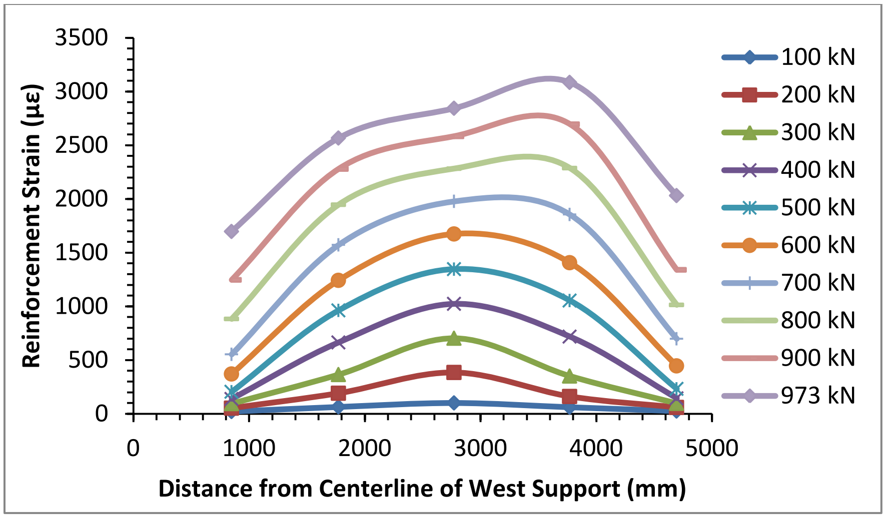

Figure C.4-7: Specimen S1000-B1 Longitudinal Reinforcement Strains at Various Load Stages

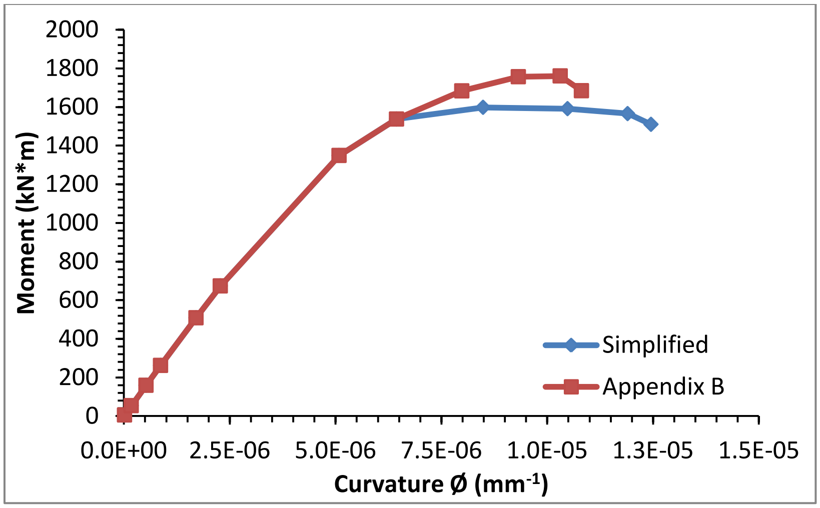

Figure C.4-8: Specimen S1000-B1 Predicted Moment-Curvature Relationships

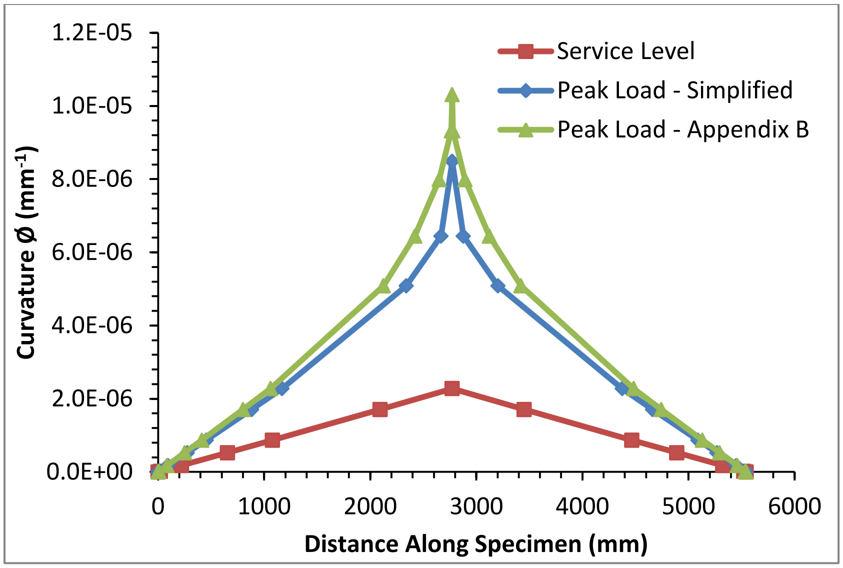

Figure C.4-9: Predicted Curvatures Along the Length of Specimen S1000-B1

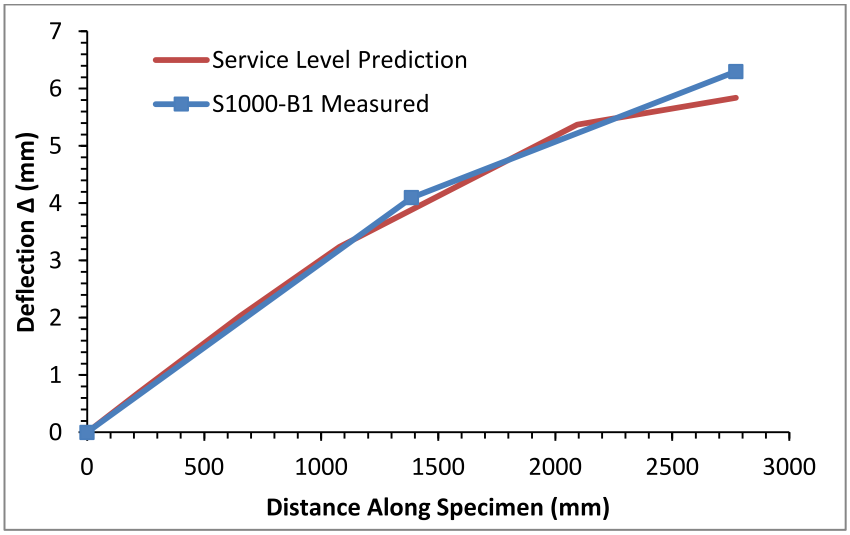

Figure C.4-10: Comparison of Predicted and Measured Service Load Deflections the Along Length of Specimen S1000-B1

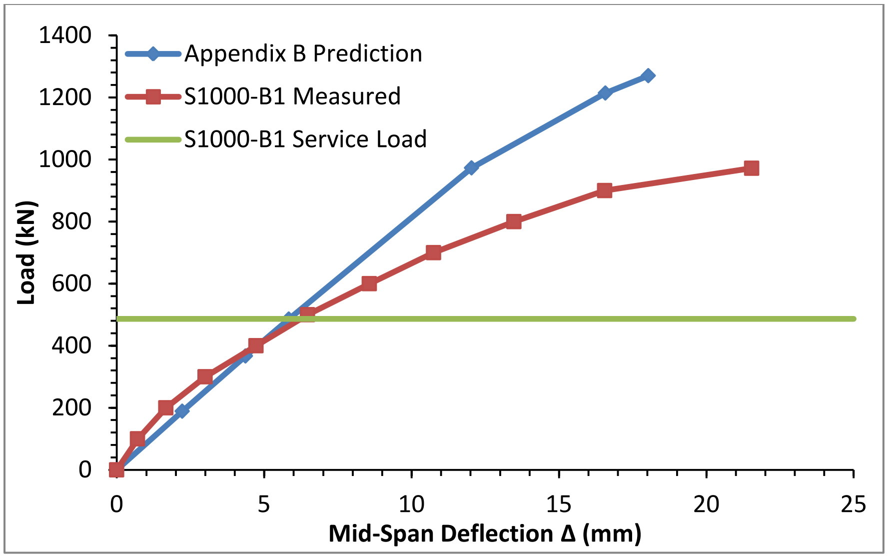

Figure C.4-11: Comparison of Predicted and Measured Load-Mid-Span Deflection Relationships for Specimen S1000-B1

C.5 Specimen S1000-B2

Specimen S1000-B2 was the second specimen from Casting B to be tested, and the fourth specimen overall. The displacement controlled loading rate used was 0.25 mm/min. Failure occurred in the west end of the specimen.

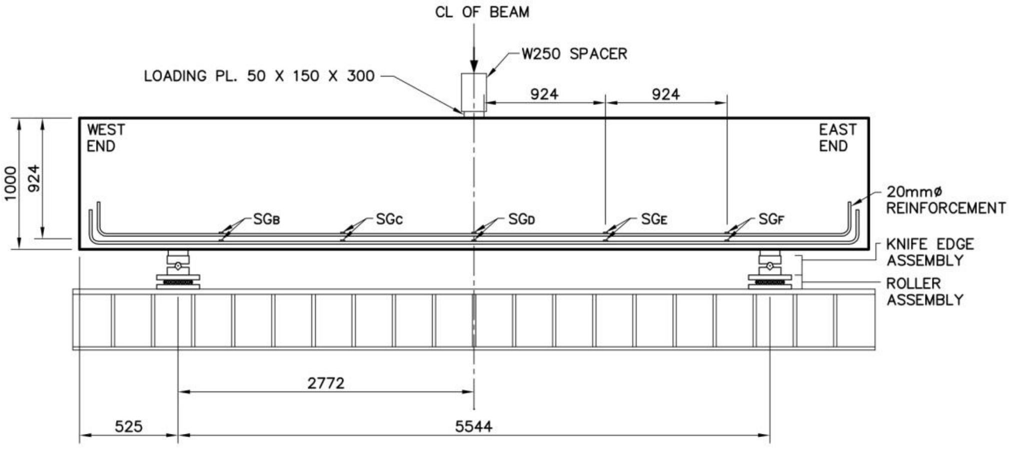

Figure C.5-1: Specimen S1000-B2 Test Setup and Configuration

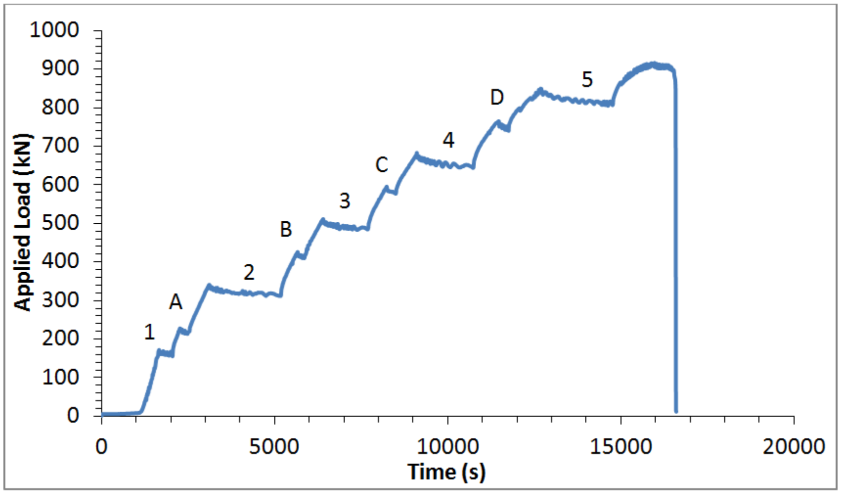

Figure C.5-2: Specimen S1000-B2 Load Stages

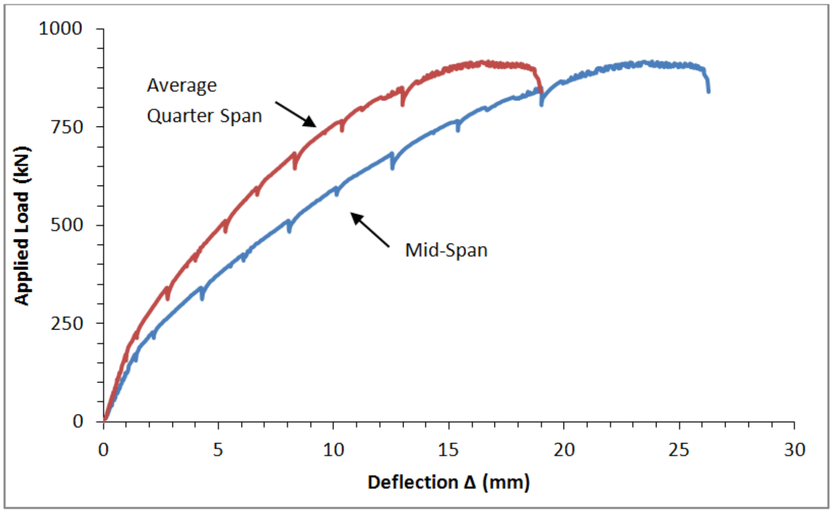

Figure C.5-3: Specimen S1000-B2 Load-Deflection Relationships

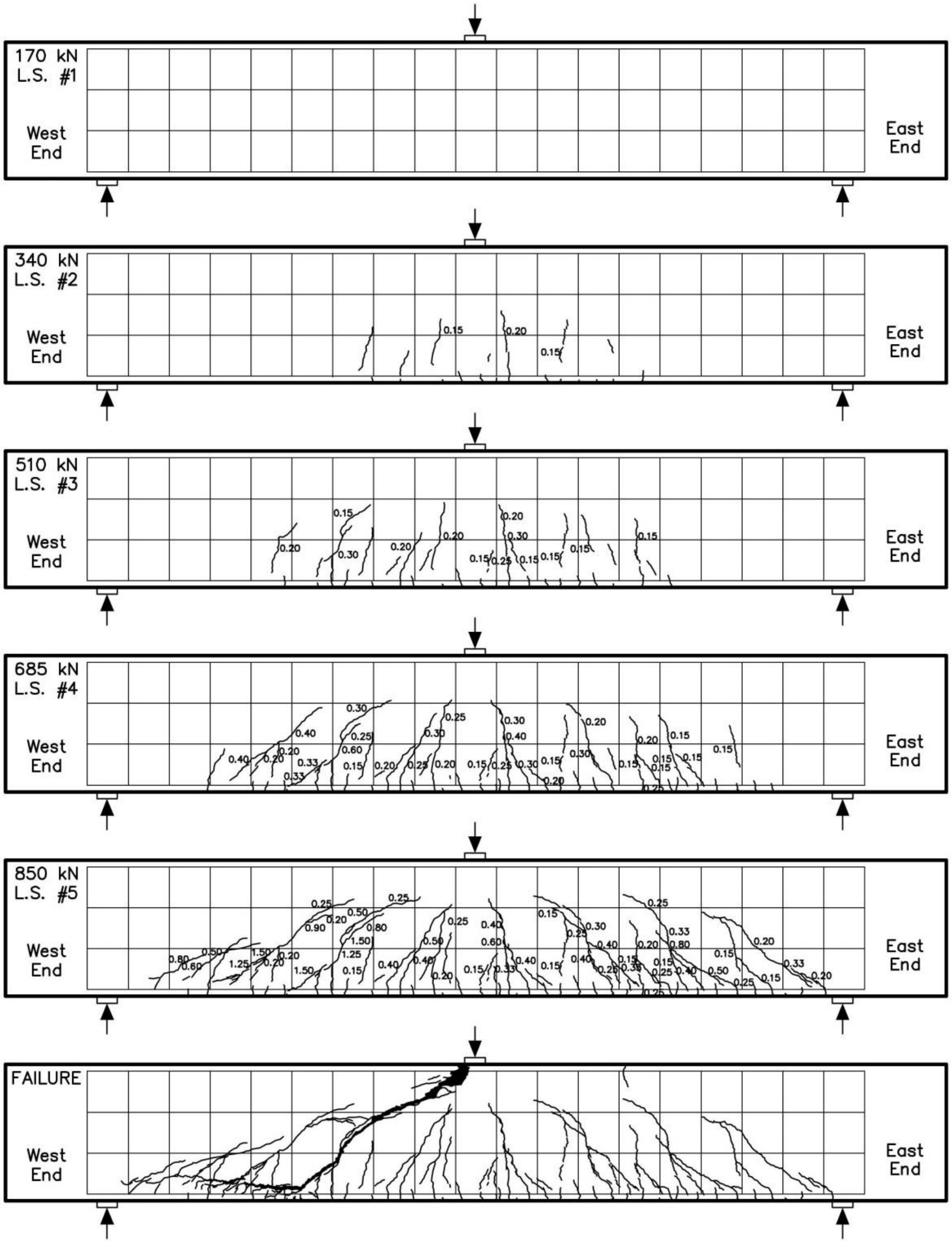

Figure C.5-4: Specimen S1000-B2 Crack Patterns and Widths at Each Numbered Load Stage

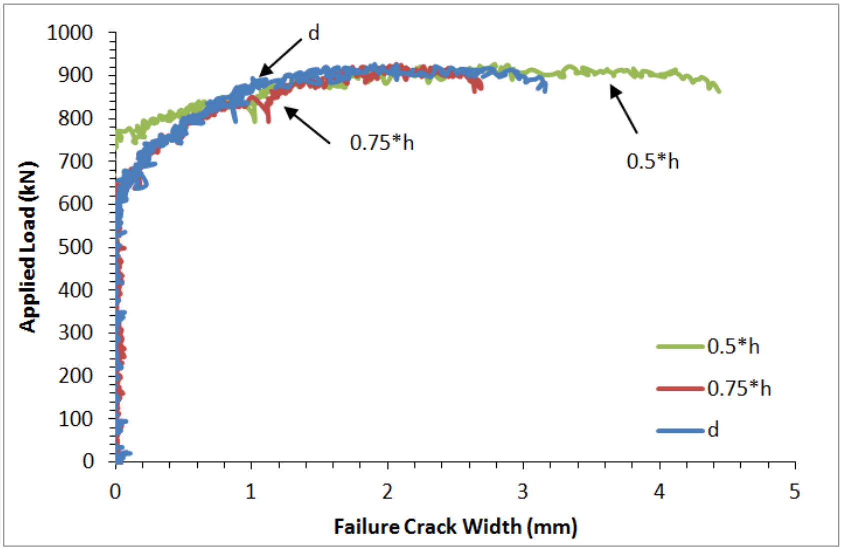

Figure C.5-5: Specimen S1000-B2 Failure Crack Growth Throughout Testing

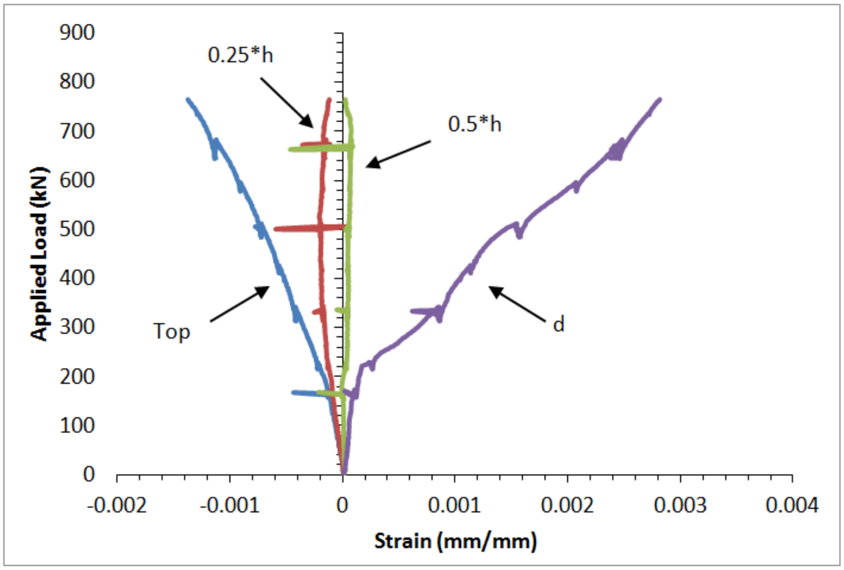

Figure C.5-6: Specimen S1000-B2 Concrete Surface Strains as Measured by PI Gauges Throughout Testing

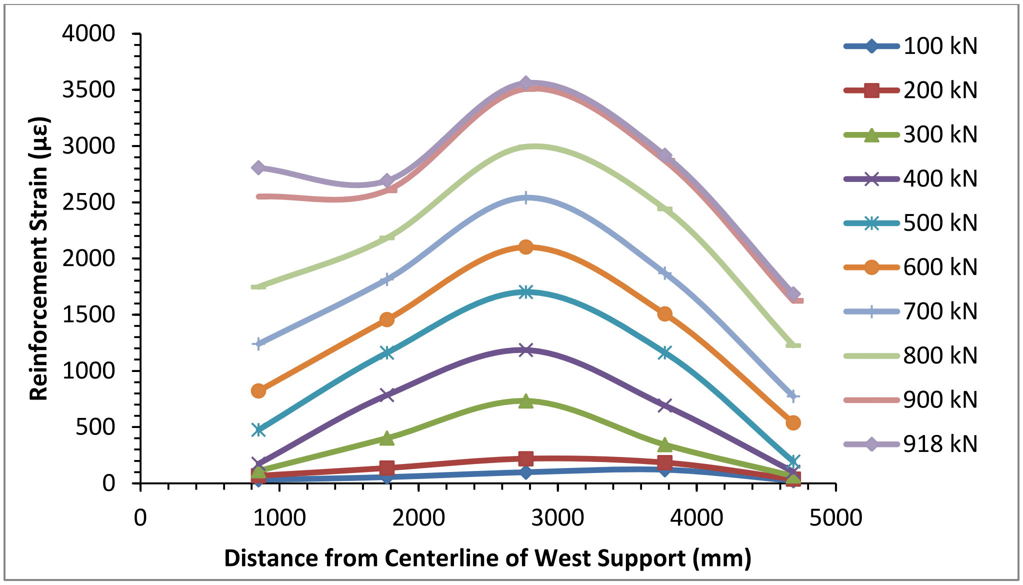

Figure C.5-7: Specimen S1000-B2 Longitudinal Reinforcement Strains at Various Load Stages

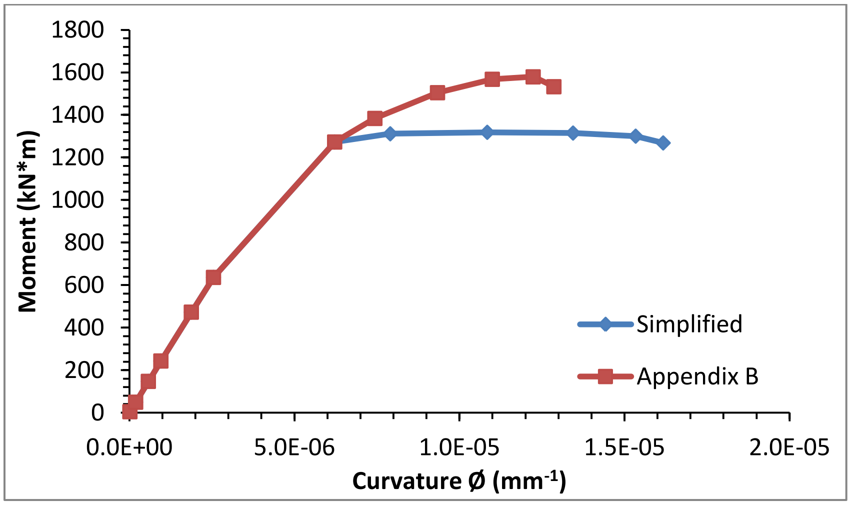

Figure C.5-8: Specimen S1000-B2 Predicted Moment-Curvature Relationships

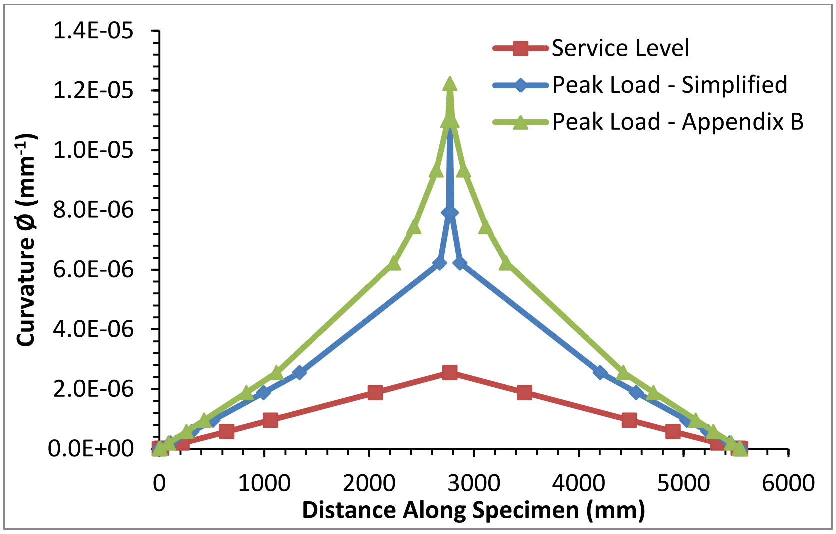

Figure C.5-9: Predicted Curvatures Along the Length of Specimen S1000-B2

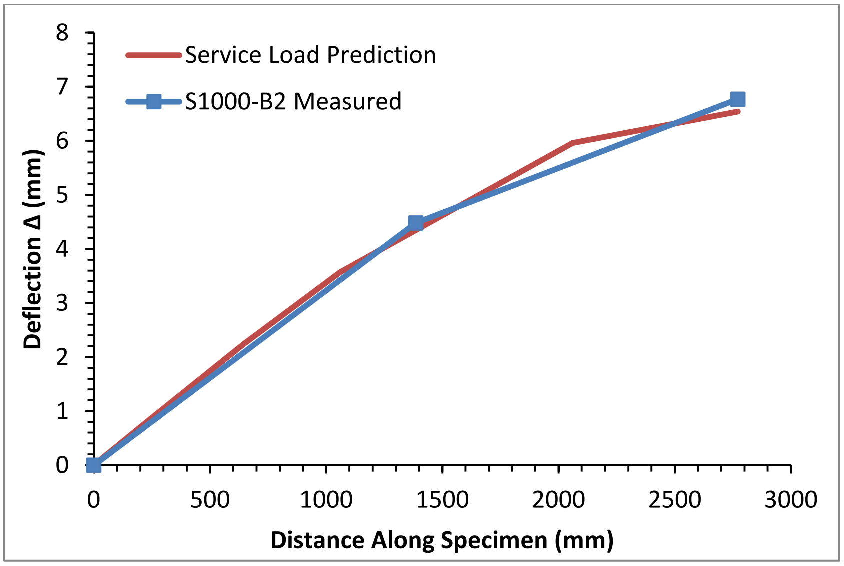

Figure C.5-10: Comparison of Predicted and Measured Service Load Deflections Along the Length of Specimen S1000-B2

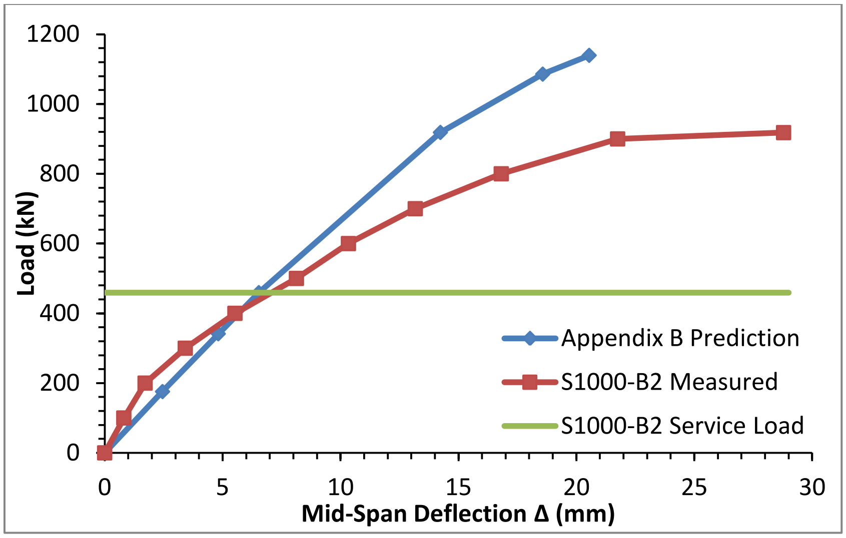

Figure C.5-11: Comparison of Predicted and Measured Load-Mid-Span Deflection Relationships for Specimen S1000-B2

C.6 Specimen S1000-A3

Specimen S1000-A3 was the second specimen from Casting A to be tested, and the second specimen overall. A displacement controlled loading rate of 0.40 mm/min. Failure occurred in the east end of the specimen.

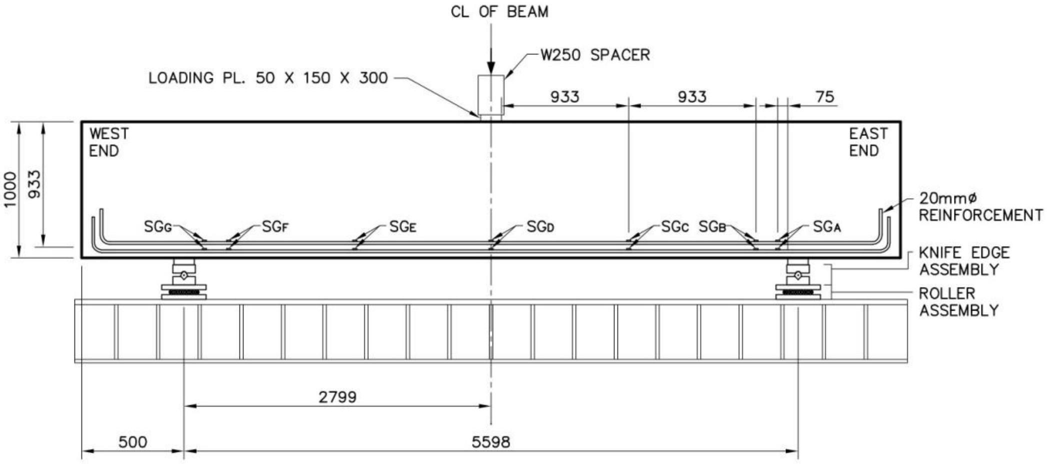

Figure C.6-1: Specimen S1000-A3 Test Setup and Configuration

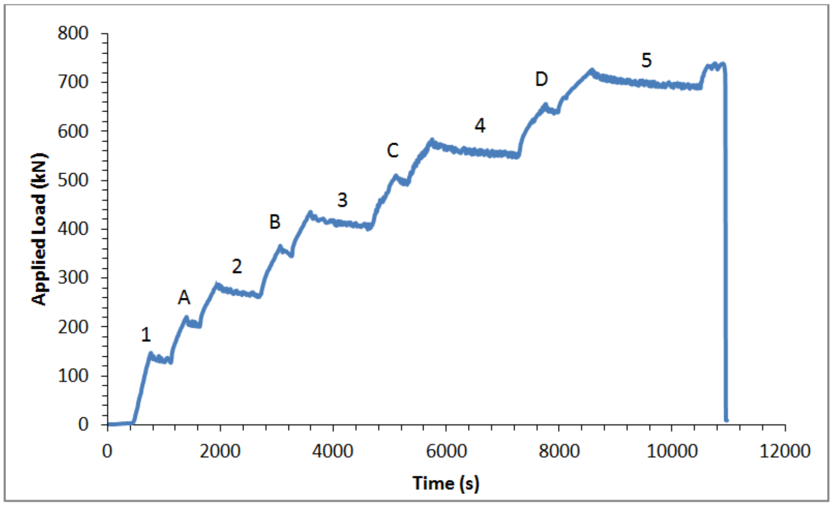

Figure C.6-2: Specimen S1000-A3 Load Stages

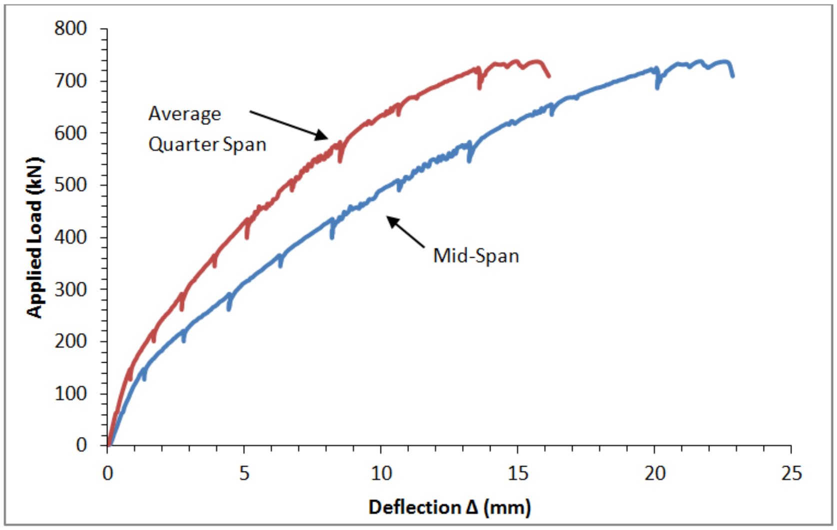

Figure C.6-3: Specimen S1000-A3 Load-Deflection Relationships

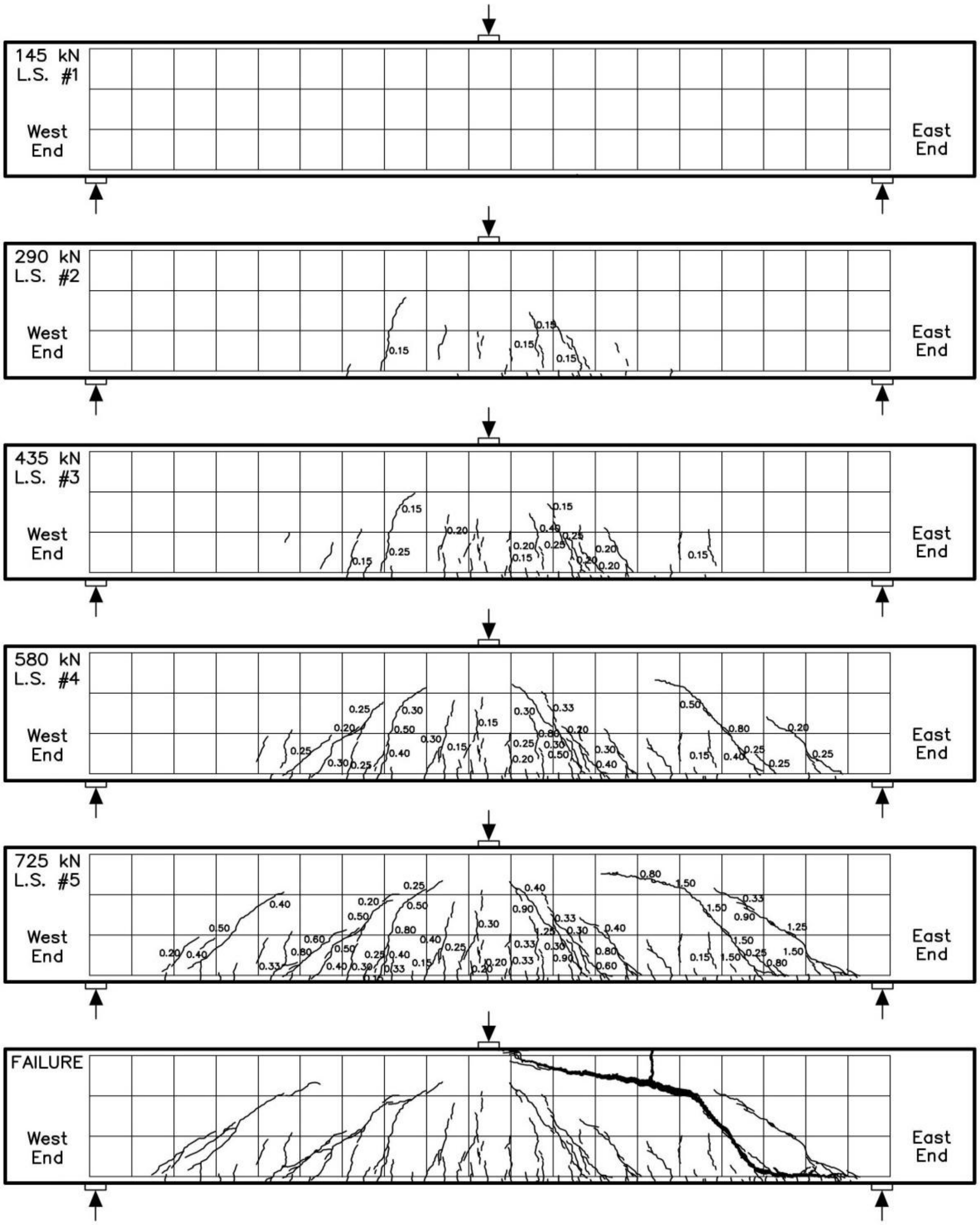

Figure C.6-4: Specimen S1000-A3 Crack Patterns and Widths at Each Numbered Load Stage

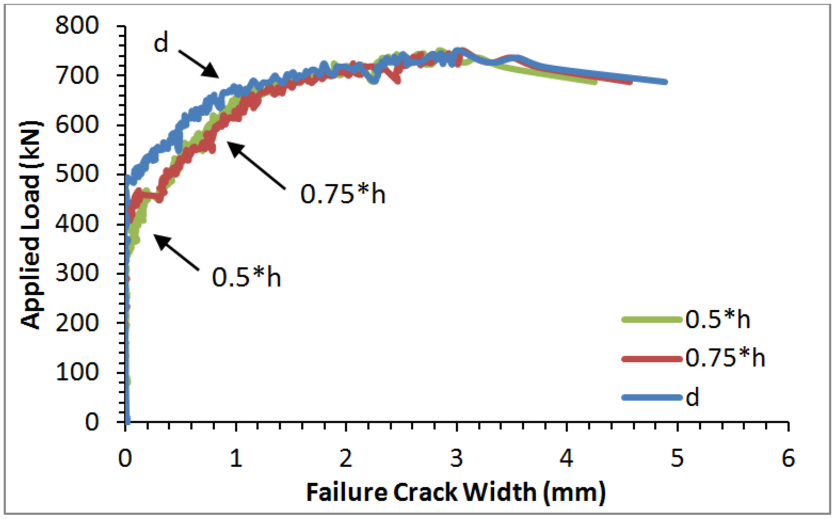

Figure C.6-5: Specimen S1000-A3 Failure Crack Growth Throughout Testing

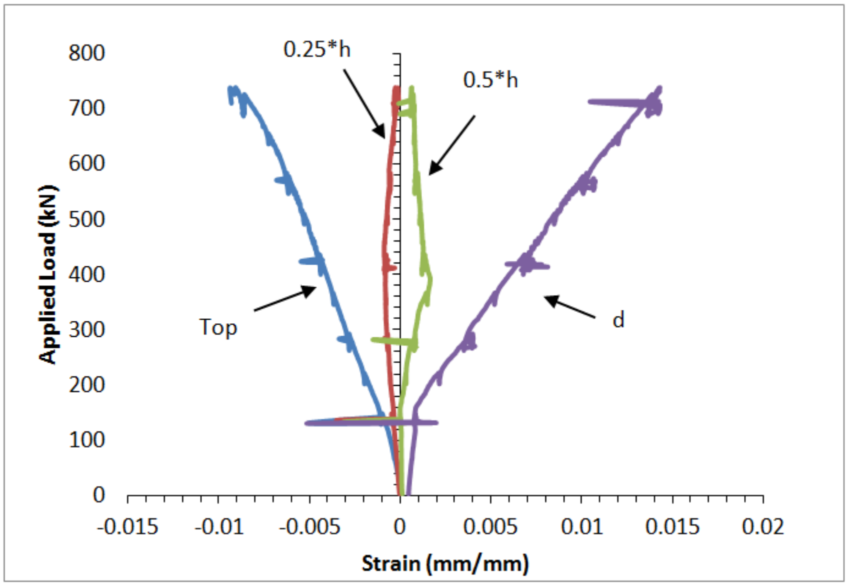

Figure C.6-6: Specimen S1000-A3 Concrete Surface Strains as Measured by PI Gauges Throughout Testing

The strain gauge located adjacent to the west support failed prior to testing. Although data is unavailable at this end, the strain gauge at the opposite support was successful (refer to Figure C.6-7).

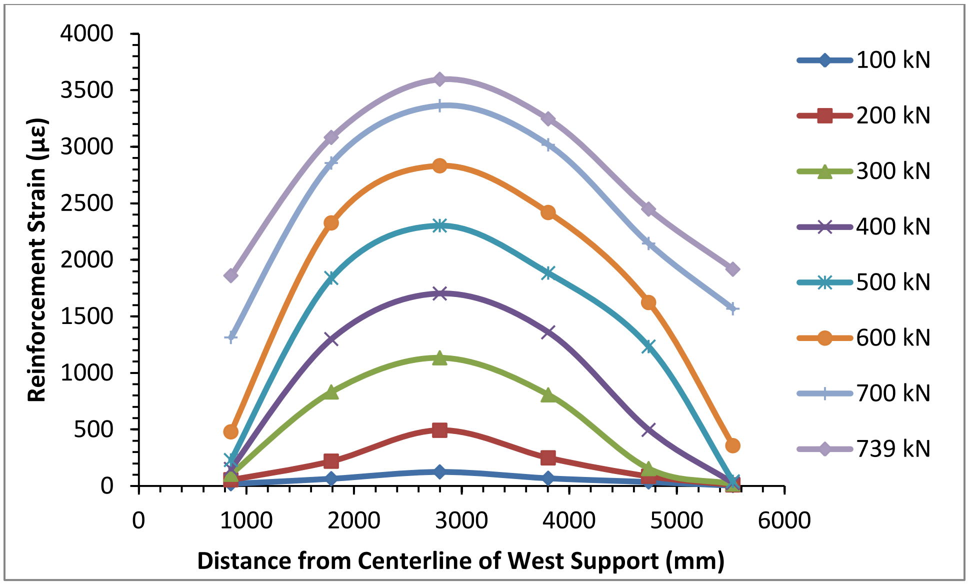

Figure C.6-7: Specimen S1000-A3 Longitudinal Reinforcement Strains at Various Load Stages

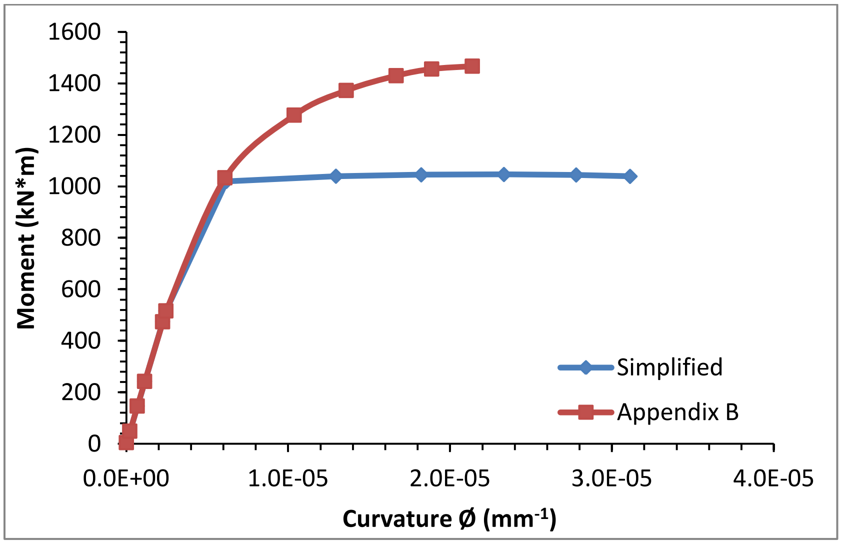

Figure C.6-8: Specimen S1000-A3 Predicted Moment-Curvature Relationships

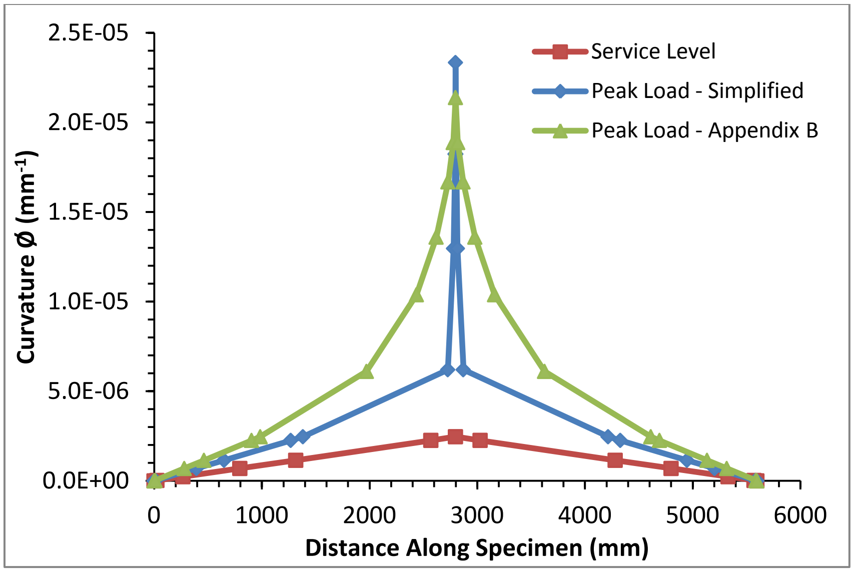

Figure C.6-9: Predicted Curvatures Along the Length of Specimen S1000-A3

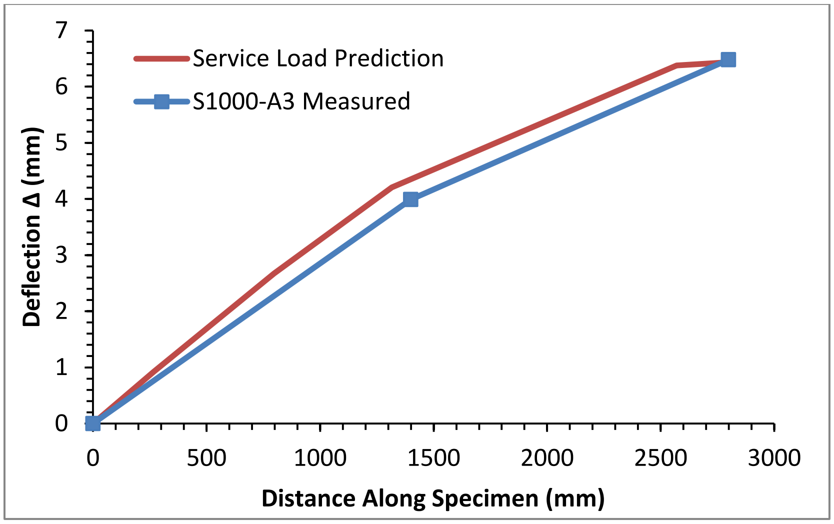

Figure C.6-10: Comparison of Predicted and Measured Service Load Deflections Along the Length of Specimen S1000-A3

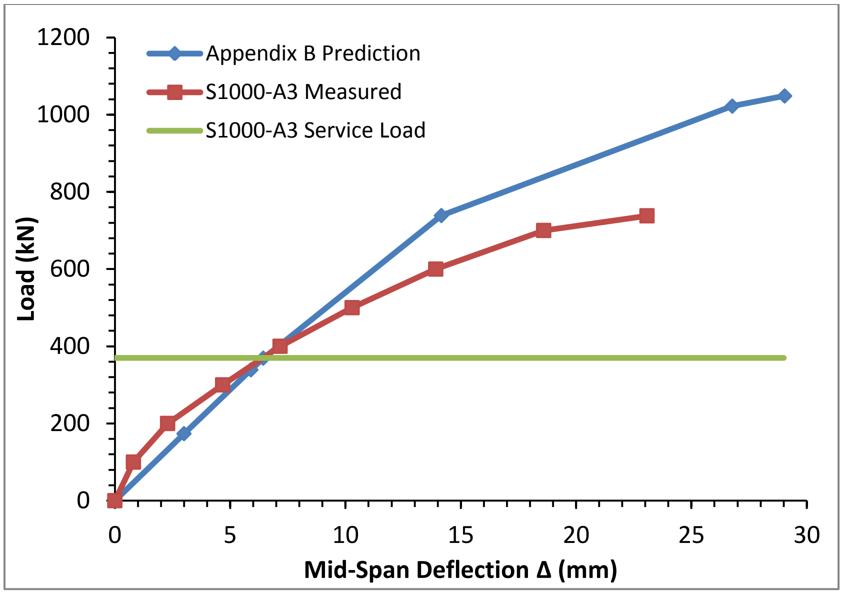

Figure C.6-11: Comparison of Predicted and Measured Load-Mid-Span Deflection Relationships for Specimen S1000-A3

C.7 Specimen S1000-A4

Specimen S1000-A4 was the first specimen tested. A displacement controlled loading rate of 0.20 mm/min was used for the initial stages of testing, but was increased to 0.25 mm/min at Stage 5 (approximately 550 kN). Failure occurred in the west end of the specimen.

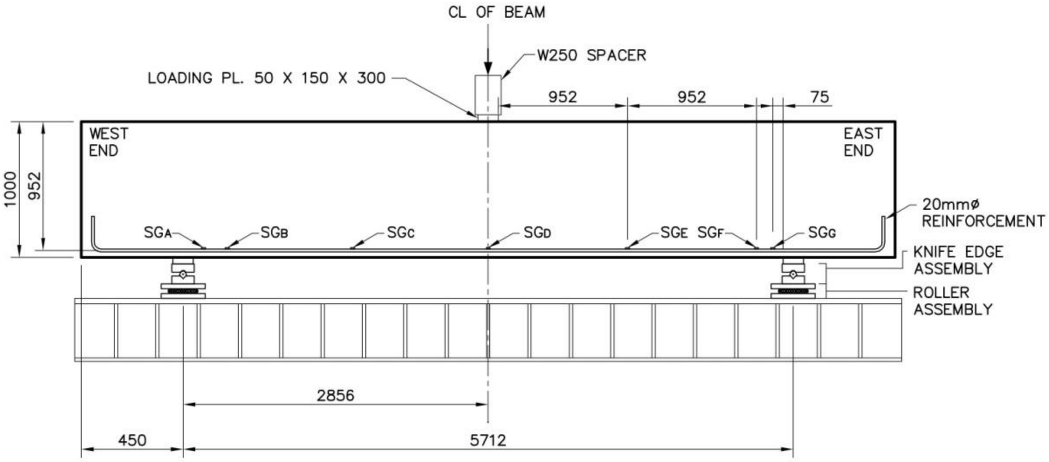

Figure C.7-1: Specimen S1000-A4 Test Setup and Configuration

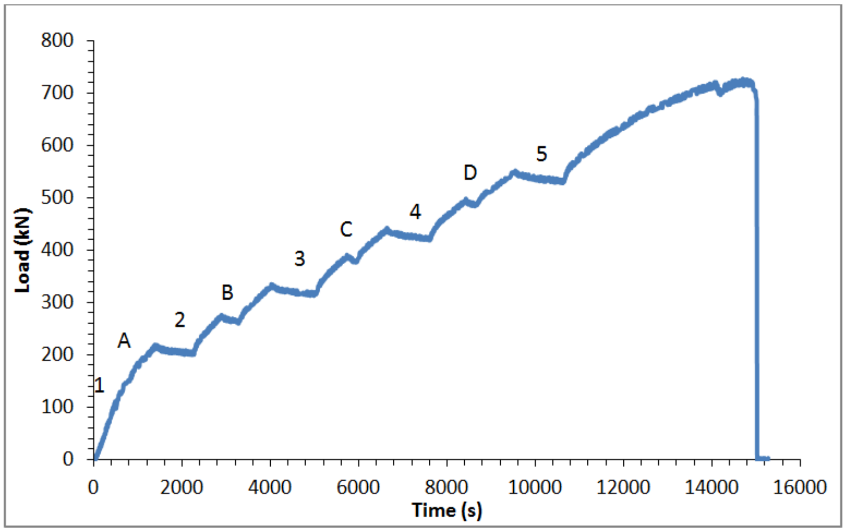

Figure C.7-2: Specimen S1000-A4 Load Stages

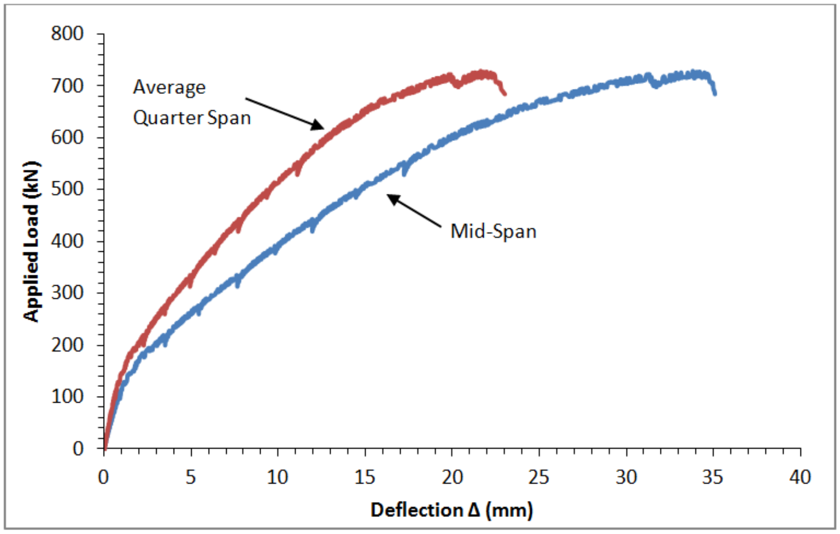

Figure C.7-3: Specimen S1000-A4 Load-Deflection Relationships

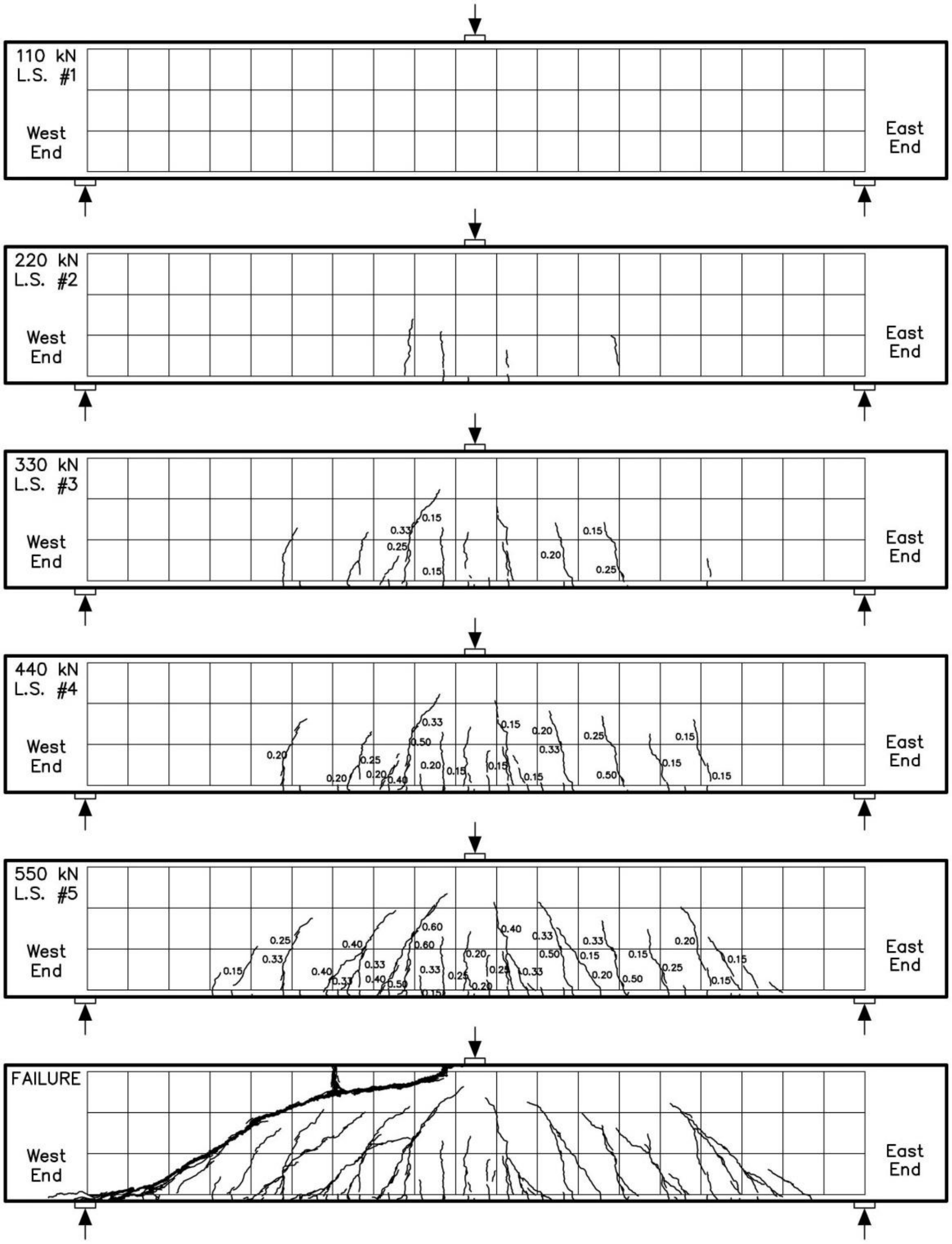

Figure C.7-4: Specimen S1000-A4 Crack Patterns and Widths at Each Numbered Load Stage

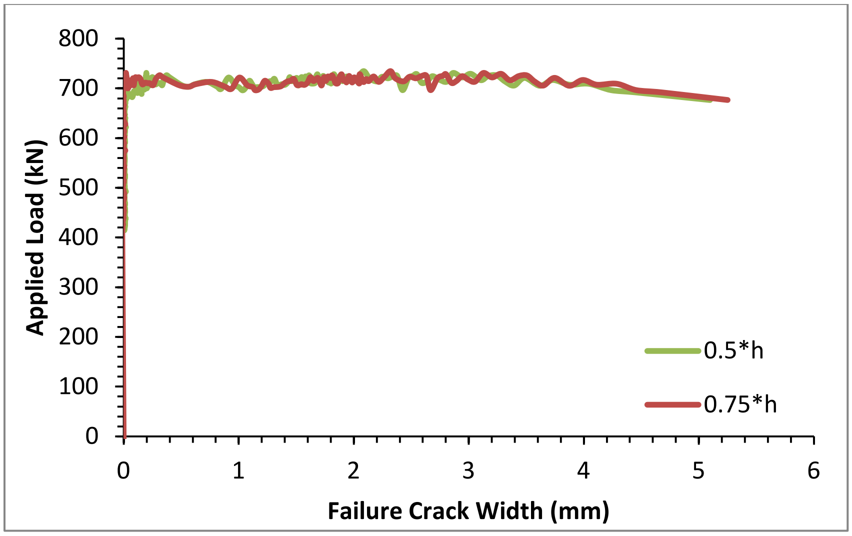

Figure C.7-5: Specimen S1000-A4 Failure Crack Growth Throughout Testing

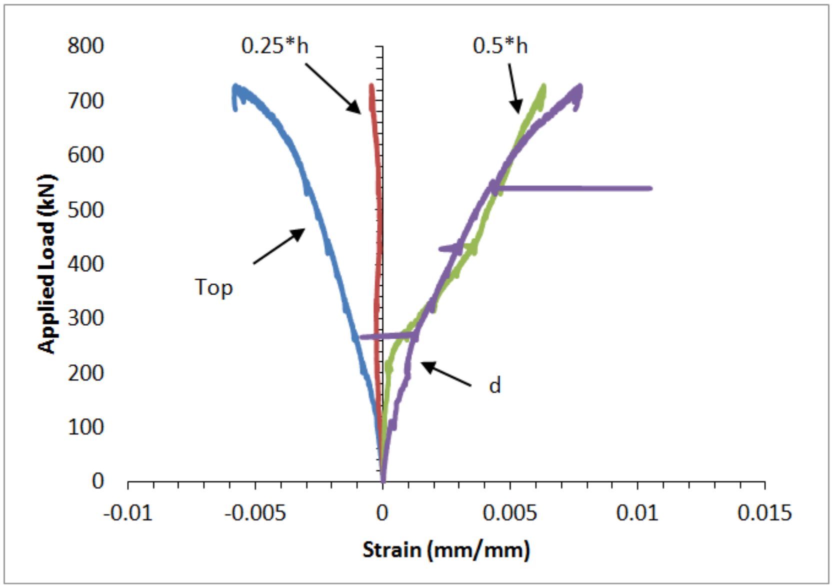

Figure C.7-6: Specimen S1000-A4 Concrete Surface Strains as Measured by PI Gauges Throughout Testing

The mid-span strain gauges on the longitudinal reinforcement at mid-span and adjacent to the west support failed prematurely and are not included in Figure C.7-7.

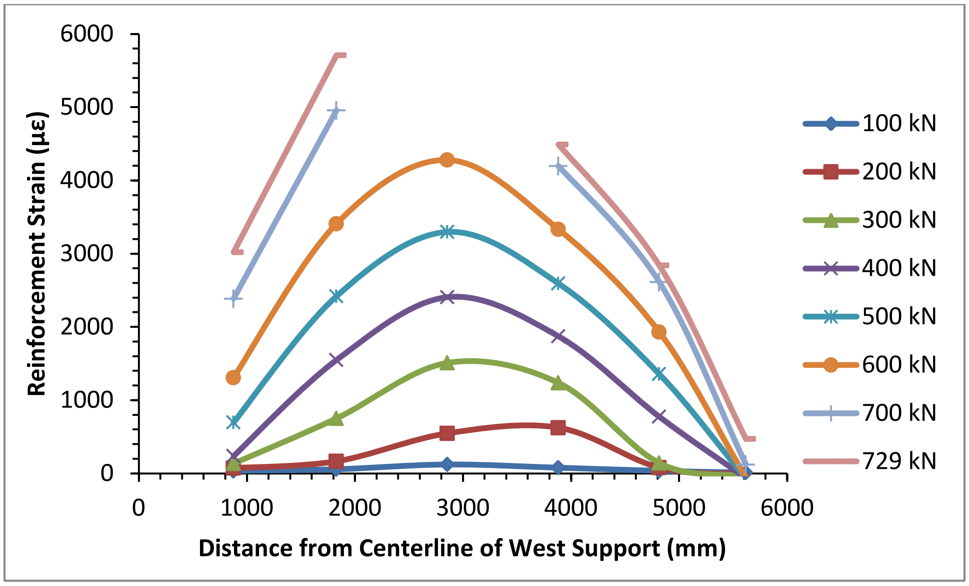

Figure C.7-7: Specimen S1000-A4 Longitudinal Reinforcement Strains at Various Load Stages

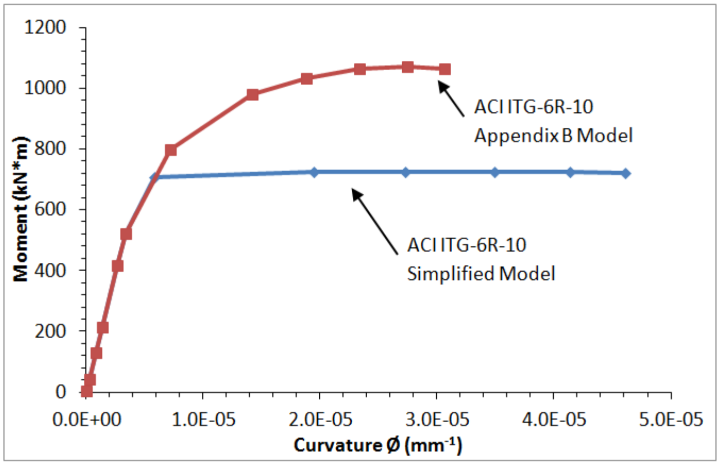

Figure C.7-8: Specimen S1000-A4 Predicted Moment-Curvature Relationships

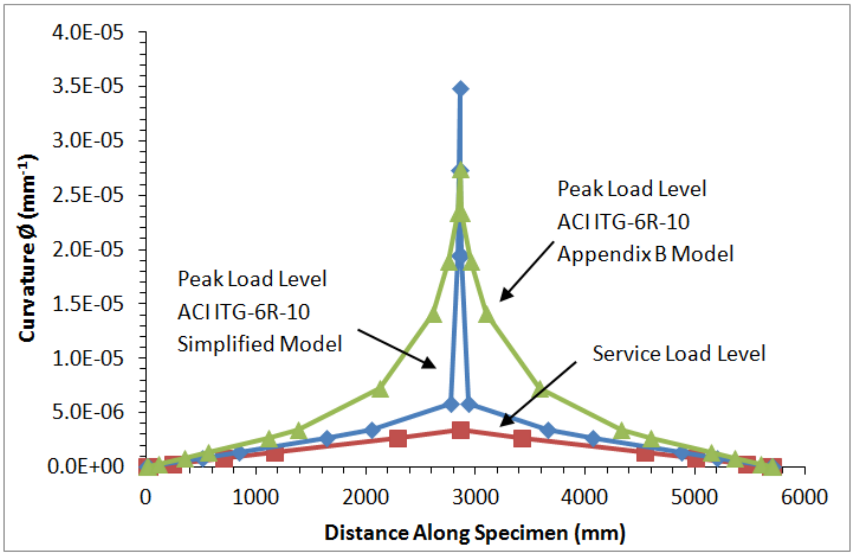

Figure C.7-9: Predicted Curvatures Along the Length of Specimen S1000-A4

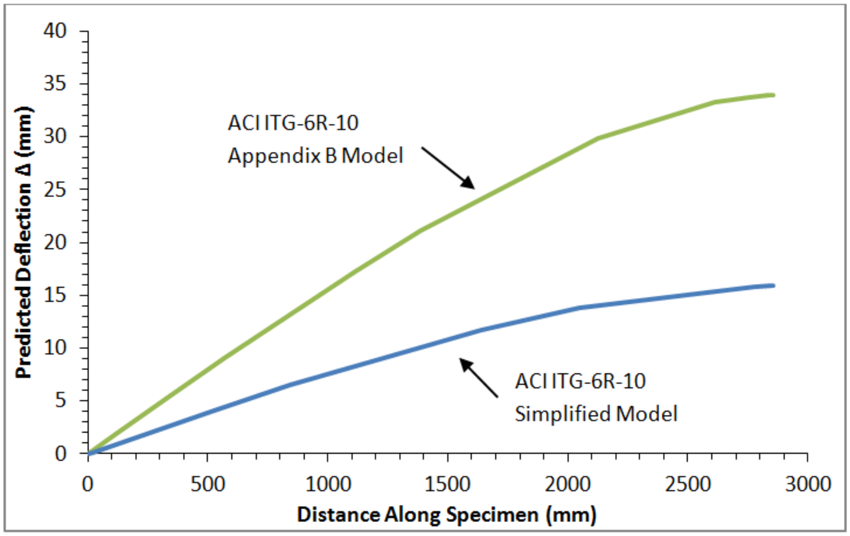

Figure C.7-10: Predicted Peak Load Deflections Along the Length of Specimen S1000-A4

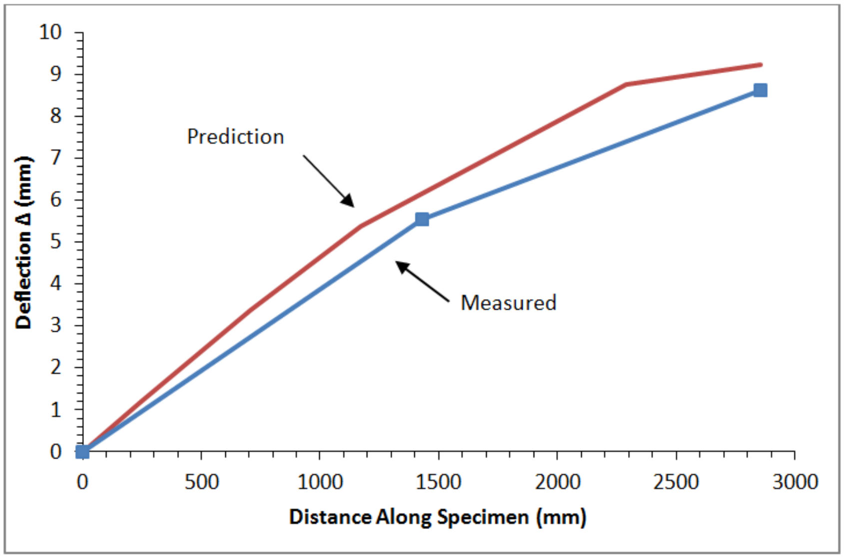

Figure C.7-11: Comparison of Predicted and Measured Service Load Deflections Along the Length of Specimen S1000-A4

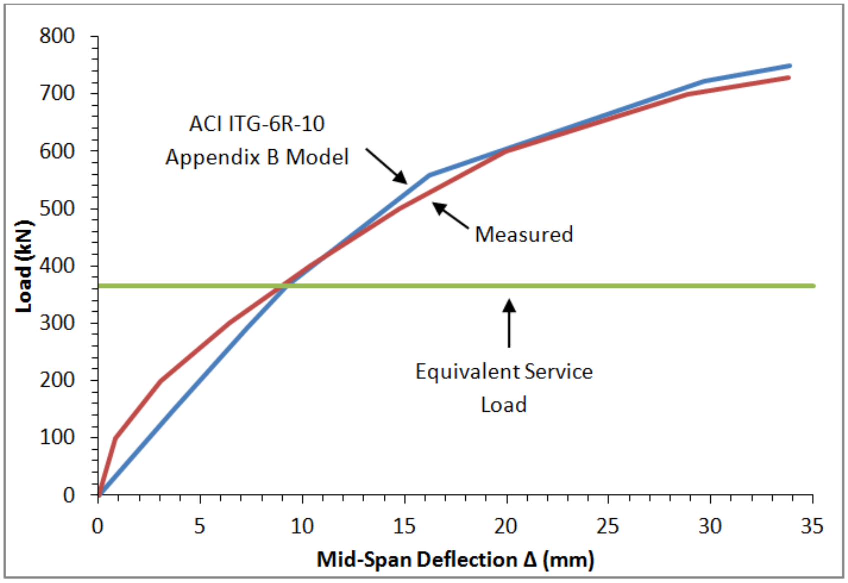

Figure C.7-12: Comparison of Predicted and Measured Load-Mid-Span Deflection Relationships for Specimen S1000-A4